COMPUTATIONAL OPTIMIZATION OF DESIGN AND VARIABLE OPERATION OF CO_2-CAPTURE-ENABLED COAL-NATURAL GAS POWER PLANTS

A DISSERTATION SUBMITTED TO THE DEPARTMENT OF
ENERGY RESOURCES ENGINEERING
AND THE COMMITTEE ON GRADUATE STUDIES OF
STANFORD UNIVERSITY IN PARTIAL FULFILLMENT OF
THE REQUIREMENTS FOR THE DEGREE OF
DOCTOR OF PHILOSOPHY

Charles A Kang
July 2015

This dissertation is online at: http://purl.stanford.edu/xc022ty7016

I certify that I have read this dissertation and that, in my opinion, it is fully adequate in scope and quality as a dissertation for the degree of Doctor of Philosophy.

Adam Brandt, Primary Adviser

I certify that I have read this dissertation and that, in my opinion, it is fully adequate in scope and quality as a dissertation for the degree of Doctor of Philosophy.

Louis Durlofsky, Primary Adviser

I certify that I have read this dissertation and that, in my opinion, it is fully adequate in scope and quality as a dissertation for the degree of Doctor of Philosophy.

Sally Benson

Approved for the Stanford University Committee on Graduate Studies.

Patricia J. Gumport, Vice Provost for Graduate Education

This signature page was generated electronically upon submission of this dissertation in electronic format. An original signed hard copy of the signature page is on file in University Archives.

Abstract

Climate change mitigation will require large reductions in CO_2 emissions from electricity production. Some of these cuts will come from increased use of renewable energy resources, but it is likely that thermal power plants will be used for an extended period of time to maintain grid stability and accommodate seasonal variability in renewable generation. Therefore, thermal power plants with CO_2 capture and storage (CCS) capability may coexist with renewable generation to provide reliable low-carbon electricity. Moreover, CCS-enabled facilities designed for constant operations are not necessarily optimal under the conditions that are likely to occur with increased renewable penetration. There is therefore a need to devise optimal designs and operating plans for flexible thermal power stations equipped with CCS.

In this work, computational optimization is used to determine the design and operating plan of a coal-natural gas power station with CO_2 capture, under a CO_2 emission performance standard. The facility consists of a coal power plant undergoing a retrofit with solvent-based post-combustion CO_2 capture. The heat for CO_2 capture solvent regeneration is provided by a combined cycle gas turbine (CCGT) designed for combined-heat-and-power service. Variable facility operations are represented by discrete operating modes dispatched using the electricity price-duration curve.

Two problem formulations are considered. In the 'simplified-capture' problem formulation, the CO_2 capture system is represented using a single variable for capacity, while heat integration (including a detailed treatment of the heat recovery steam generator component of the CCGT) is optimized jointly with variable operations. In the 'full-system' problem formulation, the detailed design of the CO_2 capture system

is optimized alongside a full treatment of heat integration and variable operations. To accomplish this, a computationally efficient proxy model of the CO_2 capture system is developed that reproduces the behavior of a full-physics Aspen Plus model. Both problem formulations are incorporated in a bi-objective mixed-integer nonlinear program in which total capital requirement (TCR) is minimized and net present value (NPV) is maximized. Pareto frontiers are generated for six scenarios constructed from recent historical data from West Texas, the United Kingdom, and India. All six scenarios are considered using the simplified-capture problem formulation. The West Texas base scenario and the India scenario, which differ greatly from each other, are considered using the full-system problem formulation as well.

Results between the two formulations are quite consistent and show that hourly electricity price variability and the choice of objective function can have a large effect on optimal design and planned operations. In the West Texas base scenario, which has high price variability, the maximum NPV facility in the full-system formulation (NPV of $201 million, TCR of $510 million) has a time-varying operating plan in which the CO_2 capture system has a utilization factor of 66% (out of a maximum of 85%). In this scenario the minimum TCR facility (NPV of $101 million, TCR of $333 million) has a constant operating profile. In contrast, low price variability in the India scenario results in constant operations regardless of objective. Two advanced CO_2 capture processes—the mixed salt and piperazine processes—are considered using the simplified-capture formulation for the West Texas base scenario. The advanced processes are shown to outperform the standard monoethanolamine (MEA) process, with the mixed salt process outperforming the MEA process by 16% for maximum NPV and 14% for minimum TCR. The full-system formulation using the MEA process provides generally similar results to those from the simplified-capture formulation in both the India and West Texas base scenarios. However, the inclusion of the detailed design of the CO_2 capture process in the full-system problem formulation provides valuable design information, such as the effect of the integer nature of the number of CO_2 capture trains. Taken in total, the results of this study highlight the value of applying computational optimization to consider integrated plant design and variable operations together.

Acknowledgements

I begin by thanking my advisers, Louis Durlofsky and Adam Brandt, who have been insightful, supportive, and all around terrific advisers. Working with them has been a wonderful way to learn and grow in many ways, including in research skills, communication skills, and professionalism. I would also like to thank the other members of my defense committee, Sally Benson, Anthony Kovscek, and William Mitch. In particular, Sally Benson helped with framing my research within the broader energy landscape, and she also read this thesis and provided helpful comments.

I am grateful to everyone who shared resources or collaborated with me. Philip Brodrick helped with many aspects of organizing and testing the code developed in this work. Obiajulu Isebor provided the BiPSOMADS optimization code, and helped me extensively in its use. Indira Jayaweera shared data about the mixed salt process. Howard Herzog shared the MEA CO_2 capture Aspen Plus model that Anusha Kothandaraman developed. Adelaide Calbry-Muzyka helped with Aspen Plus, and Dennis Michael helped with the parallel computing cluster.

Many people have provided advice that informed parts of this work. I thank Anthony Pavone and Christopher Edwards for conversations about HRSGs and plant design, Jennifer Wilcox and Dale Simbeck for discussions about CO_2 capture processes and power plants, Nicholas Jenkins and Ram Rajagopal for discussions about electricity markets, Michal Bialkowski for conversations about gas turbines, Srikanta Mishra and Sumeet Trehan for advice on statistical proxy models, and Yuanqing Zhu for preliminary Aspen Plus model development. I also thank Vena Kostroun, Gary

Dorris, Patrick Sullivan, Walter Short, and Stuart Macmillan for opportunities to explore energy systems in summer internships with their organizations.

The students, staff, and faculty of the Department of Energy Resources Engineering and other organizations at Stanford have created a wonderful culture to learn and work in, and I thank all of them for their hard work. My officemates Obi, Mike, Mark, Phil, Jack, and Michael deserve special recognition for the long hours we have spent together. I also thank the Illich-Sadowsky Stanford Interdisciplinary Graduate Fellowship and the Two Elk Energy Park Integrated Clean Energy Solutions Fund for supporting my studies.

My friends and family have greatly enriched my life over the past six years. Thank you to the trivia and hat crew, Sandwich Club associates, LGCC folks, the Italy crew, and other friends for keeping it real. Last but certainly not least, I thank my family—my sister Cheryl, my dad Andy, and my mom Nina—for all their love and support. I would not be who I am today without them.

Contents

List of Tables

List of Figures

Chapter 1

Introduction

In major economies around the world, a large number of coal-fired power plants exist with decades of life remaining. Furthermore, over 1,400 GW of new coal-fired generation capacity were proposed to be added worldwide as of 2012 (Yang and Cui, 2012). Given the challenge of global climate change, reducing CO_2 emissions from these power plants is of great importance. Carbon dioxide capture and storage (CCS) is attractive as this technology can greatly reduce CO_2 emissions from fossil-fuel-fired power generation (Metz et al., 2005). If combined with biofuels, CCS could even allow net capture of CO_2 from the atmosphere (Budzianowski, 2012).

Additionally, renewable penetration in the electricity system is likely to increase in the future. With increasing renewable penetration, thermal power generation assets are likely to be required to operate increasingly variably to meet consumer demand. For example, on April 8, 2015, in California, non-renewable power generation (including nuclear, imports, and thermal generation) experienced intra-daily variation in output from 16 GW to 23 GW. This resulted from variability in generation from renewable resources: While total system output was 25 GW at both 1 p.m. and 11 p.m. on that day, renewables provided 9 GW of electric power generation at 1 p.m., and only 2 GW at 11 p.m.

Even in scenarios with very high rates of renewable penetration, substantial thermal generation capacity (though not from traditional baseload assets) will likely be

required to maintain system stability (Elliston et al., 2012; Hart and Jacobson, 2011). Interestingly, with high renewable penetration, the overall electricity system may exhibit diminishing incremental CO_2 emission abatement from adding renewables (Hart and Jacobson, 2012). While Hart and Jacobson (2012) suggest that seasonal-scale energy storage may be a way to achieve full electric decarbonization alongside nearly 100% renewable penetration rates, a plausible complement would be to use CCS-enabled thermal power generation to provide low-carbon grid stabilization in high renewable penetration scenarios. Therefore, there may be a need to develop CCS-enabled thermal power stations that operate variably in time. Such facilities will work in coordination with renewables to achieve deep reductions in CO_2 emissions from electric power generation.

Unfortunately, CCS has drawbacks. First, CCS has large capital costs. Second, CCS can reduce generation capacity for a plant substantially. For solvent-based post-combustion capture processes (which are a leading candidate technology for CO_2 capture), this reduction results primarily from demand for heat for solvent regeneration, and also demand for electrical work for CO_2 compression. The reduced generation capacity from CCS leads to greatly increased operating cost per unit of electricity produced, and additionally may be problematic in regions with growing demand or with supply-constrained grids. Lastly, it is not clear at this time how to best design a CO_2-capture-enabled power station to provide generation flexibility.

In our previous work (Kang et al., 2011, 2012), we developed a modular representation of an integrated energy system similar to the CO_2-capture-enabled coal-natural gas power station we consider here. Those studies developed and applied procedures for the optimization of facility operation, but not for the optimization of facility design. We found that substantial benefits could be obtained from flexible operations, but that the benefit from flexibility was affected by the design of the facility. This indicated that it was necessary to consider both facility design and planned operations together.

In this thesis we apply computational optimization to the design and operation of a CO_2-capture-enabled coal-natural gas power station. We consider a solvent-based post-combustion CO_2 capture system powered by a combined cycle gas turbine (CCGT) system designed for combined-heat-and-power service. In this 'auxiliary' concept, net electricity generation is increased instead of reduced as in 'parasitic' configurations in which steam for solvent regeneration is drawn from the coal plant steam cycle. Our system uses a self-contained heat- and power-integrated capture system based on mature CCGT technology, potentially reducing engineering costs compared to configurations that require site-specific retrofits. Additionally, by using the CCGT to supply heat for the CO_2 capture process, we obtain operational flexibility that would not be achievable with many existing coal-fired power plants.

We consider a bi-objective problem formulation for the minimization of total capital requirement (TCR) and the maximization of net present value (NPV), under a CO_2 emission performance standard. Other objectives could be specified, but these objectives allow us to quantify the tradeoffs between systems with low upfront investment and systems with high economic value. We generate the Pareto frontier, which consists of system designs and operating profiles that are Pareto efficient. For Pareto-efficient solutions, improvement in one objective cannot be achieved without degradation in the other objective. Thus, our Pareto frontiers identify the optimal tradeoff curves between TCR and NPV. This bi-objective formulation provides a rich characterization of the considerations involved in designing a facility for a given scenario.

1.1 Literature review

We draw from four main bodies of literature in this work. The following discussion focuses on developments that are relevant to the modeling and optimization of CO_2-capture-enabled power plants as considered in this thesis. First, we review the growing body of research that concerns the design and variable operation of power plants with CO_2 capture. Next, we review literature on the optimization of the design of

the heat recovery steam generator (HRSG) component of CCGT systems, because our treatment of heat integration draws heavily from this literature. We follow this with a discussion of the use of proxy models in engineering optimization to support the methods we use in our CO_2 capture system model. Finally, we describe some optimization algorithms that have been applied to power system problems, including the ones that we employ in this thesis.

1.1.1 Design and operation of CO_2-capture-enabled power stations

A number of investigators have previously considered the design and operation of power plants with CO_2 capture. We begin by discussing the application of optimization techniques to the design of CO_2 capture systems.

Some of the earliest work in this area addressed the optimal design of CCGT facilities with CO_2 capture (Pelster, 1998; Pelster et al., 2001). In that work, genetic algorithms were applied to minimize the environmental impact and economic costs associated with electricity generation using CCGTs. These optimizations were formulated as mixed-integer nonlinear programming problems. Later, Hasan et al. (2012) applied computational optimization to the design of two different competing CO_2 capture processes (the monoethanolamine, or MEA, process, and membrane separation), and proposed a method to make consistent comparisons of competing candidate processes. Romeo et al. (2009) considered the optimal integration of the CO_2 compression train with the steam cycle of a coal-fired power plant, and observed that integrating the CO_2 compression intercoolers with the low pressure steam turbine chain could yield reductions in compression work duty of up to 40%. Khalilpour and Abbas (2011) optimized the heat integration of a parasitic CO_2 capture retrofit of a coal plant. They showed that careful use of waste heat streams from the coal plant could reduce the energy penalty associated with CO_2 capture from 19.4% to 15.9% in one case study. Multi-objective optimization was applied in designing heat integration for parasitic coal CCS retrofits, identifying tradeoffs between cost and

power output, and power output and CO_2 emissions (Harkin et al., 2012a,b). The above-cited studies all focused on facilities with constant operations.

A growing body of literature has explored variable operation of CCS-enabled thermal power stations (Bui et al., 2014). Several studies have proposed that MEA-based CO_2 capture can be dispatched variably on timescales of approximately one hour or less. Ziaii et al. (2009a) presented modeling results indicating that after a change in partial load of 80%, transient effects were small (of order 1%). These transients dissipated within 20 minutes when ramping capture rates up from 20% to 100%, and within 90 minutes when ramping down from 100% to 20%. In other modeling work, Ziaii et al. (2009b) found that carefully designed control strategies could yield relaxation times of order one minute for 10% step changes in regeneration rate. Chalmers et al. (2009) showed that the addition of CO_2 capture on coal plants would not necessarily reduce the ability of the coal plants to engage in time-varying operations, depending on low-level retrofit design choices. Similarly, Brasington and Herzog (2012) performed dynamic simulations of an MEA-based CO_2 capture system and found that the dynamic response of this system would not be a limiting factor in the time-varying operation of a coal plant outfitted with CO_2 capture. In addition, existing coal plants retrofitted with CO_2 capture may have a degree of flexibility, even if flexibility was not explicitly considered in the retrofit (Chalmers et al., 2011).

Several studies have applied computational optimization to consider the operations of CO_2-capture-enabled power stations. Our earlier work, Kang et al. (2011), considered the optimization of a power station with coal, natural gas, wind energy, and CO_2 capture operating under a CO_2 emission performance standard, and found that time-varying operations could enable improvements in operating profit by up to 20% over a heuristic (nearly constant) operating plan. This work was extended to consider a CO_2 tax (Kang et al., 2012). Cohen et al. (2012) considered a coal plant with CO_2 capture operating under several different operating plans including constant and time-varying operations, and similarly found that flexible operations provided improved operating profit. Arce et al. (2012) coupled a method for determining the high-level time-varying operations of a facility with a low-level control scheme

required to achieve the desired high-level operating states. In addition, optimization-based assessments have shown that the larger power system may benefit from flexible CO_2 capture because peak electricity demand could be met in part by temporarily shutting off CO_2 capture, thereby reducing capital expenditures for new generation assets (Chen et al., 2010; Cohen et al., 2010).

In a study methodologically similar to our earlier work (Kang et al., 2011), Zaman and Lee (2015) applied formal optimization procedures to determine the optimal hour-to-hour operation (including partial capture of flue gas CO_2) of a CO_2-capture-enabled power plant with time-varying electricity prices, for a set of fixed facility designs. Consistent with our earlier work, Zaman and Lee (2015) found that flexible CO_2 capture could result in substantially improved operating economics in a CO_2-capture-enabled facility compared to a facility with constant CO_2 capture rate. Additionally, some studies have found value in temporary CO_2 solvent storage, which can be used to time-shift the heat demands associated with solvent regeneration (Cohen et al., 2012; Kang et al., 2011; Versteeg et al., 2013; Zaman and Lee, 2015).

One observation arising from operation-focused studies such as Kang et al. (2011), Cohen et al. (2012), and Zaman and Lee (2015) is that operational flexibility typically entails increased capital investment. Thus, operational flexibility is not always economically preferable to constant operations. To determine whether operational flexibility is desirable, it is necessary to include both facility design and flexible operations within a single optimization formulation.

Some work has been published recently that considers CO_2 capture from coal plants using a coupled treatment of operations and design. Mac Dowell and Shah (2013) demonstrated a method to optimize design and operations of CO_2 capture at a coal plant. They minimized cost using dynamic process models. For a specific facility under specific economic conditions, they found that the optimal CO_2 capture fraction was high (95%). Khalilpour (2014) applied a mixed integer linear optimization formulation to determine CO_2 capture retrofit decisions for a coal plant operating under a gradually tightening CO_2 emission regulation. In later work, Mac Dowell and Shah (2015) applied a multiperiod optimization approach to treat the operation

of a coal-fired power plant with parasitic post-combustion CO_2 capture, for several power generation profiles. Improvements in operating profit of up to 16% in one scenario were achieved by controlling lean solvent loading to vary the rate of solvent regeneration in time. As can be seen in the above studies, significant progress has been made in optimization of CO_2 capture systems considering both design and operations. However, the above-cited studies focused primarily on the CO_2 capture system, and did not consider either the integration of the CO_2 capture system with the power plant, or the design of the power plant, in detail.

Taken together, the previous literature on design and operation of CO_2 capture systems indicates a need for integrative work that considers variable operations alongside all aspects of CCS-enabled power station design. Such an integrated study would include appropriate representations of both the CO_2 capture system and the power plant. Work along these lines is presented in this thesis.

1.1.2 Heat recovery steam generator (HRSG) design

Because the CCGT subsystem requires a specialized HRSG (which produces steam using the hot exhaust from the gas turbine (GT) component of the CCGT) to provide the process heat demanded by the CO_2 capture process, we employ modeling and optimization methods adapted from the literature on HRSGs. Computational optimization has been applied to solve thermodynamic and thermoeconomic HRSG optimization problems (Casarosa et al., 2004). Two-step optimization has been used to optimize high-level design (i.e., HRSG pressures and temperatures) as well as detailed physical design (e.g., tube diameters) (Franco and Giannini, 2005, 2006). In addition, optimization has been used to identify functional relationships for optimal HRSG design under varying economic conditions (Godoy et al., 2011).

In work that has some parallels with ours, a two-stage approach for optimizing heat recovery steam cycles was applied to Shell's design for an integrated gasification combined cycle facility with CO_2 capture (Martelli et al., 2011), and to an integrated reforming combined cycle (IRCC) system (Martelli et al., 2012; Nord and Bolland,

2011). Net efficiency improvements of up to 0.5-0.9%, out of 45.3%, were attained for this system (Martelli et al., 2012).

In previous HRSG optimization work, HRSG configuration—the number and ordering of HRSG components—generally is held fixed within an optimization run. Different configurations are typically considered through enumeration: several possible configurations are posited, and each is optimized separately. This is perhaps because it is difficult to manage the categorical variables inherent to describing HRSG configurations. Mohagheghi and Shayegan (2009) published a treatment of HRSG configuration optimization using a pruning process based on groups of related configurations called 'comprehensive layouts.' This method is not fully general because the set of possible configurations considered is limited to those contained within the set of comprehensive layouts. HRSG configuration potentially has a large impact on other aspects of HRSG design, which in turn can affect the design of other aspects of the CO_2-capture-enabled power plant. Therefore, direct and fully general optimization of HRSG configuration, as is accomplished in this work, is potentially of great value.

1.1.3 Proxy methods in engineering optimization

A central challenge in engineering design optimization is that modeling complex systems can be computationally costly. As such, direct use of full-physics engineering models for all function evaluations required during optimization is often impractical. Several alternative approaches have been applied for optimizing systems with computationally costly model evaluations. These approaches can be divided broadly into three categories: 1) development of procedures that efficiently provide gradients for use in optimization; 2) use of simplified (i.e., reduced physics) models; and 3) use of statistical proxy models. We now present an overview of these three approaches to provide context and motivation for our method. Our work primarily employs statistical proxy models, though we also apply some physical simplifications.

Combined forward modeling and gradient construction is commonly employed for the optimization of engineered systems. This approach has been applied successfully to

the design of air separation units for oxycombustion and in PDE-constrained optimal control problems (Choi, 2012; Dowling and Biegler, 2015). The key advantage of this treatment is that gradient information, which is used for gradient-based optimization, is generated very efficiently in conjunction with the solution of the forward model. The main disadvantage of this approach is that it is invasive with respect to the modeling code, so it cannot be applied without access to source code. This is a major limitation if commercial software is used for the forward model.

The second approach is to introduce physical simplifications to build a fast model for use in optimization. This approach has been demonstrated in the optimization of boiler design in oxycombustion systems by Dowling et al. (2014). In that work, the simplified physics model consisted of a local linearization of a full-physics model, and the optimization procedure used a trust region approach to update the linear model. One difficulty with simplified physics methods is that the required simplifications are specific to the physical system under consideration and can be difficult to generalize.

The third approach is the use of statistical proxy models. With this treatment, evaluations of the full-physics model are fully or partially replaced by evaluations of statistical regression surfaces ('statistical proxy models') that are constructed from prior evaluations of the full-physics model. Because they require only forward simulations of the full-physics code, statistical proxy models are non-invasive, meaning they are applicable for use with any modeling tool, even when source code is unavailable. For example, Booker et al. (1999) and Queipo et al. (2005) employed statistical proxy models in aerospace engineering. These methods have also been used in some CCS-related problems. Neveux et al. (2013) applied a gradient-based optimization method to maximize the energy efficiency of a solvent-based CO_2 capture system using a neural-network proxy model. Statistical proxy models have also found application in the modeling of geological CO_2 sequestration (Schuetter et al., 2014).

1.1.4 Optimization procedures

A wide variety of optimization algorithms have been applied to power plant design. Gradient-based methods were employed by Dowling and Biegler (2015) for oxycombustion systems. Martelli et al. (2011) applied particle swarm optimization (PSO, a derivative-free stochastic search algorithm) to HRSG design, and later Martelli et al. (2012) applied PSO for the design of an IRCC system. Manassaldi et al. (2011) treated integer variables in HRSG design using the classical Branch and Bound technique for mixed integer nonlinear optimization problems. The MILP formulation of Khalilpour (2014) was solved using the CPLEX code, which applies a specialized form of the Branch and Cut algorithm for integer variables.

In this work, we apply the BiPSOMADS algorithm presented in Isebor (2013) and Isebor and Durlofsky (2014). This algorithm combines PSO with Mesh Adaptive Direct Search (MADS, which is a gradient-free direct search algorithm that can converge to a local optimum), within a procedure that performs bi-objective optimization via a sequence of single objective optimizations (Audet et al., 2009; Isebor, 2013; Isebor and Durlofsky, 2014). One advantage of the BiPSOMADS algorithm is that it can treat discrete variables in a straightforward manner. The BiPSOMADS algorithm and its precursors were originally applied in oil field management problems (Isebor et al., 2014; Shirangi and Durlofsky, 2015), and in this work we find that it is quite effective when applied in CO_2 capture plant design and operations.

1.2 Scope of work

The goal of this thesis is to develop new methods to address the need for thermal power stations to reduce CO_2 emissions, and accommodate increasing renewable penetration in the electricity system. Two different formulations of the optimal plant design and operation problem are considered. The formulations differ in their treatment of the CO_2 capture system. Both formulations apply the same treatment of operations, and both optimize facility design in coordination with operations.

The first formulation, which we call the 'simplified-capture' problem formulation, focuses on optimizing the design of heat integration in the facility (including the GT, HRSG, and steam cycle) alongside variable operations, and represents the CO_2 capture system in terms of only its CO_2 capture capacity (heat and work duty requirements are represented using constant parameters taken from a separate model). The central modeling component developed in the simplified-capture formulation is the model of the CCGT, and in particular the HRSG component of the CCGT. Our method determines the optimal configuration (number and sequential arrangement) of HRSG internal components and the sizes of these components, while accounting for the effects of physical design specifications such as tube diameters and fin heights.

The second formulation, which we call the 'full-system' problem formulation, incorporates the detailed design of the CO_2 capture system alongside all of the design considerations of the simplified-capture formulation. The core extension of the full-system formulation beyond the simplified-capture formulation is the development of an integrated proxy model for the CO_2 capture system. This model uses statistical proxy models for the CO_2 absorption and solvent regeneration blocks, and employs simplified physics to represent other system components. The integrated proxy model calculates key performance metrics for the CO_2 capture system including heat duty, work duty, and capital cost. The proxy model is embedded within the physics-based heat integration model applied in the simplified-capture formulation.

Below are the specific topics treated in this thesis.

- Motivated by the large existing base of coal-fired power plants, we consider a CO_2 capture retrofit of an existing coal plant. Because of the capacity reduction associated with performing a parasitic CO_2 capture retrofit (in which heat for the solvent regeneration is taken parasitically from the coal plant steam cycle), we consider a prepackaged retrofit that does not require substantial modifications to the coal plant and does not reduce power output. The retrofit consists of a CO_2 capture configuration in which the CO_2 capture solvent regeneration heat demand is provided by a gas-fired CCGT.

- The CCGT is designed for combined-heat-and-power service, where the heat is used for CO_2 capture solvent regeneration. The HRSG component of the CCGT is a key driver of CO_2 capture economics because of the heat-driven nature of temperature-swing CO_2 capture technologies. The entire HRSG configuration is modeled and optimized, including the number, size, and arrangement of HRSG elements. This results in a challenging mixed-integer nonlinear programming (MINLP) optimization problem.

- We incorporate variable facility operations in the form of discrete operating modes, which allow CO_2 capture to be turned on and off in response to time-varying electricity prices (partial capture is also allowed). Taken in total, we perform the simultaneous optimization of both the detailed design of all major components, as well as key time-varying operational controls, for a CO_2-capture-enabled power station. Temporary storage of CO_2 solvent is not considered in this thesis, but we examined this in earlier work (Kang et al., 2011).

- A bi-objective optimization framework is applied to minimize the total capital requirement and maximize the net present value of the overall system, while satisfying engineering design constraints and meeting a CO_2 emission performance standard of 499 kg CO_2/MWh. This bi-objective approach provides a richer characterization of designs than can be achieved by considering only a single objective; notably, it enables the identification of a Pareto frontier that shows the optimal tradeoff between these two objectives. This represents an application of the BiPSOMADS algorithm outside its original application area of petroleum engineering.

- Two advanced CO_2 capture processes, namely the mixed salt process and the piperazine process, are evaluated and compared with the baseline MEA process using our modeling and optimization framework. These advanced processes are considered within the simplified-capture problem formulation.

- We develop and apply a technique that enables computational optimization of the detailed design of the CO_2 capture system alongside the design of the rest of

the power plant. Using Aspen Plus models of the CO_2 capture system within the optimization is cumbersome because these model runs are very time-consuming relative to the computations for the rest of the facility. Therefore, we develop an efficient integrated proxy model of the CO_2 capture system that reproduces the behavior of Aspen Plus. The integrated proxy model runs in less than one second, thereby enabling computational optimization of the detailed design of the CO_2 capture system.

1.3 Thesis outline

In Chapter 2, we describe the methods used in the simplified-capture problem formulation. Each of the components of the process model is described, including the coal plant, CO_2 capture system, gas turbine, HRSG, and steam cycle. We also describe our representation of the electricity market and time-varying facility operations using discrete operating modes. The optimization framework, which includes decision variables, objective functions, constraints, and the optimization algorithm, is presented. Extensive technical details relevant to the formulation in Chapter 2 are provided in Appendix A.

The results of the simplified-capture problem formulation are presented and discussed in Chapter 3. Six scenarios (four based on West Texas, and one each for India and the United Kingdom) are treated using the MEA process, and detailed results are presented for each of these scenarios. The optimal facility designs and operations are shown to be strongly dependent on scenario characteristics. In Chapter 3, we also present results for the application of two advanced CO_2 capture processes—namely, the mixed salt and piperazine processes—for the West Texas base scenario. A few supporting details for Chapter 3 are provided in Appendix A.

In Chapter 4, we describe the full-system problem formulation, which incorporates the detailed design of the CO_2 capture system within our modeling and optimization framework. The main focus of Chapter 4 is the development of the computationally efficient CO_2 capture proxy model, and its use in the full-system problem

formulation. We describe the construction of the proxy model, and verify its accuracy. The optimization results from the full-system formulation are shown to be consistent with the results of the simplified-capture formulation, but to also provide valuable information about the detailed design of the CO_2 capture system. Appendix B provides detailed supporting information for Chapter 4.

We conclude with Chapter 5, in which we summarize our methodological advances and optimization results. Possible directions for future research are also discussed.

Chapter 2

Simplified-capture optimization methods

In this chapter, we present the process model and optimization procedure associated with the simplified-capture problem formulation. As part of this exposition, we also describe our representation of variable facility operations and electricity markets using the electricity price-duration curve. This way of representing operations is used in both the simplified-capture formulation treated here and in Chapter 3, and also in the full-system formulation presented in Chapter 4.

This chapter proceeds as follows. In Section 2.1, we describe our process and capital cost models. Verification of the process model and validation of the capital cost model are discussed in Section 2.2. We describe our representation of facility operations in Section 2.3, and present the optimization framework in Section 2.4. Further details on our modeling procedures are provided in Appendix A, and also in Kang et al. (2011).

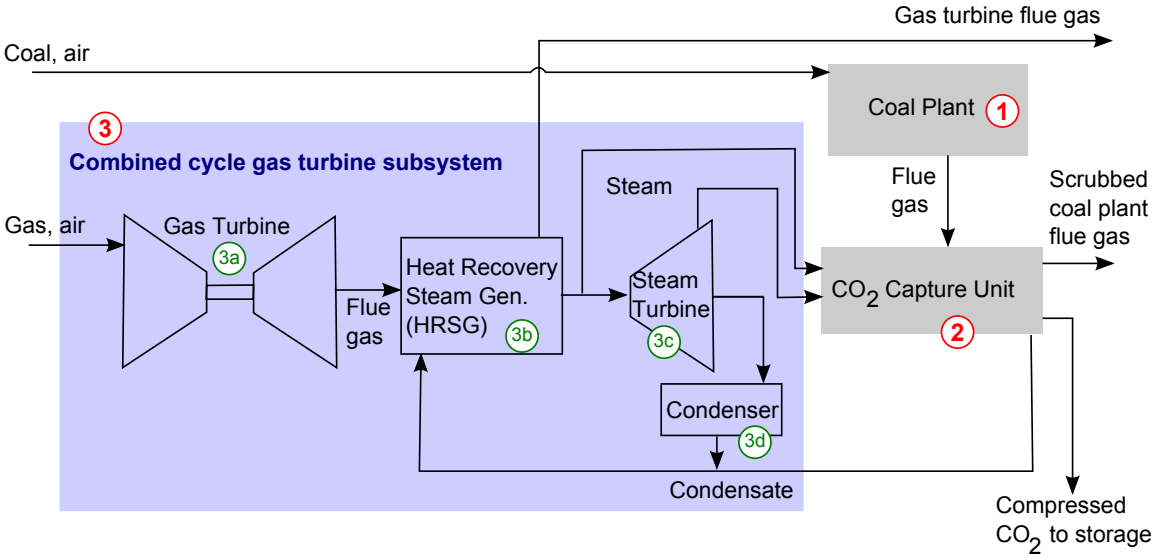

Figure 2.1: Schematic of the overall facility.

2.1 Process model and system integration

The facility considered in this thesis is shown in Figure 2.1. A coal plant (CP, location 1 in Figure 2.1) operates at baseload, producing constant power output. Coal plant flue gas, rich in CO_2, is scrubbed in the CO_2 capture system (2). The CO_2 capture system has a large demand for heat, which is supplied by steam drawn from the CCGT subsystem (3). We do not consider CO_2 transport and storage in this thesis, though cost estimates for these operations will be provided in Section 3.1.

The CCGT subsystem consists of three major units. A gas turbine (3a) burns natural gas, producing electric power and hot flue gas. The hot flue gas is used to generate steam in the HRSG (3b). Steam from the HRSG is expanded in steam turbines (3c), generating electricity. The condenser (3d) returns condensate to the HRSG. Steam can be drawn from the CCGT subsystem at several locations for use in the CO_2 capture system.

Optimization decision variables include gas turbine capacity and number, CO_2 capture system capacity, and specification of the steam cycle including HRSG design.

Because the focus of this chapter and Chapter 3 is in heat integration, we model and optimize the HRSG in substantial detail. Other system components are also optimized but are modeled at a higher level of abstraction. The process model is implemented in C++. We now describe the models of each of the major system components. Further details on the process models can be found in our earlier work (Kang et al., 2011) and in Appendix A.

2.1.1 Coal plant (CP)

The model in Kang et al. (2011) of a pulverized coal power plant is used in this thesis. All environmental controls other than CO_2 mitigation are contained within the CP block. The CP has a capacity of 440 MW_e, and HHV efficiency of 36.3%. Coal properties differ across scenarios and are summarized in Appendix A.

2.1.2 CO_2 capture system

In the base case, an aqueous amine (MEA) solvent-based temperature-swing process is used for CO_2 capture. Our model includes heat and work requirements for solvent regeneration, compression, and pumping (pumps and blowers). We consider the default amine CO_2 capture design for a pulverized coal plant from the Integrated Environmental Control Model (IECM), version 8.0.2, and use data from IECM and other sources (Berkenpas et al., 2009; Jassim and Rochelle, 2006; Rubin et al., 2007a). Regeneration heat duty is 3.68 MJ_{th}/kg CO_2, with temperature requirement of 407 K (300 kPa steam). Compression work duty to pressurize the CO_2 to 13.8 MPa is 335 kJ_e/kg CO_2. Work duty for solvent pumps and blowers is 40 kJ_e/kg CO_2.

We do not consider temporary solvent storage in this thesis, although that can be used to time-shift the heat requirements for solvent regeneration (Kang et al., 2011). The reason that we do not consider temporary solvent storage is that this process couples system operation across hours, which greatly increases the complexity of determining optimal facility operations. By setting aside solvent storage here, we are able to represent facility operations using a technique (described in Section 2.3) that

allows very efficient determination of optimal planned operations alongside design. We note finally that, in related work that extended the models developed in this thesis (Brodrick et al., 2015), temporary solvent storage was shown to be effective in coal-gas-solar CCS systems.

We assume that the CO_2 capture system can be operated at partial load without a decrease in operational efficiency. Previously it has been shown that specific reboiler heat duty is not a strong function of operational partial loading (Ziaii et al., 2009a), and one study presented results indicating that reboiler heat duty may even improve somewhat under partial load (Arce et al., 2012). Furthermore, in our optimization results we found that Pareto-efficient designs did not exhibit strong use of partial load in the CO_2 capture system. Thus our model assumption of no efficiency loss with partial load in the CO_2 capture system has a minimal impact on our results. This is discussed further in Section 3.2.

We also consider two advanced capture processes, namely the mixed salt and piperazine processes (Boot-Handford et al., 2014; Jayaweera et al., 2014; Rochelle et al., 2011). We now describe how these processes differ from the MEA process. Our representations for both advanced processes include a reboiler approach temperature of 10 K.

The piperazine process is very similar to the MEA process, and uses similar equipment but with a different solvent. Some piperazine process designs use a two-stage flash instead of a column (as is used in the MEA process) for solvent regeneration (Rochelle et al., 2011), but this level of detail is not resolved in our representation of the process. The piperazine process has regeneration heat duty of 2.6 MJ_{th}/kg CO_2, at 433 K (618 kPa steam) (Boot-Handford et al., 2014; Rochelle et al., 2011). Because the piperazine solvent regeneration process operates at higher pressure than the MEA process, the compression work duty is 220 kJ_e/kg CO_2. We assume that pump work duty for solvent pumps and blowers is the same as in the MEA process, 40 kJ_e/kg CO_2.

The mixed salt process is also generally similar to the MEA process, but involves two-stage absorption and regeneration processes and more complex solvent

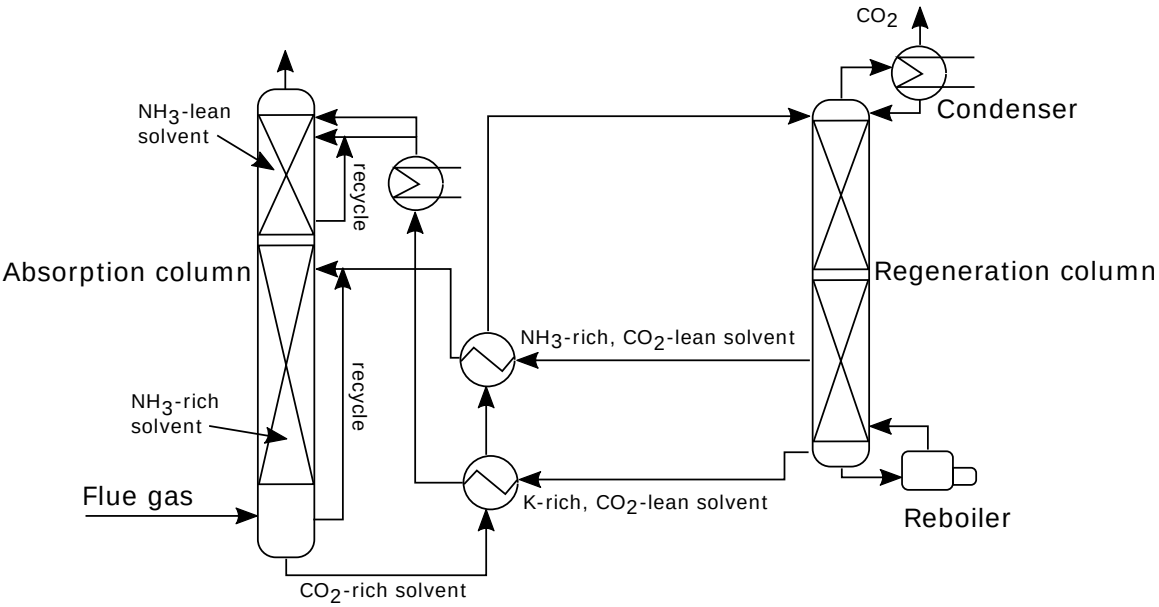

Figure 2.2: Conceptual diagram of the mixed salt process. Adapted from Jayaweera et al. (2014).

flow paths between the absorption column and regeneration column. The key idea of the mixed salt process is to use ammonia to absorb CO_2 from the flue gas, and potassium carbonate to control ammonia slip (Jayaweera et al., 2014). Figure 2.2 shows a conceptual design of the mixed salt process. The lower bed in the absorption column has ammonia-rich solvent at the bottom (with ammonia concentration decreasing upwards), and the upper bed has ammonia-lean solvent. This enables the ammonia to be captured in the upper bed, which decreases ammonia loss. In order to maintain this differential concentration in the absorption column, two solvent streams (one rich in ammonia, the other rich in potassium) are taken from the regeneration column. This entails the application of heat in the regeneration column at two different temperatures (though only one reboiler is shown in Figure 2.2).

The mixed salt process base case regeneration heat duty is specified as follows: 0.44 MJ_{th}/kg CO_2 at 433 K (618 kPa steam), and 1.76 MJ_{th}/kg CO_2 at 403 K (270 kPa steam), for a total of 2.20 MJ_{th}/kg CO_2. The need for reboiler heat provided at two temperatures requires a small modification to the steam cycle model to enable steam

Table 2.1: Key operating parameters for the MEA, piperazine, and mixed salt CO_2 capture processes.

Quantity	Units	MEA	Piperazine	Mixed salt
Reboiler steam temp.	K	407	433	433–443 and 403–413
Reboiler steam pressure	kPa	300	618	618–790 and 270–360
Specific reboiler heat	MJ_{th}/kg CO_2	3.68	2.6	0.44–0.66 and 1.76–2.65
Specific compress. work	kJ_e/kg CO_2	375	220	176
Specific pump work	kJ_e/kg CO_2	40	40	40

to be extracted from the steam cycle turbine at two pressures. This modification is described in Section 2.1.5 and in Appendix A. As with the piperazine process, solvent regeneration in the mixed salt process occurs at high pressure. Compression work duty is 176 kJ_e/kg CO_2. These specifications were provided by the principal investigator of the mixed salt process based on experimental results and modeling performed by SRI (Indira Jayaweera, direct communication, May 2014). We also assume that pump work duty for solvent pumps and blowers is the same as in the MEA process, 40 kJ_e/kg CO_2.

Because the mixed salt process is newer and more uncertain than the piperazine and MEA processes, we perform a three-case sensitivity study on reboiler heat duty and reboiler approach temperature, varying one parameter at a time. In the first two sensitivity cases, we vary specific reboiler heat duty by increments of +25% (0.55 MJ_{th}/kg CO_2 at 433 K, and 2.20 MJ_{th}/kg CO_2 at 403 K) and +50% (0.66 MJ_{th}/kg CO_2 at 433 K, and 2.65 MJ_{th}/kg CO_2 at 403 K). In the third sensitivity case, reboiler approach temperature is increased from 10 K to 20 K, which results in steam requirements of 0.44 MJ_{th}/kg CO_2 at 443 K (790 kPa steam), and 1.76 MJ_{th}/kg CO_2 at 413 K (360 kPa steam).

Table 2.1 displays the key operating parameters (or their ranges in the case of the mixed salt process) for the three processes considered.

2.1.3 Gas turbine

Our model includes a natural gas combustion turbine as described in Kang et al. (2011) and Kim (2004). The gas turbine (GT) has an HHV efficiency of 36.7%, specific power of 489 kJ/kg working fluid, and a flue gas outlet temperature at full load of 921 K, assuming an environment temperature of 298 K (Kang et al., 2011; Kim, 2004). In this thesis, the GT does not operate at partial load (i.e., it either operates at full capacity or it is shut off). In earlier work, which considered hour-to-hour operations and allowed for partial load GT operation, we found that this type of on-off behavior was often optimal (Kang et al., 2011).

2.1.4 Heat recovery steam generator

The HRSG is treated as a sequence of discrete heat exchangers ('elements'). We model the transfer of thermal energy from flue gas to water in a sequence of elements through which water and gas flow. This method of HRSG analysis and design has been used in thermodynamic and thermoeconomic studies on HRSGs and CCGTs (Mansouri et al., 2012; Woudstra et al., 2010), and in the optimization of these systems (Bassily, 2007; Franco and Russo, 2002; Kaviri et al., 2013; Norouzi et al., 2012).

HRSG elements are classified according to the state of the water stream, and are described by design water stream pressure p_{pl} [kPa] (pl denotes pressure level) and gas-side surface area A_{g} [m^2]. The four types of elements are economizers, evaporators, superheaters, and reheaters. In an economizer liquid water is heated, while in an evaporator water is boiled. In a superheater, steam is heated above the saturation temperature, and in a reheater, steam that has previously been expanded partially in a steam turbine is heated.

Figure 2.3 shows a one-pressure HRSG consisting of one economizer, one evaporator, and one superheater. Flue gas enters from the right with high enthalpy and leaves with low enthalpy, transferring energy to the water stream. Water enters from the left as compressed liquid and exits as superheated steam on the right.

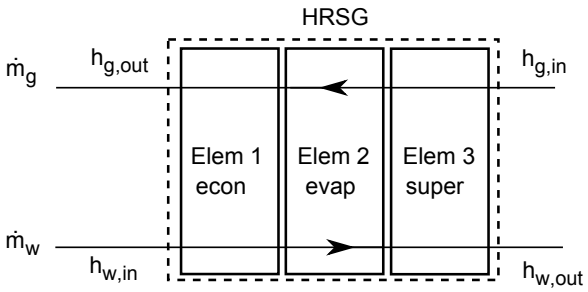

Figure 2.3: Flows in a one-pressure HRSG.

Substantial irreversibilities occur in one-pressure systems due to large temperature gradients between the gas and water streams. These occur in locations such as the gas inlet of the evaporator. Producing steam at two or more pressures can reduce the size of the temperature gradients and thereby reduce irreversibility and increase efficiency, at the cost of greater complexity and investment requirement. In HRSGs that generate steam at more than one pressure, multiple sets of economizers, evaporators, superheaters and/or reheaters are employed, with water streams of different pressures interleaved across elements.

Another consideration in HRSG design is the issue of gas-side pressure drop, Δp_{gas} [kPa]. This quantity is effectively a back pressure to the GT and can affect GT performance; with large Δp_{gas}, GT power output decreases (Zhao et al., 2003). Within the optimization, we apply a nonlinear constraint of $\Delta p_{\text{gas}} < 4.5$ kPa (cumulative over the entire HRSG) to ensure that HRSG back pressure does not negatively impact GT performance. We provide more details on our treatment of gas-side pressure drop in Appendix A.

2.1.4.1 HRSG element

Each HRSG element is characterized by a 'heat transfer size' UA_{g} [W/K] and by the number of passes n_{pass}. The latter is a geometric property described in detail in Appendix A. The quantity UA_{g} is the product of the overall heat transfer coefficient U [W/(m^2-K)] and the gas-side contact area of the HRSG element A_{g}. The coefficient

U can be either a constant parameter or it can be calculated given the physical design specifications of the HRSG element. More details on U are provided in Appendix A.

HRSG elements are modeled using algebraic relations. We use the effectiveness-number of transfer units method of heat exchanger analysis (Kays and London, 1984; Nellis and Klein, 2009; Shah and Sekulic, 2003) to determine the heat transfer within the element, $\dot{Q}_{\text{actual}}$ [W_{th}]. This necessitates the calculation of a nondimensional variable ε ($0 \leq \varepsilon \leq 1$), called effectiveness, that relates $\dot{Q}_{\text{actual}}$ to the theoretical maximum rate of heat transfer $\dot{Q}_{\text{max}}$ [W_{th}], where $\dot{Q}_{\text{actual}} = \varepsilon \dot{Q}_{\text{max}}$. The quantity ε is a function of HRSG element design and fluid states. Further information on HRSG element modeling is available in Appendix A.

2.1.4.2 HRSG model

The states of all HRSG elements are coupled and must be determined simultaneously. Each element carries seven state variables, so a system with N_{elem} elements has $7N_{\text{elem}}$ state variables. The variables are the effectiveness ε, the mass flow rate of water $\dot{m}_{\text{w}}$ [kg/s], the enthalpies of the water at the inlet and outlet, $h_{\text{w,in}}$ and $h_{\text{w,out}}$ [J/kg], the temperatures of the gas at the inlet and outlet, $T_{\text{g,in}}$ and $T_{\text{g,out}}$ [K], and the overall heat transfer coefficient U. A typical three-pressure HRSG contains 10–14 elements.

Heat transfer and thermodynamic relationships within each of the HRSG elements provide four equations, giving a total of $4N_{\text{elem}}$ equations. The first such equation enforces energy conservation, while the second equation relates ε to the rate of energy transfer between the water and gas streams. The other two equations determine ε and U from the fluid states (alternatively, U can be specified as a constant).

Boundary conditions and links between elements provide $3N_{\text{elem}}$ equations. Boundary conditions include the water inlet temperature (from the condenser and/or CO_2 capture solvent regeneration reboiler), the flue gas inlet temperature (from the GT), and the evaporator water outlet enthalpy at each pressure level (given by the water saturation curve). The boundary conditions provide $(2 + N_{\text{pl}})$ equations, where N_{pl} is the number of HRSG pressure levels. Links between elements enforce conservation

of mass, consistency in flue gas temperature between elements ($T_{\mathrm{g,in}}$ of an element equals $T_{\mathrm{g,out}}$ of the previous element), and consistency of water stream enthalpy between elements. The links between elements account for $(3N_{\mathrm{elem}} - 2 - N_{\mathrm{pl}})$ equations. Thus, we have a total of $4N_{\mathrm{elem}} + (2 + N_{\mathrm{pl}}) + (3N_{\mathrm{elem}} - 2 - N_{\mathrm{pl}}) = 7N_{\mathrm{elem}}$ equations, so the system is well posed.

The nonlinear system of $7N_{\mathrm{elem}}$ equations and $7N_{\mathrm{elem}}$ unknowns is solved using a modified form of Newton's method. See Appendix A for more details on the HRSG model.

2.1.5 Steam cycle

In a typical CCGT system, HRSG steam is fully expanded in steam turbines to a low condenser pressure to maximize electric power output. Typical condenser temperatures are approximately $300 - 350$ K, depending on the availability of cooling. Expansions through multiple turbines are common, and are required for HRSGs that produce steam at more than one pressure.

Here, the steam exiting the HRSG can either be fully expanded, or it can be used to provide heat for CO_2 solvent regeneration. Steam can be extracted in a partially expanded state from the steam turbine chain, or diverted from the HRSG directly, bypassing the steam turbines. The design of the CO_2 capture system has an important interaction here, as it affects the pressure at which steam is extracted from the steam cycle. The MEA process requires steam at 300 kPa (407 K), and the piperazine process requires steam at 618 kPa (433 K). The mixed salt process requires steam at two pressures (618 kPa (433 K) and 270 kPa (403 K) in the base case), which entails taking two extraction streams from the lowest-pressure steam turbine. The facility uses water cooling, with the condenser modeled as a counterflow heat exchanger. We use a condenser temperature of 330 K. See Appendix A for other details on the steam cycle.

2.1.6 Capital cost

Determining the optimal design of a facility requires accurate quantification of capital investment. We use the Guthrie method of capital cost estimation (Couper et al., 2007; Ulrich and Vasudevan, 2004, 2009). This cost estimate is prepared at the Class 4, or 'equipment-factored,' level, which corresponds to approximately ±30% accuracy (Couper et al., 2007; Ulrich and Vasudevan, 2004).

In the Guthrie method, individual component 'purchased equipment costs' are estimated using an exponential scaling rule. All costs are adjusted for escalation using the Chemical Engineering Plant Cost Index (CEPCI) on a component-by-component basis. The purchased equipment costs are multiplied by 'module factors' to obtain 'bare module costs' of each component (Ulrich and Vasudevan, 2004). The component bare module costs are summed to give the facility bare module cost, which is then multiplied by a 1.18 contingency and fee factor to obtain the facility 'total module cost.' This is then multiplied by a 1.30 auxiliary facility factor to obtain the 'total capital cost' of the facility (Ulrich and Vasudevan, 2004). Interest during construction is calculated using uniform construction progress over three years, cost of capital equal to the discount rate, and backward escalation of project cost at the escalation rate, giving the total capital requirement (TCR). We use the same discount and escalation rates in the interest during construction calculation as in the NPV calculation described in Section 2.4.1, with numerical values provided in Section 3.1.

The exponential scaling rule used to estimate purchased equipment costs expresses the purchased equipment costs C_{PE} [\$] in terms of the size of the item S:

$$\frac{C_{\mathrm{PE}}}{C_{\mathrm{PE,ref}}} = \left(\frac{S}{S_{\mathrm{ref}}}\right)^{\alpha}, \tag{2.1}$$

where $C_{\mathrm{PE,ref}}$ [\$] is the reference cost of the item, S_{ref} is the reference size of the item, and α is the scaling exponent. See Appendix A for further details on the capital cost methodology.

2.2 Model verification and validation

We verified our HRSG and steam cycle models against several sets of results presented in the literature. Our model provides predictions of steam mass flow rate, steam temperature, and total heat transfer rate that match an existing reference solution to within 0.8% for a simple one-pressure system (Ganapathy, 1991). For a complex three-pressure system presented by Franco and Giannini (2006), our model (with calculated U values) produces predictions that deviate from the reference solution by 5.0% or less in all quantities. Detailed comparisons for these two systems are presented in Appendix A.

To validate our capital cost model for the CCGT subsystem, optimization runs with maximization of NPV as the objective were performed for the CCGT. The components considered were the GT, HRSG, steam turbines, and condenser. In the range of 50-450 MW_e, the CCGT total capital cost determined by the model matched published values for actual constructed facilities (Farmer, 2010) to within 3.3% in all cases. Our model predictions for the cost proportions attributed to the different CCGT components are generally in accord with those given in publicly available sources (Kehlhofer et al., 1999; Ragland and Stenzel, 2000; Zhao et al., 2003), with our GT constituting a somewhat higher predicted proportion of cost than in the references. More detailed cost model validation is given in Appendix A.

2.3 Operational model

The previous discussion concerned the system components and process models. We now consider the ways in which the facility can operate. Facility operations are represented by four mutually exclusive operating modes that are each allocated an operating duration in a year. Optimization is used to determine the duration in each of these modes. The modes (designated A–D) are as follows:

A. Steam for power only: The GT(s) operate at full power. Steam is expanded fully to condenser conditions ($p = 17.3$ kPa, $T_{\text{sat}} = 330$ K), maximizing steam cycle electricity output.

B. Steam extraction: The GT(s) operate at full power. Steam is expanded partially in the steam turbines and is then used to supply heat for solvent regeneration in the CO_2 capture system ($p_{\text{extract}} \approx 270 - 620$ kPa, $T_{\text{sat}} \approx 400 - 430$ K). Mode B produces less electricity than mode A but more than modes C and D.

C. Steam diversion: The GT(s) operate at full power. Steam bypasses the steam turbines and is used only for solvent regeneration. Mode C produces less electricity than modes A and B but more than mode D.

D. Coal only: The GT(s) do not operate, no steam is produced in the CCGT subsystem, and no CO_2 capture occurs. Mode D produces the least electricity of all four modes.

The four operating modes are well ordered in net electricity generation (sales), with mode A providing the most power and mode D providing the least. Modes A, B and C are well ordered in their CO_2 emission rates, with mode A having the greatest emissions rate and mode C having the least. The CO_2 emission rate [kg CO_2/s] in mode D is less than in mode A, but can be more or less than in modes B and C depending on the design of the overall system.

The solvent regeneration reboiler requires a heat source at $\gtrsim 400$ K. For some designs, mode C involves the use of higher temperature steam for solvent regeneration in the CO_2 capture process; this may involve an additional heat exchanger in the CO_2 capture process. Because the cost of heat exchangers is only a small component of the cost of the CO_2 capture process, we do not include this cost in the model.

The treatment of modes B and C leads to a potential redundancy between these modes, and in fact a majority of optimized designs exhibited this redundancy. The potential redundancy occurs because mode C uses excess steam (steam beyond what the CO_2 capture system can use) for power generation in the steam turbines. In

systems in which mode B supplies enough steam to run the CO_2 capture system at full capacity, this leads to redundancy between modes B and C: in such systems, both modes B and C operate the CO_2 capture system at full capacity, so the two modes are equivalent. The systems that exhibit this redundancy thus do not have a mode that operates the CO_2 capture system at partial load. Therefore, it is possible for two systems that have different durations in modes B and C to exhibit identical performance metrics. This redundancy does not pose a problem for the optimizer.

The instantaneous optimal operating mode depends only on the operating profit associated with each mode. If the prices of fuel, operations and maintenance (O&M), electricity, and CO_2 emissions are known, then the optimal operating mode is the mode with the highest operating profit. Furthermore, for a given set of conditions, the first three modes are ordered optimally (A-B-C) in price of electricity, from high to low. Finally, under the conditions used in this thesis, the price of natural gas is low enough that mode D is preferred only at times with the lowest electricity prices. This ordering (A-B-C-D) holds for a CO_2 limit as well as for a CO_2 price because the constraint on CO_2 emissions induces an implicit shadow price for CO_2 emissions.

Figure 2.4 shows a wholesale electricity price-duration curve, which consists of the hours of a year sorted by the wholesale market price of electricity. We use this curve to represent wholesale electricity market dynamics. The fact that the operating modes are well ordered in electricity price enables us to represent operations using threshold electricity prices, or 'strike prices,' which are the prices at which the operating mode switches. The strike prices shown in Figure 2.4 are the operational decision variables and are determined algorithmically alongside the design variables.

Our use of the electricity price-duration curve in representing system operations prevents the model from including transient system behavior because the price-duration curve does not retain information about the sequential ordering of hours in time. Furthermore, in using hourly data in our operational model, we assume that the auxiliary-powered CO_2 capture system can be controlled on an hourly time scale. We believe this assumption to be reasonable because it has previously been shown that CO_2 capture system transients typically dissipate on time scales of order one

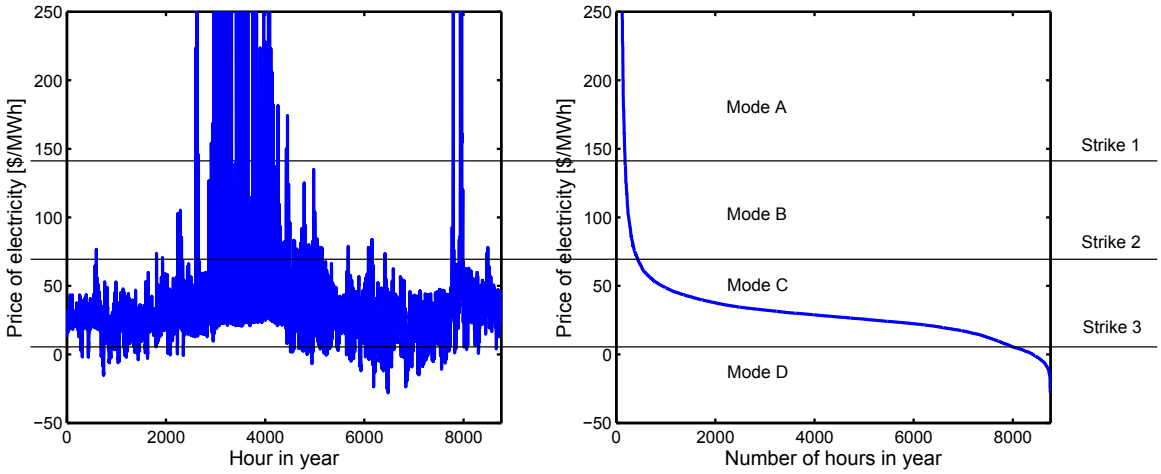

Figure 2.4: Wholesale electricity hourly price (left) and price-duration curve (right), West Texas Hub Bus, 2011 (Electric Reliability Council of Texas, 2013).

hour and that capture operations are not strongly affected by partial load plant operations (Brasington and Herzog, 2012; Chalmers and Gibbins, 2007; Chalmers et al., 2009; Ziaii et al., 2009b). We note that the downstream effects of time-varying CO_2 capture can be managed in part by the use of CO_2 interim storage (Farhat and Benson, 2013).

2.4 Optimization formulation

As noted earlier, in this thesis operations and design are optimized simultaneously. This coupling is necessary because design affects the optimal planned operating profile, and the planned operating profile is necessary to evaluate the economics of a candidate design. We consider two objectives—maximization of net present value and minimization of total capital requirement—and pose the joint design and operation problem as a bi-objective MINLP problem of the following form:

$$\max_{\mathbf{u}_{\text{des}},\mathbf{u}_{\text{ops}}} \left[-C_{\text{TCR}}\left(\mathbf{x},\mathbf{u}_{\text{des}}\right), \quad V_{\text{NP}} = -C_{\text{TCR}}\left(\mathbf{x},\mathbf{u}_{\text{des}},\mathbf{u}_{\text{ops}}\right) + P_{\text{op}}\left(\mathbf{x},\mathbf{u}_{\text{des}},\mathbf{u}_{\text{ops}}\right)\right] \quad (2.2)$$

subject to

$$\mathbf{u}_{\text{des}}, \mathbf{u}_{\text{ops}} \in \Omega \tag{2.3}$$

$$\mathbf{c}\left(\mathbf{x}, \mathbf{u}_{\text{des}}, \mathbf{u}_{\text{ops}}\right) \leq 0. \tag{2.4}$$

In this formulation, $\mathbf{x}$ indicates state variables, $\mathbf{u}_{\text{des}}$ indicates design decision variables, and $\mathbf{u}_{\text{ops}}$ represents operational decision variables (strike prices). The symbol C_{TCR} [\$] designates total capital requirement, V_{NP} [\$] is net present value, P_{op} [\$] represents capitalized operating profits over the planned lifetime of the facility, Ω represents bound constraints on the decision variables, and $\mathbf{c}$ are general constraints, which can be nonlinear. These are discussed further in Sections 2.4.1 and 2.4.2.

Within the bi-objective optimization framework, we apply a PSO-MADS algorithm (Isebor, 2013; Isebor and Durlofsky, 2014) to minimize a single objective derived from Equation 2.2 (as explained below). The quantities C_{TCR}, V_{NP} and $\mathbf{c}$ are evaluated by repeated calls to the process model, which solves for the state variables $\mathbf{x}$. PSO-MADS is a derivative-free optimization algorithm built upon the open-source NOMAD project (Abramson et al.; Audet et al., 2009; Le Digabel, 2011). It combines Particle Swarm Optimization (PSO, a stochastic global search method) with Mesh Adaptive Direct Search (MADS, a randomized direct search method). The algorithm proceeds by alternating between PSO iterations performed on a population of candidate solutions, and MADS iterations performed on the best PSO population member. By alternating between PSO and MADS in this way, the algorithm incorporates global exploration (through the PSO component) as well as convergence to a local optimum (provided by the MADS component). The procedure uses filter-based treatments to handle nonlinear constraints. With this approach, the aggregate constraint violation is minimized alongside the objective function (in a bi-objective fashion) to enforce constraint satisfaction.

Bi-objective optimization is accomplished here by performing a sequence of single-objective optimizations. The goal is to trace the Pareto frontier, which defines the set of Pareto-efficient solutions (as defined previously). The 'single-objective

product formulation' (SOPF) (Audet et al., 2008) is applied for this purpose. PSO-MADS is used as the underlying optimization algorithm, and the overall framework, explained in detail in Isebor (2013) and Isebor and Durlofsky (2014), is referred to as BiPSOMADS.

The procedure entails first optimizing the two individual objectives, denoted f_1 and f_2, separately. In the following illustration, the goal is to maximize each of these objectives. The solutions computed during these optimizations provide a very coarse approximation to the Pareto frontier. Figure 2.5(a) illustrates the result after the maximization of f_1, and Figure 2.5(b) shows the result after the subsequent maximization of f_2. The region in which the Pareto frontier is the least resolved is then identified, and this enables the determination of the so-called reference point $\mathbf{r}$, which lies below the current estimate of the Pareto frontier in objective function space.

In the next step of BiPSOMADS, we search for solutions that maximize the 'distance' from the reference point. Figure 2.5(c) illustrates the procedure after the first SOPF maximization. Here distance is defined as the product of the squared differences between the objective functions and the corresponding components of $\mathbf{r}$. Specifically, the single objective D we seek to maximize is given by:

$$D(\mathbf{x}) = \left(\max\left[0, f_1(\mathbf{x}) - r_1\right]\right)^2 \left(\max\left[0, f_2(\mathbf{x}) - r_2\right]\right)^2, \tag{2.5}$$

where f_1 and f_2 are the values of the two objective functions and r_1 and r_2 are the coordinates of the reference point in objective function space. The results of this optimization provide improved resolution of the Pareto frontier. The region in which the Pareto frontier is the least resolved is then identified, and this provides the next value of $\mathbf{r}$. This process (determine $\mathbf{r}$, perform a PSO-MADS run to maximize D in Equation 2.5, update the estimate of the Pareto frontier) is continued until a stopping criterion is reached, which could be a specified number of PSO-MADS runs or a particular level of resolution in the Pareto frontier.

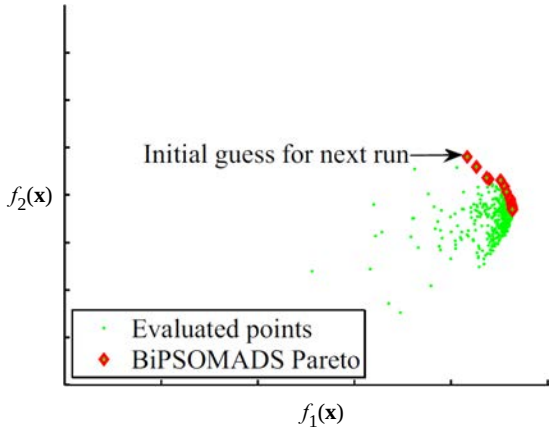

(a) Maximization of f_1

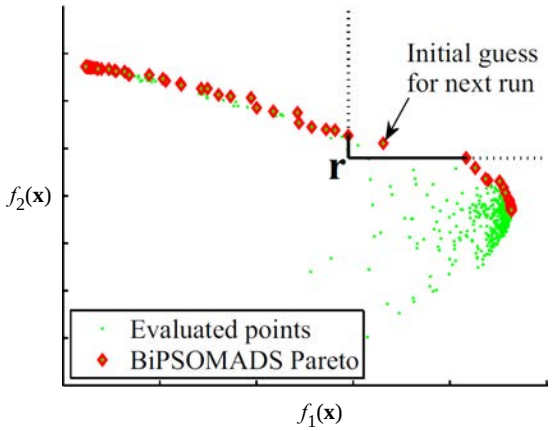

(b) Maximization of f_2

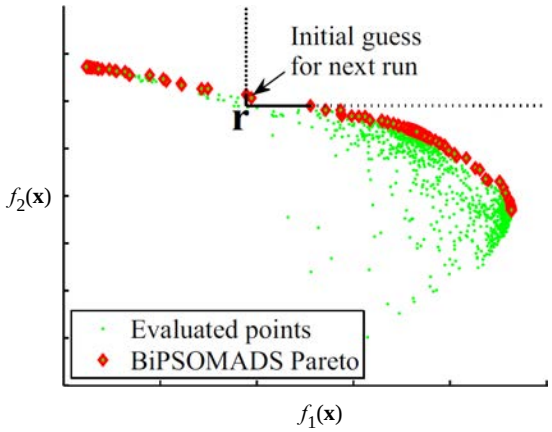

(c) First iteration of SOPF maximization

Figure 2.5: Pareto frontier approximations after three BiPSOMADS steps, adapted from Isebor and Durlofsky (2014).

Our bi-objective optimizations are accomplished in two stages. We first run BiPSOMADS, as described above, to provide an estimate of the Pareto frontier, using several initial guesses. In each BiPSOMADS run, ten PSO-MADS runs are performed. Because the frontiers associated with our problems can be complex and 'patchy,' and because regions of particular interest are not always sufficiently resolved by the initial ten PSO-MADS runs, we then identify a number of additional points to be used as initial guesses for second-stage BiPSOMADS runs. Following these runs, the final Pareto frontier is constructed from the combined results of all BiPSOMADS optimizations. The total number of BiPSOMADS optimization runs performed to obtain each Pareto frontier was in the range of 12-16.

In this chapter and Chapter 3, all optimizations were run using parallel computation. In each BiPSOMADS run we typically accessed 20-50 computational cores.

2.4.1 Objective functions and decision variables

We consider two objective functions: TCR, which is minimized, and NPV, which is maximized. These two objective functions are essential quantities for any decision-making process. TCR represents the up-front cost of a project, while NPV represents the long-term economic value of a project. A decision-maker would likely consider both of these quantities when choosing from several potential courses of action. In particular, locations on the Pareto frontier where a substantial improvement in one objective can be obtained with only a slight deterioration in the other objective may be of special interest to a decision-maker.

NPV is calculated based upon cash flows received at midyear over 30 years:

$$V_{\mathrm{NP}} = -C_{\mathrm{TCR}} + \sum_{y=0}^{29} \frac{0.85\left(R_{\mathrm{elec}} - C_{\mathrm{fuel}} - C_{\mathrm{O\&M}}\right)\left(1 + r_{\mathrm{esc}}\right)^{y+0.5} - C_{\mathrm{tax},y}}{\left(1 + r_{\mathrm{disc}}\right)^{y+0.5}}, \qquad (2.6)$$

where R_{elec} [\$] is revenue from electricity sales in one year, C_{fuel} [\$] is the total cost of fuel in one year, $C_{\mathrm{O\&M}}$ [\$] is the total cost of operations and maintenance in one year, r_{esc} is the escalation rate, $C_{\mathrm{tax},y}$ [\$] is the corporate income tax paid in each year, and

r_{disc} is the nominal discount rate. Data for the calculation of $C_{\text{O\&M}}$, which includes both fixed and variable O&M, are provided in Appendix A. The coefficient of 0.85 to the pre-tax operating profit ($R_{\text{elec}} - C_{\text{fuel}} - C_{\text{O\&M}}$) accounts for the capacity factor of the CP (the CCGT and CO_2 capture system only operate when the CP is operating). The quantity $C_{\text{tax},y}$ varies yearly and is calculated from the pre-tax operating profit, with depreciation allowance, using a combined federal and state corporate income tax rate of 40%. Depreciation is evaluated using the 20-year 150% declining balance method, mid-quarter convention (Islegen and Reichelstein, 2011; US Internal Revenue Service, 2013).

The optimization problem contains discrete (integer and categorical) and continuous decision variables. All decision variables are collected in a single vector and treated using BiPSOMADS. Table 2.2 provides a list of the optimization variables along with bound constraints. For a system with up to three HRSG pressure levels and 14 elements, we have a total of 42 decision variables (26 continuous variables and 16 discrete variables).

The integer variables are the number of gas turbines n_{GT} (this is also the number of HRSGs because we have one HRSG for each gas turbine) and the number of pressure levels n_{pl}. The categorical variables are the specification of type and pressure level of each element in the HRSG, $\mathbf{e}_{\text{pl,type}}$. The domain of $\mathbf{e}_{\text{pl,type}}$ is the Cartesian product of the possible types of HRSG elements (economizer, evaporator, superheater, reheater) and the possible pressure levels of the elements (1, 2, 3), with an additional setting to indicate deactivation of the element.

The continuous variables are total gas turbine capacity $n_{\text{GT}} s_{\text{GT}}$ [MW_e], CO_2 capture system capacity C_{cap} [kg CO_2/s], water/steam pressure at each HRSG pressure level p_{pl} [kPa], high pressure reheat steam pressure $p_{\text{HP,rh}}$ [kPa], pressure of steam extraction p_{ext} [kPa], variables controlling the HRSG element gas-side surface areas $\mathbf{A}_{\text{g}}$, and strike prices $\mathbf{u}_{\text{ops}}$ [\$/MWh]. Reheat is only allowed in three-pressure systems, for the highest pressure level. Note that the total GT capacity is a decision variable, and that the capacity of each individual GT is calculated with all GTs being identical.

Table 2.2: Optimization decision variables.

Variable	Type	Symbol	# Vars	Units	Lower bound	Upper bound
Number of GTs	Integer	n_{GT}	1	–	1	3
Total GT capacity	Real	$n_{\mathrm{GT}} s_{\mathrm{GT}}$	1	MW	1	400
HRSG # press. levels	Integer	N_{pl}	1	–	1	3
HRSG steam pressures	Real	p_{pl}	3	kPa	100	19,000
HRSG extract press.	Real	p_{ext}	1	kPa	300	5,000
HRSG HP reheat press.	Real	$p_{\mathrm{HP,rh}}$	1	kPa	100	20,000
HRSG element type & pl	Categ.	$\mathbf{e}_{\mathrm{pl,type}}$	14	–	-1	11
HRSG nondim. elem. size	Real	$a_{\mathrm{g},0}$	1	–	0.1	3
HRSG rel. elem. sizes	Real	$\mathbf{a}_{\mathrm{g,rel}}$	14	–	0.1	3
CCS relative capacity	Real	c_{cap}	2*	Fraction	0.0	0.9
Strike prices	Real	$\mathbf{d}_{\mathrm{sp}}$	3	\$/MWh	(0, -20, -30)	(200, 150, 100)

* One variable for absorption and one variable for regeneration and compression. These two variables converge to the same value during optimization.

We found that a better search was obtained by decomposing the HSRG element surface areas into $\mathbf{A}_{\mathrm{g}} = A_{\mathrm{g},0}\mathbf{a}_{\mathrm{g,rel}}$ where $A_{\mathrm{g},0}$ [m^2] is the HRSG element characteristic gas-side surface area and $\mathbf{a}_{\mathrm{g,rel}}$ are relative HRSG element surface areas for each element. Furthermore, it is convenient to express $A_{\mathrm{g},0}$ as related proportionally to the gas turbine size; i.e., $A_{\mathrm{g},0} = a_{\mathrm{g},0}s_{\mathrm{GT}}/\kappa$, where $a_{\mathrm{g},0}$ is the nondimensional HRSG element size and $\kappa = 9{,}162\ \mathrm{W_e/m^2}$ is a constant chosen such that $a_{\mathrm{g},0}$ takes on values of order one. The decision variables for the HRSG element surface areas are then $a_{\mathrm{g},0}$, which controls the overall size of the HRSG, and $\mathbf{a}_{\mathrm{g,rel}}$, which controls the size of each element.

The HRSG has a predefined set of slots for HRSG elements. Associated with each slot i are one categorical variable ($e^i_{\mathrm{pl,type}}$) and one continuous variable ($a^i_{\mathrm{g,rel}}$). If the categorical variable of a slot indicates that it is deactivated, the continuous variable has no effect on the HRSG design.

The CO_2 capture capacity is expressed in nondimensional terms as $c_{\mathrm{cap}} = C_{\mathrm{cap}}/\dot{m}_{\mathrm{CP,fgCO_2}}$, where $\dot{m}_{\mathrm{CP,fgCO_2}}$ [kg CO_2/s] is the CP flue gas CO_2 emission rate. We implemented c_{cap} as two variables, one representing absorption capacity and the other representing regeneration and compression capacity. Over the course of an optimization run these two variables converge to the same value.

2.4.2 Optimization constraints

Three kinds of constraints apply to the facility. The first class of constraints ensure that the HRSG design is physically valid; candidate designs that violate these constraints are discarded. The second class of constraints are bound and linear constraints on the decision variables that limit the search space. The third class of constraints are general constraints applied to model-calculated quantities. These constraints enforce physical design standards and CO_2 policy requirements, and many of them are related to HRSG states. Below we describe the CO_2 policy constraints. See Appendix A for a full listing of the other constraints.

We use an emission performance standard of 499 kg CO_2/MWh (1,100 lb/MWh). This is the level that the US Environmental Protection Agency has proposed for new coal power plants (US Environmental Protection Agency, 2013). In this thesis, we investigate the impact of the application of this standard to an existing CP, so the CP would need a CCS retrofit to continue operating. The emission performance standard applies to CO_2 emission intensity, which is calculated as E/G [kg CO_2/MWh] where E [kg CO_2] is the amount of CO_2 emitted and G [MWh] is the amount of electricity exported to the power grid. We can also treat other CO_2 regulations such as a carbon price without difficulty.

The emission performance standard acts as a constraint applied to each of the following system emission intensities:

Entire facility: Emission intensity of the entire facility including CP, CCGT, and CO_2 capture

Scrubbed CP: Emission intensity calculated from coal plant net power output (440 MW_e) and scrubbed CO_2 emissions

CCGT: Emission intensity calculated from the power output of GT(s) and CCGT steam turbines, and CO_2 emissions from the GT(s).

All of these emission intensities must be below 499 kg CO_2/MWh. The constraint is applied in this way to prevent dilution of CP emissions with the inherently less CO_2-intensive CCGT system. The CO_2 capture electricity demands are attributed to the facility as a whole, not to either of the major subsystems.

2.5 Summary

In this chapter, we presented the process model and optimization procedures for the simplified-capture problem formulation. The overall process model was described, along with each of the major components. We discussed the simplified representation of the CO_2 capture system used in the simplified-capture formulation, including the

advanced mixed salt and piperazine CO_2 capture processes. The detailed model of the heat recovery steam generator was also overviewed. Additionally, we discussed our treatment of variable operations using discrete operating modes and the price-duration curve. Finally, we presented the formal optimization problem associated with the simplified-capture problem formulation, and described briefly the BiPSOMADS algorithm that we employed to solve this problem.

Chapter 3

Simplified-capture optimization results and discussion

The simplified-capture problem formulation described in Chapter 2 is applied to six different scenarios in this chapter. These scenarios represent a wide domain of realistic conditions, and demonstrate the robustness of our modeling and optimization procedure. We begin by describing the different scenarios in Section 3.1. Results for the four West Texas scenarios are presented in Section 3.2, and for the UK and India scenarios in Section 3.3. In Section 3.4, we discuss results for the mixed salt and piperazine processes applied within the context of the West Texas base scenario. Additional details supporting this chapter are presented in Appendix A.

3.1 Scenario construction

We constructed six scenarios (one base scenario and five sensitivity scenarios) from historical data. The four US scenarios are based around West Texas, which we selected in part because this region has a large amount of grid-connected wind power, and so may be representative of future power systems. Our other two scenarios are based on the United Kingdom and India. We used a nominal discount rate of $r_{\text{disc}} = 11.0\%/\text{a}$,

Table 3.1: Scenario parameters.

Scenario name	P_{elec} mean [$/MWh]	P_{elec} std. dev. [$/MWh]	$P_{\text{nat.gas}}$ [$/GJ] ([$/MMBtu])	P_{coal} [$/GJ] ([$/MMBtu])	CCS capital cost multiplier
WTX-Base	40.73	126.74	4.48 (4.73)	1.34 (1.41)	1.00
WTX-HighCapCost	40.73	126.74	4.48 (4.73)	1.34 (1.41)	1.25
WTX-HighEnergyCost	55.62	126.74	6.12 (6.46)	1.34 (1.41)	1.00
WTX-LowEnergyCost	24.27	40.65	3.21 (3.39)	1.34 (1.41)	1.00
UK	74.83	13.53	8.60 (9.08)	5.20 (5.49)	1.00
India	72.29	24.42	11.56 (12.20)	1.10 (1.16)	1.00

and an escalation rate of $r_{\text{esc}} = 3.3\%/\text{a}$. We assume that the coal plant already exists and thus constitutes a sunk cost that does not affect the retrofit decision, so we do not include the CP capital cost in the objective functions. Therefore, the coal plant NPV involves only revenue, operating expenses, and corporate income tax.

The economic scenario has a substantial impact on the optimal decisions, with the economic parameters in different scenarios leading to substantially different designs and objective function values. The sensitivity of the results to economic assumptions suggests that it will be important to use a robust approach for economic forecasting. Despite the wide range of designs and objective function values, our procedure performs well for all scenarios considered.

The scenario data are shown in Table 3.1. We constructed the base scenario (WTX-Base) electricity price-duration curve, displayed in Figure 2.4, using hourly day-ahead electricity market prices for the West Texas Hub Bus in 2011 (Electric Reliability Council of Texas, 2013). We used a natural gas price equal to the average price of gas delivered to US electric power generators in 2011 (US Energy Information Administration, 2013). The coal price was $1.34/GJ ($1.41/MMBtu), which is approximately the long-run average price of sub-bituminous Wyoming Powder River Basin coal delivered to Texas (US Energy Information Administration, 2014a,b).

The three West Texas sensitivity scenarios are high CCS capital cost (WTX-HighCapCost), high energy prices (WTX-HighEnergyCost), and low energy prices (WTX-LowEnergyCost). In constructing the scenario WTX-HighCapCost, we applied

a constant multiplier of 1.25 to the capital cost of the CO_2 capture facility, while holding all other prices the same as in WTX-Base. The scenario WTX-LowEnergyCost was constructed using electricity prices for the West Texas Hub Bus in 2012 (Electric Reliability Council of Texas, 2013) and the corresponding 2012 average natural gas price for electricity (US Energy Information Administration, 2013). To construct the scenario WTX-HighEnergyCost, we added \$1.64/GJ (\$1.73/MMBtu, corresponding to an increase of 36.5%) to the WTX-Base natural gas price, and \$14.89/MWh (a 36.5% increase in terms of average price) to the WTX-Base electricity prices. Coal prices were not modified in this scenario. We constructed WTX-HighEnergyCost in this way to account for correlation between electricity and natural gas prices.

We developed two international scenarios using data for the United Kingdom and India in the year 2011. The UK scenario used half hour (averaged to hourly) electricity reference price data in 2011 given by the UK power market (APX Group, 2014). The India scenario used hourly average day-ahead market wholesale electricity prices from an Indian power market for the Gujarat-Maharashtra pricing area in 2011 (Indian Energy Exchange, 2014). Natural gas prices for the year 2011 were drawn from the FERC LNG Market Archives (US Federal Energy Regulatory Commission, 2014), which includes data on landed gas prices in the United Kingdom and India. The price for UK natural gas from this source is essentially the same as for the UK National Balancing Point trading hub. Coal prices for the year 2011 were taken from the IEA Medium-Term Coal Market Report 2012 (International Energy Agency, Gas, Coal and Power Division, 2012), which includes data for average coal price delivered to power plants in Northwest Europe and India.

As mentioned in Section 2.1, our model does not include costs associated with CO_2 transport or storage. If the captured CO_2 were to be transported by pipeline and stored in an onshore saline aquifer, the cost would be approximately \$4-21 million/a using a combined transport and storage cost of \$3-15/tonne CO_2 (Grant et al., 2013; Metz et al., 2005). This amounts to a net present cost of transport and storage of \$47-249 million (excluding tax implications, which would tend to decrease this net present cost). This cost is not included in the results presented in this thesis. If the

captured CO_2 were used for enhanced oil recovery, the cost for transport and storage could be much lower or even negative.

Further details on scenario construction, including currency conversions and fuel properties, are provided in Appendix A.

3.2 West Texas

The existing coal plant without CCS has a NPV of $476 million in WTX-Base. As we will see, this is greater than the NPV of any system with CCS. Performing CO_2 capture thus represents an overall cost to the owner: the difference between the NPVs of the retrofitted systems and the NPV of the coal plant alone can be interpreted as the net present cost associated with meeting the emission performance standard by performing an auxiliary CCS retrofit. Importantly, however, the NPVs for optimal systems in the base scenario are still positive, indicating that the CO_2 capture retrofit is preferred to simply decommissioning the coal plant in response to the CO_2 regulation.

During the course of the optimization, 4.66×10^6 candidate designs were evaluated, of which 1.52×10^5 were unique and feasible. From these we construct a Pareto frontier for minimum TCR and maximum NPV, shown in Figure 3.1. The Pareto frontier defines the optimal tradeoff between NPV and TCR, with each point on the frontier representing a different system (design and operational settings). From any point on the Pareto frontier (Pareto-efficient points), no improvement in one objective can be obtained without a degradation in the other objective. Non-Pareto-efficient points in Figure 3.1 are shown only as gray '×'s, while Pareto-efficient points are marked with colored symbols, with symbol and color indicating the number of HRSG pressure levels. Note that the frontier is smooth in some regions, but discontinuous and 'patchy' in other regions. Some discontinuities in the frontier in Figure 3.1, such as that between the one-pressure (blue open circles) and two-pressure systems (red open squares), are due to the discrete nature of the design space. Other discontinuities may result from the fact that our search is not exhaustive. More resolution in the

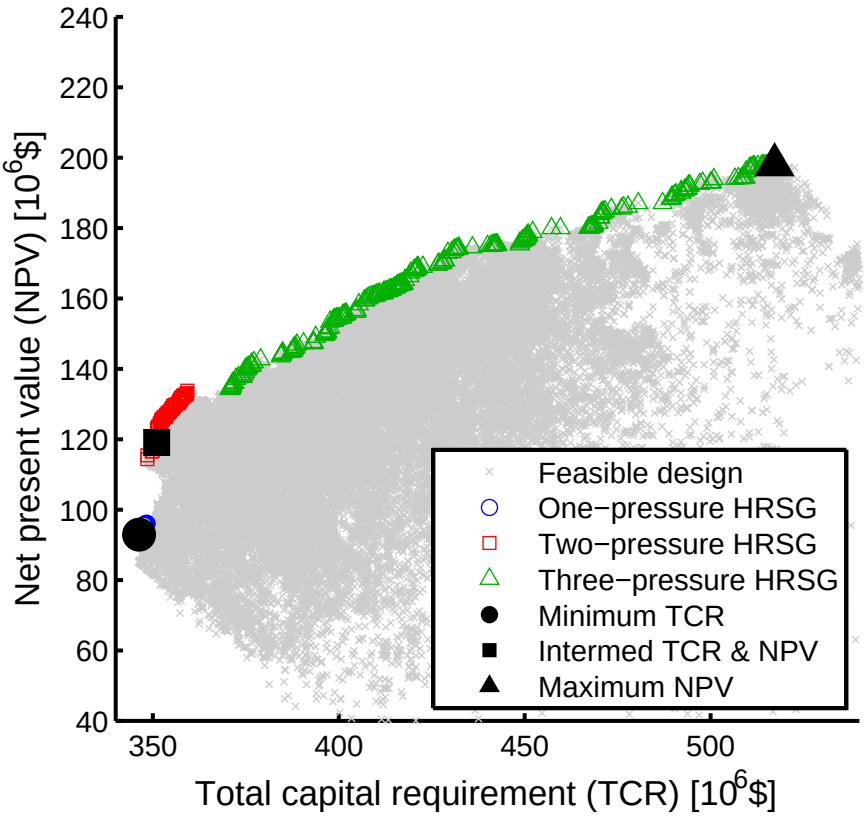

Figure 3.1: Pareto frontier for base scenario (WTX-Base).

frontier could be achieved by performing additional PSO-MADS runs, but because the general features of the solution are clearly evident in Figure 3.1, this was not attempted here.

Given a plot such as that in Figure 3.1, the decision maker would choose which Pareto-efficient point to implement based on his or her specific preferences. A point on (rather than below) the frontier would always be chosen. Otherwise the solution selected would be suboptimal, since improvement in one of the objectives could be attained without any deterioration in the other objective by moving to the frontier.

The Pareto frontier obtained for the base scenario consists of 391 distinct solutions. The range of NPVs is \$93-198 million, and the range of TCRs is \$346-517 million. Subtracting from the NPV for the CP-only case, we find that in this scenario the net present cost of meeting the emission performance standard ranges from \$278-383 million. It is evident from Figure 3.1 that the TCR and NPV objectives are in conflict, and that increased capital investment is required for increased NPV. The different objectives lead to noticeably different HRSG designs. The design associated with the minimum TCR solution (solid circle; NPV of \$93 million, TCR of \$346 million) corresponds to a one-pressure HRSG, while that for the maximum NPV solution entails a three-pressure HRSG (solid triangle; NPV of \$198 million, TCR of \$517 million).

A key advantage of resolving the full Pareto frontier is that intermediate, or 'compromise,' solutions can be identified. The best such solutions provide a significant improvement in one objective with only a minimal degradation in the other objective (as such, these solutions are often associated with sharp 'bends' in the frontier). One such intermediate solution (solid square) is identified in Figure 3.1. This solution corresponds to a two-pressure HRSG and has an NPV of \$119 million and a TCR of \$351 million. This indicates that, relative to the minimum TCR solution, by investing an additional \$5 million in capital, we can achieve an increase of \$26 million in NPV.

With reference to Figure 3.1, a general increase in the complexity of the HRSG, from one-pressure to two-pressure to three-pressure designs, is observed as we move along the Pareto frontier. The HRSG temperature profiles (in mode A) for the three

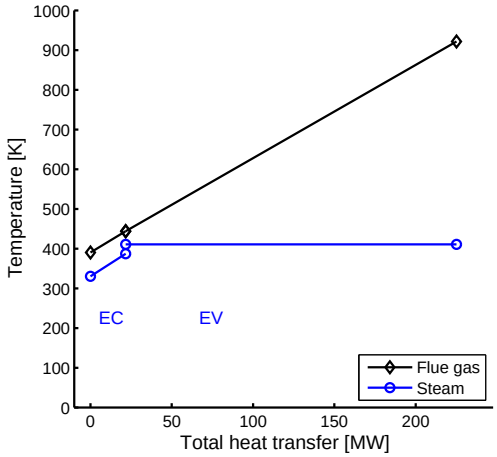

(a) Minimum TCR

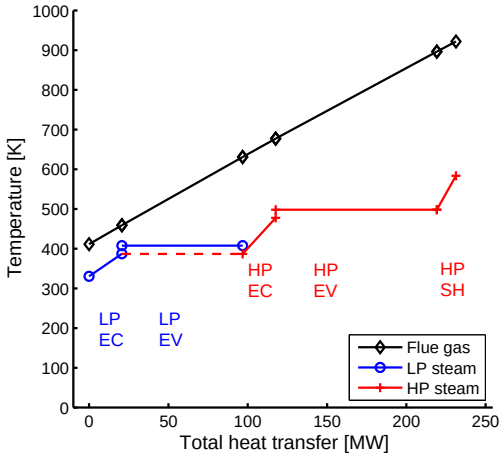

(b) Intermediate TCR and NPV

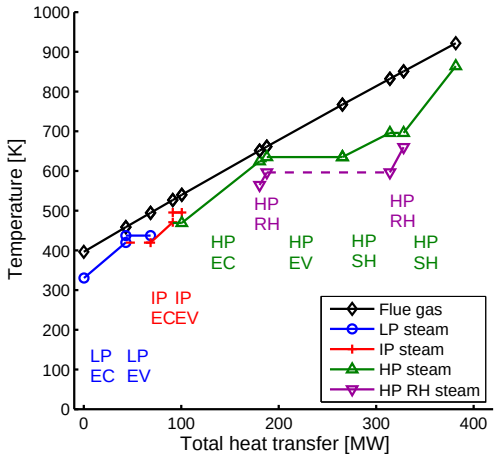

(c) Maximum NPV

Abbreviation key

Abbr.	Definition
LP	Low pressure (steam)
IP	Intermed. press. (steam)
HP	High pressure (steam)
EC	Economizer element
EV	Evaporator element
SH	Superheater element
RH	Reheater element

Figure 3.2: Temperature profiles of optimized HRSG designs in the base scenario (WTX-Base). Dashed lines indicate water bypass streams.

highlighted designs are shown in Figure 3.2. The one-pressure HRSG design in Figure 3.2(a), which is the solution for minimum TCR, contains only two elements, while the three-pressure design (which maximizes NPV) in Figure 3.2(c) is composed of 10 elements. The two-pressure intermediate design contains five elements. The area between the flue gas temperature profile and the (stair-step) steam-water profile is related to exergy destruction in the heat transfer operation. It is apparent that more complex (and more expensive) configurations lead to higher efficiencies, and thus more electricity generation.

In WTX-Base, the lowest partial load of the capture system in any Pareto-efficient design is 94.8%. A majority of Pareto-efficient designs do not use partial load at all, and of the optimal designs that do use partial load, the mean CO_2 capture partial load is 98.9%. System behavior at such high partial loads likely does not differ substantially from behavior at full load, so the assumption of negligible partial load efficiency loss for the CO_2 capture system (discussed in Section 2.1.2) is justified.

Figure 3.3 displays the relationships between NPV and four major system parameters: total HRSG gas-side surface area, total GT generation capacity, CO_2 capture capacity, and CO_2 capture utilization factor. The first three parameters together indicate the size of the auxiliary system that is constructed, while the CO_2 capture utilization factor is a metric for the planned operating profile of the facility. NPV increases with increasing size of the auxiliary retrofit system. The one-pressure HRSG systems indicated by the blue circles in Figure 3.3(a) have greater CO_2 capture capacity than might be expected because the CCGT systems in these facilities are inefficient, so more CO_2 must be captured from the CP for the overall facility to meet the emission standard.

The relationships shown in Figure 3.3 are not Pareto frontiers, since the quantities plotted along the x-axes are not objective functions. The relationship between NPV and HRSG size for Pareto-efficient systems, shown in Figure 3.3(a), indicates that a given NPV can be achieved with several different HRSG sizes. One cause for this is that differences in non-HRSG variables across designs with similar HRSG sizes can have a large impact on NPV. In addition, the direct contribution of HRSG size

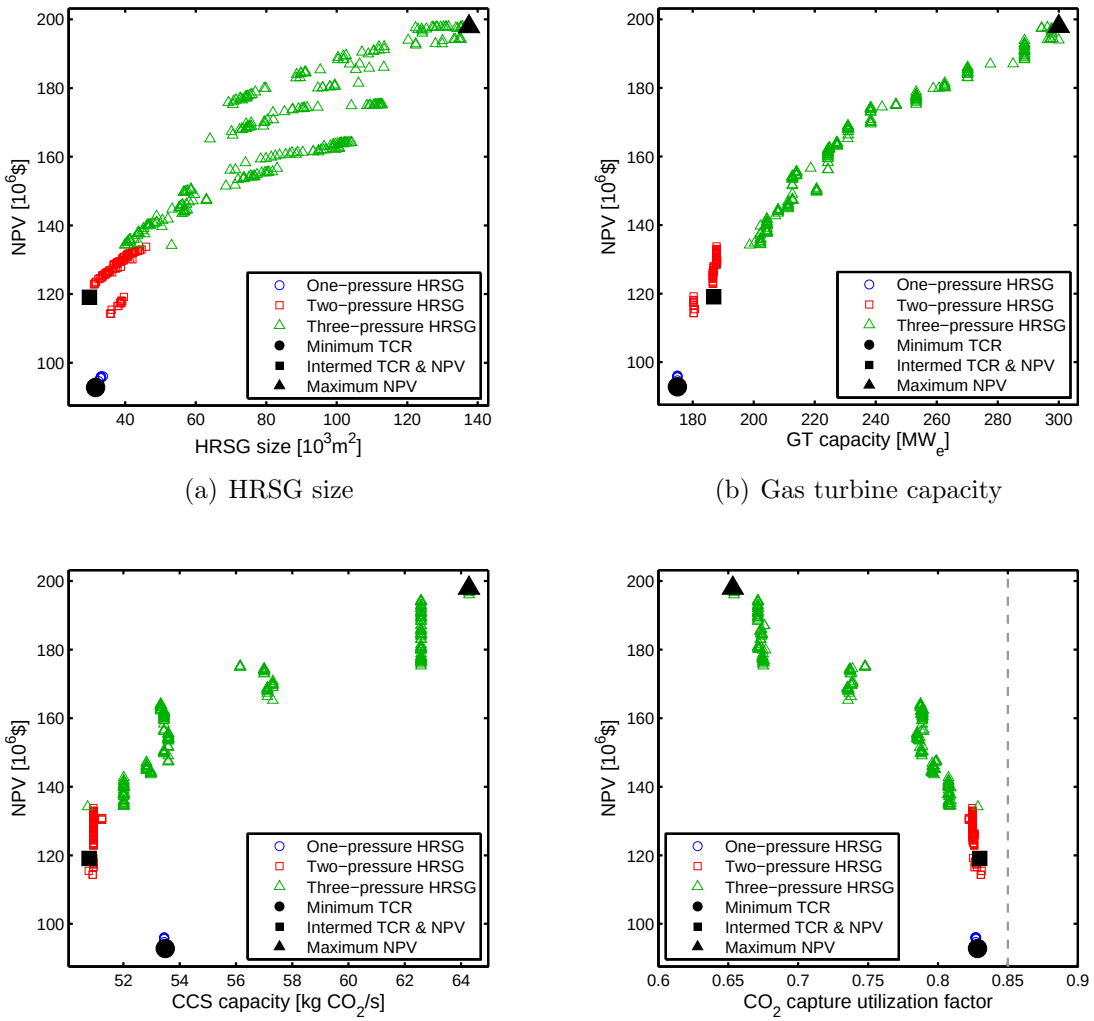

(a) HRSG size

(b) Gas turbine capacity

(c) CO_2 capture capacity

(d) Utilization factor of CO_2 capture system

Figure 3.3: Relationship between NPV and system parameters for Pareto-efficient designs in the base scenario (WTX-Base).

to NPV (via capital cost) is relatively small. Furthermore, HRSG size is an aggregate measure of several HRSG design variables, so significantly different HRSG designs can be of the same size.

Facility operations also show clear trends. The CO_2 capture utilization factor is inversely related to NPV, as seen in Figure 3.3(d). This indicates that higher NPV designs correspond to low (or zero) CO_2 capture rates during many hours of the

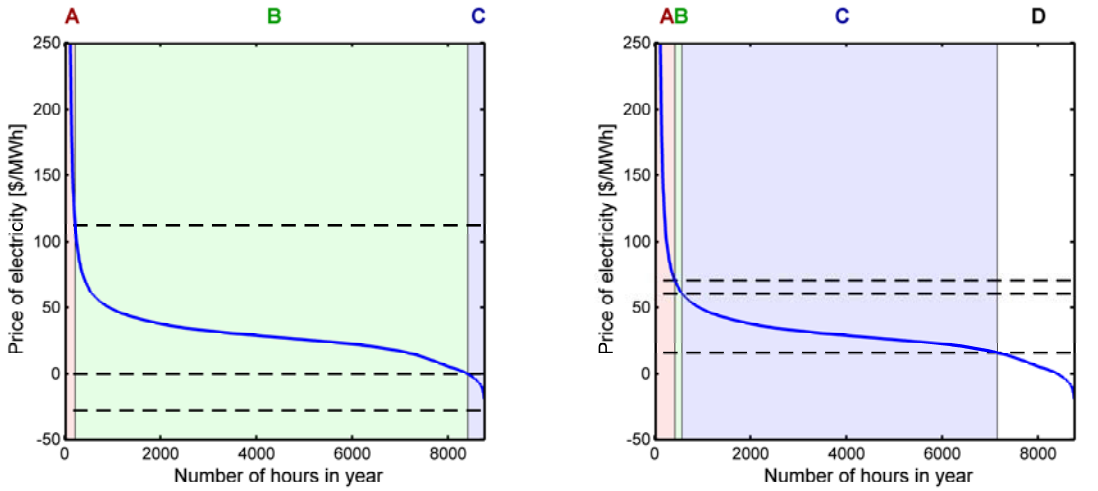

(a) Minimum TCR example strike prices (mode D usage is too small to see)

(b) Maximum NPV example strike prices

Figure 3.4: Example operations of Pareto-efficient systems in the base scenario (WTX-Base).

year (recall that the maximum CO_2 capture utilization factor is 0.85 because the CP capacity factor is 0.85). The strike price operating profiles of the minimum TCR and maximum NPV systems are shown in Figure 3.4 (the strike prices for the intermediate case are very close to those of the minimum TCR case). The system operates in mode D for more time in the NPV-maximizing case (Figure 3.4(b)) than in the TCR-minimizing (and intermediate) cases (Figure 3.4(a)). In fact, facilities toward the minimum-TCR end of the Pareto frontier are not designed to have flexibility with respect to the CO_2 constraint, so they must operate mostly in modes B and C to satisfy the constraint. Variation in CO_2 capture utilization is primarily associated with mode D duration, which is consistent with the fact that the CO_2 capture utilization factor is lowest for the NPV-maximizing system.

Several trends in Pareto-efficient systems can be seen in Figures 3.3 and 3.4. Minimizing TCR leads to systems with lower CO_2 capture capacity, smaller CCGT systems, and greater utilization of CO_2 capture. Maximizing NPV favors facilities with higher CO_2 capture capacity, larger CCGT systems, and greater duration in mode D, in which both CO_2 capture and the CCGT system are inactive. The major

reason for this behavior is that the NPV objective pushes the system to improve operational profitability by avoiding power generation during times with low power prices (as seen in the use of mode D in Figure 3.4(b)), while the TCR objective is not affected by selling power at low prices. CCGT systems with greater generation capacity (larger GT and HRSG) appear in NPV-maximizing systems because the CCGT is profitable under the economic conditions used here. TCR minimization, by contrast, leads to the selection of a CCGT system with less generation capacity in part because profit earned from power generation does not contribute toward TCR.

Table 3.2: Summary of sensitivity scenario results.

(a) Ranges of Pareto frontier objective functions

Scenario name	CP-only NPV [10^6\$]	Pareto NPV range [10^6\$]	Pareto TCR range [10^6\$]
WTX-Base	476	93 – 198	346 – 517
WTX-HighCapCost	476	79 – 148	398 – 570
WTX-HighEnergyCost	836	423 – 589	348 – 519
WTX-LowEnergyCost	84	-352 – -338	342 – 347
UK	381	-73 – 105	331 – 481
India	1,301	513 – 576	337 – 359

(b) Ranges of system parameters for Pareto-efficient systems

Scenario name	GT capacity [MW]	HRSG gas-side surface area [10^3m^2]	CCS capacity [kg CO_2/s]	CCS util. factor [%]
WTX-Base	175 – 300	29.3 – 137.5	50.7 – 66.3	65.3 – 83.1
WTX-HighCapCost	183 – 300	31.8 – 139.4	50.5 – 62.6	67.1 – 83.3
WTX-HighEnergyCost	182 – 300	25.4 – 159.5	50.6 – 62.6	67.1 – 83.6
WTX-LowEnergyCost	172 – 182	32.0 – 41.4	49.8 – 52.3	84.2 – 84.5
UK	173 – 300	23.8 – 193.2	48.5 – 50.7	82.8 – 84.9
India	169 – 186	30.4 – 58.7	49.5 – 51.9	83.2 – 84.2

The other three West Texas scenarios were optimized in the same manner as WTX-Base. A summary of results is presented in Table 3.2. The WTX-HighCapCost and WTX-HighEnergyCost scenarios exhibit many characteristics in common with each other and with WTX-Base. Namely, these scenarios display Pareto frontiers with positive NPV (though the actual values differ greatly), indicating that a CCS retrofit would be preferred over decommissioning in the face of the CO_2 emission regulation

(though we note that including transport and storage in saline aquifers, at a net present cost of approximately $47-249 million, may impact the economic viability of retrofits for WTX-Base and WTX-HighCapCost). Finally, it is of interest that the Pareto-efficient system parameters, shown in Table 3.2(b), in WTX-HighCapCost and WTX-HighEnergyCost exhibit similar ranges as in WTX-Base.

In contrast, the WTX-LowEnergyCost scenario exhibits quite different characteristics than the other West Texas scenarios, as seen in Table 3.2. The NPV in the WTX-LowEnergyCost scenario is negative for all points found (ranging from -$352 million to -$338 million), indicating that a CCS retrofit would not be preferred over decommissioning in this scenario. Additionally, the ranges of Pareto-efficient objective functions and system parameters are much narrower than in the other West Texas scenarios.

The fact that WTX-Base, WTX-HighEnergyCost and WTX-HighCapCost exhibit similar trends suggests that the optimized designs are in some sense robust with respect to realistic future scenarios. In other words, a facility designed for WTX-Base will not be highly suboptimal in either of the reasonably plausible scenarios of WTX-HighEnergyCost and WTX-HighCapCost. The WTX-LowEnergyCost scenario is unlikely to occur in a CO_2-constrained world, so the fact that results for this scenario indicate decommissioning is preferred should probably not be viewed as cause for concern.

3.3 United Kingdom and India

The UK results exhibit broadly similar trends to the WTX-Base results. The UK Pareto frontier shown in Figure 3.5(a) has a similar overall shape as the WTX-Base Pareto frontier, and likewise demonstrates a clear conflict between the TCR and NPV objectives. Furthermore, the Pareto frontier structure is also similar, with one-pressure systems filling the low NPV region, three-pressure systems filling the middle and high NPV region, and two-pressure systems present in an intermediate region. Also of interest is that the UK Pareto frontier has both positive and negative NPVs. In this

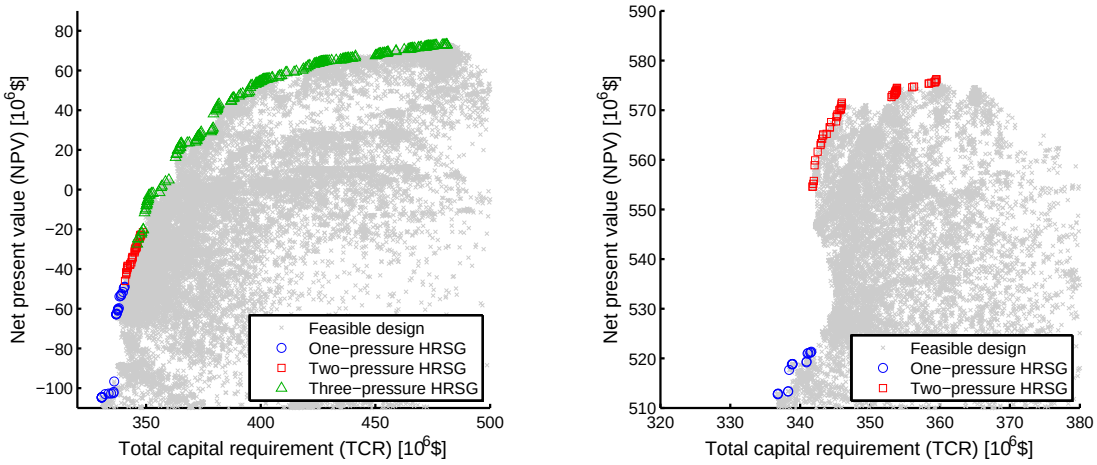

(a) United Kingdom (b) India

Figure 3.5: Pareto frontiers for the UK and India scenarios.

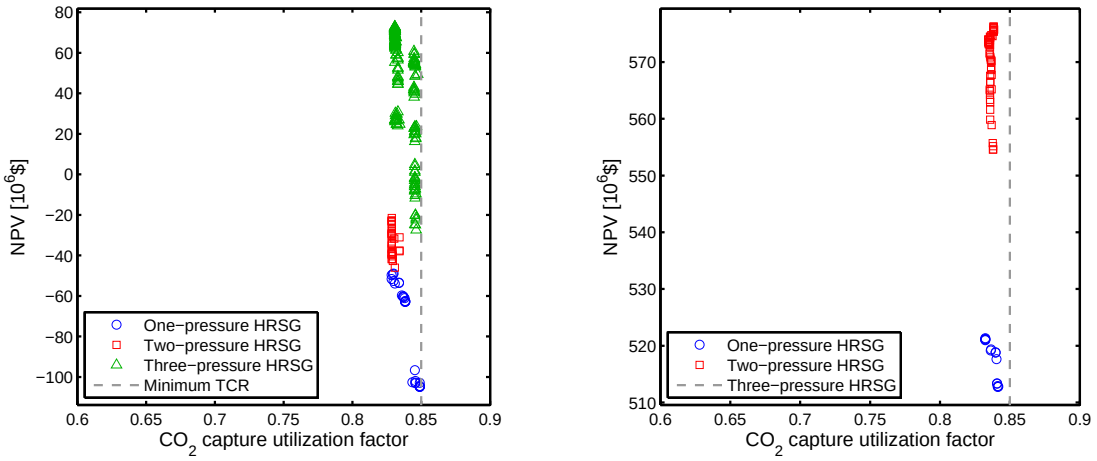

(a) United Kingdom (b) India

Figure 3.6: CO_2 capture utilization factors of Pareto-efficient systems in the UK and India scenarios.

situation, the choice of objective could determine whether an auxiliary CO_2 capture retrofit is economically preferable to decommissioning, because a system designed to minimize TCR would not be economically viable, while a system designed to maximize NPV would be.

A key difference in the UK results as compared to the WTX-Base results is that flexibility plays a smaller role in the UK scenario than in WTX-Base. With reference to Table 3.2(b), the UK scenario includes HRSGs with greater total surface area than in WTX-Base. Additionally, the UK scenario exhibits a narrow range in CO_2 capture capacity, of 48.5-50.7 kg CO_2/s, in contrast to WTX-Base, which exhibits a range of 50.7-66.3 kg CO_2/s. These results indicate that systems in the UK scenario gain greater value from investment for high efficiency in the CCGT system (as seen in having larger HRSGs) than from investment for system flexibility (as seen in having lower CO_2 capture capacities). The decreased importance of flexibility is also seen in the absence of a correspondence between high NPV and low CO_2 capture utilization in Figure 3.6(a) for the UK scenario. The strong association between lower CO_2 capture utilization and high NPV that is present in WTX-Base, as seen in Figure 3.3(d), is not present in the UK scenario. The low importance of system flexibility is consistent with the fact that electricity price variability in the UK scenario (σ = \$13.53/MWh) is substantially less than in WTX-Base (σ = \$126.74/MWh); less electricity price variability leads to less value for flexibility.

The results for the India scenario differ greatly from WTX-Base. As seen in Figure 3.5(b), the Pareto frontier consists only of one- and two-pressure systems, and spans a narrower range in both TCR and NPV than in WTX-Base. In fact, the range of TCR is similar to that in WTX-LowEnergyCost. Moreover, the ranges for the design parameters of Pareto-efficient systems in the India scenario are similar to those for WTX-LowEnergyCost, as seen in Table 3.2(b). The range in NPVs in the India scenario is narrower than in WTX-Base and wider than in WTX-LowEnergyCost. This indicates a lesser degree of conflict between the TCR and NPV objectives than in WTX-Base, but a greater degree of conflict than in WTX-LowEnergyCost. The NPVs found in the India scenario have highly positive values because of the high

price of electricity and low price of coal in this scenario. However, the effective net present cost of the auxiliary gas-fired CO_2 capture retrofit in the India scenario is very large, \$725-788 million. This indicates that an auxiliary gas-fired CO_2 retrofit is a very costly way to mitigate CO_2 emissions in the India scenario.

As in the UK scenario, system flexibility in the India scenario is of lesser importance than in WTX-Base. This can be seen in Table 3.2(b), with the India results exhibiting similar CO_2 capture capacities and CO_2 capture facility utilization factors as in the UK results. This is further corroborated by the lack of a strong relationship between NPV and CO_2 capture utilization factor in the India scenario, as seen in Figure 3.6(b). The low importance of system flexibility is consistent with low electricity price variability (σ = \$24.42/MWh) in the India scenario.

3.4 Advanced CO_2 capture processes

We next perform bi-objective optimizations using the WTX-Base scenario for systems that employ the mixed salt and piperazine processes described in Section 2.1.2. Comparing the results of these optimizations with the WTX-Base results for the MEA process provided in Section 3.2 yields an evaluation of the value of these advanced solvent processes.

In modeling the advanced processes, we use the same capital cost as for the MEA process. The results of the optimization then indicate the value that these technologies can provide under this assumption. We believe this to be a reasonable way to pose the optimization problem because the piperazine and mixed salt processes are quite similar to the MEA process and use similar equipment. In addition, changes in capital costs for individual components in the advanced processes may offset each other to some extent. For example, increases in the cost of the regeneration column with the mixed salt process (which result because the column operates under higher pressure in this process and is thus likely to require thicker walls) would be offset by decreases in the capital cost of the compressors (which result because the compressors would be required to supply a smaller pressure ratio due to the increased regeneration pressure).

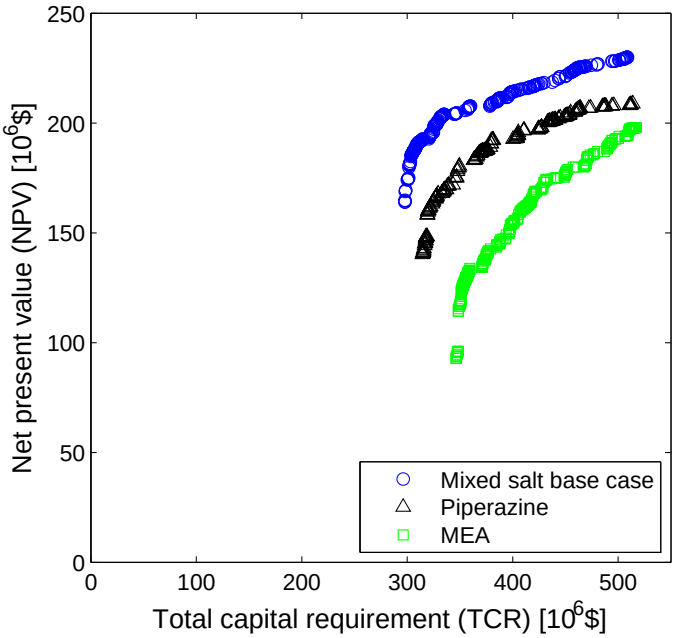

Figure 3.7: Comparison of WTX-Base Pareto frontiers for mixed salt, piperazine, and MEA processes.

Figure 3.7 shows Pareto frontiers for the mixed salt base case, piperazine, and MEA processes. Table 3.3(a) summarizes the ranges of Pareto frontier objective functions for the three processes, and Table 3.3(b) provides the ranges of system parameters for Pareto-efficient facilities. From Figure 3.7 and Table 3.3(a), it is evident that the mixed salt process exhibits superior performance for both objective functions compared to the piperazine and MEA processes, while the piperazine process in turn outperforms the MEA process. For the maximum NPV objective, the mixed salt process achieves a NPV that is 10% higher than that for the piperazine process and 16% higher than that for the MEA process. For the minimum TCR objective, the mixed salt process achieves TCR 5% lower than the piperazine process and 14% lower than the MEA process. Interestingly, comparing the minimum TCR designs, the mixed salt process achieves NPV 17% higher than the piperazine process and 76% higher than the MEA process.

We note that the differences in the TCR and NPV of these systems are, in many cases, less than the 30% capital cost uncertainty associated with our capital cost method. Errors in capital cost estimates are likely correlated, however, because the different processes use very similar equipment. Thus, differences of less than 30% of capital cost may well be significant in these cases.

The reason that the NPV-maximizing facilities using the advanced processes outperform the NPV-maximizing facility with the MEA process is that the advanced processes have smaller duty requirements for reboiler heat and compression work. This results in increased net power output from the facility because more electricity can be generated from the steam cycle, and less electricity is used to compress the CO_2. Similarly, the lower energy duty requirements for the mixed salt process compared to the piperazine process result in the NPV-maximizing mixed salt facility outperforming the NPV-maximizing piperazine facility. The different energy duty requirements for the three processes do not appear to have a large impact on time-varying operations, however, as can be seen in the similar ranges for CO_2 capture system utilization factor in Table 3.2(b) for all cases considered.

Table 3.3: Summary of advanced solvent heat integration results.

(a) Ranges of Pareto frontier objective functions

Process	Pareto NPV range [10^6\$]	Pareto TCR range [10^6\$]
Mixed salt base case	164 – 230	298 – 509
Piperazine	140 – 209	314 – 514
MEA	93 – 198	346 – 517
Mixed salt +10 K reboiler approach temp.	167 – 225	298 – 518
Mixed salt +25% specific reboiler duty	158 – 229	315 – 517
Mixed salt +50% specific reboiler duty	134 – 219	336 – 530

(b) Ranges of system parameters for Pareto-efficient systems

Scenario name	GT capacity [MW]	HRSG gas-side surface area [10^3m^2]	CCS capacity [kg CO_2/s]	CCS util. factor [%]
Mixed salt base case	109 – 300	15.4 – 138.1	50.7 – 62.8	66.8 – 83.0
Piperazine	129 – 300	20.6 – 135.7	50.2 – 63.8	66.2 – 83.6
MEA	175 – 300	29.3 – 137.5	50.7 – 66.3	65.3 – 83.1
Mixed salt +10 K reboiler approach temp.	109 – 300	17.6 – 141.8	50.8 – 64.2	65.4 – 83.3
Mixed salt +25% specific reboiler duty	136 – 300	22.3 – 135.5	50.4 – 65.5	64.1 – 83.5
Mixed salt +50% specific reboiler duty	163 – 300	28.3 – 135.1	51.4 – 68.5	61.3 – 81.9

The advanced process TCR-minimizing facilities outperform the TCR-minimizing MEA facility because the advanced processes have lower specific heat duty requirements. The smaller heat duty requirement entails a smaller CCGT system to capture the same amount of CO_2, thus reducing capital cost, even for CO_2 capture systems with similar capacities. This can be seen in Table 3.2(b), in which the TCR-minimizing systems all have CO_2 capture capacity of $\approx$ 50.5 kg CO_2/s, but the minimum GT

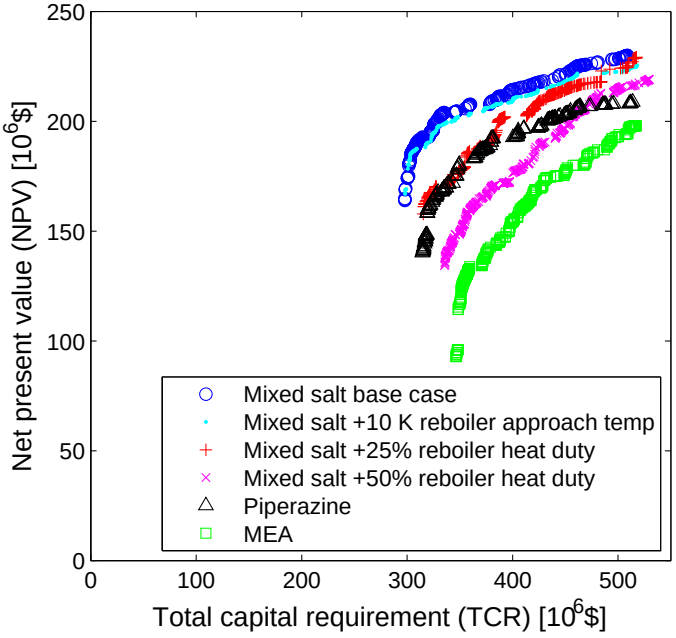

Figure 3.8: WTX-Base Pareto frontiers for the mixed salt process sensitivity study.

capacity varies substantially, from 109 MW (mixed salt) to 175 MW (MEA). A similar pattern can be seen in total HRSG gas-side surface area. This reduced capital investment also contributes toward the large differential in NPV observed in the TCR-minimizing designs using the different processes.

Because the mixed salt process is at an early stage of development, the parameters associated with it are more uncertain than those for the piperazine and MEA processes. Therefore, as discussed in Section 2.1.2, we perform a three-case sensitivity study on the mixed salt process in which we vary the specific reboiler heat duty and reboiler approach temperature. Figure 3.8 shows Pareto frontiers for this sensitivity study. Increasing the reboiler approach temperature by 10 K has a marginally negative impact on NPV for TCR-minimizing systems, and greater negative impact for NPV-maximizing systems. In contrast, increasing reboiler heat duty results in a decrease of NPV along the entire Pareto frontier. With reference to Table 3.3(a), we note that, for +25% reboiler heat duty and +10 K reboiler approach temperature, the mixed salt sensitivity cases outperform the piperazine process along the entirety

of their Pareto frontiers. This is in part because the mixed salt process has a lower specific compression work duty than the piperazine process. This can be seen by comparing the mixed salt +25% specific reboiler heat duty sensitivity case with the piperazine process. With reference to Table 2.1 and Section 2.1.2, both of these cases have similar total heat duty (2.75 MJ/kg CO_2 for the mixed salt +25% reboiler duty sensitivity, and 2.6 MJ/kg CO_2 for piperazine), so both processes have similar minimum GT capacity and HRSG surface area (as seen in Table 3.3(b)). The mixed salt sensitivity case, however, has greater net power sales due to the lower compression work duty.

This assessment of advanced CO_2 capture processes illustrates the applicability of our heat integration optimization framework. By changing the parameters used to represent the CO_2 capture process, we are able to evaluate the mixed salt and piperazine processes and compare them on a consistent basis. These results indicate that the advanced processes outperform the MEA process, and that the mixed salt process in particular is quite promising.

3.5 Summary

In this chapter, we discussed results for the simplified-capture problem formulation. We described the six scenarios considered (four based on West Texas, one based on the United Kingdom, and one based on India). For each of these scenarios, we identified the Pareto frontiers for minimum TCR and maximum NPV, and showed that facility designs are strongly affected by the economic scenario. In particular, facilities designed for time-varying operations are preferred in scenarios with high variability in hourly electricity prices such as the West Texas base scenario, but are not preferred in scenarios with low electricity price variability such as the India scenario. We also performed heat-integration optimizations using the advanced mixed salt and piperazine processes to assess the value of these new technologies. Both of these technologies outperform the MEA process, and the mixed salt process appears to outperform the piperazine process.

Chapter 4

Full-system optimization

In this chapter, we describe and apply the full-system problem formulation, in which we optimize the design and operation of the entire facility. The optimization decision variables include design specifications of the CO_2 capture system, gas turbine (GT) number and capacity, design specifications for the steam cycle in the combined-cycle gas turbine (CCGT) subsystem, and planned time-varying operations. This contrasts with the simplified-capture problem formulation of Chapters 2-3 and Appendix A, in which we optimized the design of the CCGT subsystem in detail, but treated CO_2 capture capacity with a single variable. Here we retain all of the design and operations variables of the simplified-capture formulation, but replace the single CO_2 capture capacity variable used in the simplified-capture formulation with a set of decision variables that represents the detailed design of the CO_2 capture system. The full-system formulation will be shown to yield broadly similar results to the simplified-capture formulation, though the full-system formulation provides additional valuable information on the detailed design of the CO_2 capture system.

This chapter proceeds as follows. In Section 4.1, we briefly present the overall process model for the facility treated in this chapter. The detailed model for the CO_2 capture system, which is the core of the full-system formulation, is described in Section 4.2. The optimization procedure is described in Section 4.3. In Section 4.4, we

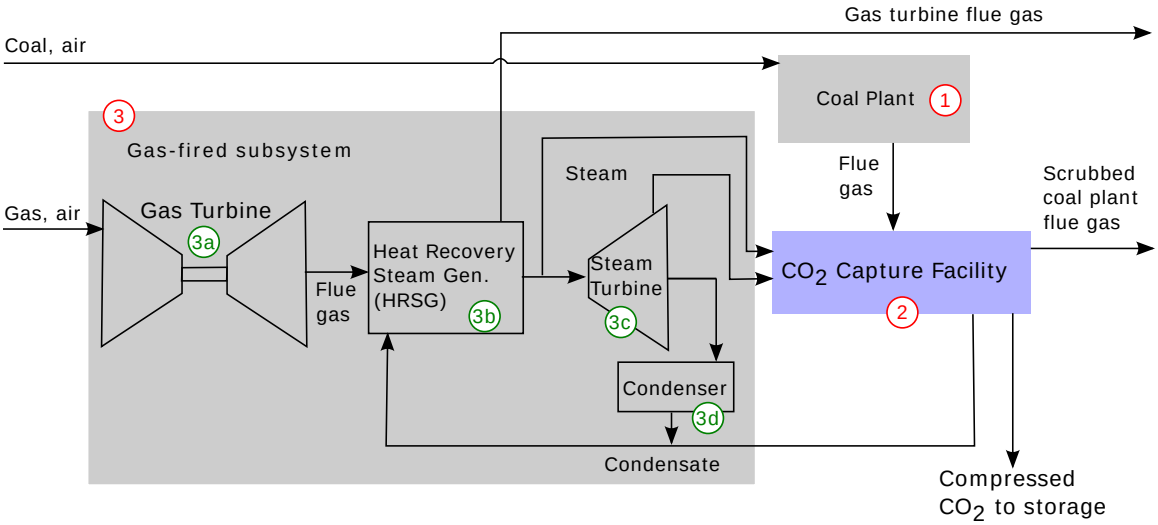

Figure 4.1: Process model of whole system. Modified from Chapter 2.

present results for two scenarios, which are identical to the WTX-Base and India scenarios described in Chapter 3. Additional details for the CO_2 capture system models employed in this chapter are provided in Appendix B.

4.1 Overall facility process model

We describe the overall facility in this section to provide context for the full-system formulation treated in this chapter. Because the full-system formulation incorporates the simplified-capture formulation, this section follows closely some of the discussion in Chapter 2. Figure 4.1 shows the facility considered in this chapter, which is the same as that treated in Chapters 2 and 3. The baseload coal plant (location 1 in Figure 4.1) produces a constant power output of 440 MW. The CO_2 capture system (2), which is the focus of this chapter, scrubs CO_2 from the coal plant flue gas. The CO_2 capture system is described in detail in Section 4.2. Heat required for the CO_2 capture system is supplied as steam drawn from the gas-fired subsystem (3). Note that the CO_2 capture system scrubs only the coal plant flue gas; flue gas from the CCGT subsystem is not scrubbed. As noted previously, transport and long-term storage of CO_2 are not considered in this thesis.

The CCGT subsystem, which was the focus of the simplified-capture formulation, remains unchanged from its representation in Chapters 2-3 and Appendix A. This includes the extraction of steam for solvent regeneration in the CO_2 capture process, in which steam can be taken from the CCGT subsystem at two locations: either bypassing the steam turbines entirely, or in a partially expanded state from the steam turbines.

The coal plant and CCGT subsystem are represented in terms of overall energy and mass balances. The heat recovery steam generator (HRSG) in the CCGT subsystem is represented in detail and uses nonlinear algebraic correlations to model heat transfer. In total, the models for the coal plant and CCGT subsystem include approximately 100-200 state variables, depending on system design. Details on the models for these components can be found in Chapter 2, Appendix A, and our earlier work (Kang et al., 2011).

4.2 CO_2 capture process model

Computational optimization can require thousands to millions of function evaluations, so computational efficiency is essential. In our case, the full-physics model (which is run in Aspen Plus version 7.3) is cumbersome to use directly in optimization because model evaluations require approximately 300 seconds (including overhead) and are difficult to parallelize. Aspen Plus can, however, reliably model the complex physical phenomena involved in the CO_2 absorption and solvent regeneration processes. Therefore, we develop a proxy model for use in optimization that employs the modeling capabilities of Aspen Plus while greatly improving computational efficiency. This enables us to perform optimizations with a model that represents physical phenomena at essentially the same level of detail as Aspen Plus.

The proxy model consists of several distinct submodels, some of which are themselves proxy models. We thus use the term 'integrated proxy model' to refer to the entire CO_2 capture system proxy model. The individual submodels, which represent

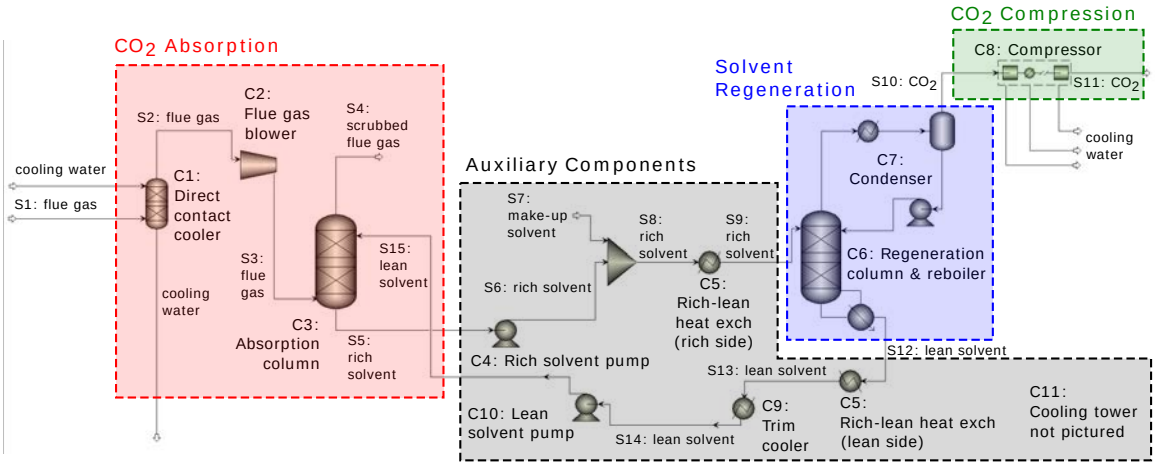

Figure 4.2: Full-physics Aspen Plus model (Kothandaraman, 2010) of CO_2 capture system showing division into blocks. C# indicates numbered component, and S# indicates numbered stream.

all of the system components in the full-physics model, employ several different methods. These include statistical regression with experimental design sampling, boosted decision trees, and direct physics-based representations. By linking these submodels together, our integrated proxy model achieves high computational efficiency and provides predictions that match closely with results from the validated full-physics model. The integrated proxy model achieves a speedup factor of approximately 300 compared to the full-physics model, and can be used readily in a parallel computing environment. The total time required to construct the statistical proxy models for the absorption and regeneration blocks (excluding time required to evaluate the sampled points in the full-physics model) was 10-20 minutes for the training sets used in this chapter.

We now present the CO_2 capture process model developed in this chapter. In the following sections, we first describe the full-physics Aspen Plus model, followed by the submodels developed for the various components. The bottom-up capital cost estimation procedure and optimization-directed retraining are also discussed.

4.2.1 Aspen Plus model

Figure 4.2 depicts the full-physics Aspen Plus process model (hereafter referred to as the full-physics model) used in this chapter. The model is modified from one described in Kothandaraman et al. (2009) and Kothandaraman (2010). The full-physics model treats the CO_2 capture process using a rate-based approach in the absorption and regeneration columns. Aqueous 30 %(wt.) MEA is used as the solvent.

The flue gas (stream S1 in Figure 4.2) from the coal power plant is cooled to 313 K in the direct contact cooler (component C1 in Figure 4.2). The cooled flue gas (S2) is then pressurized slightly ($\sim$ 10 kPa) in the blower (C2), and enters the absorption column (C3) from the bottom. Scrubbed flue gas (S4), which is low in CO_2, leaves from the top of the absorption column. A stream of CO_2-lean solvent (S15, hereafter referred to as lean solvent) enters the top of the absorption column at a temperature of 303 K, and exits the absorption column at the bottom as CO_2-rich solvent (S5, 'rich solvent'), having absorbed CO_2 from the flue gas. The temperature of stream S5 is typically $\sim$330 K.

The rich solvent then is pumped (C4) through the rich-lean heat exchanger (C5) to recover heat from the lean solvent stream (S12) returning from the regeneration column. Note that the rich-lean heat exchanger appears in two locations in Figure 4.2 because the same piece of equipment is represented twice: once for the rich side and once for the lean side. After exiting the rich-lean heat exchanger, the rich solvent stream enters the regeneration column (C6). In the regeneration column, where CO_2 is desorbed from the solvent, heat is applied in the reboiler, which is supplied steam at $\sim$ 400 K ($\sim$ 300 kPa) by the CCGT system. Lean solvent (S12) exits the bottom of the regenerator at $\sim$ 400 K and proceeds to the rich-lean heat exchanger (C5). After being cooled partially to $\sim$ 330 K, the lean solvent (S13) is cooled further in a trim cooler (C9) to 313 K, and pumped (C10) back into the absorption column.

The gas at the top of the regeneration column is cooled to 323 K in the condenser (C7, depicted as a heat exchanger and flash tank). The condensible content (which is essentially all water) of the column product gas is refluxed into the regeneration

column. The uncondensed content of the column product gas is a nearly pure CO_2 stream (S10), which is compressed in a multistage intercooled compressor (C8) to a pipeline pressure of 14 MPa.

Our model includes most of the features in the original system considered by the Kothandaraman (2010) model. Specifically, we left unchanged the following modeling characteristics: thermodynamic modeling approach, correlations for transport phenomena and holdup, number of vertical discretization stages for the packed columns, and locations of discretization points for liquid film modeling within the packed columns. The model includes nine liquid-phase chemical species and five chemical reactions, of which three are treated as equilibrium reactions and two are treated using a rate-based approach. Newly available chemical kinetics data from Thee et al. (2012) are incorporated in the model. Additionally, we changed the absorption and regeneration columns to use the structured packing material Flexipac 1Y, in addition to the random packing material IMTP no. 40 (Tsai et al., 2011; Zhang et al., 2009). Further details on the full-physics model, including validation with experimental data, are provided in Appendix B.

4.2.2 Division of process model into submodels

We divide the full-physics model into four major blocks, shown in Figure 4.2: CO_2 absorption, solvent regeneration, CO_2 compression, and auxiliary components. Streams that cross the boundaries of a process component are treated as input or output variables for that component. Input and output variables for the absorption and regeneration blocks, which are the key components in the integrated proxy model, are summarized in Tables 4.1 and 4.2.

Some of the input variables to each submodel are specified by the system designer (in our case, the optimization algorithm), while others are calculated during the evaluation of the integrated proxy model. We call the input variables that are specified by the optimization algorithm 'design variables.' For the absorption block, all of the input variables listed in Table 4.1(a) are design variables. For the regeneration block,

Table 4.1: Input variables for CO_2 absorption and solvent regeneration blocks.

(a) Absorption block

Variable name	Symbol	Units	Component or stream in Figure 4.2
Absorp col. pack diam.	D_{abs}	m	C3
Absorp col. pack height	Z_{abs}	m	C3
Flue gas flow rate	$\dot{m}_{\text{S1}}$	kg flue gas/s	S1
Lean solvent flow rate	$\dot{m}_{\text{S15}}$	kg solvent/s	S15
Lean solvent loading	L_{S15}	mol CO_2/mol MEA	S15

(b) Regeneration block

Variable name	Symbol	Units	Component or stream in Figure 4.2
Regen. col. pack diam.	D_{regen}	m	C6
Regen. col. pack height	Z_{regen}	m	C6
Regen. col. pressure	p_{regen}	kPa	C6
Reboiler heat duty	$\dot{Q}_{\text{reb}}$	MW_{th}	C6
Rich solvent flow rate	$\dot{m}_{\text{S9}}$	kg solvent/s	S9
Rich solvent CO_2 loading	L_{S9}	mol CO_2/mol MEA	S9

the following variables are design variables: regeneration column packed diameter D_{regen} [m], regeneration column packed height Z_{regen} [m], and regeneration column operating pressure p_{regen} [kPa]. The other three regeneration block input variables are calculated in the course of the optimization. The rich solvent flow rate $\dot{m}_{\text{S9}}$ [kg/s] and rich solvent CO_2 loading L_{S9} [mol CO_2/mol MEA] are calculated from the outputs of the absorption block. The reboiler heat duty $\dot{Q}_{\text{reb}}$ [MW_{th}] is controlled so that the regeneration block outlet lean solvent CO_2 loading is equal to the absorption block inlet lean solvent CO_2 loading (this procedure is described in greater detail in Appendix B).

The output variables enumerated in Table 4.2 serve different purposes. Some output variables are used only for evaluating constraints in the optimization procedure, while others are used for overall energy accounting calculations but are not used explicitly in the solution of the integrated proxy model. Some variables are used directly as inputs in other system components within the integrated proxy model. For example, in both the absorption and regeneration blocks, the column flood and pressure drop output variables are constrained quantities in the optimization. Absorption column pressure drop Δp_{abs} [kPa] and regeneration column condenser duty $\dot{Q}_{\text{cond}}$ [MW_{th}] are used in calculating blower work and cooling tower duty, respectively, as described in Appendix B. Output variables such as CO_2 desorption rate $\dot{m}_{\text{S10}}$ [kg CO_2/s] in the regeneration block, and rich solvent flow rate $\dot{m}_{\text{S5,S6}}$ [kg/s] in the absorption block, are key quantities in the integrated proxy model, as they are used as input variables for other system components.

4.2.3 CO_2 absorption block

In this section we describe our procedure for constructing the statistical proxy for the absorption block. The procedure consists of three main steps: sampling, model fitting, and model verification. In the sampling step, we use the full-physics model to evaluate a set of points in the space of input variables. The output variables for each point are recorded. When running sample points in the full-physics model, we include only those components of the full-physics model that are contained within the block. For

Table 4.2: Output variables for CO_2 absorption and solvent regeneration blocks.

(a) Absorption block

Variable name	Symbol	Units	Component or stream in Figure 4.2
CO_2 absorption rate	$\dot{m}_{CO_2abs}$	kg CO_2/s	C3, S1–S4
Abs. col. pressure drop	Δp_{abs}	kPa	C3
Abs. col. flood	f_{abs}	fraction flood	C3
Rich sol. flow rate	$\dot{m}_{S5,S6}$	kg solvent/s	S5, S6
Rich sol. CO_2 loading	$L_{S5,S6}$	mol CO_2/mol MEA	S5, S6
Rich sol. temperature	T_{S5-S8}	K	S5–S6, S8
Makeup sol. flow rate	$\dot{m}_{S7}$	kg solvent/s	S7

(b) Regeneration block

Variable name	Symbol	Units	Component or stream in Figure 4.2
CO_2 desorption rate	$\dot{m}_{S10}$	kg CO_2/s	C6, S10
Regen. col. pressure drop	Δp_{regen}	kPa	C6
Regen. col. flood	f_{regen}	fraction flood	C6
Regen. condenser duty	$\dot{Q}_{cond}$	MW_{th}	C6
Lean sol. flow rate	$\dot{m}_{S12-S15}$	kg solvent/s	S5, S6
Lean sol. CO_2 loading	$L_{S12-S15}$	mol CO_2/mol MEA	S12–S15
Lean sol. temperature	T_{S12}	K	S12

example, with reference to Figure 4.2, the full-physics model used for the absorption block includes only components C1-C3 and streams S1–S5, S15, and cooling water. In the model fitting step, we construct statistical regressions for each of the output variables. In the model verification step, we evaluate the accuracy of the proxy models relative to the full-physics model. If the proxy model displays insufficient accuracy for particular sets of input variables, we retrain the model in appropriate regions, as described in Section 4.2.8.

We take a 'gray box' approach in our treatment of the absorption block, meaning that we do not view the system simply as a black box. There are two reasons for this. First, our capital cost estimation technique (described in Section 4.2.7) requires specifications for the design of each individual component within the absorption block. Additionally, the flue gas blower (C2 in Figure 4.2), a component of the absorption block, is necessary for computations in Aspen Plus, but it is physically simple and thus does not require treatment using the statistical proxy method. Instead, we calculate blower work directly using a physics-based approach, as described in Appendix B.

4.2.3.1 Input variable sampling

We construct our set of sample points using a combination of deterministic and randomized experimental designs. The deterministic experimental designs are the Box-Behnken and central composite designs as implemented in the MATLAB functions `bbdesign` and `ccdesign`. These designs specify points on edges, corners, and faces of the sample bounds. The randomized designs are determined using Latin hypercube sampling (LHS), which specifies space-filling points within the sample bounds, as implemented by the function `lhsdesign`. Details on Box-Behnken, central composite, and LHS experimental designs can be found in Myers et al. (2009). Figure 4.3 shows example experimental designs in three dimensions with coordinates bounded by -1 and 1. The full set of sample points is the superset of points appearing in any of the deterministic and randomized designs. Table 4.3 shows the sampling bounds used for each of the variables. We sampled 600 points in this step.

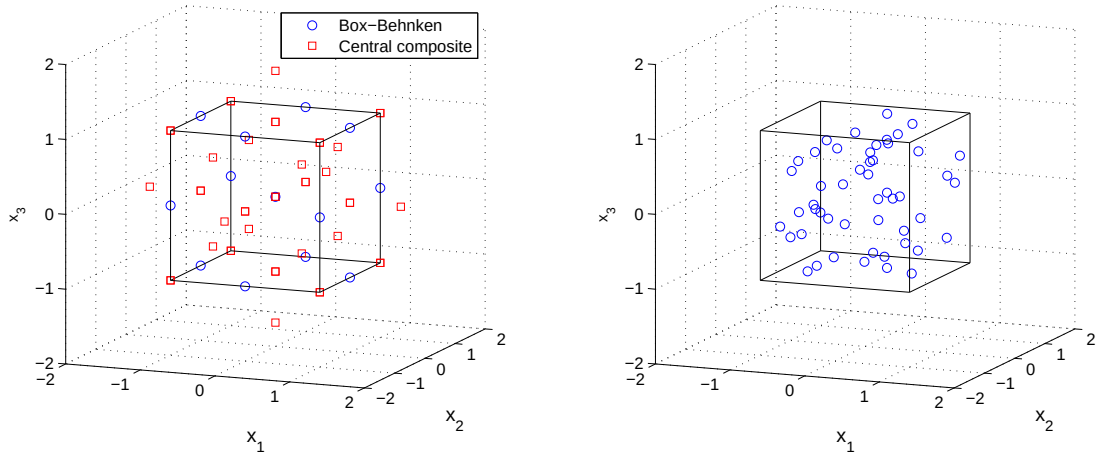

(a) Box-Behnken and central composite (deterministic), 41 unique points

(b) Latin hypercube (randomized), 50 unique points

Figure 4.3: Example experimental designs in three dimensions.

Table 4.3: Bounds on absorption block sampled variables.

Variable name	Symbol	Units	Lower bound	Upper bound
Column packed diameter	D_{abs}	m	0.5	13.0
Column packed height	Z_{abs}	m	5.0	22.0
Flue gas flow rate	$\dot{m}_{\text{FG}}$	kg/s	100	250
L/G ratio	$R_{\text{L/G}}$	kg solv./kg flue gas	2.0	5.0
Lean solvent loading	L_{lean}	mol CO_2/mol MEA	0.1	0.3

In order to draw sample points from a realistic physical domain, we transform the input variable lean solvent flow rate $\dot{m}_{\mathrm{S15}}$ [kg solvent/s]. In this transformation, we divide $\dot{m}_{\mathrm{S15}}$ by the flue gas flow rate $\dot{m}_{\mathrm{S1}}$ [kg flue gas/s] to obtain the liquid/gas ratio (L/G ratio) variable $R_{\mathrm{L/G}}$ [kg solvent/kg flue gas]. We then sample on $R_{\mathrm{L/G}}$ and calculate $\dot{m}_{\mathrm{S15}}$ as $\dot{m}_{\mathrm{S15}} = \left(R_{\mathrm{L/G}}\right) \dot{m}_{\mathrm{S1}}$. Appendix B provides further discussion of the sampling procedure.

4.2.3.2 Absorption proxy model fitting

Once the input variables are fully defined, we simulate the absorption block using Aspen Plus. Kriging is then applied to produce the statistical regression surface for the output variables specified in Table 4.2(a) (Couckuyt et al., 2012, 2014). Each output variable is fit with an independent surface. Kriging can be understood as a locally-weighted regression method, which matches training output exactly at the training points, while accounting for correlation between training data points. We use the MATLAB-based Object Oriented Design and Analysis of Computer Experiments (ooDACE) implementation of kriging (Couckuyt et al., 2012, 2014). We found that fitting the logarithm of the column pressure drop resulted in improved performance compared to fitting pressure drop directly. All other output variables were fit directly. Further information on kriging and the ooDACE toolbox can be found in Couckuyt et al. (2012, 2014).

The full-physics Aspen Plus model does not converge for all points sampled. This is likely because some of the sample points correspond to scenarios that are not physically feasible (or are nearly infeasible). We treat points that fail to converge in the process model as infeasible in the optimization procedure. In this way, the proxy model is essentially consistent with the full-physics model.

Conveniently, the absorption block does not require any special treatment to predict convergence failure. This is because the points that fail to converge in the absorption block almost always violate nonlinear constraints in the optimization procedure (namely, maximum absorption column flood fraction of 0.80 and maximum absorption column pressure drop of 5 kPa). Out of the 600 points sampled using the

procedure in Section 4.2.3.1 (31 of which failed to converge), only one point would be evaluated as satisfying the nonlinear constraints. Thus, candidate designs that would lead to convergence failure in the absorption block are very unlikely to be reported as feasible in the optimization procedure.

4.2.3.3 Absorption proxy model verification

We verify the accuracy of the absorption proxy model with respect to the full-physics model by evaluating a test set of 150 points (which is disjoint from the training set). Figure 4.4 shows parity plots of selected outputs, and Table 4.4 shows summary statistics for all of the output variables. Only points that converged in the full-physics model are included in Figure 4.4 and Table 4.4. These verification results do not involve the optimization-directed retraining procedure described in Section 4.2.8 (which improves proxy model performance in the neighborhood around points found during optimization).

The proxy model predictions for the absorption block match full-physics model predictions to a high degree of accuracy. All predicted quantities other than absorption column pressure drop have a mean absolute deviation (MAD) of less than 4% of the sample mean. Absorption column pressure drop has a MAD of 0.28 kPa, which is less than 9% of the sample mean. The optimization results presented in Section 4.4 indicate that the prediction error in absorption column pressure drop does not cause significant problems in the optimization.

4.2.4 Solvent regeneration block

The submodel for the solvent regeneration block is constructed using the same sample–train–verify procedure as was used for the absorption block submodel described in Section 4.2.3. The main distinction here is that the regeneration block requires a separate mechanism to predict simulation success, which we describe in Section 4.2.4.2. Further information on the regeneration submodel is provided in Appendix B.

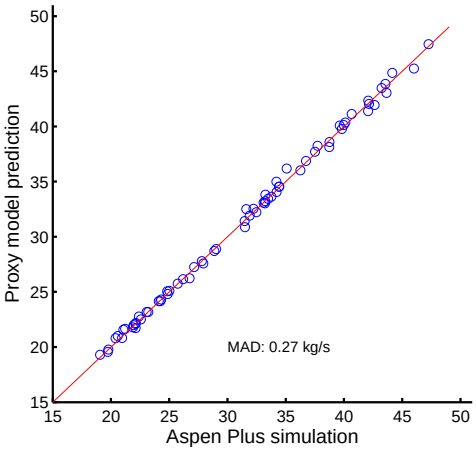

(a) CO_2 absorption rate [kg CO_2/s]

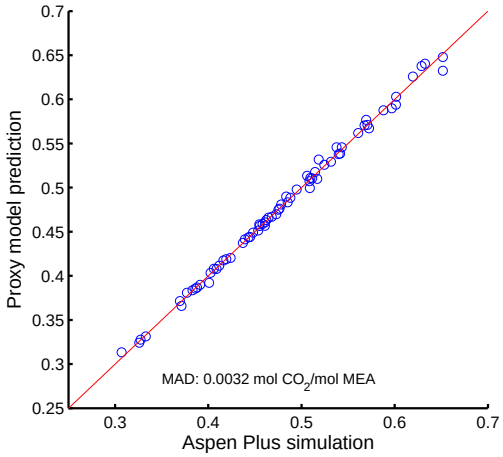

(b) Absorption column outlet rich solvent loading [mol CO_2/mol MEA]

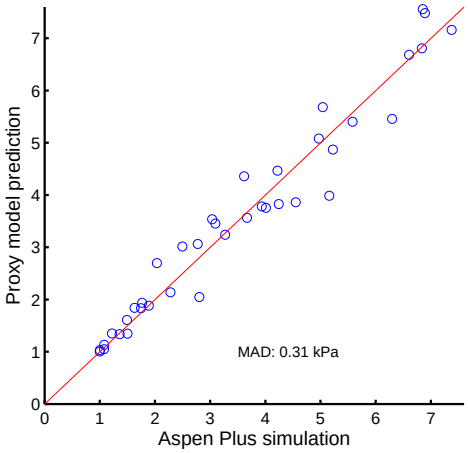

(c) Absorption column pressure drop [kPa] (range restricted to $\Delta p \leq 7.5$ kPa)

Figure 4.4: Verification of statistical proxy model for the absorption block. These points are calculated before optimization-directed retraining described in Section 4.2.8.

Table 4.4: Proxy model performance of the absorption block submodel. These results are calculated before optimization-directed retraining described in Section 4.2.8.

Variable	Units	Sample μ	MAD	MAD (%)*
CO_2 absorption rate	kg CO_2/s	31.05	0.27	0.9
Column pressure drop	kPa	3.52†	0.31†	8.8†
Column flood fraction	–	0.874‡	0.004‡	0.4‡
Rich solvent loading	mol CO_2/mol MEA	0.481	0.003	0.7
Rich solvent flow rate	kg solvent/s	605.2	0.45	0.1
Rich sol. temperature	K	334.0	0.51	2.4§
Sol. makeup required	fraction of lean sol. flow	0.023	0.001	3.8

* Mean absolute deviation as percentage of sample mean. † Includes only points with $\Delta p \leq 7.5$ kPa. ‡ Includes only points with flood ≤ 1.0. § As percentage of temperature difference between sample mean and absorption column lean solvent inlet temperature, 313 K.

Table 4.5: Bounds on regeneration block sampled variables.

Variable name	Symbol	Units	Lower bound	Upper bound
Column packed diameter	D_{regen}	m	0.5	13.0
Column packed height	Z_{regen}	m	3.0	20.0
Column pressure	p_{regen}	kPa	65	250
Rich solvent flow rate	$\dot{m}_{\text{S9}}$	kg/s	1.0	1500
Rich solvent loading	L_{S9}	mol/mol	0.20	0.70
Approx. specific reb. heat duty	$\tilde{\dot{q}}_{\text{reb}}$	MJ/kg CO_2	0.1	10.0

4.2.4.1 Sampling and model fitting

We apply the same sampling procedure in the regeneration block as in the absorption block. The sampling bounds on regeneration block input variables are shown in Table 4.5. A total of 750 points were sampled for the regeneration block.

Variable transformations are again performed to improve the performance of the proxy model. Here, to draw the input variable reboiler heat duty $\dot{Q}_{\text{reb}}$ from a realistic range, we construct an approximate specific reboiler heat duty $\tilde{\dot{q}}_{\text{reb}}$ [MJ_{th}/kg CO_2] by dividing $\dot{Q}_{\text{reb}}$ by an approximate rate of CO_2 desorption $\tilde{\dot{m}}_{\text{des,CO}_2}$ [kg CO_2/s] in the regeneration block. We then sample on $\tilde{\dot{q}}_{\text{reb}}$ and use this to calculate $\dot{Q}_{\text{reb}}$ as $\dot{Q}_{\text{reb}} = \tilde{\dot{q}}_{\text{reb}} \tilde{\dot{m}}_{\text{des,CO}_2}$.

4.2.4.2 Regeneration model fitting and prediction of simulation convergence

The kriging procedure described in Section 4.2.3.2 is again applied. As in the absorption block, we found that better performance was achieved by fitting the logarithm of regeneration column pressure. In addition, fitting the logarithm of regeneration column flood fraction also provided improved performance.

The regeneration block exhibits less favorable simulation convergence behavior than the absorption block, because many points that fail to converge in the full-physics model are evaluated as satisfying the nonlinear optimization constraints. In the regeneration block, Aspen Plus convergence failure was observed in 83 out of 750 sampled points, and of these 83 points, 46 points satisfy the constraints on maximum regeneration column flood fraction (≤ 0.80) and maximum absorption column pressure drop (≤ 5 kPa). Therefore, in order to avoid generating optimization scenarios that cannot be simulated in Aspen Plus, we implemented an independent simulation convergence prediction mechanism for the regeneration block.

We use a statistical classification approach to predict regeneration block simulation convergence, where the classification problem is as follows: Given a point consisting of a set of input variables for the regeneration block, classify the point as either having convergence success or convergence failure. To achieve this, we use the method of boosted decision trees (Hastie et al., 2009). This method entails the use of an ensemble of decision trees, where an individual decision tree proceeds by branching sequentially on the values of individual variables. The method requires the choice of three metaparameters, which we determine using a combination of exploratory analysis and statistical cross-validation. Further explanation of the method and our metaparameter selection procedure are presented in Appendix B.

Upon specifying the three required metaparameters, we obtain an algorithm that takes the regeneration block input variables and returns a real-valued number between zero and one. We use this output value to predict simulation convergence by comparison with a classification threshold T. For predictions with value less than T

Table 4.6: Proxy model performance of the regeneration block submodel. These results are calculated before optimization-directed retraining described in Section 4.2.8.

Variable	Units	Sample μ	MAD	MAD (%)*
CO_2 regeneration rate	kg CO_2/s	38.9	2.3	5.8
Column pressure drop	kPa	1.4†	0.85†	61.3†
Column flood fraction	–	0.46‡	0.073‡	15.9‡
Lean solvent loading	mol CO_2/mol MEA	0.200	0.018	9.0
Lean solvent flow rate	kg solvent/s	766.4	3.0	0.4
Lean solvent temperature	K	391.3	0.91	1.2§

* Mean absolute deviation as percentage of sample mean. † Includes only points with $\Delta p \leq 7.5$ kPa. ‡ Includes only points with flood ≤ 1.0. § As percentage of temperature difference between sample mean and absorption column lean solvent inlet temperature, 313 K.

we return a prediction of convergence failure (coded as zero); otherwise we return a prediction of convergence success (coded as one). The prediction mechanism identifies approximately 90% of successful points and 95% of failed points. We found that this level of prediction accuracy is sufficient to prevent the optimization algorithm from finding points that are not possible to simulate in Aspen Plus. In Appendix B we present more details on the regeneration block convergence prediction mechanism, including determination of T.

4.2.4.3 Regeneration proxy model verification

As seen in Figure 4.5 and Table 4.6, the regeneration block proxy model is not as accurate as the absorption block proxy model. However, the regeneration proxy model is still sufficiently accurate for use in optimization. Specifically, it produces predictions with MAD less than 10% for all quantities other than regeneration column flood fraction and regeneration column pressure drop. The optimization results in Section 4.4 indicate that this level of prediction error does not pose a significant problem in the optimization, except in the case of regeneration column flood fraction. We manage the relatively large error for this quantity (MAD of 16%) by tightening the constraint on regeneration column maximum flood fraction as described in Section 4.3.2. The

large error in regeneration column pressure drop may be an effect of complex flow and phase-change behavior in the regeneration column, in which steam is generated by the application of heat in the reboiler. The error in this quantity is not of major concern, however, because regeneration column pressure drop is used only to assess potential constraint violation in the optimization procedure, and this constraint is never binding. As with the absorption proxy model described in Section 4.2.3, the model performance results presented in this section are for the proxy model before applying the optimization-directed retraining procedure.

4.2.5 Compression block

The compression block consists of a four-stage compressor, cooled between stages to 323 K, with equal pressure ratios in each stage. The inlet pressure of the CO_2 is equal to the regenerator column pressure (which is a design decision variable that can range from 65 kPa to 250 kPa), and the outlet pressure is 14 MPa. As such, the pressure ratio of each stage ranges from 2.73 to 3.83. Each compression stage has an isentropic efficiency of 0.85 (Towler and Sinnott, 2013, p 1224; Ulrich and Vasudevan, 2004, p 160). The intercoolers are modeled as countercurrent heat exchangers.

4.2.6 Auxiliary components

There are several process components that are not modeled fully within the absorption, regeneration, or compression blocks. These components, which include the rich-lean heat exchanger, rich and lean solvent pumps, trim cooler, and cooling tower, are treated directly using simple physics-based models. We describe the models for each of these components in Appendix B.

4.2.7 Capital cost estimation

In our previous work, we developed a bottom-up capital cost estimation procedure that estimated the capital cost of the facility at the Class 4, or 'equipment-factored,'

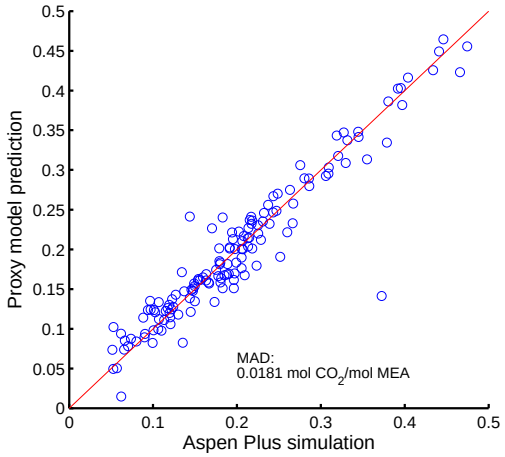

(a) Regeneration column outlet lean solvent loading [mol CO_2/mol MEA]

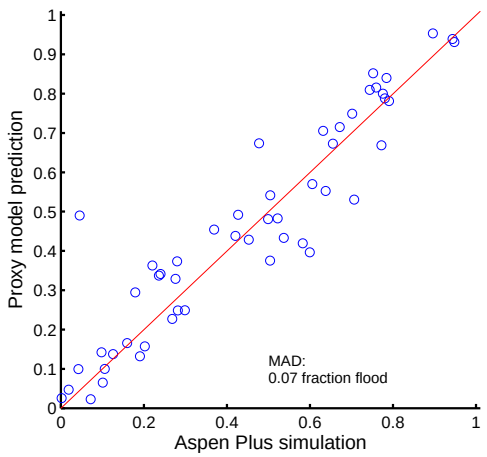

(b) Regeneration column flood fraction (range restricted to flood fraction ≤ 1.0)

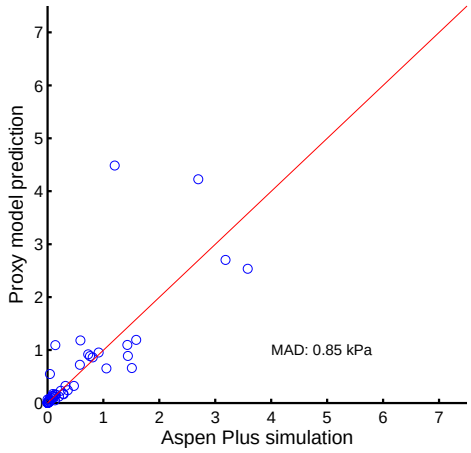

(c) Regeneration column pressure drop [kPa] (range restricted to $\Delta p \leq 7.5$ kPa)

Figure 4.5: Verification of statistical proxy models for the regeneration block. These points are calculated before optimization-directed retraining described in Section 4.2.8.

level, with ±30% accuracy (Couper et al., 2007; Towler and Sinnott, 2013; Ulrich and Vasudevan, 2004). With this approach the capital cost of each component is calculated separately, and the capital cost of the total system is the sum of the component capital costs. In Chapters 2 and 3, the capital cost of the CO_2 capture facility was treated using a single parameter based upon a regression on results from IECM 8.0.2 (Berkenpas et al., 2009; Rubin et al., 2007a). In this chapter, the capital cost of the CO_2 capture system is instead calculated using a bottom-up procedure.

For each component, we apply one of two different capital cost estimation methods, based upon the availability, quality, and appropriateness of capital cost data. The two methods, which we refer to as the Bare Module method and the Battery Limits method, are similar to each other and are both forms of the Guthrie method (Couper et al., 2007; Guthrie, 1969; Towler and Sinnott, 2013; Ulrich and Vasudevan, 2004). These methods entail applying a sequence of multipliers to purchased equipment cost to obtain the capital cost for a fully installed and operational component. As used here, the methods differ from each other in their purchased equipment cost correlations and in the sequence of multipliers that are applied. Because of data availability, our cost calculations in Chapters 2 and 3 used the Bare Module method.

For each component, regardless of method, we calculate the 'total capital cost' (a term of art which is equivalent in both methods) at the component level. We then sum total capital cost across all components to obtain the total capital cost of the system. The total capital cost includes nearly all costs associated with building a process facility, such as equipment purchase, transportation, installation, labor, site preparation, piping, construction insurance, certain taxes, contingency allowances, engineering costs, auxiliary buildings, and off-site facilities. As such, the total capital cost for a component includes costs that are not specifically associated with that component, but which are necessary for the functioning of the entire facility. Interest during construction is not included in the total capital cost. By multiplying the total capital cost by a constant that accounts for the cost of interest during construction, we obtain total capital requirement. Total capital requirement is one of the optimization

objective functions considered in this thesis. It is also a component of net present value, which is the other optimization objective function of interest.

Appendix B provides a full description of the capital cost estimation methodology, including procedures for the Bare Module and Battery Limits methods, data, our handling of interest during construction, and details on the treatment of each component.

4.2.8 Optimization-directed retraining

The statistical proxy models for absorption and regeneration resulting from the sample–fit–verify procedure described in Sections 4.2.3 and 4.2.4 perform well for random test points, as shown in Sections 4.2.3.3 and 4.2.4.3. However, we found that during optimization of the full system, it was common for the optimization algorithm to find points for which the integrated proxy model was inaccurate for the absorption and/or regeneration blocks, which led to unreliable or inaccurate results. To address this problem, we apply an optimization-directed retraining procedure to improve integrated proxy model performance in regions likely to be searched during optimization.

The retraining procedure consists of the following four steps. This procedure can be repeated (iterated) until consistent results are achieved:

1. Apply the integrated proxy model (in which the absorption and regeneration statistical proxy models are constructed using the training set described in Sections 4.2.3 and 4.2.4) in representative optimization runs until convergence is achieved.

2. Identify a new set of sample points ('update set') based upon the optimized results. The update set consists of the optimal points found by the optimization algorithm, augmented with a randomized sample of points in the neighborhood of the optimal points.

3. Evaluate the update set using the full physics model.

4. Incorporate the update set in the training set and retrain the absorption and regeneration statistical proxy models.

In this procedure, we could in principle use the full-system optimization problem defined in Section 4.3. Here we instead apply a more computationally efficient approach in which we optimize only the CO_2 capture system for several linear combinations of four objectives: minimum specific total capital requirement [\$/(kg CO_2/s)], minimum specific operating cost [\$/kg CO_2], minimum total annualized cost [\$], and maximum CO_2 capture capacity [kg CO_2/s]. To simplify the procedure, in specifying these objective functions we use a constant price of electricity, ignore taxes, apply an approximate representation of reboiler steam supply, and assume constant operation. In each round of optimization, the linear combinations considered are determined by inspection of results from previous iterations. We also enforce constraints on maximum pressure drop and maximum flood fraction in the absorption and regeneration columns. In total, we performed four iterations of optimization-directed retraining, which entailed a total of 150 retraining points. This provided an integrated proxy model that was sufficiently reliable for use in the full-system optimization problem, as we now illustrate.

Figure 4.6 shows the prediction accuracy of the integrated proxy model with respect to the full-physics model for CO_2 absorption rate, specific reboiler heat duty, and regeneration column flood fraction. The points shown in Figure 4.6(b)–4.6(d) all correspond to unique CO_2 capture system designs associated with Pareto-efficient points for the West Texas scenario (described in Section 4.4.1) evaluated using the integrated proxy model following each round of optimization-directed retraining. We use these points to assess the proxy model because they represent performance in the region of interest. (Note that the points calculated in the optimization-directed retraining procedure are used to train the model, so they are fit perfectly at the next round.) Integrated proxy model prediction accuracy for CO_2 absorption rate improves with each round of retraining. However, prediction accuracy worsens in the first round of retraining for both the regeneration column flood fraction and specific reboiler heat duty (see Figure 4.6(a)). Over the course of retraining, regeneration column flood

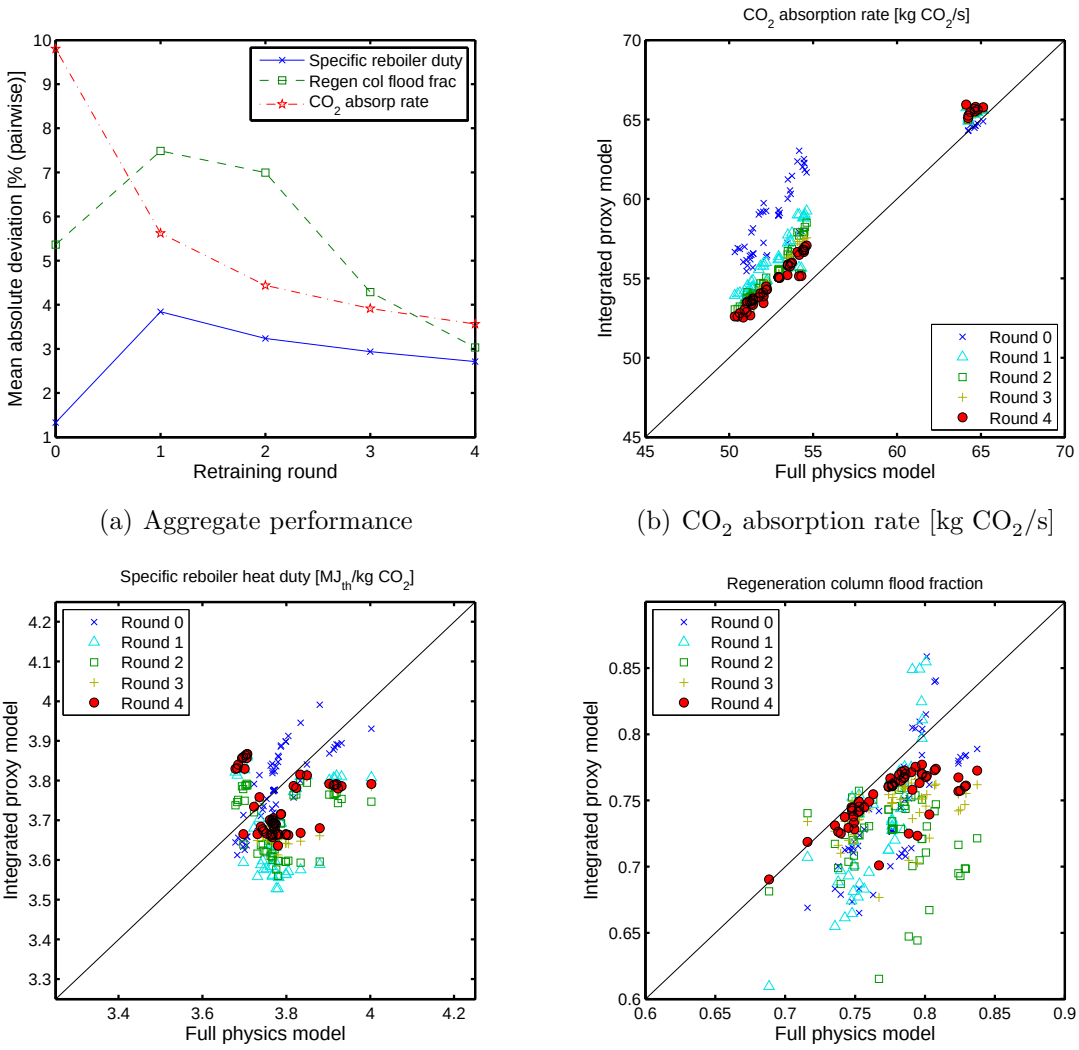

(a) Aggregate performance

(b) CO_2 absorption rate [kg CO_2/s]

(c) Specific reboiler heat duty [MW_{th}/kg CO_2]

(d) Regeneration column flood fraction

Figure 4.6: Accuracy of predictions from integrated proxy model after each round of optimization-directed retraining.

fraction prediction accuracy improves beyond its Round 0 starting point, while specific reboiler heat duty prediction accuracy does not recover its Round 0 performance.

A possible cause of this worsening–then–improving behavior is that the kriging surfaces in the statistical proxy models may be 'overfit' in the region near the evaluated points during the first round of retraining. Subsequent rounds of retraining then resolve this overfit, fully in the case of regeneration column flood fraction, but only partially in the case of specific reboiler heat duty. Nevertheless, the prediction error for all quantities important for optimization is less than 4% for the evaluated points after the optimization-directed retraining procedure is terminated. This level of accuracy is sufficient for the optimizations performed in this chapter. If greater accuracy were desired, additional retraining (possibly incorporating points resulting from actual full-system optimization runs) could be performed.

4.3 Optimization procedure

As in Section 4.1, portions of the discussion below follow closely after Chapter 2. Consistent with the simplified-capture optimization formulation of Chapter 2, the two objectives treated here are minimization of total capital requirement (TCR) and maximization of net present value (NPV). The optimization problem is formally expressed as:

$$\max_{\mathbf{u}_{\text{des}},\mathbf{u}_{\text{ops}}} \left[-C_{\text{TCR}}\left(\mathbf{x},\mathbf{u}_{\text{des}}\right), \quad V_{\text{NP}} = -C_{\text{TCR}}\left(\mathbf{x},\mathbf{u}_{\text{des}},\mathbf{u}_{\text{ops}}\right) + P_{\text{op}}\left(\mathbf{x},\mathbf{u}_{\text{des}},\mathbf{u}_{\text{ops}}\right)\right] \tag{4.1}$$

subject to

$$\mathbf{u}_{\text{des}}, \mathbf{u}_{\text{ops}} \in \Omega \tag{4.2}$$

$$\mathbf{c}\left(\mathbf{x},\mathbf{u}_{\text{des}},\mathbf{u}_{\text{ops}}\right) \leq 0. \tag{4.3}$$

Here, $\mathbf{x}$ represents state variables (which are solved for in the process model), $\mathbf{u}_{\text{des}}$ represents design decision variables, and $\mathbf{u}_{\text{ops}}$ are the strike prices. Both $\mathbf{u}_{\text{des}}$ and $\mathbf{u}_{\text{ops}}$ are determined by the optimization algorithm. The quantity C_{TCR} [\$] is the

TCR objective, V_{NP} [$] is the NPV objective, P_{op} [$] is capitalized operating profits, and $\mathbf{c}$ represents general constraints, some of which are nonlinear. The vector $\mathbf{u}_{\mathrm{des}}$ includes decision variables for the detailed design of the CO_2 capture system along with design decision variables for the rest of the facility, including the GT, HRSG, and steam cycle. This is a key difference from the optimizations in Chapters 2 and 3, in which $\mathbf{u}_{\mathrm{des}}$ did not include the detailed design of the CO_2 capture system.

The above optimization problem is solved using the PSO-MADS algorithm (Isebor, 2013; Isebor and Durlofsky, 2014; Isebor et al., 2014). This algorithm combines two derivative-free methods: Particle Swarm Optimization (PSO), a stochastic global search method, and Mesh Adaptive Direct Search (MADS), a direct search method that converges to a local optimum for many problems. The PSO-MADS algorithm, then, can provide global exploration as well as convergence to a locally optimal solution. Nonlinear constraints are treated using a filter technique, which entails a bi-objective approach to minimize constraint violations along with the objective function.

The PSO-MADS algorithm performs bi-objective optimization to minimize TCR and maximize NPV by solving a sequence of single-objective optimization problems. The objective functions for the single-objective runs are combinations of TCR and NPV. The goal of this procedure is to identify a set of points on the Pareto frontier. This procedure, referred to as BiPSOMADS, employs the 'single-objective product formulation' (Audet et al., 2008). This procedure, which was applied in Chapters 2 and 3, is explained in detail in Isebor (2013) and Isebor and Durlofsky (2014).

BiPSOMADS optimizations were repeated multiple times in order to provide high resolution in the Pareto frontiers. Specifically, we performed about 20 BiPSOMADS optimization runs, each of which consisted of five single-objective PSO-MADS optimizations. Each bi-objective optimization run accessed eight cores simultaneously (several bi-objective runs were performed in parallel, so in total we accessed 50-100 cores at a time) and required about one day of computation, of which communication, read/write, and other overhead accounted for 50-70% of time requirements.

4.3.1 Objective functions and decision variables

The TCR objective is calculated by the procedure described in Section 4.2.7. The NPV objective, which incorporates operating economics and TCR, is calculated as follows:

$$V_{\mathrm{NP}} = -C_{\mathrm{TCR}} + \sum_{y=0}^{29} \frac{0.85\left(R_{\mathrm{elec}} - C_{\mathrm{fuel}} - C_{\mathrm{O\&M}}\right)\left(1 + r_{\mathrm{esc}}\right)^{y+0.5} - C_{\mathrm{tax},y}}{\left(1 + r_{\mathrm{disc}}\right)^{y+0.5}}. \tag{4.4}$$

Here, R_{elec} [\$] represents yearly revenue from electricity sales, C_{fuel} [\$] represents yearly fuel expenses, $C_{\mathrm{O\&M}}$ [\$] represents yearly O&M costs, r_{esc} is the cost escalation rate, $C_{\mathrm{tax},y}$ [\$] represents yearly corporate income tax payments, and r_{disc} is the nominal discount rate. The quantity $C_{\mathrm{O\&M}}$ includes both fixed and variable O&M and is calculated using the same procedure as in Chapters 2 and 3, with data presented in Appendix A. The term $0.85\left(R_{\mathrm{elec}} - C_{\mathrm{fuel}} - C_{\mathrm{O\&M}}\right)$ is the yearly operating profit excluding taxes, and includes a coefficient of 0.85 to represent the capacity factor of the coal plant, which accounts for planned and unplanned outages. (The CO_2 capture system and CCGT subsystem operate only when the coal plant is operating.) The yearly tax payment $C_{\mathrm{tax},y}$ is a function of pre-tax operating profit and depreciation allowance (which is evaluated with the 20-year 150% declining balance method as in Chapters 2 and 3), and applies a corporate income tax rate of 40% to represent combined federal and state tax.

Continuous and discrete variables are present in the optimization problem. Ordered discrete variables are called integer variables, and unordered discrete variables are called categorical variables. All decision variables are aggregated into a single vector $\mathbf{u} = [\mathbf{u}_{\mathrm{des}}; \mathbf{u}_{\mathrm{ops}}]$, which is summarized in Table 4.7. For a system with up to three HRSG pressure levels and 14 elements, we have a total of 49 decision variables. The first nine decision variables in Table 4.7 specify the detailed design of the CO_2 capture system, the next 37 determine the detailed design of the CCGT subsystem, and the last three variables are the strike prices, which are the operational decision variables.

Table 4.7: Optimization decision variables.

Variable	Type	Symbol	# Vars	Units	Lower bound	Upper bound
Number of CCS trains	Integ.	n_{CCS}	1	–	1	8
Absorp. col. packed diam.	Real	D_{abs}	1	m	0.5	13.0
Absorp. col. packed height	Real	Z_{abs}	1	m	5.0	22.0
Absorp. col. inlet flue gas flow rate	Real	$\dot{m}_{\text{FG}}$	1	kg/s	100	250
Absorp. col. L/G ratio	Real	$R_{\text{L/G}}$	1	kg/kg	2.0	5.0
Lean solvent CO_2 loading	Real	L_{lean}	1	mol/mol	0.1	0.3
Regen. col. packed diam.	Real	D_{regen}	1	m	0.5	13.0
Regen. col. packed height	Real	Z_{regen}	1	m	3.0	20.0
Regen. col. operating press.	Real	p_{regen}	1	kPa	65	250
Number of gas turbines	Integ.	n_{GT}	1	–	1	3
Total GT capacity	Real	$n_{\text{GT}} s_{\text{GT}}$	1	MW	1	400
HRSG # press. levels	Integ.	N_{pl}	1	–	1	3
HRSG steam pressures	Real	p_{pl}	3	kPa	100	19,000
HRSG extraction pressure	Real	p_{ext}	1	kPa	300	5,000
HRSG HP reheat press.	Real	$p_{\text{HP,rh}}$	1	kPa	100	20,000
HRSG element type & pl	Categ.	$\mathbf{e}_{\text{pl,type}}$	14	–	-1	11
HRSG nondim. elem. size	Real	$a_{\text{g,0}}$	1	–	0.1	3
HRSG rel. elem. sizes	Real	$\mathbf{a}_{\text{g,rel}}$	14	–	0.1	3
Strike prices	Real	$\mathbf{u}_{\text{ops}}$	3	\$/MWh	(0, -20, -30)	(200, 150, 100)

The first design decision variable for the CO_2 capture system is the number of CO_2 capture trains n_{CCS}. (All CO_2 capture trains are identical.) The next two CO_2 capture system design decision variables specify the packed diameter D_{abs} [m] and packed height Z_{abs} [m] of the absorption column. Following these are variables that define the ratio of mass flow rate of lean solvent to flue gas in the absorption column $R_{L/G}$ (this is the same quantity used in sampling), and the lean solvent CO_2 loading rate L_{lean} [mol CO_2/mol MEA]. Next are two variables that specify the diameter D_{regen} [m] and height Z_{regen} [m] of the regeneration column, followed by a variable that specifies the regeneration column operating pressure p_{regen} [kPa].

The CCGT subsystem decision variables are described in detail in Chapter 2. Briefly, these variables are as follows: n_{GT} is the number of gas turbines, $n_{GT}s_{GT}$ [MW] is the total GT capacity, N_{pl} is the number of pressure levels in the HRSG, p_{pl} [kPa] are the steam pressures produced by the HRSG, p_{ext} [kPa] is the pressure of steam extraction from the HRSG in operating mode B, $p_{HP,rh}$ [kPa] is the reheat steam pressure in the HRSG, $\mathbf{e}_{pl,type}$ specifies the structure of the HRSG (including number, type, and arrangement of internal components), and $a_{g,0}$ and $\mathbf{a}_{g,rel}$ together specify the sizes of the HRSG internal components.

4.3.2 Optimization constraints

There are three sets of constraints in the optimization problem. The first set of constraints enforces physical validity in the HRSG design. The second set of constraints contains bound and linear constraints on the decision variables, and the third set of constraints contains nonlinear constraints applied to quantities calculated in the process model. The third set of constraints include constraints that apply to the outputs of the CO_2 capture integrated proxy model, constraints that enforce the CO_2 emission performance standard, and constraints related to the design of the CCGT subsystem. Below we describe the constraints that are related to the CO_2 capture system. All of the optimization constraints described in Chapter 2 are also active in the problem treated in this chapter. These include constraints that enforce the CO_2 emission performance standard, and heat integration design constraints.

The CO_2 capture system has five nonlinear constraints. Three constraints apply to outputs from the absorption submodel, and two apply to outputs from the regeneration submodel. The constraints are as follows:

1. Maximum absorption column pressure drop, $\Delta p_{\text{abs}} \leq 5$ kPa
2. Maximum absorption column flood fraction, $f_{\text{abs}} \leq 0.80$
3. Maximum rich solvent CO_2 loading, $L_{\text{S5,S6}} \leq 0.56$ mol CO_2/mol MEA
4. Maximum regeneration column pressure drop, $\Delta p_{\text{regen}} \leq 5$ kPa
5. Maximum regeneration column flood fraction, $f_{\text{regen}} \leq 0.775$.

Note that we constrain predicted regeneration column flood fraction to be at most 0.775, even though the engineering design limit is 0.80. This is done to mitigate the effect of the prediction inaccuracy of the regeneration proxy submodel for this quantity. The optimization algorithm often finds points for which the integrated proxy model underpredicts regeneration column flood fraction, so by applying a tighter constraint we find more points that satisfy the physical constraint ($f_{\text{regen}} \leq 0.80$).

4.4 Results and discussion

We consider two scenarios, summarized in Table 4.8. One scenario is based on West Texas, USA in 2011, and the other is based on the Gujarat-Maharashtra electricity market region of India, also in 2011. These scenarios are identical to the 'WTX-Base' and 'India' scenarios treated in Chapter 3. In both scenarios, the nominal discount rate is $r_{\text{disc}} = 11.0\%$/a, and the escalation rate is $r_{\text{esc}} = 3.3\%$/a, resulting in a real discount rate of 7.5%/a. Our modeling and optimization procedure, which incorporates the integrated proxy model for the CO_2 capture system, works effectively in these two quite different scenarios, demonstrating the robustness of this approach.

We again highlight the relationship between the full-system problem formulation treated in this chapter and Appendix B and the simplified-capture problem

Table 4.8: Scenario parameters.

Scenario	P_{elec} mean [$/MWh]	P_{elec} std. dev. [$/MWh]	$P_{\text{nat.gas}}$ [$/GJ] ([$/MMBtu])	P_{coal} [$/GJ] ([$/MMBtu])
West Texas	40.73	126.74	4.48 (4.73)	1.34 (1.41)
India	72.29	24.42	11.56 (12.20)	1.10 (1.16)

formulation treated in Chapters 2-3 and Appendix A. In the full-system formulation, variables for the detailed design of the CO_2 capture system are determined alongside the design of the rest of the facility (GT, HRSG, and steam cycle), while in the simplified-capture formulation the CO_2 capture facility is represented by a single variable for CO_2 capture capacity.

4.4.1 West Texas scenario

In the West Texas scenario, the standalone coal plant (which does not have carbon capture, and therefore does not meet the CO_2 emission performance standard) has a NPV of $476 million. The NPV for optimized facilities with CO_2 capture is less than this quantity, indicating that CO_2 capture represents a net present cost to the facility. However, facilities optimized for minimum TCR and maximum NPV have NPV greater than zero, indicating that installing CO_2 capture to meet the emission performance standard is preferred to decommissioning. This finding coincides with that in Chapter 3.

Evaluated separately, the objectives of minimum TCR and maximum NPV lead to very different designs for both the CO_2 capture system and the CCGT subsystem. Figure 4.7 illustrates the planned operations and facility designs of the minimum TCR and maximum NPV systems. The minimum TCR system performs CO_2 capture (operating in modes B and C) for essentially the entire year, indicating nearly constant operations. This facility has a 181 MW GT, a one-pressure 30,700 m^2 surface area HRSG, and two CO_2 capture trains with total capture capacity of 53.5 kg CO_2/s. In contrast, the maximum NPV system operates variably, with the CO_2 capture facility and CCGT subsystem turned off (mode D) for 18% of the year. This facility has a

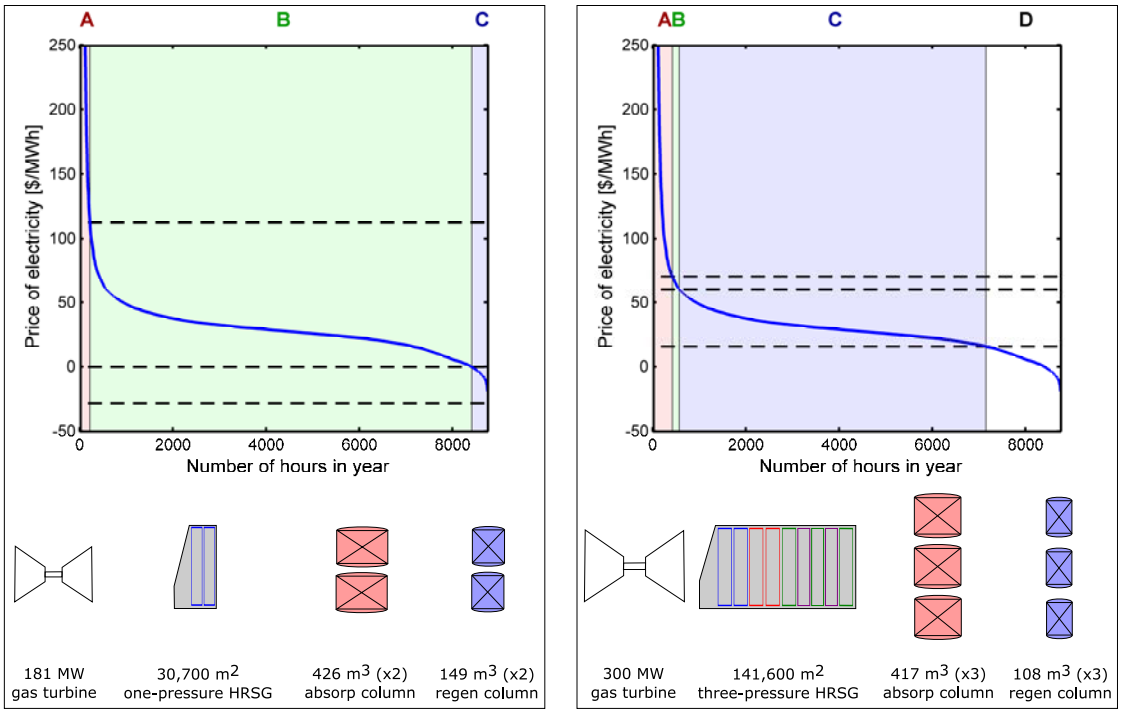

(a) Minimum TCR (mode D is too small to see) (b) Maximum NPV

Figure 4.7: Planned operations and design sizes of selected components for minimum TCR and maximum NPV facilities. Sizes of component diagrams correspond to sizes of components.

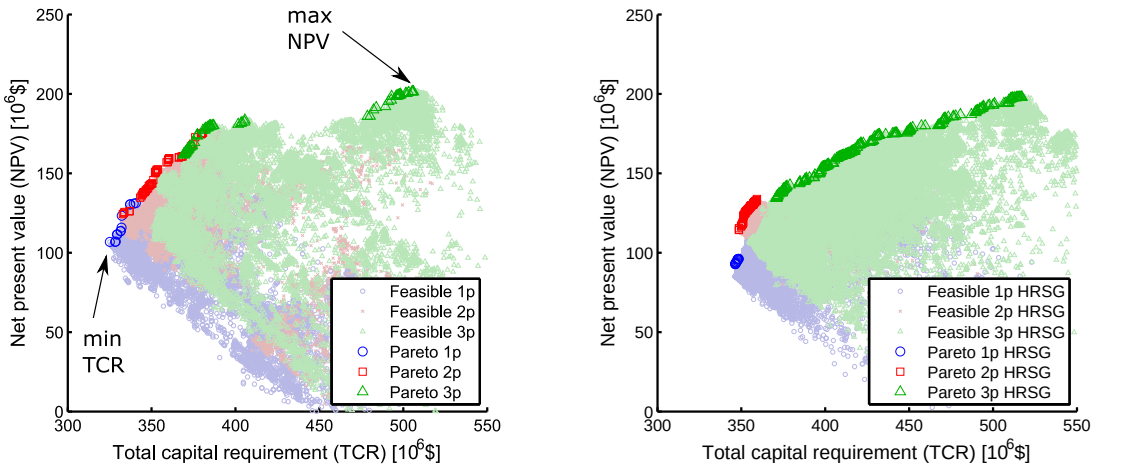

(a) Full-system formulation (calculated here)

(b) Simplified-capture formulation (modified from Chapter 3)

Figure 4.8: West Texas scenario Pareto frontiers for full-system and simplified-capture problem formulations.

300 MW GT capacity, a three-pressure, 141,600 m^2 surface area HRSG, and three CO_2 capture trains with total capture capacity of 65.2 kg CO_2/s. The greater CO_2 capture capacity enables variable operation of the facility, because CO_2 capture can be turned off during economically unfavorable hours.

The full-system and simplified-capture formulations produce similar Pareto frontiers, as shown in Figure 4.8. In both Pareto frontiers, one-pressure HRSG systems are dominant at the minimum TCR extreme (lower left), three-pressure HRSG systems are dominant at the maximum NPV extreme (upper right), and two-pressure HRSG systems occupy an intermediate region. Table 4.9 shows that the TCR objective exhibits similar ranges in both formulations, with the full-system Pareto frontier having a range of $325-506 million and the simplified-capture Pareto frontier having a range of $346-517 million. The NPV objectives in both problem formulations also display similar ranges. Other key system parameters for the two extreme cases, also summarized in Table 4.9, are similar in both problem formulations.

In spite of the significant differences in the modeling of the CO_2 capture system between the full-system formulation here and the simplified-capture formulation of

Table 4.9: System parameters of optimal designs for minimum TCR and maximum NPV objectives, for full-system and simplified-capture problem formulations.

		West Texas				India			
		min TCR		max NPV		min TCR		max NPV	
Quantity	Units	full	simpl.	full	simpl.	full	simpl.	full	simpl.
Net present value	10^6\$	107	93	201	198	517	513	592	576
Total capital requirement	10^6\$	325	346	506	517	314	337	368	359
Gas turbine capacity	MW	181	175	300	300	177	170	208	186
HRSG surface area	$10^3 m^2$	30.7	31.6	141.6	137.5	25.7	30.4	79.9	58.7
CCS capacity	kg CO_2/s	53.5	53.5	65.2	65.5	51.1	51.9	51.3	49.5
CCS utilization factor	%	79.6	82.8	65.9	65.3	84.1	84.1	81.3	83.8

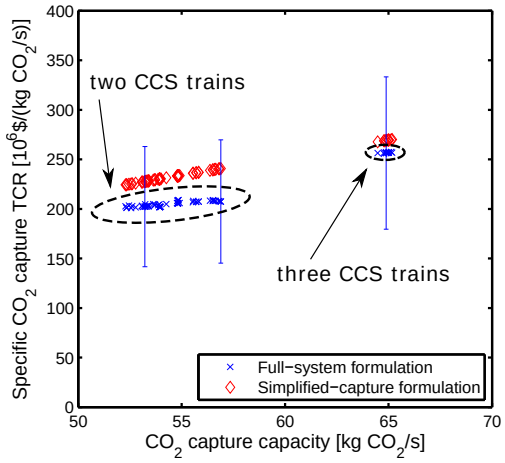

(a) Comparison of CO_2 capture total capital requirement in full-system and simplified-capture formulations; error bars indicate 30% uncertainty

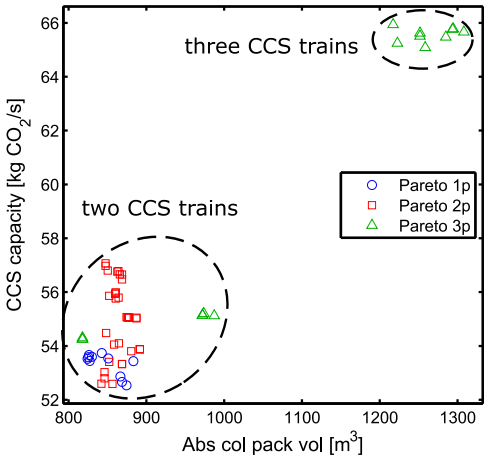

(b) CO_2 capture capacity vs. absorption column packed volume

Figure 4.9: CO_2 capture system parameters of Pareto-efficient facilities, West Texas scenario. CO_2 capture capacity displayed is total across all trains.

Chapters 2 and 3, the two systems resemble one another fairly closely. This is largely because the specifications used in the simplified-capture cases are essentially recovered in our solution here. For example, the range of reboiler heat duty in the full-system formulation is 3.64–3.87 MJ/kg CO_2, compared to 3.68 MJ/kg CO_2 in the simplified-capture formulation. Similarly, the range of total CO_2 capture work duty (which includes compression, pumps, and blowers) is 344–376 kJ/kg CO_2 in the full-system formulation results, compared to 375 kJ/kg CO_2 in the simplified-capture formulation.

The capital cost of the CO_2 capture system is also similar in the two formulations. Figure 4.9(a) compares the total capital requirement of the CO_2 capture system in the full-system formulation and in the simplified-capture formulation. The full-system formulation TCRs deviate from the simplified-capture formulation TCRs by -4.2% to -13.8%, with overall mean deviation of -10.5%. This is well within the 30% uncertainty of the capital cost estimation procedure.

The results from the two problem formulations do, however, differ in some important respects. The full-system Pareto frontier (Figure 4.8(a)) has a discontinuity

in the TCR range $400-475 million. This discontinuity results from the fact that the number of CO_2 capture trains is an integer decision variable that jumps from two in the left cluster to three in the right cluster. This is also evident in the grouping of system designs in Figure 4.9, in which the facilities with two CO_2 capture trains are clearly distinct from the facilities that have three trains. For this scenario, no Pareto-efficient designs were found that had CO_2 capture capacity in the range 57-64 kg CO_2/s.

In addition to resolving the discrete aspects of the CO_2 capture system design, the full-system formulation also yields other information that is not available from the simplified-capture formulation. For example, Figure 4.9(b) shows the relationship between CO_2 capture capacity and absorption column packed volume (total across all CO_2 capture trains), which the simplified-capture formulation cannot provide. Table 4.10 provides ranges for selected parameters of CO_2 capture system designs for Pareto-efficient points. Note that the ranges are the minimum and maximum value for each individual parameter across all Pareto-efficient points. Therefore, a design specified by using the endpoints of each range in Table 4.10 does not in general correspond to a Pareto-efficient design, in contrast to those summarized in Table 4.9 and Figure 4.7, which do define Pareto-efficient points.

4.4.2 India scenario

The Pareto frontiers for the full-system and simplified-capture problem formulations for the India scenario are shown in Figure 4.10. For reference, the standalone coal plant (without CCS) has NPV of $1,301 million. As in the West Texas scenario, the implementation of CO_2 capture reduces NPV, but not below zero, indicating that a CO_2 capture retrofit is preferred to decommissioning in response to a CO_2 emission intensity limit. Optimization based on the full-system and simplified-capture formulations again leads to similar Pareto frontiers, with the full-system formulation displaying lower minimum TCR and slightly higher NPV due to lower capital cost for the CO_2 capture facility. An interesting difference between the results of the two formulations is that the full-system Pareto frontier includes a region with three-pressure

Table 4.10: Ranges of selected CO_2 capture system design parameters in Pareto-efficient designs, full-system formulation.

Parameter	Units	West Texas		India	
		min	max	min	max
Specific reboiler heat duty	MJ_{th}/kg CO_2	3.64	3.87	3.69	3.76
Specific work duty	kJ_e/kg CO_2	344	376	344	361
Regen. col. operating pressure	kPa	152	204	168	203
Lean solvent CO_2 loading	mol CO_2/mol MEA	0.17	0.24	0.19	0.22
Rich solvent CO_2 loading	mol CO_2/mol MEA	0.55	0.56	0.56	0.56
Total absorp. col. packed vol.	m^3	878	1,308	775	865
Total regen. col. packed vol.	m^3	261	350	241	284
Number of CO_2 capture trains	–	2	3	2	2

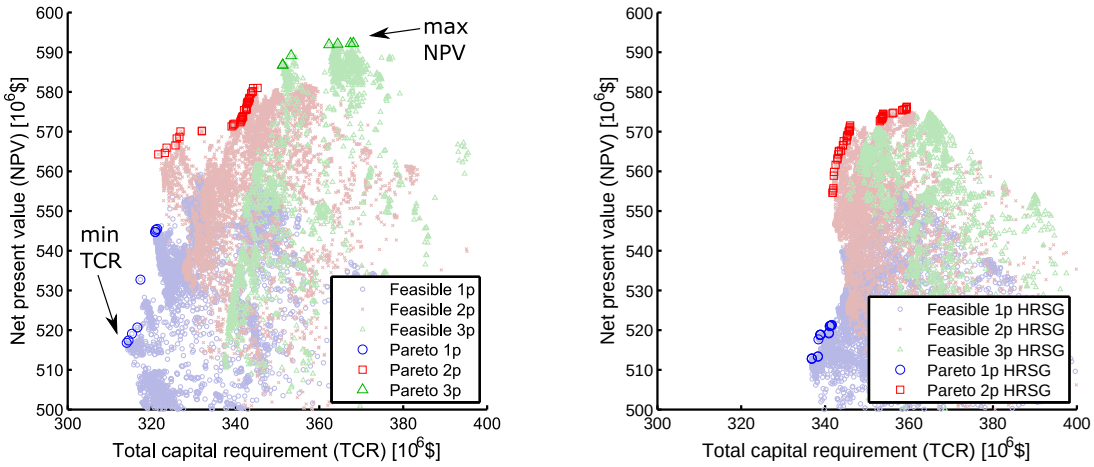

(a) Full-system formulation (calculated here)

(b) Simplified-capture formulation (modified from Chapter 3)

Figure 4.10: India scenario Pareto frontiers for full-system and simplified-capture problem formulations.

HRSG designs, which are not present in the simplified-capture Pareto frontier. This may be because of the lower capital cost of the CO_2 capture facility in the full-system formulation.

The system parameters for the minimum TCR and maximum NPV designs in the India scenario, shown in Table 4.9, are also similar between the full-system and simplified-capture problem formulations. The ranges of GT capacity and HRSG surface area extend to somewhat higher values in the full-system formulation than in the simplified-capture formulation. In contrast to the West Texas scenario, the choice of objective between minimum TCR and maximum NPV does not affect facility operations in the India scenario (constant operations are optimal for both objectives). This is because the low variability in electricity price (standard deviation of \$24/MWh in India as compared to \$127/MWh in West Texas) results in a relatively small benefit to operating economics from time-varying CO_2 capture rate. CO_2 capture design parameters are presented in Table 4.10. The variation in these parameters is consistently less than that observed in the West Texas scenario.

4.4.3 Accuracy of results calculated using integrated proxy model

The results presented up to this point are all generated using the integrated proxy model. To assess the accuracy of these results, we evaluated the CO_2 capture designs for all Pareto-efficient points in the full-physics model. We compare three quantities of interest that may affect the objective functions: CO_2 capture rate, regeneration column flood fraction, and specific reboiler heat duty. The plots shown in Figure 4.6(a) (for Round 4 of retraining) display integrated proxy model accuracy for these quantities in the West Texas scenario. The prediction error of the integrated proxy model with respect to the full-physics model is $\lesssim 4\%$, which is less than the uncertainty in the full-physics model itself ($\sim 10\%$).

We estimate the effect of integrated proxy model prediction inaccuracy on NPV and TCR using a procedure described in Appendix B. With reference to Table 4.11, we see that integrated proxy model prediction error has a small but nonzero effect on the results. For Pareto-efficient points in the West Texas scenario (considered point by point), the estimated error in NPV ranges from -$9 million to +$11 million, with mean +$6 million (i.e., using the integrated proxy model overpredicts NPV by $6 million on average), and the estimated error in TCR ranges from -$3 million to -$9 million, with mean -$7 million (i.e., using the integrated proxy model underpredicts TCR by $7 million on average). Similar effects are seen in the India scenario. The errors in TCR and NPV are substantially less than the 30% capital cost estimation uncertainty

Table 4.11: Adjustment for integrated proxy model prediction error of NPV and TCR of Pareto-efficient points.

	Pareto NPV [10^6\$]		Pareto TCR [10^6\$]	
Scenario	Before adj.	After adj.	Before adj.	After adj.
West Texas	107 – 201	101 – 201	325 – 506	333 – 510
India	517 – 592	510 – 587	314 – 368	323 – 376

Table 4.12: Parameters used to represent renewable energy technologies.

Technology	Capital cost*,† [$/kW]	O&M cost† [$/kW/y]	Capacity factor	Constr. time† [y]
Photovoltaic	3,049	48	0.243‡	1
Solar thermal	8,203	50	0.40†	2
Class 3 wind	2,304	60	0.32†	1
Class 5 wind	2,304	60	0.41†	1

* Includes interest during construction calculated using the same nominal discount rate and escalation rate as for coal-gas-CCS systems. † Data from Black & Veatch (2012). ‡ For a location with high insolation (International Energy Agency, Renewable Energy Division, 2014, p 12).

associated with the CO_2 capture facility, which corresponds to uncertainty of ±$60-75 million in TCR and NPV, depending upon the design. This highlights the efficacy of the integrated proxy model for the optimizations performed in this chapter.

4.4.4 Comparison to other low-carbon technologies

To provide context for evaluating the coal-gas-CCS power plant treated in this work, we perform a high-level economic assessment of three renewable electricity generation technologies: solar photovoltaic, solar thermal with thermal storage, and onshore wind. The parameters describing these technologies are provided in Table 4.12.

The renewable technologies are considered under two different sets of tax incentive policy regimes. Under the 'small tax incentive' policy regime, the only tax incentive that the renewable technologies receive is the use of the five-year 150% declining balance method, midquarter convention (US Internal Revenue Service, 2013). This provides more favorable economics compared to the 20-year method used for conventional electricity technologies, which is applied to the coal-gas-CCS power plant. Under the 'large tax incentive' policy regime, the renewable technologies receive a 30% investment tax credit (ITC) and 50% bonus accelerated depreciation. The 30% ITC reduces the capital cost of the plant to 70% of the unincentivized capital cost, and reduces the capital cost basis used for tax depreciation purposes to 85% of the

unincentivized capital cost. With the 50% bonus accelerated depreciation incentive, 50% of capital cost is depreciated in the first year and the remaining 50% of capital cost is depreciated using the five-year method. Both the 30% ITC and 50% bonus accelerated depreciation tax incentives considered in the large tax incentive regime have been instituted previously in the United States (and may continue in the future).

We compare the technologies using the metrics of levelized cost of electricity (LCOE) and cost of CO_2 avoided. These two metrics provide a general indication of the economic viability of low-carbon energy technologies. Calculating the cost of CO_2 avoided requires the definition of a reference plant, which we take to be the NPV-maximizing coal-gas-CCS facility with the CO_2 capture facility removed. This facility has a CO_2 emission intensity of 748 kg CO_2/MWh, a real LCOE of \$63/MWh, and a nominal LCOE of \$84/MWh. Because LCOE amortizes the cost of capital investment over all electricity generated, it is necessary to include a charge for the capital cost of the coal plant in the reference facility and the coal-gas-CCS facility. Therefore, we apply a capital cost charge of \$1,593 million for the coal plant based on the 440 MW capacity and capital cost data provided in Black & Veatch (2012). All calculations are performed for the West Texas 2011 base scenario, and do not include any correction for proxy model error.

Table 4.13 shows LCOE and cost of CO_2 avoided for the different energy technologies. The coal-gas-CCS systems generally outperform solar photovoltaic and solar thermal systems on both LCOE and cost of CO_2 avoided. With large tax incentives, solar photovoltaic may be competitive with coal-gas-CCS in terms of cost of CO_2 avoided, with nominal cost of \$56/kg CO_2 as compared to \$62-80/kg CO_2 for the coal-gas-CCS systems. The onshore wind systems appear to outperform the coal-gas-CCS systems in terms of cost of CO_2 avoided, and are competitive in terms of LCOE. Interestingly, onshore wind with a Class 5 resource and large tax incentive exhibits a negative cost of CO_2 avoided because these systems have lower LCOE than the reference system. This indicates that high-quality wind resources are economically viable without CO_2 regulations, which is consistent with the observation that these resources have recently seen high rates of development.

Table 4.13: Comparison of levelized cost of electricity and cost of CO_2 avoided for coal-gas-CCS and selected renewable energy technologies.

Technology	CO_2 emission intensity [kg CO_2/MWh]	LCOE [$/MWh]		Cost of CO_2 avoided [$/1,000 kg CO_2]	
		Real	Nominal	Real	Nominal
Coal-gas-CCS (max NPV)*	460	72	96	46†	62†
Coal-gas-CCS (min TCR)*	498	78	104	60†	80†
Photovoltaic (large tax incent.)	0	100	134	56	76
Photovoltaic (small tax incent.)	0	152	205	136	183
Solar thermal (large tax incent.)	0	141	189	118	159
Solar thermal (small tax incent.)	0	227	304	249	334
Class 3 wind (large tax incent.)	0	66	88	5	6
Class 3 wind (small tax incent.)	0	96	129	50	68
Class 5 wind (large tax incent.)	0	51	69	-17	-23
Class 5 wind (small tax incent.)	0	75	101	19	25

* Calculated including capital cost of $1,593 million for the coal plant (Black & Veatch, 2012).
† Cost includes CO_2 capture only; including storage in saline aquifers would increase the cost of CO_2 avoided by $5-15/kg CO_2.

We note that LCOE and cost of CO_2 avoided are imperfect metrics. They do not account for the time-varying value of electricity, do not include the value of 'dispatchability,' do not account for resource limitations, and are highly dependent upon uncertain economic assumptions. Therefore, we emphasize that the results presented in Table 4.13 should not be taken to indicate that any one technology (such as onshore wind) dominates the other technologies. In particular, these two metrics tend to undervalue the contributions of dispatchable power, and hence tend to undervalue solar thermal with thermal storage and CCS-enabled fossil fuel systems. Adding electricity storage to wind and solar photovoltaic could make these technologies dispatchable, but would also increase the LCOE of these technologies. An assessment at this level of detail, however, is beyond the scope of this work.

4.5 Summary

In this chapter, we presented the full-system problem formulation. We described our representation of the CO_2 capture system using a full-physics Aspen Plus model, and

with a computationally efficient integrated proxy model developed using statistical and simplified physics techniques. The full-system formulation of the optimization problem was also presented. Finally, we ran the full-system formulation using two scenarios (based on West Texas and India) taken from among the six scenarios first described in Chapter 3. The results of the full-physics formulation were found to be consistent with the results of the simplified-capture formulation, and also provided more detailed information on the CO_2 capture system, most notable of which was the impact of considering the integer number of CO_2 capture trains to build.

Chapter 5

Conclusions

5.1 Summary

In this work, we developed a modeling and optimization framework for the design and operations of a coal-natural gas power plant with CO_2 capture. Two related formulations were developed: the simplified-capture problem formulation emphasizing the detailed design of the heat recovery steam generator (HRSG) in the natural gas-fired component of the system, and the full-system problem formulation, which includes the detailed design of the CO_2 capture system alongside heat integration. In both formulations, we treated facility design and operations together in a bi-objective mixed integer nonlinear optimization problem, and investigated a coal-fired power plant being retrofit with a natural gas-powered CO_2 capture system to meet a 499 kg CO_2/MWh emission performance standard. The two objectives considered were the minimization of total capital requirement (TCR) and the maximization of net present value (NPV).

This capability entailed several new developments in process modeling. The configuration of the HRSG was optimized in a novel way, by representing the number and sequence of HRSG elements as unordered discrete (categorical) variables within a modular HRSG model. To render the CO_2 capture system amenable to computational optimization, we developed an integrated proxy model of the CO_2 capture

system that reproduced the behavior of an experimentally validated full-physics Aspen Plus model, but which ran several hundred times faster. The integrated proxy model employed a combination of statistical proxy and simple physics models. A candidate CO_2 capture system design could be evaluated using the integrated proxy model in less than one second, which was on the same time scale as the evaluation of the heat integration model including the HRSG. Because of this, both the full-system and simplified-capture formulations could be treated using the same computational optimization algorithm (which required $\sim 10^6$ function evaluations for these problems).

Time-varying facility operation in a competitive electricity market was represented through the definition of four discrete operating modes (which correspond to different controls for fuel use, CO_2 capture rate, and electricity sales) dispatched using the electricity price-duration curve. Combined with a bottom-up, component-by-component capital cost estimation procedure, this enabled us to resolve tradeoffs between capital investment and operating performance, and thus optimize facility design in coordination with planned operations. Using historical data, we constructed six scenarios (four based in West Texas, one based in the United Kingdom, and one based in India, all for the year 2011).

In the base scenario constructed from 2011 West Texas data, the coal plant operating on its own without CO_2 capture (and therefore not meeting the emission performance standard) had NPV of \$476 million. All Pareto-efficient facilities identified had NPV less than this number, indicating that performing CO_2 capture represented a net cost. However, all of the NPVs were greater than zero, indicating that CO_2 capture retrofit was preferred to decommissioning in the West Texas base scenario. Subtracting the NPV of a facility with CO_2 capture from \$476 million yields a value that can be interpreted as the net present cost of meeting the emission performance standard by an auxiliary CO_2 capture retrofit.

In the West Texas base scenario, the two objectives were clearly in conflict in the simplified-capture formulation, and systems on different portions of the Pareto frontier were noticeably different from one another. The TCR-minimizing system

(TCR of $346 million, NPV of $93 million, net present cost of $383 million) had a one-pressure HRSG, a 175 MW gas turbine, and a CO_2 capture system with a capacity of 53.5 kg CO_2/s. The NPV-maximizing system (TCR of $517 million, NPV of $198 million, net present cost of $278 million), by contrast, had a three-pressure HRSG, 300 MW gas turbine, and a CO_2 capture system with a capacity of 65.5 kg CO_2/s. The greater capital investment in the NPV-maximizing system enabled greater operational flexibility. These results highlight the strong impact of the decision maker's preference in objective function on the optimal design and operation plan.

Two of the three West Texas sensitivity scenarios exhibited trends in objective functions and system parameters similar to those in the base scenario. These scenarios had the same or higher expected future energy prices (for both electricity and natural gas) relative to the base scenario. In contrast, the third West Texas sensitivity scenario indicated that CO_2 capture would be highly uneconomic under low energy prices.

The successful application of the simplified-capture formulation in the UK and India scenarios demonstrates the viability of our method in worldwide contexts and further illustrates the importance of economic assumptions on optimal system design. The India scenario displayed positive NPVs but very large net present costs, which indicates that an auxiliary gas-fired CO_2 retrofit, although economically viable, may not be the best possible approach for CO_2 mitigation in that setting. Both the UK and India scenarios had lower electricity price variability than the West Texas scenarios, leading to a smaller benefit from flexibility in optimal system design.

Two advanced solvent processes, namely the mixed salt process and the piperazine process, were evaluated using the simplified-capture formulation in the West Texas base scenario. Both of the advanced processes clearly outperformed the MEA process across the entire range of their Pareto frontiers. Additionally, the mixed salt process outperformed the piperazine process. This indicates that the mixed salt process is a promising candidate for further investigation and develoment.

Using the full-system formulation, we again considered the West Texas base scenario and the India scenario. The full-system formulation yielded results, including

Pareto frontiers, that were very similar to the results of the simplified-capture formulation in these two scenarios. This is because the performance parameters and capital cost scaling of the CO_2 capture system used in the simplified-capture formulation were largely recovered by the optimization in the full-system formulation. This occurred even though the CO_2 capture system model in the full-system formulation was constructed independently from the parameterization used in the simplified-capture formulation.

Notably, the effects of electricity price variability observed in the full-system formulation results were similar to those in the simplified-capture formulation. The West Texas scenario (which had high electricity price variability) showed quite different behavior depending upon the choice of objective. The minimum TCR objective favored constant operations, while the maximum NPV objective favored variable operations. In contrast, both objectives in the India scenario, which had low price variability, favored constant operations.

Including the detailed CO_2 capture system in the optimization, however, provided substantially more information about optimal system design, and in particular demonstrated the importance of considering the integer nature of the required number of CO_2 capture trains. Integrated proxy model prediction accuracy was evaluated with respect to the full-physics model for the set of facilities constituting the Pareto frontiers, and these results showed that the proxy model produced sufficiently accurate predictions for both objective functions.

The differences in results among the different scenarios in both problem formulations show the strong impact of the economic forecast on the optimal facility design. We note especially that forecasts of hourly-timescale electricity price variability, not just overall electricity price level, can have a significant effect on system design. The importance of economic forecasts observed here is consistent with the findings of Khalilpour (2014), which indicated that optimal decisions for parasitic CO_2 capture retrofits are highly sensitive to forecasted CO_2 prices and other economic parameters.

Taken in total, our overall modeling and optimization methodology, including the detailed model of the HRSG and the integrated proxy model for the CO_2 capture

system, is applicable to a broad range of plant design and operation optimization problems, and should be particularly useful for systems that face complex capital-operating tradeoffs.

5.2 Future work

Future investigations could proceed along several lines. Below we list some of the potential continuations of this work.

- The modeling and optimization capability developed in this work is readily applicable to systems burning only natural gas. Work in this area could consider different designs of natural-gas fired systems, ranging from post-combustion capture applied directly to existing CCGTs, to exhaust gas recirculation CCGT schemes, to oxycombustion systems.

- The mixed salt and piperazine CO_2 capture processes could be treated in a similar manner to the MEA process in the full-system problem formulation (i.e., proxy models based on Aspen Plus simulations developed for the mixed salt and piperazine processes). This would enable evaluation of detailed design decisions for each of the processes. As such, this would provide a richer and potentially fairer assessment of the value of these advanced technologies.

- The CO_2 capture system integrated proxy model can be improved and applied in new ways. Improved accuracy could be achieved by using a more formal retraining scheme that incorporates directly the results of optimization (as suggested in Section 4.2.8). In addition, the integrated proxy model appears to be well suited for use in investigating off-design performance, so investigation of the application of this approach for partial load operation may be worthwhile.

- The representation of system dynamics including transients should be improved. A major assumption that underlies both the price-duration curve representation of the electricity market, and our modeling of facility operations, is that

system transients are of low importance. However, if electricity markets move to faster (sub-hourly) dispatch schedules, as is likely with increased renewable penetration and 'smarter' power grids, this assumption may become invalid. In addition, treatment of temporary solvent storage should be considered because this has been shown to be useful in some scenarios. One possible way to approach this set of challenges is to shift the optimization paradigm to use dynamic programming.

- Uncertainty in capital cost and economic scenarios should be investigated and quantified. An implicit assumption in this work is that future economic conditions are known with certainty during the design phase of the retrofit. In reality, economic conditions are highly uncertain, so extending this work to treat uncertainty would be very useful. Dynamic programming again could be a useful paradigm to address this issue.

- Integration of the CO_2-capture-enabled thermal power station with renewable resources is potentially a rich area of research. In this work we viewed CCS-enabled power as being coordinated with renewable power generation through the electricity grid. However, this is not necessarily the best way to support renewable power generation. For example, integration of renewable thermal energy (e.g., solar thermal) into the steam cycle and/or solvent regeneration processes could yield performance benefits beyond what is achievable through integration via the power grid.

Appendix A

Heat integration model verification and implementation

This appendix contains methodological details and discussion to support the simplified-capture problem formulation presented in Chapters 2-3. A schematic of the facility treated, including major system components and design optimization variables, is shown in Figure A.1. The bulk of this appendix concerns the process model, which is called by the optimization procedure. This appendix also contains further information on model verification and validation, and on constraints applied in the optimization procedure.

The process model computes system response for each candidate design proposed by the optimization algorithm. These system responses are used to evaluate the objective functions and constraint violations required for the optimization algorithm to proceed. Computation of the system responses of the HRSG and steam cycle for a candidate design entails an extended computation procedure. These calculations are described in detail in this appendix. As explained in Chapter 2, the coal plant, gas turbine (GT), and CO_2 capture components of the facility are modeled at a higher level of abstraction than the HRSG and steam cycle, and as such entail simpler computational procedures. The models for these components are described fully in Chapter 2 and Kang et al. (2011) and are not discussed further here.

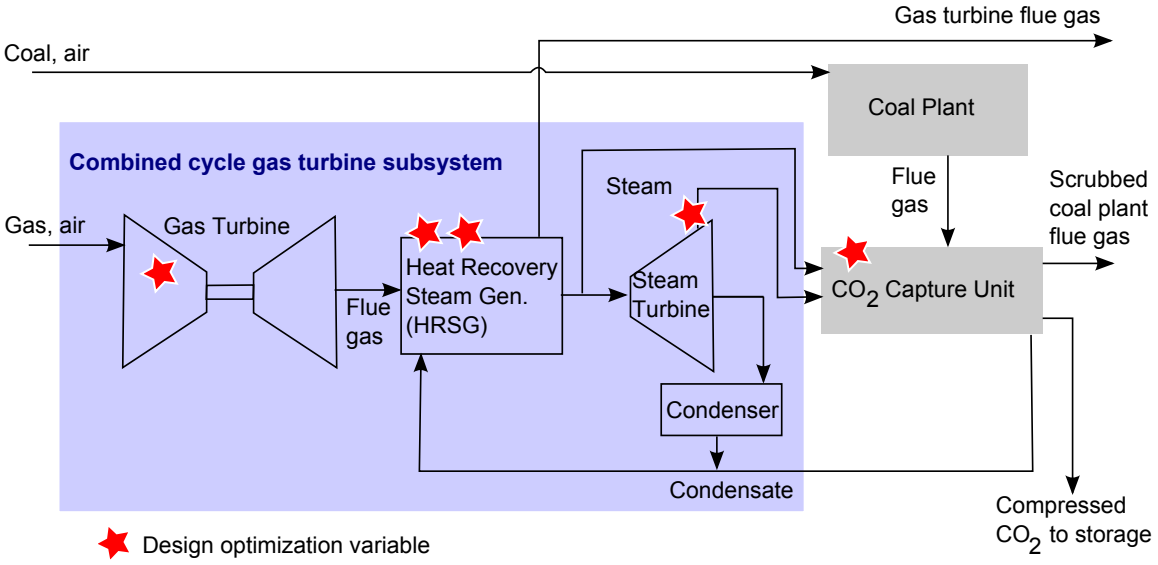

Figure A.1: Schematic of facility.

In Section A.1 of this appendix, we discuss HRSG model implementation including mathematical formalism, correlations used, and data. Details on steam cycle components other than the HRSG are given in Section A.2. We describe the data used for capital cost estimation for all components in Section A.3, and describe scenario construction details in Section A.4. We provide operations and maintenance cost data in Section A.5. In Section A.6, we give the sources of our physical property data. HRSG model verification and capital cost validation details are given in Section A.7, and we describe constraints other than those given in Chapter 2 in Section A.8. Throughout this appendix, symbols are defined at first use. Definitions of major symbols are also provided in the Nomenclature section of this thesis.

A.1 HRSG model details

As described in Chapter 2, we model the HRSG as a sequence of interacting HRSG elements. This modeling approach represents the HRSG with a system of equations of size $7N_{\text{elem}}$ with $7N_{\text{elem}}$ variables, where N_{elem} is the number of HRSG elements. The variables for each HRSG element are effectiveness ε, mass flow rate of water $\dot{m}_{\text{w}}$ [kg/s],

water enthalpies at the inlet and outlet $h_{\mathrm{w,in}}$ and $h_{\mathrm{w,out}}$ [J/kg], gas temperatures at the inlet and outlet $T_{\mathrm{g,in}}$ and $T_{\mathrm{g,out}}$ [K], and overall heat transfer coefficient U [W/(m^2-K)]. HRSG element internal relationships provide $4N_{\mathrm{elem}}$ equations, boundary conditions provide $(2 + N_{\mathrm{pl}})$ equations (where N_{pl} is the number of HRSG pressure levels) and links (interactions) between HRSG elements provide $(3N_{\mathrm{elem}} - 2 - N_{\mathrm{pl}})$ equations. This system of algebraic equations is solved using a modified form of Newton's method.

We first discuss our general model for an individual HRSG element in Section A.1.1. In Section A.1.2, we describe our treatment of links between elements and HRSG boundary conditions. The calculation procedures for the overall heat transfer coefficient are given in Section A.1.3. Additional remarks on the mathematical solution process are provided in Section A.1.4. Finally, we describe our procedure for calculating gas-side pressure drop in Section A.1.5.

A.1.1 HRSG element

As mentioned in Chapter 2, we use the ε-N_{TU} representation of heat exchangers to model an HRSG element. In the ε-N_{TU} method, $\dot{Q}_{\mathrm{actual}}$ [W$_{\mathrm{th}}$], the physically realized rate of heat transfer within the heat exchanger, is expressed as $\dot{Q}_{\mathrm{actual}} = \varepsilon \dot{Q}_{\mathrm{max}}$, where ε $(0 \leq \varepsilon \leq 1)$ is the effectiveness of the heat exchanger and $\dot{Q}_{\mathrm{max}}$ [W$_{\mathrm{th}}$] is the maximum theoretical heat transfer possible, corresponding to a countercurrent heat exchanger of infinite size. The effectiveness ε depends on the capacities (i.e., flowing heat capacity) of the two streams C_{w} [W/K] (capacity of the water stream) and C_{g} [W/K] (capacity of the gas stream), the heat exchanger geometry, and the number of transfer units, $N_{TU} = UA_{\mathrm{g}}/C_{\mathrm{min}}$, which is the nondimensional size of the element. Here, U [W/(m^2-K)] is the overall heat transfer coefficient of the HRSG element, A_{g} [m^2] is the gas-side surface area of the HRSG element, and C_{min} [W/K] is the capacity of the lower capacity stream in the HRSG element. The quantity C_{min} is calculated as $C_{\mathrm{min}} = \min(C_{\mathrm{w}}, C_{\mathrm{g}})$.

We analyze HRSG elements using the control volume shown in Figure A.2. Each

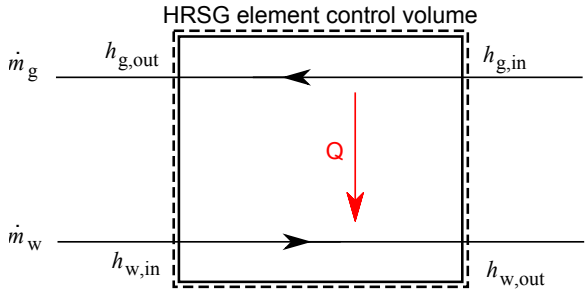

Figure A.2: Schematic of an HRSG element.

HRSG element has four nontrivial equations derived from thermodynamic and heat transfer relations. These equations are written in residual form, i.e., $\mathbf{g}(\mathbf{x}) = \mathbf{0}$.

Energy conservation requires that energy leaving the gas be transferred to the water:

$$\dot{m}_{\mathrm{w}} \left(h_{\mathrm{w,out}} - h_{\mathrm{w,in}}\right) - \dot{m}_{\mathrm{g}} c_{\mathrm{p_g}}\left(\bar{T}_{\mathrm{g}}\right) \left(T_{\mathrm{g,in}} - T_{\mathrm{g,out}}\right) = 0, \tag{A.1}$$

where $\dot{m}_{\mathrm{g}}$ [kg/s] is the mass flow rate of gas, and $c_{\mathrm{p_g}}$ [J/(kg-K)] is the specific heat capacity of the gas, evaluated at $\bar{T}_{\mathrm{g}}$ [K], the mean of the gas inlet and outlet temperatures. We do not include thermal shell losses.

The effectiveness is calculated from the properties of the HRSG element:

$$\varepsilon - E\left(UA_{\mathrm{g}}, C_{\mathrm{w}}, C_{\mathrm{g}}\right) = 0, \tag{A.2}$$

where $E\left(UA_{\mathrm{g}}, C_{\mathrm{w}}, C_{\mathrm{g}}\right)$ is the effectiveness equation produced by combining Equations A.5 and A.6 (below). Here, C_{w} and C_{g} [W/K] are stream capacities (described in Section A.1.1.2) specified in Equations A.7 and A.8. In turn, ε is used to specify the rate of energy transfer into the water stream:

$$\varepsilon C_{\mathrm{min}} \Delta T_{\mathrm{max}} - \dot{m}_{\mathrm{w}} \left(h_{\mathrm{w,out}} - h_{\mathrm{w,in}}\right) = 0, \tag{A.3}$$

where ΔT_{max} [K] is the maximum temperature difference possible across the HRSG element, equal to the temperature difference between the inlets of the two fluids. Note

Table A.1: Constant U_{ref} values.

Element type	U_{ref} [W/(m^2-K)]
Economizer	42.6*, 49.1†
Evaporator	43.7*, 52.3†
Superheater	50.0*, 38.2†
Reheater	50.0*, 38.2†

* Casarosa et al. (2004). † Calculated from Kim and Ro (1997)

that Equation A.3 uses the rate of heat transfer into the water, $\dot{m}_{\text{w}} (h_{\text{w,out}} - h_{\text{w,in}})$; it could be written equivalently with the rate of heat transfer out of the gas.

The overall heat transfer coefficient is calculated from the properties of the HRSG element:

$$U - \upsilon \left(A_{\text{g}}, \varepsilon, \dot{m}_{\text{w}}, h_{\text{w,in}}, h_{\text{w,out}}, T_{\text{g,in}}, T_{\text{g,out}}, \{\text{HRSG element specifications}\} \right) = 0. \tag{A.4}$$

The functional form of υ in Equation A.4 depends upon the way that U is treated. If U is treated as a constant, the formula for υ is simply of the form $\upsilon = U_{\text{ref}}$, where U_{ref} is a constant. Table A.1 shows values of U_{ref} from two literature sources. The values of U_{ref} differ because the sources consider different designs. If U is calculated, the formula for υ is obtained by incorporating all of the individual components of the thermal circuit equation, given in Section A.1.3 as Equation A.18.

We now discuss the analysis of HRSG elements as heat exchangers. This analysis involves the concept of capacity, which is discussed in Section A.1.1.2.

A.1.1.1 Heat exchanger analysis: effectiveness and number of passes

Each HRSG element is modeled as a multi-pass overall-counterflow heat exchanger with fluids mixed between passes. Figure A.3 shows a schematic of such a heat exchanger. The overall flow of fluids within an element is countercurrent, but each constituent pass in an element is internally a crossflow heat exchanger with one side

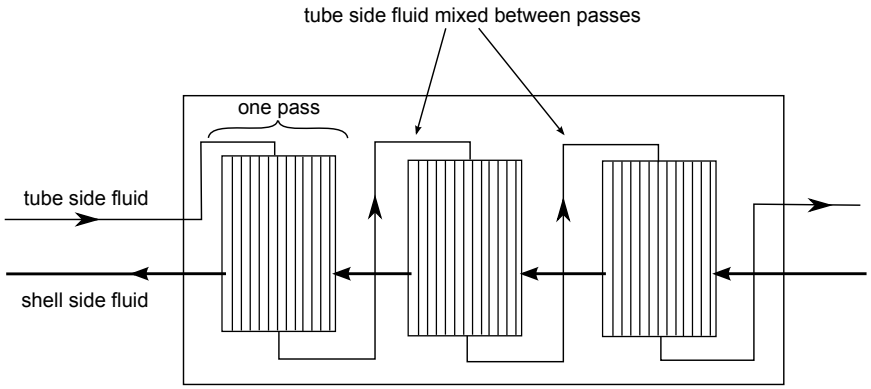

Figure A.3: Schematic of a three-pass overall-counterflow heat exchanger with crossflow (one fluid mixed, one fluid unmixed) passes.

mixed and one side unmixed. The water is the unmixed (tube-side) fluid, while the flue gas is the mixed (shell-side) fluid. Both fluids are well mixed between passes.

The effectiveness of a single pass within a multi-pass heat exchanger is given by the following relation for the effectiveness of a crossflow heat exchanger with one fluid mixed and one fluid unmixed (Kays and London, 1984, pp 20-21):

$$\varepsilon_p = \left\{ \begin{array}{ll} 1 - \exp\left\{ \left[1 - \exp\left(N_{TU} \dfrac{C_{\min}}{C_{\max}} \right) \right] \dfrac{C_{\max}}{C_{\min}} \right\} & \text{if } C_{\max} = C_{\text{unmixed}} \\ \dfrac{C_{\max}}{C_{\min}} \left(1 - \dfrac{C_{\min}}{C_{\max}} \exp\left\{ - \left[1 - \exp\left(-N_{TU} \right) \right] \right\} \right) & \text{otherwise} \end{array} \right\}, \tag{A.5}$$

where $C_{\max}$ [W/K] is the capacity of the higher capacity stream.

The effectiveness of a multi-pass overall-counterflow heat exchanger (an HRSG element) is given by the following relation (Kays and London, 1984, pp 21-22):

$$\varepsilon = \frac{\left(\dfrac{1 - \varepsilon_p C_{\min}/C_{\max}}{1 - \varepsilon_p} \right)^{n_{\text{pass}}} - 1}{\left(\dfrac{1 - \varepsilon_p C_{\min}/C_{\max}}{1 - \varepsilon_p} \right)^{n_{\text{pass}}} - \dfrac{C_{\min}}{C_{\max}}}, \tag{A.6}$$

where ε_p is the effectiveness of a single pass in the heat exchanger, and n_{pass} is the number of passes. All passes within a single multi-pass element are treated as identical.

A.1.1.2 Capacity

The capacity of a stream C_{stream} [W/K] is the change in enthalpy of the stream for a given change in temperature in that stream. For the single-phase water streams in the economizer, superheater and reheater, capacity is evaluated using the enthalpy and temperature differences between the inlet and outlet states:

$$C_{\text{w}} = \dot{m}_{\text{w}} \left(\frac{h_{\text{w,in}} - h_{\text{w,out}}}{T_{\text{w,in}} - T_{\text{w,out}}} \right). \tag{A.7}$$

The capacity of the two-phase water stream in an evaporator is infinite because the difference in temperature from inlet to outlet is zero. For the single-phase flue gas stream in a HRSG element, capacity is evaluated using the specific heat capacity of the gas at the mean gas-side temperature of the element:

$$C_{\text{g}} = \dot{m}_{\text{g}} c_{\text{p}_{\text{g}}}\left(\bar{T}_{\text{g}}\right). \tag{A.8}$$

The maximum theoretical heat transfer rate $\dot{Q}_{\text{max}}$ [W] is defined as the heat transfer needed to raise or lower the temperature of the low capacity stream at its inlet to the temperature of the high capacity stream at its inlet. For example, if water is the low capacity stream in an economizer, then $\dot{Q}_{\text{max}}$ is the change in enthalpy of the water stream if it were raised to the temperature of the hot gas entering the economizer.

A.1.2 Links between elements and HRSG boundary conditions

Elements within the HRSG interact with each other and with components outside the HRSG. Interactions between elements are governed by the equations provided below,

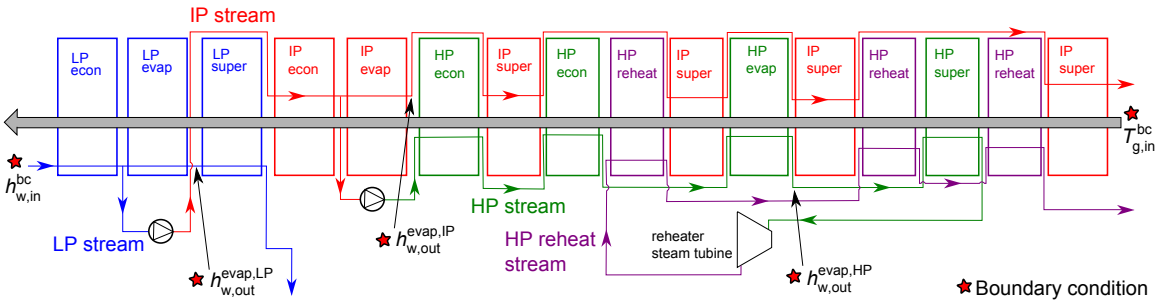

Figure A.4: A three-pressure, 15-element HRSG.

while interactions of elements with components outside the HRSG are governed by boundary conditions. Collected together, links between elements and HRSG boundary conditions provide $3N_{\text{elem}}$ equations, as we now describe.

A.1.2.1 Links between elements

Links between HRSG elements derive from three types of physical effects: flue gas temperature continuity, water enthalpy continuity, and water mass conservation. These links are governed by a set of rules that are based upon the flow pathways of water and gas. Flue gas temperature continuity provides $(N_{\text{elem}} - 1)$ equations, water enthalpy continuity gives $(N_{\text{elem}} - 1)$ equations, and mass conservation yields $(N_{\text{elem}} - N_{\text{pl}})$ equations. Collectively, they provide a total of $(3N_{\text{elem}} - 2 - N_{\text{pl}})$ equations. Flow pathways for an example three-pressure HRSG are illustrated in Figure A.4.

Flue gas temperature continuity

In a HRSG, the gas moves sequentially through the individual HRSG elements, so the element to element inlet and outlet gas temperatures $T_{\text{g,in}}$ and $T_{\text{g,out}}$ are linked by the following equation:

$$T^{k}_{\text{g,in}} - T^{k+1}_{\text{g,out}} = 0 \quad \text{for} \quad 1 \leq k < N_{\text{elem}}, \tag{A.9}$$

where k is the index of the HRSG element. Thus for a N_{elem} element HRSG, there are $(N_{\text{elem}} - 1)$ equations linking the flue gas temperature across units.

Water enthalpy continuity

Water flow paths in HRSGs are in general more complicated than flue gas flow paths, and thus the links between water inlet and outlet enthalpy are more complicated. We begin by discusing the special cases of first economizers and first reheaters at a given pressure level. Next, the pattern of water flow for other units is discussed. Water enthalpy links collectively provide $(N_{\text{elem}} - 1)$ equations for an N_{elem} element HRSG.

The first economizer at a given pressure level is fed by the outlet water of the last economizer at the next lower pressure level. For example, in a two-pressure system, the water entering the first HP economizer comes from the outlet of the last LP economizer. This flow pattern is expressed in the following equation:

$$h_{\text{w,in}}^{i_{\text{econ,first}},j_{\text{pl}}} - h_{\text{w,out}}^{i_{\text{econ,last}},j_{\text{pl}}-1} = 0 \quad \text{for} \quad 2 \leq j_{\text{pl}} \leq N_{\text{pl}}, \tag{A.10}$$

where $i_{\text{econ,first}}, j_{\text{pl}}$ indicates the first economizer at a given pressure level j_{pl}, and $i_{\text{econ,last}}, j_{\text{pl}}$ indicates the last economizer at that pressure level. Note that this equation assumes that the effect of the pump on enthalpy can be ignored; this assumption is reasonable because liquid water is nearly incompressible. For the economizer at the lowest pressure level ($j_{\text{pl}} = 1$), the inlet water enthalpy is determined by Equation A.15 (a boundary condition, below).

The inlet water enthalpy of the first reheater at a particular pressure level corresponds to the enthalpy of expanded steam from the last non-reheater element $i_{\text{nonRH,last}}, j_{\text{pl}}$ (typically a superheater) at the same pressure level. This enthalpy is computed by performing a steam expansion calculation using the steam turbine module. This is written as follows:

$$h_{\text{w,in}}^{i_{\text{RH,first}},j_{\text{pl}}} - h_{\text{expand}}\left(\eta_{\text{ST}}, p_{\text{reheat}}, h_{\text{w,out}}^{i_{\text{nonRH,last}},j_{\text{pl}}}\right) = 0, \tag{A.11}$$

where h_{expand} [J/kg] is the enthalpy of the expanded steam at the pressure level j_{pl}. Here, the inlet water enthalpy is given by $h_{\text{w,out}}^{i_{\text{nonRH,last}},j_{\text{pl}}}$ [J/kg], which is the outlet water enthalpy of the last non-reheater element at the pressure level j_{pl}. The inlet

water enthalpy of the reheater is equal to the outlet water enthalpy of a steam turbine expanding the steam to the design reheat pressure. This steam turbine outlet enthalpy is a function of the inlet water enthalpy $h_{\mathrm{w,out}}^{i_{\mathrm{nonRH,last}},j_{\mathrm{pl}}}$ [J/kg], the inlet pressure $p_{j_{\mathrm{pl}}}$ [kPa] (the pressure of pressure level j_{pl}), and the efficiency of the turbine. The reheater steam turbine is modeled using the same method as is used for other steam turbines, described in Section A.2. This provides the value of h_{expand} in Equation A.11.

Except as described above for the special cases of first economizers and first reheaters at a pressure level, the inlet water enthalpy is equal to the outlet water enthalpy of the previous element in the water flow path operating at the same pressure level. This is represented by the following equation:

$$h_{\mathrm{w,in}}^{i_{\mathrm{fp}}} - h_{\mathrm{w,out}}^{i_{\mathrm{fp}}-1} = 0, \tag{A.12}$$

where i_{fp} refers to the element, and $i_{\mathrm{fp}} - 1$ refers to the previous element in the water flow path (i.e., the element that feeds water to the element i_{fp}). For evaporators, superheaters, and economizers that are not the first economizer, i_{fp} is the previous non-reheater element at that pressure level. For reheaters that are not the first reheater, i_{fp} is the index of the previous reheater element at that pressure level.

Water mass conservation

The mass flow rate of water at a pressure level is equal to the flow rate through the evaporator at that pressure level. This is because the evaporator determines the throughput of steam: only as much water flows at a pressure level as can be boiled in the evaporator. For non-economizer elements, this means that the water flow rate through that element is equal to the water flow rate through the evaporator at the same pressure level:

$$\dot{m}_{\mathrm{w}}^{i,j_{\mathrm{pl}}} - \dot{m}_{\mathrm{w}}^{i_{\mathrm{evap}},j_{\mathrm{pl}}} = 0 \quad \text{for} \quad 1 \leq j_{\mathrm{pl}} \leq N_{\mathrm{pl}}, \quad i \neq i_{\mathrm{evap}} \quad \text{and} \quad i \neq i_{\mathrm{econ}}, \tag{A.13}$$

where i indicates the index of the element for pressure level j_{pl}. We note that because evaporators control the mass flow rate of water through the system, specifying water mass conservation for evaporators in the same way as for other element types would

lead to an over-specification. The evaporator water outlet enthalpy boundary condition, given as Equation A.17 in Section A.1.2.2, serves a role in evaporators that is analogous to the role of the water mass conservation condition in other elements.

Economizers at pressure level j_{pl} heat water for higher pressure levels in addition to water for pressure level j_{pl}. Thus, for economizers, the water flow rate is equal to the water flow rate at the pressure level of that element plus the water flow rate at all higher pressure levels:

$$\dot{m}_{\mathrm{w}}^{i_{\mathrm{econ}},j_{\mathrm{pl}}} - \sum_{k=j_{\mathrm{pl}}}^{N_{\mathrm{pl}}} \dot{m}_{\mathrm{w}}^{i_{\mathrm{evap}},k} = 0 \quad \text{for} \quad 1 \leq j_{\mathrm{pl}} \leq N_{\mathrm{pl}}. \tag{A.14}$$

Thus all elements other than evaporators have an additional mass conservation equation, giving a total of $N_{\mathrm{elem}} - N_{\mathrm{pl}}$ equations from water mass conservation.

A.1.2.2 Boundary conditions

Three kinds of boundary conditions apply to the HRSG system. The HRSG feed water enthalpy and flue gas inlet temperature are specified externally. Evaporator water outlet enthalpy is specified by the saturation temperature of water at the design pressure, which is specified externally; water exits the evaporator as saturated steam. Thus in total boundary conditions provide $(2 + N_{\mathrm{pl}})$ equations. The example three-pressure HRSG shown in Figure A.4 has boundary conditions indicated by red stars.

The water inlet enthalpy boundary condition is as follows:

$$h_{\mathrm{w,in}}^{i_{\mathrm{econ,first}},j_{\mathrm{pl}}=1} - h_{\mathrm{w,in}}^{\mathrm{bc}} = 0 \quad \text{for} \quad j_{\mathrm{pl}} = 1, \tag{A.15}$$

where $h_{\mathrm{w,in}}^{i_{\mathrm{econ,first}},j_{\mathrm{pl}}=1}$ [J/kg] indicates the inlet water enthalpy of the first economizer at the lowest pressure level, and $h_{\mathrm{w,in}}^{\mathrm{bc}}$ [J/kg] is the feed water enthalpy. The feedwater enthalpy is specified to be the enthalpy of saturated water at the temperature of the condenser and/or CCS solvent regeneration reboiler, described in Section A.2. For first

economizers that are not at the lowest pressure level, the inlet state is determined by links between HRSG elements as described in Section A.1.2.1.

The gas inlet temperature boundary condition is as follows:

$$T_{\mathrm{g,in}}^{i_{\mathrm{last}}} - T_{\mathrm{g,in}}^{\mathrm{bc}} = 0, \tag{A.16}$$

where $T_{\mathrm{g,in}}^{i_{\mathrm{last}}}$ [K] indicates the inlet flue gas temperature of the last HRSG element in the HRSG, and $T_{\mathrm{g,in}}^{\mathrm{bc}}$ [K] is the flue gas inlet temperature boundary condition. This temperature is defined by the outlet temperature of the gas turbine, described in Chapter 2.

The evaporator outlet water enthalpy boundary condition(s) are as follows:

$$h_{\mathrm{w,out}}^{i_{\mathrm{evap}},j_{\mathrm{pl}}} - h_{w}^{p_{j_{\mathrm{pl}}}} = 0 \quad \text{for} \quad 1 \leq j_{\mathrm{pl}} \leq N_{\mathrm{pl}}, \tag{A.17}$$

where $h_{\mathrm{w,out}}^{i_{\mathrm{evap}},j_{\mathrm{pl}}}$ [J/kg] is the outlet enthalpy, and $h_{\mathrm{w}}^{p_{j_{\mathrm{pl}}}}$ [J/kg] is the enthalpy of saturated water vapor, at the pressure level j_{pl}.

A.1.3 Overall heat transfer coefficient U and thermal circuit equation

The overall heat transfer coefficient, U, is a key quantity used in the HRSG element models described in Section A.1.1. Our model can treat U either as a specified parameter, or can calculate it as part of the heat transfer solution process. If U is a specified parameter, the model uses literature values, with different element types having different U values.

If U is calculated, the values of U for each element are determined using algebraic heat transfer correlations that require physical design specifications such as tube diameters and fin heights. These specifications, discussed in Section A.1.3.1, could in principle differ across designs (the focus of much previous HRSG work), but here we use values based upon reference designs to reduce the size of the optimization problem.

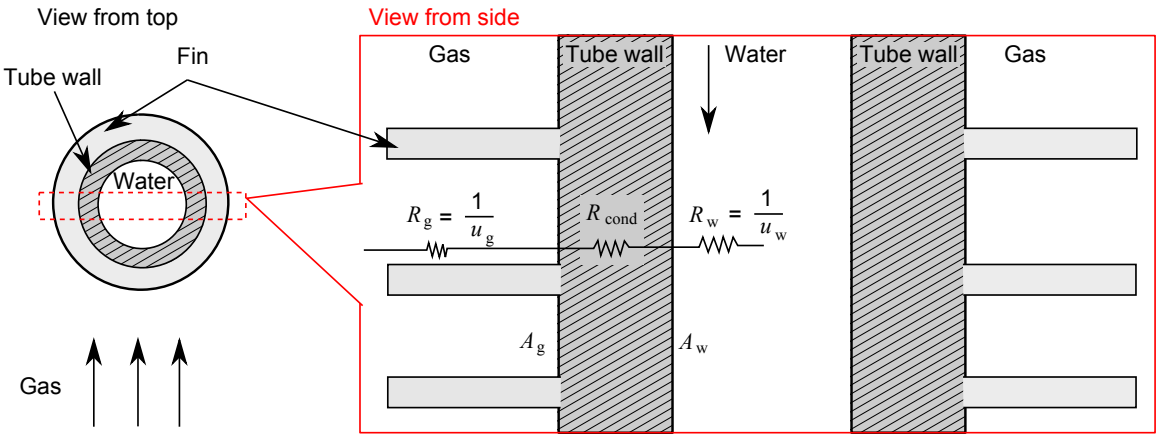

Figure A.5: Schematic of thermal circuit in finned tube heat transfer.

The overall heat transfer coefficient is calculated using a thermal circuit equation that combines the thermal resistances of the gas side, water side, and heat exchanger construction material (Kays and London, 1984, p 15):

$$U = \left(\frac{1}{u_g} + \frac{A_g}{u_w A_w} + R_{cond} \right)^{-1}, \tag{A.18}$$

where u_g [W/(m^2-K)] is the gas-side heat transfer coefficient, u_w [W/(m^2-K)] is the water-side heat transfer coefficient, A_w [m^2] is the water-side surface area, A_g [m^2] is the gas-side surface area including fins, and R_{cond} [m^2-K/W] is the thermal conductive resistance of the HRSG element construction material. This equation combines the thermal resistances between the gas side and water side, as seen in Figure A.5. The gas-side thermal resistance is usually dominant. Values of U typically fall in the range 30-50 W/(m^2-K).

To obtain U, we need to calculate the unknown quantities in Equation A.18: R_{cond}, u_g and u_w. In Section A.1.3.1, we describe the HRSG geometric specifications needed for calculating these quantities. The simple calculation for R_{cond} is given in Section A.1.3.2. The calculation of u_g involves two steps, as described in Section A.1.3.3. In Section A.1.3.4, we present the water-side heat transfer coefficient calculation, which involves different correlations for different types of HRSG elements.

A.1.3.1 Geometric specifications

We now consider the values and relationships used to determine the geometric specifications for calculating U. Figure A.6 illustrates several of the major geometric variables. Tables A.2 and A.3 show constant values for certain geometric parameters. The values in Table A.2 are taken from several published sources (Albrecht et al., 2012; Franco and Giannini, 2006; Ganapathy, 1996), and the values in Table A.3 are averages calculated from designs in Franco and Giannini (2006).

Some of the quantities described in this section, including the number of tube rows, the number of tubes in each row, and the number of fins per tube, should take on integer values in realized designs. We use a continuous relaxation of these integer variables—i.e., we allow them to be described by continuous values—because this simplifies the modeling and provides well-behaved function responses (rounding, for example, may introduce discontinuities in function response that can be problematic for the optimization algorithm).

The function responses for relaxed quantities are physical when the relaxed quantities take on integer values, and are also sensible for non-integer values. For example, Equation A.6 depends upon n_{pass}, which is treated as a relaxed integer quantity (n_{pass} is related to n_{rows} as described below in Equation A.19). Equation A.6 is physical for integer values of n_{pass}, and it is also well behaved for non-integer values of n_{pass}. In an actual HRSG, the continuous (relaxed) quantities would need to be forced to take on integer values, which would entail modifications to geometric design specifications on an element-by-element basis (perhaps using a two-stage optimization technique as in Franco and Giannini (2006)). However, this is not within the scope of this work. We note finally that the overall mixed integer nonlinear optimization problem could be treated using a specialized algorithm such as Branch and Bound. Such algorithms employ relaxation strategies as part of the optimization process.

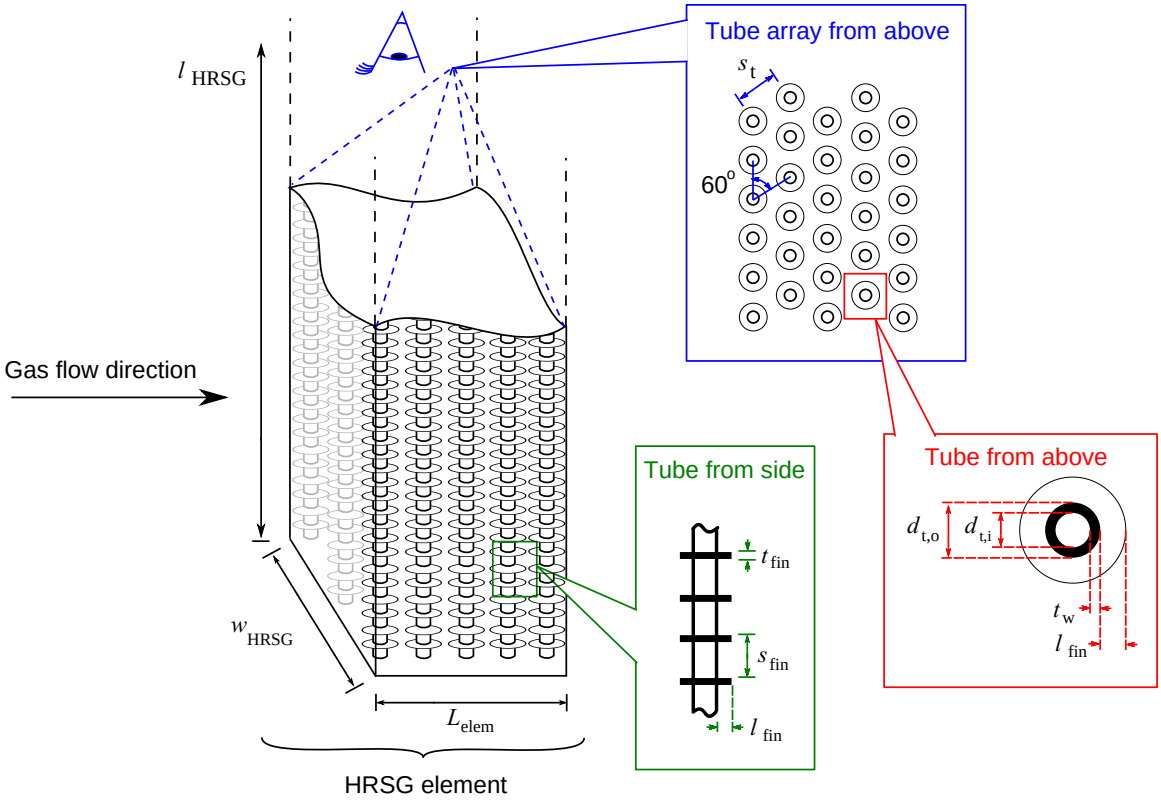

Figure A.6: Major geometric variables used in calculation of U.

Table A.2: Geometric specifications used to calculate U.

Symbol	Unit	Name	Value	Source
l_{HRSG}	m	HRSG face height	18	Franco and Giannini (2006)
t_{fin}	m	Fin thickness	0.00159	Ganapathy (1996)
t_{tw}	m	Tube wall thickness	0.00406	Albrecht et al. (2012)

Table A.3: Geometric specifications for different HRSG elements (calculated from Franco and Giannini (2006)).

			Value			
Symbol	Unit	Name	Economizer	Evaporator	Superheater	Reheater
s_{fin}	m	Fin spacing	0.00423	0.00423	0.00333	0.00324
l_{fin}	m	Fin height	0.019	0.019	0.00139	0.00132
$d_{\text{t,o}}$	m	Outer tube diam.	0.041	0.041	0.00611	0.00625
s_{t}	m	Tube spacing	0.0923	0.0923	0.108	0.109
σ_{pass}	m^2	Surf. area per pass	1620.7	1825.8	811.4	799.5

The number of passes in a HRSG element is calculated from the gas-side area and the number of tube rows as follows:

$$n_{\text{pass}} = \max\left(1, \min\left(n_{\text{rows}}, A_{\text{g}}/\sigma_{\text{pass}}\right)\right). \tag{A.19}$$

In this equation, n_{rows} is the number of tube rows, A_{g} is the gas-side surface area, and σ_{pass} [m^2] (the average surface area per pass in a reference design) is a constant that depends on the type of HRSG element. The values for σ_{pass} are calculated from a design specified by Franco and Giannini (2006) and are shown in Table A.3. The number of passes is calculated in this way to be similar to reference HRSG designs, while maintaining geometric consistency (for example, it is not feasible to have more passes than tube rows). The number of tube rows in the HRSG element is calculated using Equation A.27 below.

The HRSG face width w_{HRSG} [m] scales with the gas-side flow rate according to the following rule, based upon the HRSG width and gas flow rate in a reference

design (Franco and Giannini, 2006):

$$\frac{w_{\mathrm{HRSG}}}{\dot{m}_{\mathrm{g}}} = 0.0157 \frac{\mathrm{m}}{(\mathrm{kg/s})}. \tag{A.20}$$

Note that the HRSG face height l_{HRSG} [m] is treated as a constant value.

We now describe several geometric variables and relationships required for HRSG model calculations, and in particular the computation of U. These relationships can be determined from simple geometric considerations and reference to Figure A.6. The bulk length of an element, L_{elem} [m], is given by

$$L_{\mathrm{elem}} = \sin(60^\circ)\, n_{\mathrm{rows}} s_{\mathrm{t}}, \tag{A.21}$$

where s_{t} [m] is the tube spacing measured from center to center, and the coefficient $\sin(60^\circ)$ reflects the geometry of the equilateral tube pitch (which refers to the staggering of the tubes when viewed from above; see Figure A.6). The gas-side free flow area, A_{ff} [m^2], is

$$A_{\mathrm{ff}} = l_{\mathrm{HRSG}} w_{\mathrm{HRSG}} - d_{\mathrm{t,o}} l_{\mathrm{HRSG}} n_{\mathrm{t,row}} - 2 n_{\mathrm{t,row}} n_{\mathrm{fin,t}} l_{\mathrm{fin}} t_{\mathrm{fin}}, \tag{A.22}$$

where $n_{\mathrm{t,row}}$ is the number of tubes per tube row in the element, $n_{\mathrm{fin,t}}$ is the number of fins per tube, l_{fin} [m] is the fin height, and t_{fin} [m] is the fin thickness. The bare tube (i.e., excluding fins) outer surface area (total for element), $A_{\mathrm{t,o,bare}}$ [m^2], is

$$A_{\mathrm{t,o,bare}} = n_{\mathrm{t,row}} n_{\mathrm{rows}} l_{\mathrm{HRSG}} d_{\mathrm{t,o}} \pi. \tag{A.23}$$

The water-side contact area (total for element) is the bare tube inner surface area, $A_{\mathrm{t,i,bare}}$ [m^2]:

$$A_{\mathrm{t,i,bare}} = n_{\mathrm{t,row}} n_{\mathrm{rows}} l_{\mathrm{HRSG}} d_{\mathrm{t,i}} \pi, \tag{A.24}$$

where $d_{\mathrm{t,i}}$ [m] is the tube inner diameter. The outer surface area (including fins) of a tube, $A_{\mathrm{t,o}}$ [m^2], is

$$A_{\mathrm{t,o}} = \pi l_{\mathrm{HRSG}} d_{\mathrm{t,o}} + 2\pi n_{\mathrm{fin,t}} \left[(l_{\mathrm{fin}} + d_{\mathrm{t,o}}/2)^2 - d_{\mathrm{t,o}}^2/4 \right]. \tag{A.25}$$

The outer surface area (including fins) of a tube row, $A_{\mathrm{tr,o}}$ [m^2], is

$$A_{\mathrm{tr,o}} = A_{\mathrm{t,o}} n_{\mathrm{t,row}}. \tag{A.26}$$

The number of tube rows, n_{rows}, is

$$n_{\mathrm{rows}} = A_{\mathrm{g}}/A_{\mathrm{tr,o}}. \tag{A.27}$$

The number of tubes per tube row, $n_{\mathrm{t,row}}$, is

$$n_{\mathrm{t,row}} = w_{\mathrm{HRSG}}/s_{\mathrm{t}}. \tag{A.28}$$

The number of fins per tube, $n_{\mathrm{fin,t}}$, is

$$n_{\mathrm{fin,t}} = l_{\mathrm{HRSG}}/s_{\mathrm{fin}}. \tag{A.29}$$

The tube inner diameter, $d_{\mathrm{t,i}}$ [m], is

$$d_{\mathrm{t,i}} = d_{\mathrm{t,o}} - 2t_{\mathrm{tw}}. \tag{A.30}$$

The tube inner cross-sectional area, $A_{\mathrm{t,xsec}}$ [m^2], is

$$A_{\mathrm{t,xsec}} = \pi d_{\mathrm{t,i}}^2/4. \tag{A.31}$$

A.1.3.2 HRSG element tube wall conduction

The quantity R_{cond} [m^{2}K/W] in Equation A.18 is calculated following Kays and London (1984, p 15):

$$R_{\text{cond}} = \frac{t_{\text{tw}} A_{\text{g}}}{k_{\text{wall}} A_{\text{m,bare}}}, \tag{A.32}$$

where $A_{\text{m,bare}} = \frac{1}{2}\left(A_{\text{t,i,bare}} + A_{\text{t,o,bare}}\right)$ [m^2] is the mean of the inner and outer bare tube surface areas, and k_{wall} [W/(m-K)] is the thermal conductivity of the wall material.

A.1.3.3 Gas-side heat transfer coefficient

The HRSG elements are modeled as finned-tube heat exchangers with equilateral tube pitch. The gas-side heat transfer coefficient calculation proceeds in two steps. First we obtain a gas-side heat transfer coefficient that does not include fin effects (i.e., does not account for the fact that the fin tip is hotter than the fin base). We then calculate the fin efficiency, which accounts for these fin effects.

Gas-side heat transfer coefficient, uncorrected for fin effects

The uncorrected gas-side heat transfer coefficient, $u_{\text{g,0}}$ [W/(m^2-K)], is calculated using the Briggs and Young correlation for the Colburn j-factor, as given in Webb and Kim (2005, p 156):

$$j = 0.134\text{Re}^{-0.319}\left(\frac{s_{\text{ff}}}{l_{\text{fin}}}\right)^{0.2}\left(\frac{s_{\text{ff}}}{t_{\text{fin}}}\right)^{0.11}, \tag{A.33}$$

where s_{ff} [m] is the open space between fins, calculated as $s_{\text{ff}} = s_{\text{fin}} - t_{\text{fin}}$. The Reynolds number is evaluated as $\text{Re} = \dfrac{d_{\text{t,o}}\dot{m}_{\text{g}}}{A_{\text{ff}}\mu_{\text{g}}}$, where μ_{g} [kg/(m-s)] is the dynamic viscosity of the flue gas.

The Colburn j-factor, $j = \dfrac{\text{Nu}}{\text{RePr}^{1/3}}$, is used to calculate the Nusselt number (Nu). Here, $\text{Pr} = \dfrac{c_{\text{p,g}}\mu_{\text{g}}}{k_{\text{g}}}$ is the Prandtl number. The Nusselt number is then used to

calculate the uncorrected gas-side heat transfer coefficient $u_{\mathrm{g},0} = \mathrm{Nu}\dfrac{k_{\mathrm{g}}}{d_{\mathrm{t,o}}}$ [W/(m^2-K)], where k_{g} [W/(m-K)] is the thermal conductivity of the flue gas. The quantity $u_{\mathrm{g},0}$ is referred to the gas-side surface area including fins, A_{g} (but it does not account for fin efficiency).

Fin efficiency correction for fin effects

Gas-side fin efficiency adjusts the uncorrected gas-side heat transfer coefficient for the fact that fins are hotter at the tips than at the base. The fin efficiency is used to correct the gas-side heat transfer coefficient following Kays and London (1984, p 15):

$$u_{\mathrm{g}} = u_{\mathrm{g},0}\left[1 - (1 - \eta_{\mathrm{fin}})\,\frac{A_{\mathrm{g,fin}}}{A_{\mathrm{g}}}\right], \tag{A.34}$$

where η_{fin} is the fin efficiency (calculated below in Equations A.35-A.42), and $A_{\mathrm{g,fin}}$ [m^2] is area of fins only on the gas-side, calculated as $A_{\mathrm{g}} - A_{\mathrm{t,o,bare}}$. The quantity u_{g} [W/K] is the gas-side heat transfer coefficient used in Equation A.18. Typical values of η_{fin} are 0.5-0.7.

The fin efficiency is calculated for a circular tube with solid annular fins by the following correlation adapted from Shah and Sekulic (2003, p 283):

$$\eta_{\text{fin}} = \begin{cases} \frac{\tanh\phi}{\phi} & \text{if } \phi \leq 0.6 + 2.257\left(r^*\right)^{-0.445} \\ a\left(l_e\right)^{-b} & \text{otherwise} \end{cases}, \tag{A.35}$$

$$\phi = m l_e \left(r^*\right)^n, \tag{A.36}$$

$$a = \left(r^*\right)^{-0.246}, \tag{A.37}$$

$$b = \begin{cases} 0.9107 + 0.0893 r^* & \text{if } r^* \leq 2 \\ 0.9706 + 0.17125 & \text{otherwise} \end{cases}, \tag{A.38}$$

$$l_e = l_{\text{fin}} + 0.5 t_{\text{fin}}, \tag{A.39}$$

$$m = \left(\frac{2u_{\text{g,0}}}{k_{\text{fin}} t_{\text{fin}}}\right)^{0.5}, \tag{A.40}$$

$$n = \exp\left(0.13 m l_e - 1.3863\right), \tag{A.41}$$

$$r^* = \frac{2l_{\text{fin}} + d_{\text{t,o}}}{d_{\text{t,o}}}. \tag{A.42}$$

The fin construction material thermal conductivity, k_{fin} [W/(m-K)], is evaluated at the mean temperature of the gas and water streams.

A.1.3.4 Water-side heat transfer coefficient

The water-side heat transfer coefficient u_{w} [W/(m^2-K)], used in Equation A.18, is referred to the water-side contact area. The method for calculating u_{w} depends upon the kind of flow: liquid water only, two-phase boiling, and dry steam only. Fluid properties are evaluated at the mean temperature of water (liquid or vapor) within each element.

Liquid only (economizer)

The Gnielinski correlation (Collier and Thome, 1994, p 275; Franco and Giannini, 2006; Nellis and Klein, 2009, p 667) is employed to calculate the Nusselt number in

single-phase liquid water:

$$\mathrm{Nu} = \frac{(f_{\mathrm{Darcy}}/8)\,(\mathrm{Re} - 1000)\,\mathrm{Pr}}{1 + 12.7\sqrt{f_{\mathrm{Darcy}}/8}\left(\mathrm{Pr}^{-2/3} - 1\right)}. \tag{A.43}$$

The friction factor is calculated using the Petukhov correlation (Collier and Thome, 1994, p 275; Franco and Giannini, 2006; Nellis and Klein, 2009, p 654):

$$f_{\mathrm{Darcy}} = \left(-1.64 + 0.7904 \ln \mathrm{Re}\right)^{-2}. \tag{A.44}$$

The Reynolds number is given by $\mathrm{Re} = \dfrac{d_{\mathrm{t,i}}\dot{m}_{\mathrm{t,w}}}{A_{\mathrm{t,xsec}}\mu_{\mathrm{lw}}}$, where μ_{lw} [kg/(m-s)] is the dynamic viscosity of liquid water, and $\dot{m}_{\mathrm{t,w}}$ [kg/s] refers to the water flow rate through a single tube.

Two phase (evaporator)

The method used to calculate the water-side heat transfer coefficient is that of Steiner and Taborek (1992) as described in Collier and Thome (1994, pp 269-279). The correlation is quite complex and is presented here without substantial discussion. The central idea is to asymptotically combine correlations for the two main boiling regimes, nucleate boiling and convective boiling, in the following equation:

$$u_{\mathrm{w,evap}} = \left[\left(h_{\mathrm{NcB0}}F_{\mathrm{NcB}}\right)^3 + \left(h_{f0}F_{TP}\right)^3\right]^{1/3}. \tag{A.45}$$

Here, the term $h_{\mathrm{NcB0}}F_{\mathrm{NcB}}$ represents nucleate boiling and the term $h_{f0}F_{TP}$ represents convective boiling.

Nucleate boiling

The local nucleate pool boiling coefficient is a constant with value $h_{\mathrm{NcB0}} = 25,580$ W/(m^2-K) (Collier and Thome, 1994, p 278). The nucleate boiling correction factor, F_{NcB}, has the following form (Collier and Thome, 1994, p 276):

$$F_{\mathrm{NcB}} = F_{PF}\left(\frac{\phi}{\phi_0}\right)^{nf}\left(\frac{d_{\mathrm{t,i}}}{d_0}\right)^{-0.4}\left(\frac{R_p}{R_{p0}}\right)^{0.133}F_M. \tag{A.46}$$

The pressure factor, F_{PF}, is evaluated according to the following equation (Collier and Thome, 1994, p 276):

$$F_{PF} = 2.816 p_r^{0.45} + \left(3.4 + \frac{1.7}{1 - p_r^7}\right), \tag{A.47}$$

where p_r is the reduced pressure. The heat flux, ϕ [W/m^2], is treated as constant along the tube as follows:

$$\phi = \frac{\Delta h_{\mathrm{w,vap}} \dot{m}_{\mathrm{w}}}{A_{\mathrm{w}}/n_{\mathrm{tube}}}, \tag{A.48}$$

and the reference heat flux has value $\phi_0 = 150,000$ W/m^2 (Collier and Thome, 1994, p 278). The heat flux exponent, nf, is evaluated as follows (Collier and Thome, 1994, p 278):

$$nf = 0.8 - 0.1 \exp\left(1.75 p_r\right). \tag{A.49}$$

The reference tube inner diameter is $d_0 = 0.01$ m. The quantity (R_p/R_{p0}) refers to the roughness of the tube material and is treated as having a value of unity (Collier and Thome, 1994, p 278). The residual correction factor, F_M, is a constant, with value $F_M = 0.72$ (Collier and Thome, 1994, p 279).

Convective boiling

The local liquid phase forced convection coefficient, h_{f0} [W/(m^2-K)], is calculated using the following expression from Collier and Thome (1994, pp 274-275):

$$h_{f0} = \mathrm{Nu} k_{\mathrm{lw}}/d_{\mathrm{t,o}}, \tag{A.50}$$

where k_{lw} [W/(m-K)] is the thermal conductivity of liquid water, and Nu is evaluated using the Gnielinski correlation (Equation A.43), the fluid properties of liquid water, and the total mass flow rate including both phases.

The two-phase multiplier for convection, F_{TP}, is calculated by the following equation (Collier and Thome, 1994, p 275):

$$F_{TP} = \left[(1-x)^{1.5} + 1.9 x^{0.6} \left(\frac{\rho_{\mathrm{lw}}}{\rho_{\mathrm{vw}}} \right)^{0.35} \right]^{1.1}, \tag{A.51}$$

where x is the steam quality (evaluated at $x = 0.5$), and ρ_{lw} and ρ_{vw} [kg/m^3] are the densities of water liquid and vapor.

Dry steam (superheaters and reheaters)

The Dittus-Boetler correlation is used for the water-side heat transfer coefficient in modeling superheaters and reheaters (Franco and Giannini, 2006):

$$u_{\mathrm{w,shrh}} = 0.023 \mathrm{Re}^{0.8} \mathrm{Pr}^{0.4} \frac{k_{\mathrm{vw}}}{d_{\mathrm{t,i}}}. \tag{A.52}$$

Here, k_{vw} [W/(m-K)] is the thermal conductivity of dry steam. The Reynolds number is evaluated as $\mathrm{Re} = \dfrac{d_{\mathrm{t,i}} \dot{m}_{\mathrm{vw}}}{A_{\mathrm{t,xsec}} \mu_{\mathrm{vw}}}$, where $\dot{m}_{\mathrm{vw}}$ [kg/s] is the mass flow rate of steam, and μ_{vw} [kg/(m-s)] is the dynamic viscosity of steam.

A.1.4 Solution process

The system of $7N_{\mathrm{elem}}$ equations is written in residual form ($\mathbf{g}(\mathbf{x}) = \mathbf{0}$). We apply a damped Newton's method/steepest descent procedure for solving this set of nonlinear algebraic equations. The Jacobian matrix, $\mathbf{J}$, with $J_{ij} = \dfrac{\partial g_i}{\partial x_j}$, is computed using numerical finite differences. The initial guess is generated automatically with a heuristic based upon a pinch analysis.

Within each iteration of the nonlinear solution process, a damped Newton step is first attempted. This entails solving the following equation for $\boldsymbol{\delta}_{k+1}$:

$$\mathbf{J}_k \boldsymbol{\delta}_{k+1} = -\mathbf{g}_k, \tag{A.53}$$

where $\mathbf{J}_k$ is the Jacobian matrix at iteration k, $\boldsymbol{\delta}_{k+1}$ is the Newton update, and $\mathbf{g}_k$ is the residual. The quantity $\boldsymbol{\delta}_{k+1}$ is then used to form the full (undamped) Newton update, $\hat{\mathbf{x}}_{k+1}$, as follows:

$$\hat{\mathbf{x}}_{k+1} = \mathbf{x}_k + \boldsymbol{\delta}_{k+1}. \tag{A.54}$$

We do not use $\hat{\mathbf{x}}_{k+1}$ directly, but instead damp it as follows:

$$\mathbf{x}_{k+1} = (1-\gamma)\,\mathbf{x}_k + \gamma\hat{\mathbf{x}}_{k+1}, \tag{A.55}$$

where $\mathbf{x}_{k+1}$ is the damped Newton candidate and γ is a damping coefficient ($0 < \gamma \leq 1$). The value of γ depends upon the success or failure of previous iterations. If $\|\mathbf{g}_{k+1}\|_2 < \|\mathbf{g}_k\|_2$, the candidate is accepted as the starting point for the next iteration of the damped Newton procedure.

We found that the overall solution method could be made more effective by the use of steepest descent in addition to the damped Newton technique (i.e., more systems could be solved with the use of steepest descent steps in combination with damped Newton steps than with only damped Newton steps). This may be because the alternative search directions provided by steepest descent enable the procedure to avoid problems related to discontinuities in the steam property functions. Our implementation of steepest descent is motivated by an algorithm given in Burden and Faires (2005, pp 624-630). Within an iteration, if the Newton step described above is unsuccessful ($\|\mathbf{g}_{k+1}\|_2 \geq \|\mathbf{g}_k\|_2$), then a new candidate is determined using the direction of steepest descent, $-\dfrac{\partial}{\partial \mathbf{x}_k}\left(\mathbf{g}_k^T\mathbf{g}_k\right) = -2\mathbf{J}_k\mathbf{g}_k$. The new candidate is defined as $\tilde{\mathbf{x}}_{k+1} = \mathbf{x}_k - \lambda\dfrac{\mathbf{J}_k\mathbf{g}_k}{\|\mathbf{J}_k\mathbf{g}_k\|_2}$, where $\lambda > 0$ is the step length. The value of λ is determined using information about the slope at $\mathbf{x}_k$ and the value of $\|\mathbf{g}(\tilde{\mathbf{x}}_{k+1})\|_2$ (this entails the evaluation of $\mathbf{g}(\mathbf{x})$ at more than one value of λ). Upon finding a candidate state vector for which $\|\mathbf{g}(\tilde{\mathbf{x}}_{k+1})\|_2 < \|\mathbf{g}_k\|_2$, the state vector $\tilde{\mathbf{x}}_{k+1}$ is accepted and is used as the starting point for the next iteration.

The solution process (in each iteration, first attempt a damped Newton update; if/when the Newton update is unsuccessful, switch to steepest descent) is repeated until the stopping criterion $\mathbf{g}_k^T \mathbf{D} \mathbf{g}_k < \epsilon_{\text{tol}}$ is reached. Here, $\mathbf{D}$ is a positive diagonal matrix that is used to scale $\mathbf{g}_k$, and ϵ_{tol} is the stopping tolerance. The matrix $\mathbf{D}$ accounts for the fact that residual vector entries have units of different magnitudes. If the stopping criterion is not reached within 200 iterations, the solution process is terminated and the candidate design is treated as infeasible (this occurs in less than 0.4% of function evaluations). Typically, the process converges within 20 iterations.

The equations in the model are valid only for states within a certain domain, and inaccuracies result if states outside these domains are reached. For example, the capacity equations in Section A.1.1.2 for single-phase systems are invalid if a phase change occurs between the water inlet and outlet, so a state in which an economizer heats water above the saturated liquid enthalpy would be invalid. Our algorithm allows iteration through invalid states because the solution process may encounter these states before reaching a final valid state. Converged systems with invalid solution states (as opposed to systems with valid solution states arrived at via invalid intermediate iterates) are rejected due to violation of the optimization constraints.

A.1.5 Gas-side pressure drop

Following the computation of the HRSG states as described above, we calculate Δp_{gas} [kPa] for a single HRSG element using the total pressure drop in the core of a tube-fin heat exchanger (Franco and Giannini, 2006; Shah and Sekulic, 2003, pp 388-392):

$$\Delta p_{\text{gas}} = \frac{f_{\text{Fann}} L_{\text{elem}} \dot{m}_{\text{g}}^2}{2 \rho_{\text{gas}} A_{\text{ff}}^2 r_{\text{hyd}}}. \tag{A.56}$$

Here, f_{Fann} is the Fanning friction factor, L_{elem} [m] is the bulk length of the element, ρ_{gas} [kg/m^3] is the gas density, and r_{hyd} [m] is the hydraulic radius. The gas-side pressure drop for the entire HRSG is the sum of gas-side pressure drops in each of the individual HRSG elements.

We compute Reynolds number as $\mathrm{Re} = \frac{4 r_{\mathrm{hyd}} \dot{m}_{\mathrm{g}}}{A_{\mathrm{ff}} \mu_{\mathrm{g}}}$. For turbulent flow (Re > 4,000), we calculate f_{Fann} using the method of Zigrang and Sylvester (1982). For laminar flow (Re < 2,300), the friction factor is given by $f_{\mathrm{Fann}} = 16/\mathrm{Re}$ (using the value for a circular duct). For transition flow, we linearly interpolate friction factor (based on Re) between the laminar and turbulent values. In most designs, the gas side operates in the turbulent region with Re > 4,500.

Gas-side pressure drop is computed after the system state variables are calculated. This decoupling is justified because Δp_{gas} is small and the resulting pressure variation has a negligible effect on other system variables. As mentioned in Chapter 2, in the optimization we apply a nonlinear constraint of $\Delta p_{\mathrm{gas}} < 4.5$ kPa (cumulative over the entire HRSG) so that GT performance is not negatively impacted by HRSG gas-side pressure drop. This constraint also ensures that the assumption of small pressure variation is satisfied.

A.2 Steam cycle

Steam from the HRSG is expanded in the steam turbines, which drive electric generators. This steam then condenses either in the condenser at 330 K or the CO_2 capture solvent reboiler. In the mixed salt process, the reboiler requires steam at two temperatures so a fraction of the steam is extracted from the steam turbine chain at the higher pressure, and the remainder at the lower pressure. The reboiler temperature depends upon the CO_2 capture system treated, and is equal to the temperature of the heat required for the solvent regeneration process. For the MEA process, the temperature is 407 K; for the piperazine process, the temperature is 433 K; and for the mixed salt process, the temperature is approximately 427 K (the weighted average of the two reboiler heat requirements). The condensate then becomes feed water for the HRSG. Steam turbines are modeled as multi-stage expansions (as shown in Figure A.7) in which each stage is represented by an isentropic efficiency, based on a method described in Kim and Ro (1997). The number of stages is chosen so that all stages have the same pressure ratio (typically around 1.5). Behavior below the Wilson

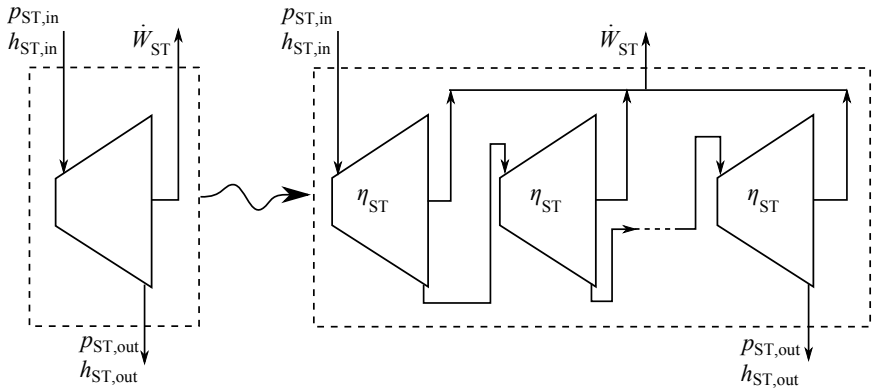

Figure A.7: Steam turbine modeled using multiple expansion stages.

line (i.e., quality less than 0.97) is modeled using a simple correlation (Kim and Ro, 1997).

The outlet enthalpy of expanded steam in a stage is given by the following relation:

$$h_{\text{expand}} = h_{\text{ST,in}} - \eta_{\text{ST}} \left[h_{\text{ST,in}} - h \left(s_{\text{ST,in}}, p_{\text{ST,out}} \right) \right], \tag{A.57}$$

where $h_{\text{ST,in}}$ [J/kg] is the stage inlet enthalpy, η_{ST} is the stage isentropic efficiency, $s_{\text{ST,in}}$ [J/(kg-K)] is the stage inlet entropy, and $p_{\text{ST,out}}$ [kPa] is the stage outlet pressure. Note that $h \left(s_{\text{ST,in}}, p_{\text{ST,out}} \right)$ is the outlet enthalpy of an ideal ($\eta_{\text{ST}} = 1$) stage. The change in enthalpy of the steam across a stage is $\Delta h_{\text{ST,actual}} = h_{\text{ST,in}} - h_{\text{expand}} = \eta_{\text{ST}} \left(h_{\text{ST,in}} - h \right)$. The power output produced by a stage is $\dot{W}_{\text{ST}} = \dot{m}_{\text{w}} \Delta h_{\text{ST,actual}}$, where $\dot{m}_{\text{w}}$ [kg/s] is the mass flow rate of steam.

The isentropic efficiency is constant for steam quality above 0.97 (Wilson line) and is computed according the following equation when the steam quality is less than 0.97 (Kim and Ro, 1997):

$$\eta'_{\text{ST}} = \eta_{\text{ST}} - 0.8 \left(1 - x \right), \tag{A.58}$$

where x is the mean steam quality of the stage evaluated using the inlet condition and the ideal ($\eta_{\text{ST}} = 1$) outlet condition. Expansion stages are processed sequentially,

with the outlet of one stage being the inlet to the next stage. The total power output is the sum of the per-stage power outputs.

For the reheater steam turbine (as in Figure A.4), Equation A.57 is used to calculate h_{expand} in Equation A.11. Part-load effects in the steam turbine are not included in this work: we assume that steam turbine performance metrics (e.g., efficiency) do not change with mass flow rate, inlet conditions, or other operating parameters. This assumption is reasonable because a change in efficiency in the steam turbines between operating modes would only have a small effect on the overall power output of the CCGT system.

The use of steam turbine isentropic efficiency in HRSG optimization has been critiqued as inaccurate (Martelli et al., 2011, 2012). As with all approximate methods this treatment is imperfect, and inaccuracies arising from its use may be problematic for certain calculations requiring high thermodynamic accuracy. However, the use of isentropic efficiency methods is less of a concern for the economic objectives targeted in this work because error in capital cost estimation is more influential than error from predicted steam turbine efficiency. Furthermore, the method that we use, based upon Kim and Ro (1997), improves on isentropic efficiency methods by correcting for behavior below the Wilson line.

The condenser is modeled with a log-mean temperature difference of $\Delta T_{\text{lm}} = 25$ K. The overall heat transfer coefficient for this water-water (liquid on one side, condensing steam on the other side) heat exchanger is $U_{\text{cond}} = 1,200$ W/(m^2-K) (Ulrich and Vasudevan, 2004, pp 206-207). The condenser contact area, A_{cond} [m^2], is given by the following equation:

$$A_{\text{cond}} = \frac{\dot{q}_{\text{cond}}}{U_{\text{cond}} \Delta T_{\text{lm}}}, \tag{A.59}$$

where $\dot{q}_{\text{cond}}$ [W] is the condenser duty.

Figure A.8 shows the flows in an example steam expansion for a three-pressure system. The HP stream is expanded in a steam turbine to the pressure of the IP stream, and then is mixed with the IP stream. This combined stream is then expanded

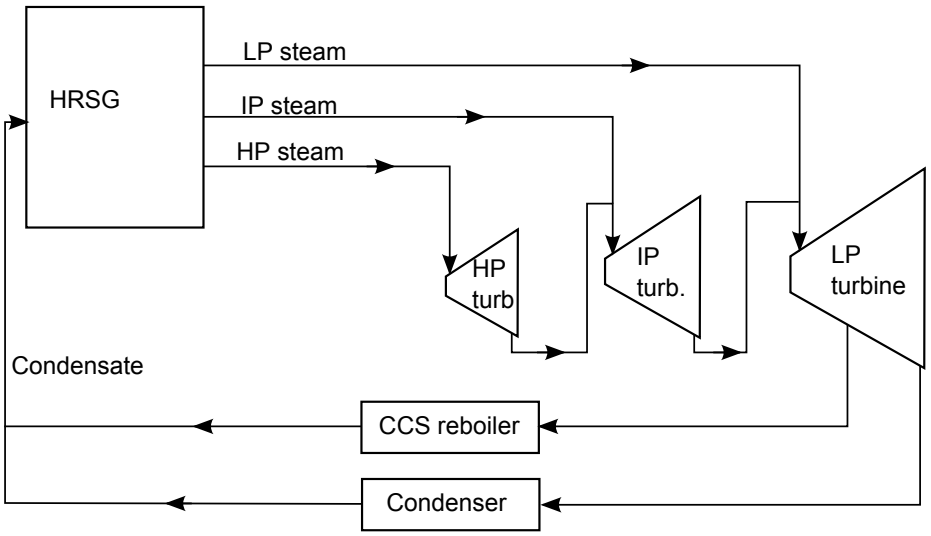

Figure A.8: Steam cycle in a three-pressure system.

to the pressure of the LP stream, and then is mixed with the LP stream. The resulting combined stream finally is expanded to the condensate pressure. The steam condenses in the condenser or CO_2 capture solvent regeneration reboiler, and the condensate is reused as HRSG feedwater. As noted above, the mixed salt process requires two steam temperatures, so a portion of the steam is extracted from the steam turbine chain at the higher pressure, and the remainder at the lower pressure. Both of these extractions occur at the lowest pressure level (i.e., after the IP turbine outlet stream has been mixed with the LP stream exiting the HRSG). A similar pattern occurs for systems with a different number of pressure levels.

In systems with reheat, steam that is to be reheated is expanded first to the reheat pressure, and then sent back to the HRSG for reheating. If the reheat pressure is close to the pressure of one of the other HRSG streams, the reheat stream is mixed with that HRSG outlet stream. In the optimization framework we enforce a constraint requiring the HP reheat pressure to be within 10 kPa of the intermediate pressure.

A.3 Capital cost

As described in Chapter 2, we use the Guthrie method of capital cost estimation. This method makes use of component-by-component cost scaling, in which purchased equipment cost C [$] grows with component size according to the following rule:

$$\frac{C}{C_{\text{ref}}} = \left(\frac{S}{S_{\text{ref}}}\right)^{\alpha}. \tag{A.60}$$

In Equation A.60, C_{ref} [$] is the reference cost of the item, S_{ref} is the reference size of the item, and α is the scaling exponent. Individual component purchased equipment costs are adjusted for escalation using the Chemical Engineering Plant Cost Index (CEPCI), which had a value of 100.0 in the period 1957-1959. Then, as described in Chapter 2, the component costs are summed and a sequence of multipliers is applied, eventually yielding the total capital requirement of the facility. Tables A.4, A.5 and A.6 show the data used for capital cost calculation.

A key feature of the Guthrie method is the scaling exponent, α. Having $\alpha < 1$ indicates that economies of scale apply for a component. In reality, the scaling exponent only applies up to a certain maximum size. Beyond this size, cost scaling no longer follows the same exponent. We use $\alpha = 1$ (linear scaling, analogous to building multiple units) beyond the maximum size, except for steam turbines and condensers in the CCGT steam cycle. For steam turbines and condensers larger than the maximum size in the data range, we use $\alpha = 0.89$, which is the scaling exponent for field-erected CCGT power plants (Ulrich and Vasudevan, 2004, p 369). We make this choice for CCGT components because the data for steam turbines and heat exchangers available in Ulrich and Vasudevan (2004) have small maximum sizes compared to units seen in large CCGT power plants, but large steam turbines and condensers do in fact exist. As such, a linear scaling would be inaccurate. Using the overall CCGT cost scaling exponent is a compromise between extrapolating cost scaling outside the data range (which would tend to understate cost for a large item) and linear scaling (which would tend to overstate cost for a large item).

Table A.4: Capital cost data I.

Equipment item	Size measure	Reference size S_{ref}	Ref. purch. equip. cost [1,000 $]	Ref. CEPCI	Reference
Gas turbine	Electric output	200 MW	47,300	550.8	Farmer (2010, p 47)
Steam turbine	Power output	1.0 MW	115	400.0	Ulrich and Vasudevan (2004)
Elec generator	Electric output	1.0 MW	65	400.0	Ulrich and Vasudevan (2004)
Condenser*	Surface area	900 m^2	70	400.0	Ulrich and Vasudevan (2004)
CCS absorption†	CO_2 abs rate	150.4 kg/s	144,500‡	585.7	Berkenpas et al. (2009); Rubin et al. (2007a)
CCS regen & comp†	CO_2 regen rt	150.4 kg/s	175,100‡	585.7	Berkenpas et al. (2009); Rubin et al. (2007a)

* Shell and tube heat exchanger. † Data inferred from regression study on IECM 8.0.2. ‡ Inferred bare module cost used as purchased equipment cost, module factor 1.0.

Table A.5: Capital cost data II.

Equipment item	α scaling exponent	Max size	Module factor	Reference
Gas turbine	0.774	230 MW	1.525	Farmer (2010, p 47)
Steam turbine	0.45	17.5 MW†	3.5	Ulrich and Vasudevan (2004)
Elec. generator	0.95	–	1.5	Ulrich and Vasudevan (2004)
Condenser*	0.752	900 m^2	3.5	Ulrich and Vasudevan (2004)
CCS absorption‡	0.834	–	1.0§	Berkenpas et al. (2009); Rubin et al. (2007a)
CCS regen & comp‡	0.853	–	1.0§	Berkenpas et al. (2009); Rubin et al. (2007a)

* Shell and tube heat exchanger. † Beyond this value, exponent of 0.89 (for field-erected CCGT power plants). (Ulrich and Vasudevan, 2004, p 369). ‡ Data inferred from regression study on IECM 8.0.2. § Use module factor of 1.0 because purchased equipment cost is a module cost.

Table A.6: HRSG capital cost data (Casarosa et al., 2004).

Element type	Purchased equipment cost [$/m^2]
Economizer	45.7
Evaporator	34.9
Superheater	96.2
Reheater	56.2

The HRSG capital cost model uses linear cost scaling in the gas-side surface area, with data drawn from Casarosa et al. (2004), which in turn were the result of a regression study. These data are summarized in Table A.6. Casarosa et al. (2004) did not specify whether the cost data are purchased equipment costs, bare module costs, or total module costs. In our model the costs are treated as purchased equipment costs and the module factor for utility boilers of 2.0 from Ulrich and Vasudevan (2004) is applied. We used a CEPCI of 402.0 for the HRSG, corresponding to the year 2003.

A.4 Scenario construction details

In the UK and India scenarios, local currencies were converted to US dollars using monthly exchange rates (US Federal Reserve Bank, 2014). The yearly average conversion rates for 2011 were 1.604 USD/GBP, and 46.62 INR/USD.

Though in principle capital costs can differ by geographic location, for the sake of simplicity we did not change the capital cost in the UK and India scenarios from those in the base scenario. This is because process plant capital costs are only about 2% higher in the United Kingdom and India than on the United States Gulf Coast (Towler and Sinnott, 2013, p 339). This 2% variation is less than the capital cost variability within the United States (Towler and Sinnott, 2013, p 339).

The natural gas used in all of the scenarios has a higher heating value (HHV) of 53.9 MW/kg, and a composition of 83.4% CH_4, 15.8% C_2H_6 and 0.8% N_2 (volume basis). These gas properties were used in our earlier work (Kang et al., 2011) and originally were taken from IECM 6.2.4 (Berkenpas et al., 2009; Rubin et al., 2007a). Coal

type for each case was selected from the USGS World Coal Quality Inventory (Tewalt et al., 2011) based on the characteristics of major coal mines in the countries considered. The properties of coal differ across scenarios and are summarized in Table A.7.

A.5 Operations and maintenance (O&M) costs

Operations and maintenance costs are shown in Table A.8. The values for CO_2 capture are calculated by taking the difference of the costs for coal plants with and without CO_2 capture as given in Black & Veatch (2012).

A.6 Physical properties

Steam properties are calculated using the open-source Freesteam C++ library (Pye, 2013), which conforms to the IAPWS-IF97 standard (Wagner et al., 2000).

A linear gas turbine flue gas specific heat capacity correlation was constructed by performing a regression on data given in Ganapathy (1993). Flue gas density is calculated using the ideal gas law. Viscosity and thermal conductivity of the flue gas are calculated from the chemical composition of the flue gas using data from Poling et al. (2007), with the Wilke method for mixtures applied as described in Poling et al. (2000).

The thermal conductivity of the HRSG construction material is drawn from a linear regression on data for carbon steel given in Beaton (1983):

$$k_{\text{wall}}(T) = 73.966 - 0.0437T, \tag{A.61}$$

where k_{wall} [W/(m-K)] is the thermal conductivity of the construction material and T [K] is the operating temperature of the HRSG element (mean of gas-side and water-side temperatures). We assume that the fins are made of the same material as the tube walls, so $k_{\text{fin}}(T) = k_{\text{wall}}(T)$.

Table A.7: Coal properties.

Scenario(s)		West Texas (WTX)	India	UK
Mine location		Powder River Basin, WY	Sohagpur, Madhya Pradesh	Northumberland
Rank		Sub-bituminous	Bituminous	Bituminous
HHV [MJ/kg]		19.4	25.7	29.7
Composition [wt%]	C	48.2	63.4	72.4
	H	3.3	4.0	4.8
	H_2O	30.2	9.7	3.5
	N	0.7	1.4	1.7
	O	11.9	8.1	8.1
	S	0.4	0.6	1.1
	Ash	5.3	12.9	8.4
Reference		IECM 6.2.4 (Berkenpas et al., 2009; Rubin et al., 2007a)	Tewalt et al. (2011)	Tewalt et al. (2011)

Table A.8: Operations and maintenance costs.

Component	Fixed O&M	Variable O&M	Source
CCGT	\$6.31/(kW-y)	\$3.67/MWh	Black & Veatch (2012, p 14)
Coal plant	\$23.0/(kW-y)	\$3.71/MWh	Black & Veatch (2012, p 18)
CO_2 capture	\$14.7/((g CO_2/s)-y)	\$0.986/(tonne CO_2)	Black & Veatch (2012, pp 18-20)

Table A.9: Reference one-pressure HRSG*.

Position	Unit	UA_g [kW/K]
1	Economizer	34.0
2	Evaporator	65.0
3	Superheater	4.2

* Ganapathy (1991, pp 216-218) Performance Case 2

A.7 Model verification and validation

A.7.1 HRSG model verification

To verify the results of our HRSG model, we present model outputs for two HRSG designs, one simple and one complex. These designs are prescribed by the reference literature; optimization was not used in these designs.

A.7.1.1 One-pressure HRSG

Ganapathy (1991) defined a one-pressure HRSG system producing steam at 3.2 MPa, specified in Table A.9. This one-pressure HRSG has a flue gas flow rate of 20.8 kg/s at an inlet temperature of 448.9 °C, and a condenser temperature of 115.6 °C. The model predictions for key variables, the steam flow rate and temperature and total heat transfer, match those of the reference to within 0.8%, as shown in Table A.10. This indicates that our model produces predictions consistent with those in the existing literature for simple systems.

Table A.10: Model verification: predictions for a one-pressure HRSG.

Quantity	Unit	Reference*	Calculated	Percent deviation
$\dot{m}_{\text{steam}}$	kg/s	2.24	2.26	0.8
T_{steam}	°C	334.4	335.0	0.2
$\dot{Q}_{\text{tot}}$	MW	5.83	5.85	0.3

* Ganapathy (1991, Figure 4-3, p 219) Performance Case 2

A.7.1.2 Three-pressure HRSG

Franco and Giannini (2006, p 3354) defined a three-pressure HRSG. This system has flue gas flow rate of 445.4 kg/s at an inlet temperature of 505 °C, and a condenser temperature of 57 °C. One complication in comparing our model with the HRSG model in Franco and Giannini (2006) is that the Franco and Giannini (2006) model uses 'multi-streaming' elements, in which multiple streams of water move alongside each other. These elements have multiple sets of side by side tubes, one for each water stream, within the HRSG enclosure. The streams in such a multi-stream element enter and exit the element at the same temperature, but can have different flow rates. Our model does not include multi-stream elements, so multi-stream elements are instead modeled by sequentially interleaving single-stream elements. For example, a multi-stream element consisting of an LP superheater and an IP economizer could be treated as a LP superheater followed by an IP economizer, or two LP superheaters (with half the contact area of the multi-stream LP superheater) sandwiching an IP economizer, or some other interleaving, while preserving A_{g}.

Another difficulty is that Franco and Giannini (2006) treat the reheat stream from the third pressure as mixing with the superheat stream at the intermediate pressure before entering the HRSG (RH pressure equals IP pressure), so the reheater is in fact a mixed reheater-superheater at the intermediate pressure. This is treated in our model by representing reheaters as interleaved IP superheaters and HP reheaters (operating at the same pressure as the IP stream) in a similar manner to the treatment of multi-stream elements. Reheater area is allocated to each substitute element in proportion to the reference flow rate of each stream.

Table A.11: A reference three-pressure HRSG.

Reference*			Our model			
Position	Element(s)	Surf. Area [m^2]	Position	Element		Surf. Area [m^2]
1	LP Econ	18,012	1	LP	Econ	18,012
2	LP Evap	17,983	2	LP	Evap	17,983
3	LP SH / IP Econ	1,450 / 6,465	3	LP	SH	1,000
4	IP Econ	8,152	4	IP	Econ	6,465
			5	LP	SH	450
			6	IP	Econ	8,152
5	IP Evap	16,458	7	IP	Evap	16,458
6	IP SH / HP Econ	2,653 / 5,513	8	IP	SH	2,653
			9	HP	Econ	5,513
7	HP Econ / RH	4,685 / 1,122	10	HP	Econ	4,685
			11	HP	RH	747
			12	IP	SH	375
8	HP Evap	13,610	13	HP	Evap	13,610
9	HP SH / RH	20,498 / 15,570	14	IP	SH	2,325
			15	HP	RH	5,865
			16	HP	SH	20,498
			17	HP	RH	4,612
			18	IP	SH	2,948

* Franco and Giannini (2006, Table 4) 'Optimized triple pressure HRSG.'

Table A.11 describes a multi-stream three-pressure HRSG specification provided in Franco and Giannini (2006), along with the equivalent single-stream specification modeled here. The LP stream is at 0.6 MPa, the IP stream is at 5.3 MPa, and the HP stream is at 16.9 MPa. The reheat pressure is the same as the IP pressure, 5.3 MPa. The reference multi-stream configuration has nine HRSG elements, four of which are multi-stream. The equivalent single-stream configuration has 18 HRSG elements. The gas-side surface areas of equivalent sets of HRSG elements and the total for the entire HRSG in the reference specification are maintained in the single-stream model.

The flow rates and steam temperatures predicted by our model (using calculated U) and given by Franco and Giannini (2006) are shown in Table A.12. Absolute deviations of model predictions from the reference results are 5.0% or less in all quantities. The use of constant U values (from Casarosa et al. (2004)) produced similar results. However, as noted in Chapter 2, using calculated U is likely to be more robust during optimization.

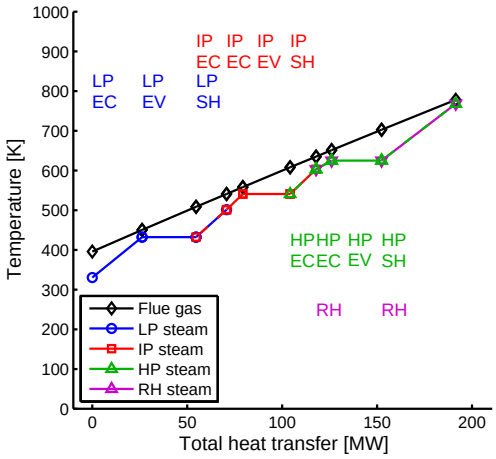

(a) Reference results for a three-pressure HRSG system (Franco and Giannini, 2006). Dashed lines represent multi-stream elements.

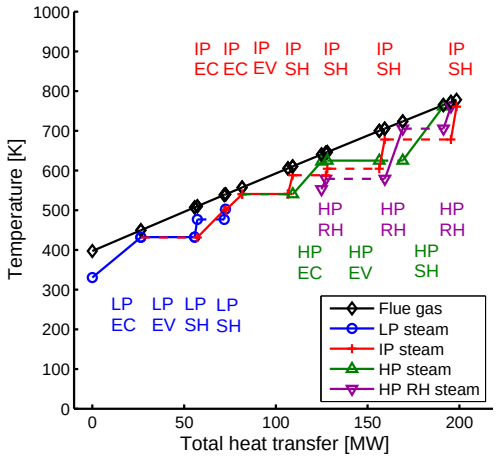

(b) Calculated results for a three-pressure HRSG system. Dashed lines represent bypass flows (steam or water moving around elements without heat transfer to flue gas).

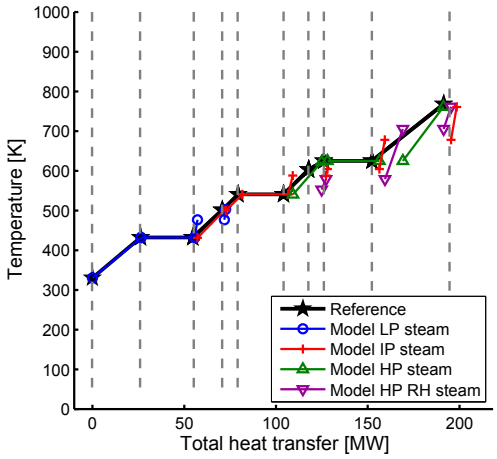

(c) Comparison of steam temperature profiles between model and reference results (Franco and Giannini, 2006). Vertical dashed lines indicate comparable locations.

Figure A.9: Temperature profiles for a three-pressure HRSG.

Table A.12: Predictions for a three-pressure HRSG.

Stream	Quantity	Unit	Reference*	Calculated	Percent deviation
LP	$\dot{m}_{\text{steam}}$	kg/s	13.62	13.31	-2.2
IP	$\dot{m}_{\text{steam}}$	kg/s	15.33	14.58	-4.9
HP	$\dot{m}_{\text{steam}}$	kg/s	30.46	30.21	-0.8
LP	$T_{\text{steam,out}}$	°C	228	229.2	1.7†
IP	$T_{\text{steam,out}}$	°C	495	487.4	-3.3†
HP	$T_{\text{steam,out}}$	°C	495	487.8	-5.0†
Reheat	$T_{\text{steam,out}}$	°C	495	487.8	-3.1†
Flue Gas	$T_{\text{gas,out}}$	°C	122.5	123.8	1.1
Heat Transf.	$\dot{Q}_{\text{tot}}$	MW	191.4	188.0	-1.8

* Franco and Giannini (2006, Table 4), 'Optimized triple pressure HRSG.'
† Relative to saturation temperature.

Furthermore, the model and reference temperature profiles, shown in Figure A.9, match closely. The flue gas temperature profiles can be compared by straightforward visual inspection. Because the reference steam temperature profile includes multi-stream elements, more care must be taken to compare the steam temperature profiles. The steam temperature profiles are best compared by plotting the reference and model results together, as in Figure A.9(c). For the sake of visual clarity, the different streams in the reference steam temperature profile are not differentiated from each other in Figure A.9(c). The model steam temperature profile is consistent with the reference steam profile, as seen by the fact that the temperatures of the reference (black star symbols) are closely tracked by the temperatures of the model predictions (colored non-star symbols) at comparable locations in terms of total heat transfer, indicated by the vertical dashed lines in Figure A.9(c). Differences in the steam temperature profiles arise from the method we use to approximate multi-stream elements using interleaved single-stream elements.

The differences in the physical configuration of the HRSG treated in our model from that given in Franco and Giannini (2006) result from the use of a different approach to HRSG modeling, not to the modeling of a different HRSG. In the limit of a large number of interleaved single stream-elements used to approximate the multi-stream elements, our process should converge. Indeed, the close fit between our model

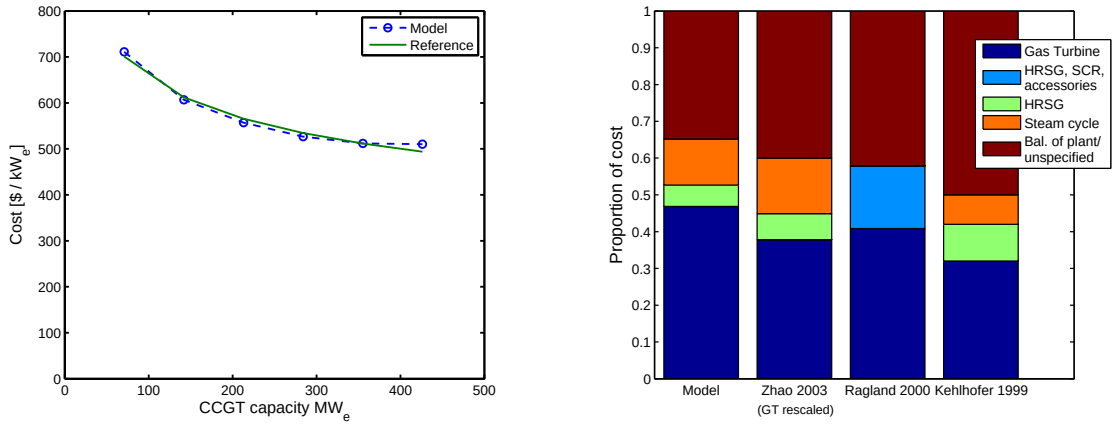

(a) Total capital cost vs reference (Farmer, 2010)

(b) Cost breakdown by component (Kehlhofer et al., 1999; Ragland and Stenzel, 2000; Zhao et al., 2003)

Figure A.10: Comparison of model CCGT capital cost with literature values.

and the reference indicates that a multi-stream element can be approximated quite well using as few as two single-stream elements.

A.7.2 Capital cost validation

Figure A.10(a) shows CCGT capital cost scaling with size for facilities, as given by an industry publication (Farmer, 2010), compared to results generated by our model (2009 US dollars). The model quantity plotted excludes certain costs such as interest during construction. The curves match very closely in the range of 50-450 MW, with maximum deviation of 3.3%.

Figure A.10(b) shows CCGT cost breakdown on a component-by-component basis as calculated by the model and as given by three different sources (Kehlhofer et al., 1999; Ragland and Stenzel, 2000; Zhao et al., 2003). The original gas turbine data given in Zhao et al. (2003) appears to be a purchased equipment cost; the value shown in Figure A.10(b) is a rescaled bare module cost using a module factor of 1.525 (our value for gas turbines as described in Section A.3). The overall cost proportions that our model produces are generally in line with those from other

sources, except that the gas turbine constitutes a somewhat higher proportion of cost. This apparent inconsistency may be due to differences in cost attribution (it is difficult to compare precisely system costs on a component-by-component basis because costs can be attributed differently). For example, some sources may attribute certain auxiliary facility costs to equipment being installed, while others may attribute these costs to the overall facility.

Taken in total, the capital cost model produces results that are consistent with external cost estimates. This is true for both the total cost and generally for the cost contribution of each major subcomponent.

A.8 Optimization constraints

This section describes constraints that are not given in Chapter 2. Three kinds of constraints are present: discrete constraints on HRSG configuration, linear constraints, and nonlinear constraints on HRSG states.

A.8.1 Discrete constraints on HRSG configuration

Candidate designs that violate the following constraints on HRSG configuration are nonphysical and/or clearly suboptimal and are discarded:

- The first element is an economizer at the lowest pressure level
- The second element is an evaporator at the lowest pressure level
- Each pressure level has at least one economizer
- Each pressure level has exactly one evaporator
- Within each pressure level, all economizers are before the evaporator
- Within each pressure level, all superheaters are after the evaporator

A.8.2 Linear constraints

The following linear and bound constraints are applied:

- Individual gas turbine capacity is bounded: $s_{\mathrm{GT}} \leq 300$ MW
- HRSG steam pressures are ordered from highest to lowest
- Steam extraction pressure is not greater than the lowest HRSG outlet steam pressure: $p_{\mathrm{ext}} \leq \min\left(\mathbf{p}_{\mathrm{pl}}\right)$
- HP reheat steam pressure is close to the IP steam pressure: $\mid p_{\mathrm{HP,rh}} - p_{\mathrm{IP}} \mid \leq$ 10 kPa
- Strike prices are ordered from highest to lowest

A.8.3 Nonlinear constraints on HRSG states

Several nonlinear (output) constraints are applied to HRSG states to ensure that the HRSG design conforms to common design standards. These constraints, which are consistent with constraints applied widely in HRSG optimization (Casarosa et al., 2004; Franco and Giannini, 2005, 2006; Martelli et al., 2011; Mohagheghi and Shayegan, 2009), are as follows:

- Evaporator approach temperature is bounded between 10 K and 20 K
- Evaporator pinch temperature (defined as the difference between the evaporator gas outlet temperature and the water saturation temperature) is at least 10 K
- Reheater inlet steam does not have steam quality less than 1.0
- Reheater pinch temperature at water inlet is at least 10 K
- Steam turbine outlet quality is at least 0.88
- HRSG flue gas outlet temperature is at least 373 K

- HRSG gas-side pressure drop is at most 4.5 kPa

The constraints are evaluated for the system operating in mode A.

Appendix B

CO_2 capture model verification, validation, and implementation

This appendix contains supplementary information on modeling details, primarily concerning the full-system problem formulation, to supplement the description provided in Chapter 4. The full-system problem formulation treats the optimal comprehensive design and variable operation of a CO_2-capture-enabled coal-natural gas power plant. The facility is represented using detailed models for two main sets of system components: 1) the CO_2 capture system, and 2) the CCGT subsystem (and related heat integration). The CCGT subsystem is described in detail in Chapter 2 and Appendix A, while in Chapter 4 and this appendix we focus on the CO_2 capture system.

The CO_2 capture integrated proxy model uses a combination of statistical proxy models to represent the behavior of the CO_2 absorption and solvent regeneration blocks, and simple physical models to represent the other system components. The statistical proxy models are constructed using a multi-step procedure (described in Chapter 4 and this appendix) to replicate the behavior of a rate-based Aspen Plus model ('full-physics model'), which has been validated against experimental results. The simple physical models used to represent other components entail calculations that are very similar to those performed by Aspen Plus for these components. Some

of the calculated quantities are used as inputs for other parts of the integrated proxy model, or for evaluation of energy duty requirements of the CO_2 capture system, while other quantities are used only for calculation of capital cost.

This document proceeds as follows. Section B.1 provides details on the Aspen Plus model used in Chapter 4, and validates this model with experimental results. We provide details for the submodels of the absorption and regeneration blocks in Section B.2, and discuss details of the submodels for auxiliary process units in Section B.3. Capital cost estimation details are presented in Section B.4, and the method for estimating the impact of inaccuracy in the integrated proxy model is described in Section B.5. Physical properties are discussed in Section B.6. In Section B.7 we summarize the overall workflows employed for constructing the integrated proxy model and performing an optimization. Note that, for completeness and clarity, there is some repetition between this document and Chapters 2 and 4, and Appendix A.

B.1 Aspen Plus model

Figure B.1, reproduced from Chapter 4, depicts the CO_2 capture system treated in Chapter 4. The depiction in Figure B.1 differs slightly from the Aspen Plus model we use to perform simulations, because some aspects can be treated more conveniently using different representations than are shown in Figure B.1. There are two differences between the depiction in Figure B.1 and the Aspen Plus model and/or integrated proxy model applied in Chapter 4. First, the recycle of lean solvent back to the absorption column (component C3 in Figure B.1, with recycle involving streams S14 and S15, and pump C10) is not explicitly present in the Aspen Plus model, though it is represented in the integrated proxy model. Instead, the model enforces a design requirement that the CO_2 loading of the solvent leaving the regeneration column (S12-S14) equals the CO_2 loading of the solvent entering the absorption column (S15). Second, the Aspen Plus model includes the pump for the reflux stream at the top of the regeneration column (C6). The work duty associated with this pump is very

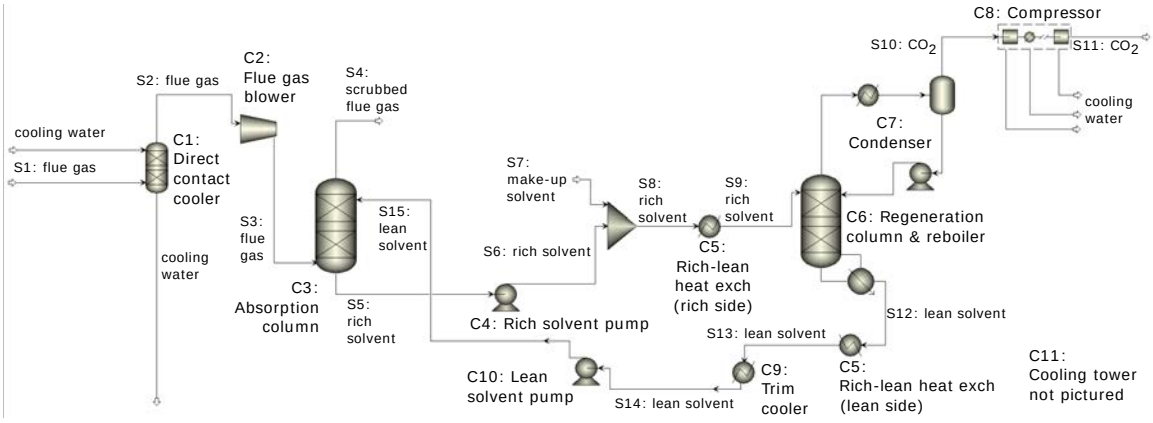

(a) Full physics Aspen Plus model

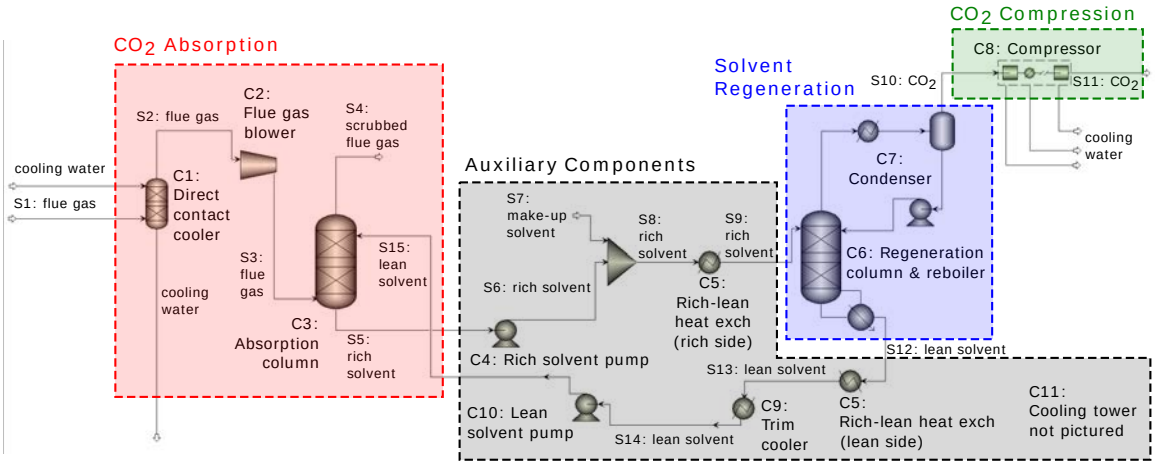

(b) Major blocks indicated

Figure B.1: Full-physics Aspen Plus model (Kothandaraman, 2010) system diagram showing division into blocks. C# indicates numbered component, and S# indicates numbered stream. Reproduced from Chapter 4.

small (< 2 kW in all points sampled), so for the sake of simplicity we do not include the pump in the integrated proxy model.

The Aspen Plus model is modified from one developed originally by Kothandaraman et al. (2009) and Kothandaraman (2010). As discussed in Chapter 4, we left unchanged many of the specifications in the original model. The model employs the electrolyte-NRTL treatment for thermodynamic properties, and applies the mass transfer correlation and interfacial area methods of Bravo et al. (1985). Heat transfer coefficients are determined using the Chilton-Colburn analogy. The holdup method used in the model is that of Bravo et al. (1992). The absorption column is modeled with eight liquid film discretization points as follows: 0.001, 0.005, 0.01, 0.05, 0.1, 0.15, 0.2, 0.3 (Kothandaraman, 2010), where 0 represents the gas/liquid interface and 1 represents the edge of the film next to the bulk phase. The regeneration column is modeled with five liquid film discretization points as follows: 0.01, 0.05, 0.1, 0.2, 0.3. The absorption column is discretized into 30 stages, while the regeneration column has 20 stages.

We treat two different packing materials. For the structured packing material Flexipac 1Y (which is employed in all optimization runs), we use the following parameters for the packing dimensions: corrugation angle, 45°; side dimension, 9 mm; base width, 12.7 mm; and height, 6.4 mm (Tsai et al., 2011). For the random packing material IMTP no. 40 (which is used in some of the full-physics model validation runs), an interfacial area factor of 1.8 is used (Zhang et al., 2009).

B.1.1 Chemical reactions

The full-physics model includes five chemical reactions in the CO_2-water-MEA system. Three of these reactions are treated as equilibrium reactions, while two are kinetically controlled (Kothandaraman, 2010). The three equilibrium reactions are as follows:

$$H_2O + MEA^+ \rightleftharpoons MEA + H_3O^+ \tag{B.1}$$

Table B.1: Kinetics data for Equations B.4 and B.5 (Thee et al., 2012).

Equation number	Direction	A	Reaction order	E_a [kJ/mol]
B.4	Forward	2.53×10^{11} M^{-1} s^{-1}	2	35.8
B.4	Reverse	2.38×10^{17} s^{-1}	1	123.2
B.5	Forward	2.62×10^{8} M^{-1} s^{-1}	2	25.3
B.5	Reverse	3.23×10^{19} s^{-1}	1	65.5

$$2\,H_2O \rightleftharpoons H_3O^+ + OH^- \tag{B.2}$$

$$HCO_3^- + H_2O \rightleftharpoons CO_3^{--} + H_3O^+, \tag{B.3}$$

and the two kinetically controlled reactions are:

$$CO_2 + OH^- \rightleftharpoons HCO_3^- \tag{B.4}$$

$$MEA + CO_2 + H_2O \rightleftharpoons MEACOO^- + H_3O^+. \tag{B.5}$$

The reaction rates k for the kinetically-controlled reactions (Equations B.4 and B.5) follow the Arrhenius equation, $k = Ae^{-E_a/(RT)}$. Here, A is the pre-exponential factor (the units of A depend on reaction order, with first-order reactions having units s^{-1}, and second-order reactions having units M^{-1} s^{-1}, where M designates molarity, mol/L). The symbol E_a [J] represents the activation energy, R [J/(mol-K)] is the universal gas constant, and T [K] is the temperature. We modified the original Aspen Plus model of Kothandaraman (2010) with new kinetics data based on recent results (Thee et al., 2012). The parameters used in our modeling are summarized in Table B.1.

B.1.2 Validation with experimental data

To validate the thermodynamics, transport, and kinetics of the full-physics model, we first simulate the MEA pilot plant presented in Zhang et al. (2009). This plant has

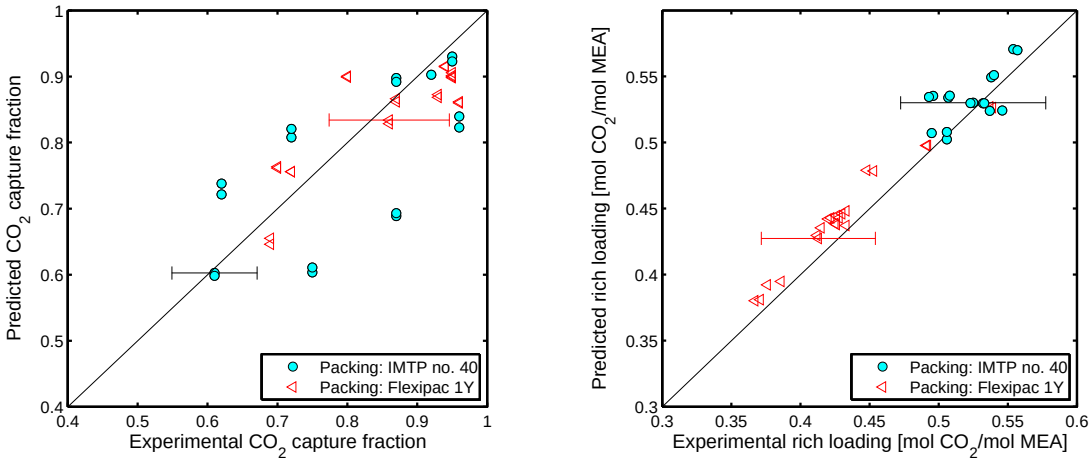

(a) CO_2 capture fraction

(b) Rich solvent loading

Figure B.2: Predictions from full-physics model compared with measurements from pilot plant (Zhang et al., 2009). Error bars indicate 10% measurement uncertainty for a single experiment for each packing type.

an absorption column with packed diameter 0.427 m and packed height 6.1 m. The solvent is modeled with aqueous 32.5 %(wt.) MEA. Note that we use 32.5 %(wt.) MEA solution here to match the experimental setup, but in the optimization runs we use 30 %(wt.) MEA solution. Both of the column packing materials used in the pilot plant study, Flexipac 1Y and IMTP no. 40, are considered.

Figure B.2 shows parity plots of predictions from the full-physics model with experimental results for CO_2 capture fraction and rich solvent loading. Taking into consideration the 10% measurement uncertainty in the pilot plant study (Zhang et al., 2009), the full-physics model gives predictions in reasonable agreement with pilot plant measurements. The results for CO_2 capture fraction display larger errors, with the IMTP no. 40 packing showing significant error. A similar degree of error is also seen in the modeling results in Zhang et al. (2009), which used a different reaction scheme than that applied here. This may indicate that model error originates from the mass transfer correlations.

B.2 Absorption and regeneration blocks

The absorption and solvent regeneration blocks are shown in Figure B.3. We employ similar methods for the submodels for these blocks. For this reason, we provide details for the two blocks together here. As discussed in Chapter 4, we developed statistics-based (proxy) submodels for these blocks. Here we discuss details of the input variable sampling technique, and describe the simulation convergence prediction mechanism for the regeneration block. We also present the calculation of the shell mass of the absorption and regeneration columns, which is required for capital cost estimation. Additional aspects of the absorption and regeneration block submodels are also considered.

B.2.1 Input variable sampling

As described in Chapter 4, we employ experimental design techniques to define a sample set of input points which are then run using the full-physics models for the absorption and regeneration blocks. We use a combination of Box-Behnken, central composite, and Latin hypercube sampling (LHS) designs. For each of these techniques, we use the built-in MATLAB functions as described in Chapter 4. The MATLAB central composite function is used three times with the modes `inscribed`, `circumscribed`, and `faced`, which correspond to different experimental designs. The experimental design functions yield a set of points with dimensionless values, which we transform into dimensional input variables by linearly interpolating between the lower and upper bounds for each variable. The central composite designs include some points outside the bounds, which are produced via linear extrapolation. These points are used directly when this is possible; otherwise, they are projected to physically meaningful values.

Table B.2 provides the number of points sampled for each of the blocks. We remove 150 points to serve as the test set for model verification, so the number of points in the training set is 150 less than the total number of evaluated points. The test set consists of a random subset of the LHS points, and the same test set is used

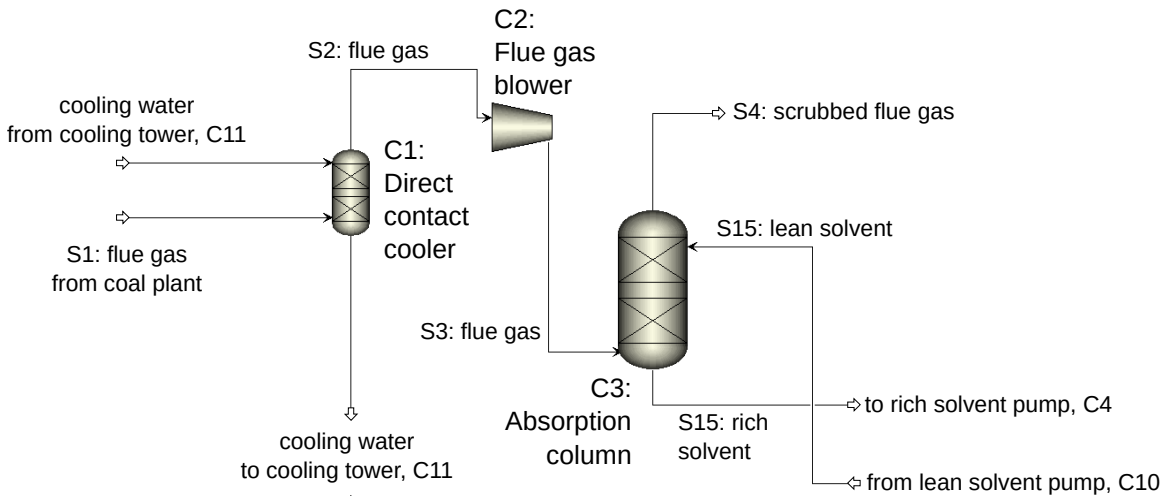

(a) Absorption

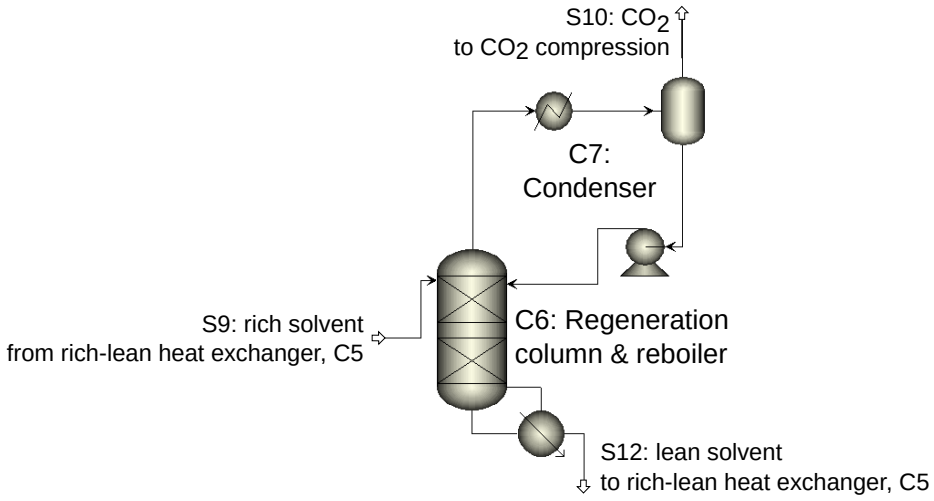

(b) Regeneration

Figure B.3: Detail of the CO_2 absorption and solvent regeneration blocks.

Table B.2: Summary of sets used for statistical proxy model training.

Block	# Variables	# Points evaluated			# Points in set	
		Deterministic	LHS	Total	Training	Test
Absorption	5	93	507	600	450	150
Regeneration	6	137	613	750	600	150

N.b.: Summary statistics above exclude 150 additional points in each block defined by optimization-directed retraining.

throughout Chapter 4 and this appendix (except for the discussion of optimization-directed retraining in Section 4.2.8, which uses the final optimized points as a test set).

When running the full-physics simulations used to construct our sample set, we need to provide the model with a complete specification of input states. Notably, both the absorption column and the regeneration column require specification of feed solvent inlet temperature (stream S15 for the absorption column in Figure B.3(a), and S9 for the regeneration column in Figure B.3(b)). For the absorption column, this is straightforward as $T_{\text{S15}} = 303$ K is a fixed design parameter maintained by the trim cooler (described in Section B.3.4). However, this is more complicated for the regeneration column because T_{S9} [K] is calculated by the rich-lean heat exchanger (which is not present in the regeneration block) and is thus a function of other system design variables.

Therefore, in order to run full-physics simulations of the regeneration block, we develop a relationship that provides T_{S9} for sampling purposes as a function of sampled input variables for the regeneration block only. Specifically, we represent T_{S9} for sampling purposes as follows:

$$\begin{aligned} T_{\text{S9}} = T_{\text{S9,regress}} &= c_0 + c_1 p_{\text{regen}} + c_2 p_{\text{regen}}^2 - \Delta T_{\text{rlhx,pinch}}, \\ c_0 = 353,\ c_1 &= 0.317,\ c_2 = -0.000435. \end{aligned} \tag{B.6}$$

Here, p_{regen} [kPa] is the regeneration column operating pressure and $\Delta T_{\text{rlhx,pinch}}$ [K] is the rich-lean heat exchanger pinch temperature, taken here to be 10 K. Equation B.6 is

determined by a regression on the relationship between regeneration column operating pressure and regeneration column lean solvent outlet temperature for a separate set of randomly sampled points for the regeneration block. We also assume that the rich-lean heat exchanger pinch occurs on the hot end of the heat exchanger. Note that excluding the term $\Delta T_{\text{rlhx,pinch}}$ from Equation B.6 provides a prediction for the regeneration column lean solvent outlet temperature. For the test set, the regeneration column lean solvent outlet temperature predictions of Equation B.6 match the full-physics simulations with mean absolute deviation of 2.7 K.

Equation B.6 is used only in the sampling step of our workflow, i.e., when we run the full-physics model for the regeneration block only. When we evaluate the integrated proxy model, we calculate regeneration block rich solvent inlet (stream S9 in Figure B.1) temperature T_{S9} directly in the rich-lean heat exchanger submodel described in Section B.3.3. We enforce consistency in temperature (between the temperature used in the regeneration block full-physics model runs and the temperature calculated by the rich-lean heat exchanger) by a method described in Section B.2.5.3. Note that Equation B.6 is not used in verification runs of the full-physics model because these runs include a full set of results from Aspen Plus, so $T_{\text{S9,regress}}$ is not necessary.

B.2.2 Model fitting

As discussed in Chapter 4, we employ the implementation of kriging provided by the Object-Oriented Design and Analysis of Computer Experiments (ooDACE) toolbox (Couckuyt et al., 2012, 2014) for the absorption and regeneration submodels in Chapter 4. The use of kriging requires the selection of several model settings and metaparameters. We apply the ooDACE utility `oodacefit`, which provides default values for all necessary settings and the metaparameters used in kriging. All settings and metaparameters are left at the `oodacefit` defaults.

B.2.3 Prediction of simulation convergence in the regeneration block

We employ a separate mechanism to predict the convergence success or failure of Aspen Plus runs of the regeneration block. This enables us to identify these points as infeasible during optimization. The method of boosted decision trees is used for this purpose. The method consists of decision trees for regression applied within a boosting framework.

A decision tree for regression works by using simple rules on individual variables to divide recursively the training set into several sets. Each tree node that is not a terminal node ('leaf') represents a single binary branching event for a particular variable (e.g., for a given point, if the value of variable k is less than some value, proceed down the left branch; otherwise, proceed down the right branch). Each branch leads to another node, which in turn may contain another branching decision rule. A leaf does not have branches, but instead defines a numerical value. In our case, each leaf corresponds to a real number between zero and one that is the proportion of observations, assigned to that leaf, that have simulation success. Figure B.4 shows an example of a decision tree for regression with four leaves. In this example, the branching rules are displayed at each non-terminal node, and the value associated with each leaf is shown.

As mentioned in Chapter 4, we coded simulation convergence failure as zero, and simulation convergence success as one. Though classification ultimately requires integer values, we allow the decision tree to have leaves with noninteger values. We interpret the value as indicating a degree of confidence. Decision trees involve a metaparameter J for the maximum number of leaves, which we control by setting a minimum number of observations in each leaf. We use the MATLAB R2013b implementation of decision trees for regression, `RegressionTree`. Further discussion of decision trees can be found in Hastie et al. (2009).

Boosting is a technique that can improve the performance of decision trees (Friedman, 2001; Hastie et al., 2009). In boosting, multiple decision trees are formed and

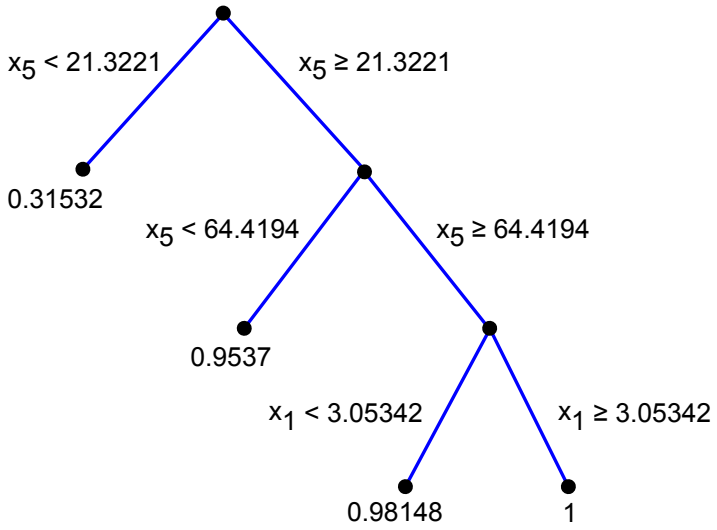

Figure B.4: A four-leaf decision tree for regression.

used together in an ensemble. We apply the MATLAB R2013b implementation of `LSBoost` associated with the command `fitensemble`. In the first iteration of the boosting algorithm, a single tree is trained on the training set. This tree is then used to make a prediction for each of the points. In the second iteration, a new tree is trained on the same set of points, except that the value for each point is replaced with the difference between the true value of the point and the prediction made by the existing tree. Similarly, in the k^{th} iteration, the k^{th} tree is constructed on the training set where the value of each point is calculated as the difference between the true value of the point and the aggregate of all predictions for the point given by the $(k-1)$ trees currently in the ensemble. In this manner, trees trained in later iterations compensate for prediction errors made by trees trained in earlier iterations.

We apply a form of boosting that requires the choice of two metaparameters: the number of boost iterations M, and the 'learning rate' ν $(0 < \nu \leq 1)$, which can be interpreted as a regularization parameter. The learning rate controls how much effect each individual boost iteration has on the prediction. A value of $\nu = 0$ means that each iteration contributes nothing to the prediction, while a value of $\nu = 1$ means that

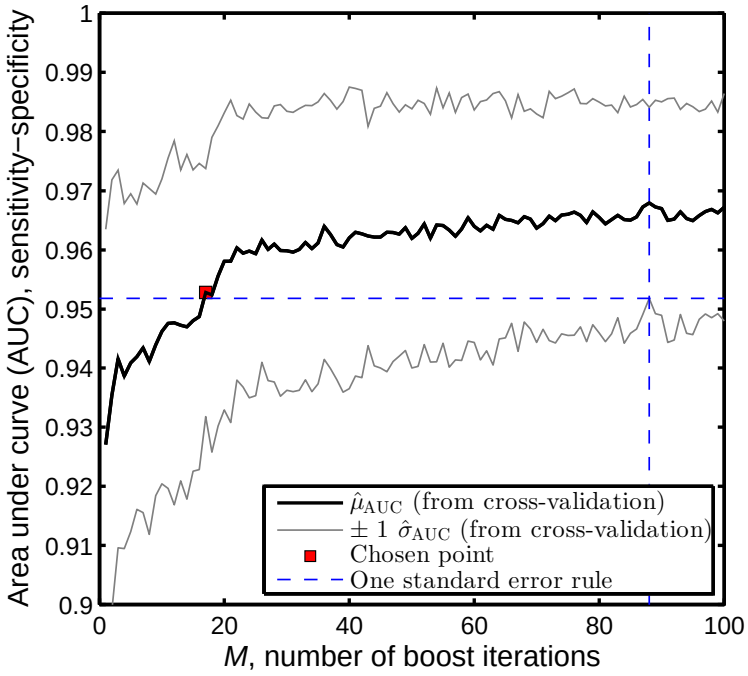

Figure B.5: Effect of number of boost iterations on classifier performance.

each iteration contributes maximally. Note that ν and M are not independent because a smaller value of ν usually entails a larger value of M. We describe our procedure for choosing the values of the metaparameters ν, J, and M in Section B.2.3.1 below. Further discussion on boosting is available in Hastie et al. (2009).

B.2.3.1 Choice of metaparameters ν, J, and M

The approach we use for determining the metaparameters ν, J and M is to maximize the area under the curve (AUC) of the sensitivity-specificity tradeoff (an example of this tradeoff is shown in Figure B.6(b)). Sensitivity is the true positive rate (the fraction of points that successfully converge in Aspen Plus that the classification mechanism predicts to succeed). Specificity is the true negative rate (the fraction of points that fail to converge that the proxy predicts to fail). The quantity AUC is calculated as the area under the curve formed by plotting sensitivity against specificity.

As mentioned in Chapter 4, we also choose a fourth parameter, classification threshold T, which controls the location on the sensitivity-specificity tradeoff curve. Higher values of classification threshold increase specificity and decrease sensitivity. Note that AUC is independent of the choice of classification threshold, and as such T is not a metaparameter in the same sense as ν, J, and M. The choice of T is discussed in Section B.2.3.2.

To limit the risk of overfitting and also to reduce computational requirements, we do not perform a full optimization to choose J and ν. Instead, we first choose a value of $\nu = 0.1$ as suggested by Hastie et al. (2009, p 365). Next, we select a value of $J = 6$ leaves for the regeneration block based upon an exploratory analysis of the dataset. This number of leaves is consistent with the typical use of boosting with 'weak predictors' (trees with a small number of leaves are classified as weak predictors). In addition, Hastie et al. (2009, p 363) suggest that the choice of $J \in [4, 8]$ works well for many problems.

After choosing ν and J, the remaining metaparameter to choose is M, which we determine using a one-dimensional search. Figure B.5 shows AUC for the regeneration block with varying values of M. We use fivefold cross-validation repeated 25 times to calculate the estimates for mean ($\hat{\mu}_{\text{AUC}}$) and standard error ($\hat{\sigma}_{\text{AUC}}$) in Figure B.5. In fivefold cross-validation, the dataset is divided randomly into five equal-size subsets. The model is trained five times with a different (one) subset left out each time. Each left-out subset is evaluated using the model trained on the other four-fifths of the data. This procedure produces an estimate of expected performance of the model given the metaparameters. In repeated cross-validation, which produces more robust performance statistics, the above procedure is performed several times with the dataset being divided into different subsets. The highest-$\hat{\mu}_{\text{AUC}}$ ensemble, which uses $M = 88$, has $\hat{\mu}_{\text{AUC}} = 0.9679$ and $\hat{\sigma}_{\text{AUC}} = 0.0162$. We apply the 'one standard error rule' (Hastie et al., 2009, p 244) to choose $M = 17$, which is the smallest number of boosting iterations to achieve $\hat{\mu}_{\text{AUC}}$ within one $\hat{\sigma}_{\text{AUC}}$ of the $\hat{\mu}_{\text{AUC}}$ of the $M = 88$ ensemble. The $M = 17$ ensemble has $\hat{\mu}_{\text{AUC}} = 0.9528$ and $\hat{\sigma}_{\text{AUC}} = 0.0210$.

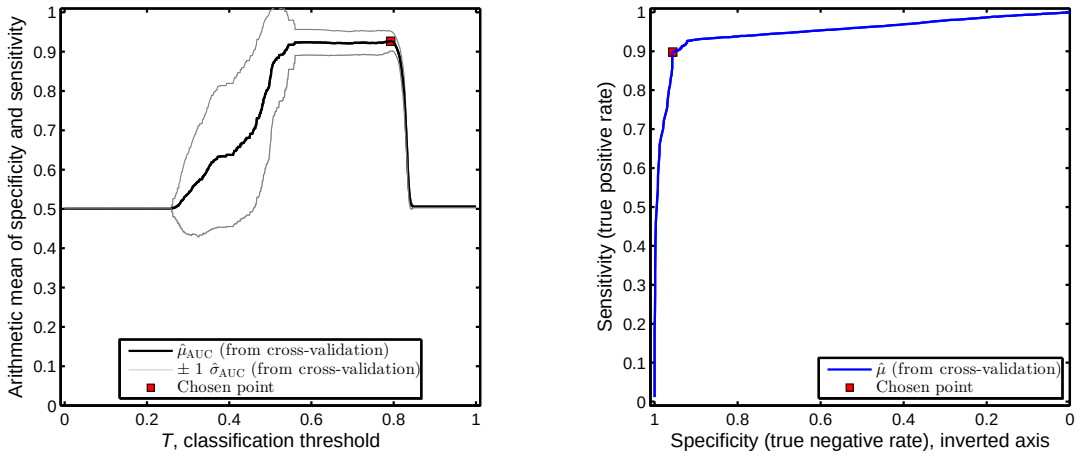

(a) Effect of choice of threshold on classifier performance

(b) Tradeoff in classifier between sensitivity and specificity

Figure B.6: Choice of classifier threshold T.

B.2.3.2 Simulation convergence prediction classifier

The choice of threshold T controls the tradeoff between sensitivity and specificity. We code simulation success as one and simulation failure as zero. Values of T closer to one result in higher specificity (predicting correctly more points with convergence failure), while values of T closer to zero result in higher sensitivity (predicting correctly more points with convergence success).

We choose T to maximize the arithmetic mean of sensitivity and specificity. (We also tested the geometric and harmonic means, which behaved similarly.) Figure B.6(a) shows classifier performance as a function of T. We observe that there is a plateau in performance in the domain $T \in [0.55, 0.80]$, with the best performance achieved by a value of $T = 0.793$. As is evident in Figure B.6(b), with this value of T the classifier achieves sensitivity of approximately 90% and specificity of approximately 95%. As described in Chapter 4, this residual 5% failure rate (one minus the specificity) does not cause a problem in the optimization procedure.

Table B.3: Performance of regeneration block simulation convergence classifier.

Metric	Cross-validation $\hat{\mu}$	Cross-validation $\hat{\sigma}$	Test
AUC	0.953	0.021	0.977
Sensitivity	0.898	0.027	0.909
Specificity	0.956	0.052	1.0 (7/7)

Table B.3 reports performance metrics for the regeneration block simulation success predictor. The table includes metrics calculated both using fivefold cross-validation repeated 25 times, and verification using the test set, which was not used in training or in choosing metaparameters. This is the same test set that is described in Section B.2.1. The results indicate that the simulation success predictor has sensitivity of approximately 90% and specificity of approximately 95%.

A major concern for statistical prediction methods is overfitting. In this context, overfitting can be detected by observing algorithm performance differing greatly between the test set and the training set evaluated using cross-validation. If algorithm performance evaluated on the test set is significantly worse than performance evaluated using cross-validation on the training set, then the proxy model has been overfit and can be unreliable. We note that all of the performance metrics presented in Table B.3 for the test set are within $\approx 1\hat{\sigma}$ of the mean estimated using cross-validation. This indicates that our classifier has not been overfit.

B.2.4 Process column shell mass

The capital cost of the absorption and regeneration columns is calculated using a method based upon the mass of the shell. The mass of the shell m_{shell} [kg] is calculated as follows (Towler and Sinnott, 2013, pp 590-591):

$$m_{\text{shell}} = C_w \pi \rho_{\text{shell}} D_{\text{shell}} \left(Z_{\text{shell}} + 0.8 D_{\text{shell}}\right) t_{\text{shell}}, \tag{B.7}$$

where $C_w = 1.15$ is a constant that reflects the weight of extra parts of the shell such as manways and internal supports, ρ_{shell} [kg/m^3] is the density of the shell construction material, D_{shell} [m] is the diameter of the shell, Z_{shell} [m] is the height of the shell, and t_{shell} [m] is the thickness of the shell wall. We use $\rho_{\text{shell}} = 8,000$ kg/m^3 for stainless steel (Towler and Sinnott, 2013, p 281), and take Z_{shell} as 3 m greater than Z_{pack} to account for vertical allowances for column internals other than the packing material. We calculate D_{shell} as $D_{\text{pack}} + t_{\text{shell}}$, where D_{pack} [m] is the diameter of the column packing, which is a design decision variable determined in the optimization procedure.

The column shell wall thickness t_{shell} is determined by structural integrity requirements to resist hoop, longitudinal, and compressive stress. We calculate the minimum wall thickness for all three stresses, and take the greatest thickness given by these different considerations.

The minimum wall thickness required to withstand hoop stress is calculated as

$$t_{\text{hoop}} = \frac{p_{\text{regen}} D_{\text{pack}}}{2 S_{\text{max,ss}} E_{\text{joint}} - 1.2 p_{\text{regen}}}, \tag{B.8}$$

where p_{regen} [kPa] is the internal pressure of the regeneration column, $S_{\text{max,ss}} = 1.0342 \times 10^8$ [kPa] is the maximum allowable stress for stainless steel, and $E_{\text{joint}} = 0.65$ is the welded joint efficiency (Towler and Sinnott, 2013, pp 573-574, 577). The minimum wall thickness required to withstand longitudinal stress is calculated as follows (Towler and Sinnott, 2013, pp 573-574, 577):

$$t_{\text{hoop}} = \frac{p_{\text{regen}} D_{\text{pack}}}{4 S_{\text{max,ss}} E_{\text{joint}} - 0.8 p_{\text{regen}}}. \tag{B.9}$$

The procedure for calculating compressive stress requires an iterative approach because the weight of the column affects the compressive stress at the base of the column, which is where compressive stress is greatest. The iterative procedure consists of a one-dimensional search in wall thickness. For a given candidate wall thickness, we calculate the maximum tolerable compressive stress and the compressive stress

at the base of the column. The wall thickness is varied until the maximum tolerable compressive stress and the compressive stress at the base of the column are equal.

The maximum tolerable compressive stress for a steel column $S_{\text{compr,max}}$ [kPa] is calculated as $S_{\text{comp,max}} = [t_{\text{wall}}/(D_{\text{pack}} + t_{\text{wall}})](2 \times 10^7 \text{ kPa})$ (Towler and Sinnott, 2013, p 589). The compressive stress at the base of the column is calculated as $S_{\text{comp}} = (m_{\text{shell}} + m_{\text{internal}})\, g/(\pi D_{\text{shell}} t_{\text{wall}})$, where m_{internal} [kg] is the mass of the column internal contents (packing and fluid) and $g = 9.81$ m/s^2 is the gravitational constant (Towler and Sinnott, 2013, p 586). We calculate m_{internal} as twice the mass of the column packing material (we assume that the liquid held up by the column structure weighs as much as the packing material). The mass of the column packing material is calculated using the density of stainless steel and assuming a void fraction of 0.96 (note that the void fraction of Flexipac 1Y is 0.98 (Kister et al., 2007, p 14-62), but we use a lower void fraction to account for liquid volume and a safety factor).

We take the greatest minimum wall thickness based on the three stress calculations and add a corrosion allowance of 0.002 m. In addition, we require wall thickness to be at least 0.012 m because of practical considerations (Towler and Sinnott, 2013, pp 574-575). For most designs considered in Chapter 4, the determinant of shell wall thickness in both absorption and regeneration columns is either compressive stress or the 0.012 m practical minimum thickness.

B.2.5 Additional modeling details in the absorption and regeneration blocks

In this section we provide modeling details for the absorption and regeneration submodels that are not included in the earlier discussion. These details generally concern quantities relevant to energy duty in the CO_2 capture system and/or capital cost estimation. For the absorption block, we discuss the flue gas blower (which pressurizes flue gas feed to the absorption column), and the handling of makeup solvent. We also describe the regeneration block rich solvent inlet temperature consistency

calculation, the reboiler surface area calculation, the reboiler heat duty calculation, and the regeneration column condenser.

B.2.5.1 Flue gas blower

The flue gas blower overcomes the pressure drop in the absorption column. We need to evaluate flue gas blower work duty to accurately account for all work duties in the CO_2 capture system, and to calculate the capital cost of this component. Blower work $\dot{W}_{\text{blower}}$ [W] is calculated using the following relationship (Ulrich and Vasudevan, 2004, p 155):

$$\dot{W}_{\text{blower}} = \dot{m}_{\text{S2}} \left(\frac{R_{\text{fg}} T_{\text{S2}} k_{\text{fg}}}{k_{\text{fg}} - 1} \right) \left(\frac{1}{\eta_{\text{blower}}} \right) \left(\frac{p_{\text{S3}}}{p_{\text{S2}}} \right)^{\frac{k_{\text{fg}}-1}{k_{\text{fg}}}-1}. \tag{B.10}$$

Here, $\dot{m}_{\text{S2}}$ [kg/s] is the flue gas flow rate (equal in streams S2 and S3 in Figure B.1), R_{fg} [J/(kg-K)] is the gas constant (we absorb the molecular weight of flue gas into the universal gas constant), T_{S2} [K] is the temperature of the flue gas inlet to the blower, η_{blower} is the isentropic efficiency of the blower, k_{fg} is the ratio of the constant pressure and constant volume specific heat capacities of the flue gas, p_{S2} [kPa] is the inlet pressure of the blower, and p_{S3} [kPa] is the outlet pressure of the blower. We have $T_{\text{S2}} = 313$ K, $\eta_{\text{blower}} = 0.80$, $k_{\text{fg}} = 1.373$, and $p_{\text{S2}} = 101.3$ kPa. We calculate p_{S3} as the pressure drop across the absorption column, as predicted by the absorption block proxy model, plus 5 kPa. The flue gas is treated as an ideal gas.

B.2.5.2 Makeup solvent

Makeup solvent (stream S7 in Figure B.1) is added to the rich solvent stream (S6). The quantity of makeup solvent is important to calculate because it affects the feed solvent stream to the regeneration block. The flow rate and composition of the makeup solvent, which consists of water and MEA, is calculated from a mass balance on the flue gas over the absorption column. Depending on the design, approximately 90 %(wt.) of the makeup solvent is water, and approximately 10 %(wt.) is MEA. We

assume that the makeup solvent has negligible effect on the temperature of the rich solvent stream entering the rich-lean heat exchanger, so $T_{\mathrm{S8}} = T_{\mathrm{S7}}$. This is justified because the amount of makeup solvent is small: within the sample set, mean makeup flow rate is less than 3% of rich solvent flow rate by mass. (In some systems there may be a water wash of the treated flue gas exiting the absorption column to recover MEA entrained in the gas. This water wash, which is not considered in Chapter 4, would tend to decrease MEA loss and could have varying effects on water loss depending on design.) The CO_2 loading of the rich solvent is first calculated at the outlet of the absorption block (S5, S6), and then is recalculated using conservation of mass after the makeup solvent is added. This slightly decreases the CO_2 loading in the rich solvent after makeup is added (S8, S9). Note also that the mass flow rate of rich solvent is slightly greater after makeup solvent is introduced (S8, S9) than at the absorption block outlet (S5, S6).

B.2.5.3 Regeneration block rich solvent inlet temperature consistency

In the sampling step described in Section B.2.1, we perform full-physics regeneration block simulations with regeneration column rich solvent inlet temperature $T_{\mathrm{S9}} = T_{\mathrm{S9,regress}}$ calculated using Equation B.6. Because the value of $T_{\mathrm{S9,regress}}$ calculated by Equation B.6 deviates from the value of $T_{\mathrm{S9,rlhx}}$ calculated by the rich-lean heat exchanger, in the integrated proxy model we calculate a rate of 'makeup' heat $\dot{Q}_{\mathrm{C6,regen,makeup}}$ [W] to enforce temperature consistency and conservation of energy across the system. The makeup heat is calculated as $\dot{Q}_{\mathrm{C6,regen,makeup}} = c_{\mathrm{pS9}}\dot{m}_{\mathrm{S9}}\left(T_{\mathrm{S9,regress}} - T_{\mathrm{S9,rlhx}}\right)$. The makeup heat correction assumes that heat applied in the reboiler is a perfect substitute for lean solvent thermal energy content in terms of regeneration column and reboiler performance. This assumption is valid for small variations in lean solvent inlet temperature to the regeneration column, which is the case here.

B.2.5.4 Reboiler surface area

In the full-physics model, the reboiler is modeled as a heat source in the bottom stage of the regeneration column. In order to calculate the capital cost of the reboiler, we need to calculate the surface area of the reboiler. We make several modeling assumptions to enable this calculation.

We model the U-tube kettle reboiler as a heat exchanger with condensing steam on the hot side and solvent on the cool side. We use an approach temperature of 10 K which is enforced in the optimization constraints by requiring the pressure of steam supplied to the reboiler to correspond to a saturation temperature 10 K greater than the regeneration column lean solvent outlet temperature T_{S12}. We use the reboiler heat duty to calculate the reboiler surface area A_{reb} [m^2] as follows:

$$A_{\mathrm{reb}} = \frac{\dot{Q}_{\mathrm{heat,tot}}}{U_{\mathrm{reb}} \Delta T_{\mathrm{reb,lm}}}, \tag{B.11}$$

where $\dot{Q}_{\mathrm{heat,tot}}$ [W] is the total heat duty in the CO_2 capture system, U_{reb} [W/(m^2-K)] is the overall heat transfer coefficient in the reboiler, and $\Delta T_{\mathrm{reb,lm}}$ [K] is the log mean temperature difference in the reboiler (we assume that $\Delta T_{\mathrm{reb,lm}} = 10$ K, which is the reboiler approach temperature). We set $U_{\mathrm{reb}} = 1270$ W/(m^2-K) (Ulrich and Vasudevan, 2004, p 207).

B.2.5.5 Reboiler heat duty calculation

Reboiler heat duty is a key quantity calculated in the integrated proxy model because it represents the primary energy duty for the CO_2 capture process, and thus has a very significant effect on the evaluation of CO_2 capture system performance. In addition, this quantity is an input to the procedure used to calculate the surface area of the reboiler, described in Section B.2.5.4, which is used for calculating the capital cost of the reboiler. In a combined system with both regeneration and absorption, the regeneration block lean solvent outlet (stream S12 in Figure B.1) is the absorption block lean solvent feed (S15). Because we choose lean loading as a design variable,

the regeneration block is required to output solvent with the design lean loading. However, our regeneration block proxy model takes reboiler duty as an input and produces lean solvent as an output. Furthermore, the model requires conservation of mass across the entire CO_2 capture system, so the rate of CO_2 desorbed from the solvent must equal the rate of CO_2 absorbed into the solvent in the absorption block.

We therefore solve iteratively for reboiler duty to achieve the design lean solvent loading and to desorb CO_2 at a rate equal to that for CO_2 absorption in the absorption block. We accomplish this by performing a one-dimensional search in reboiler duty in the regeneration block proxy model (evaluating the regeneration block proxy model repeatedly with different levels of reboiler duty), once for lean solvent loading and once for CO_2 desorption rate. The reboiler heat duty calculated using these two alternative methods is usually very similar (within 2%). If the reboiler heat duties calculated using the two methods differ by less than 10%, the larger reboiler duty is used. If the reboiler heat duties differ by more than 10%, we interpret this as indicating a failure of mass balance in the system and treat the point as infeasible.

B.2.5.6 Regeneration block condenser

The condenser is part of the regeneration block and is modeled in Aspen Plus as a cooler and a flash drum arranged in series. It is necessary to calculate condenser surface area to evaluate the capital cost of this component. We treat the condenser as a countercurrent heat exchanger, and calculate the condenser surface area in the same manner as for the trim cooler, which we describe in Section B.3.4. We use a log mean temperature difference of 20 K and an overall heat transfer coefficient of $U = 200$ W/(m^2-K) (Ulrich and Vasudevan, 2004, p 206). Note that the value of U here is lower than in the rich-lean heat exchanger (described in Section B.3.3) and in the reboiler (described in Section B.2.5.4) because the condenser operates in a gas/liquid heat transfer regime, while the rich-lean heat exchanger operates in a liquid/liquid regime and the reboiler operates in a liquid/two-phase-condensing regime. In a similar vein, the temperature differential in the condenser (20 K) is larger than the 10 K pinches in the rich-lean heat exchanger and the reboiler. This

is because high efficiency is not of major importance here (because we are simply using cooling water), while in the other two units there is greater economic value in having small temperature gradients. Cooling water for the condenser is provided by the cooling tower (C11).

B.3 Additional components

In this section, additional components appearing in the integrated proxy model are discussed. The calculations presented here concern quantities that are used in evaluating capital cost and/or energy duty of the CO_2 capture system. The components considered include the direct contact cooler (C1 in Figure B.1), pumps (C4 and C10), rich-lean heat exchanger (C5), trim cooler (C9), and cooling tower (C11).

B.3.1 Direct contact cooler (C1)

The direct contact cooler cools the coal plant flue gas (stream S1 in Figure B.1) before it enters the absorption column. We calculate cooling duty of this component in order to evaluate its capital cost, and as part of the total cooling duty in the CO_2 capture system. This component is modeled in the full-physics model, but we calculate the cooling duty independently because the process is sufficiently simple that applying the statistical method would be unnecessarily complex. We calculate the cooling duty of the direct contact cooler $\dot{Q}_{\mathrm{dcc}}$ [W] as $\dot{Q}_{\mathrm{dcc}} = \dot{m}_{\mathrm{S1}} c_{\mathrm{pfg}} \Delta T_{\mathrm{fg,dcc}}$. Here $\dot{m}_{\mathrm{fg}}$ [kg/s] is the mass flow rate of flue gas, c_{pfg} [J/(kg-K)] is the specific heat capacity of flue gas, and $\Delta T_{\mathrm{fg,dcc}}$ [K] is the temperature change of the flue gas across the direct contact cooler. The model has a fixed direct contact cooler flue gas outlet temperature (S2) of 313 K. The direct contact cooler flue gas inlet (S1) is at a constant temperature of 390 K, so $\Delta T_{\mathrm{fg,dcc}} = 77$ K. Cooling water for the direct contact cooler is provided by the cooling tower (C11).

B.3.2 Pumps (C4 and C10)

We include two pumps in the model: pump C4 for the rich solvent outlet from the absorption block, and pump C10 for the lean solvent outlet from the regeneration block. The work duties for these pumps are calculated as part of evaluating the overall energy duty of the CO_2 capture system, and also are used to calculate the capital costs of these components. We assume that both of these pumps have an efficiency of $\eta_{\text{pump}} = 0.70$. Pump work $\dot{W}_{\text{pump}}$ [W] is calculated as $\dot{W}_{\text{pump}} = \dot{m}_{\text{pump}} \Delta p_{\text{pump}} / (\rho_{\text{pump}} \eta_{\text{pump}})$, where $\dot{m}_{\text{pump}}$ [kg/s] is the mass flow rate through the pump, $\Delta \dot{p}_{\text{pump}}$ [kPa] is the pressure rise across the pump, and ρ_{pump} [kg/m^3] is the density of the fluid being pumped (i.e., either rich or lean solvent). We assume 30 kPa in frictional pressure loss for both the lean and rich solvent streams. Therefore, the lean solvent pump overcomes a pressure drop of 30 kPa $+ \max(0, -p_{\text{regen,gauge}})$, and the rich solvent pump overcomes a pressure drop of 30 kPa $+ \max(0, p_{\text{regen,gauge}})$, where the gauge pressure is referenced to 101.3 kPa. Typically, $p_{\text{regen,gauge}}$ is in the range $\sim 50 - 150$ kPa because optimized designs have p_{regen} in the range $\sim 150 - 250$ kPa.

B.3.3 Rich-lean heat exchanger (C5)

The rich-lean heat exchanger is required for efficient facility operations because the regeneration block operates at relatively high temperature ($\sim$400 K) while the absorption block operates at relatively low temperature (feed solvent temperature of 313 K), and the two blocks provide solvent feed streams to each other. The regeneration block rich solvent feed exits the absorption block at $\sim$ 330 K (S5), and the absorption block lean solvent feed exits the regeneration block at $\sim$ 400 K (S12). The rich-lean heat exchanger submodel calculates several quantities of interest. The outlet temperatures of the lean and rich solvent streams (streams S13 and S9 in Figure B.1, respectively) are used as input values in other components of the CO_2 capture system, and the rich-lean heat exchanger surface area is used to calculate the capital cost of this component.

The following variables are inputs to the rich-lean heat exchanger submodel: lean solvent temperature T_{S12} [K], lean solvent flow rate $\dot{m}_{\mathrm{S12}}$ [kg/s], rich solvent inlet temperature T_{S8} [K], and rich solvent flow rate after addition of makeup solvent $\dot{m}_{\mathrm{S8}}$ [kg/s]. In our model of the rich-lean heat exchanger, we calculate the rich solvent outlet temperature T_{S9} and the lean solvent outlet temperature T_{S13} [K]. This requires the calculation of the rich-lean thermal energy transfer rate $\dot{Q}_{\mathrm{rlhx}}$ [W].

The fundamental governing equation of the heat exchanger is as follows:

$$\dot{Q}_{\mathrm{rlhx}} = \dot{m}_{\mathrm{lowcap}} c_{\mathrm{p}_{\mathrm{lowcap}}} \Delta T_{\mathrm{lowcap,out}} = \dot{m}_{\mathrm{highcap}} c_{\mathrm{p}_{\mathrm{highcap}}} \Delta T_{\mathrm{highcap,out}}, \tag{B.12}$$

where $\dot{m}_{\mathrm{lowcap}}$ [kg/s] is the mass flow rate of the low capacity stream, $c_{\mathrm{p}_{\mathrm{lowcap}}}$ [W/(kg-K)] is the specific heat capacity of the low capacity stream, and $\Delta T_{\mathrm{lowcap}}$ [K] is the temperature change of the low capacity stream across the heat exchanger. The term 'low capacity' refers to the stream (i.e., either lean solvent or rich solvent) with lower flowing heat capacity, where flowing heat capacity is calculated as $\dot{C}_{\mathrm{stream}} = \dot{m}_{\mathrm{stream}} c_{\mathrm{p}_{\mathrm{stream}}}$ [W/K]. Variable definitions are analogous for the high capacity stream.

For the low capacity stream, the outlet temperature is calculated as

$$T_{\mathrm{lowcap,out}} = T_{\mathrm{highcap,in}} \pm \Delta T_{\mathrm{pinch}}, \tag{B.13}$$

where $T_{\mathrm{highcap,in}}$ [K] is the temperature of the high capacity stream and $\Delta T_{\mathrm{pinch}}$ [K] is the pinch temperature, 10 K. In Equation B.13, the sign on $\Delta T_{\mathrm{pinch}}$ is $(-)$ if the lean solvent is the low capacity stream, and the sign is $(+)$ if the rich solvent is the low capacity stream.

The quantity $T_{\mathrm{highcap,out}}$ is calculated using the following equation:

$$T_{\mathrm{highcap,out}} - T_{\mathrm{highcap,in}} = \pm \frac{\dot{Q}_{\mathrm{rlhx}}}{\dot{C}_{\mathrm{lowcap}}}, \tag{B.14}$$

where $\dot{C}_{\mathrm{lowcap}}$ [W/K] is the flowing heat capacity of the low capacity stream. The sign on the right hand side of Equation B.14 is $(+)$ if the rich solvent is the high capacity stream and $(-)$ if the lean solvent is the high capacity stream. Equations B.12

and B.14 are solved simultaneously to determine T_{S9} and T_{S13}. In practice, in most systems the two streams have very similar flowing heat capacity. Because of this, the temperature changes of both streams across the rich-lean heat exchanger are roughly the same, and as a consequence both ends of the rich-lean heat exchanger have temperature difference of less than 15 K in most systems.

The surface area of the rich-lean heat exchanger is calculated under the assumption that the heat exchanger is a countercurrent heat exchanger (which is consistent with its treatment in the full-physics model). We used an overall heat transfer coefficient of $U_{\text{rlhx}} = 700$ W/(m^2-K) for heat exchangers with aqueous MEA liquids on both sides (Ulrich and Vasudevan, 2004, p 207). The rich-lean heat exchanger surface area A_{rlhx} [m^2] is calculated as $A_{\text{rlhx}} = \dot{Q}_{\text{rlhx}} / (U_{\text{rlhx}} \Delta T_{\text{lm,rlhx}})$. The log mean temperature difference across the heat exchanger, $T_{\text{lm,rlhx}}$ [K], is calculated as $\Delta T_{\text{lm,rlhx}} = (\Delta T_{\text{hot}} - \Delta T_{\text{cold}}) \,/\, (\ln \Delta T_{\text{hot}} - \ln \Delta T_{\text{cold}})$, where ΔT_{hot} [K] refers to the temperature difference at the hot end of the heat exchanger (i.e., $\Delta T_{\text{hot}} = T_{S12} - T_{S9}$), and ΔT_{cold} [K] refers to the temperature difference at the cold end of the heat exchanger (i.e., $\Delta T_{\text{cold}} = T_{S13} - T_{S8}$).

B.3.4 Trim cooler (C9)

The trim cooler takes the lean solvent outlet of the rich-lean heat exchanger and cools it further to 313 K, the design lean solvent inlet temperature for the absorption block. The surface area of the trim cooler is calculated to evaluate the capital cost of this component. We calculate the trim cooler surface area A_{trim} [m^2] as $A_{\text{trim}} = \dot{Q}_{\text{trim}} / (U_{\text{trim}} \Delta T_{\text{lm,trim}})$, where $\dot{Q}_{\text{trim}}$ [W] is the cooling duty, U_{trim} [W/(m^2-K)] is the overall heat transfer coefficient for the trim cooler, and $\Delta T_{\text{lm,trim}}$ [K] is the log mean temperature difference in the trim cooler.

We calculate $\dot{Q}_{\text{trim}}$ as $\dot{Q}_{\text{trim}} = \dot{m}_{S13} c_{\text{pS13}} \Delta T_{\text{trim}}$, where $\dot{m}_{S13}$ [kg/s] is the mass flow rate of lean solvent entering the trim cooler, c_{pS13} [J/(kg-K)] is the specific heat capacity of lean solvent, and ΔT_{trim} [K] is the temperature difference between the lean

solvent exiting the rich-lean heat exchanger and 313 K. We use $U_{\text{trim}} = 700$ W/(m^2-K) (Ulrich and Vasudevan, 2004, p 206), and assume $\Delta T_{\text{lm,trim}} = 20$ K. Cooling water for the trim cooler is provided by the cooling tower (C11).

B.3.5 Cooling tower (C11)

All of the coolers in the CO_2 capture process model use the cooling tower as a heat sink. We estimate capital cost of the cooling tower based upon the volumetric flow rate of water in the cooling tower, $\dot{V}_{\text{w,cool}}$ [m^3/s]. We calculate $\dot{V}_{\text{w,cool}}$ as follows (Ulrich and Vasudevan, 2004, p 367):

$$\dot{V}_{\text{cw,cool}} = \frac{\dot{Q}_{\text{cool,tot}}}{\rho_{\text{cw}} c_{\text{p}_{\text{cw}}} \Delta T_{\text{cw}}}, \tag{B.15}$$

where $\dot{Q}_{\text{cool,tot}}$ [W] is the total cooling duty required by the CO_2 capture system, ρ_{cw} [kg/m^3] is the density of water, and ΔT_{cw} [K] is the temperature change of water in the cooling tower. We use $\Delta T_{\text{cw}} = 15$ K (Ulrich and Vasudevan, 2004, p 367).

B.4 Capital cost estimation

For each component, depending upon data availability and quality, we employ either the Bare Module or Battery Limits method to calculate capital cost. Both of these methods are described in this section. We also discuss the capital cost estimation procedure for certain components, and present our treatment of interest during construction. The Bare Module method was employed in all of the simplified-capture calculations described in Chapters 2-3 and Appendix A. Some of the discussion below closely follows the descriptions of capital cost estimation in Chapter 2 and Appendix A.

Table B.4: Capital cost data for Bare Module method.

(a) Purchased equipment cost

Component	Size metric	Units	S_{ref}	$C_{\text{PE,ref}}$ [1,000$]	α	S_{max}	CEPCI	Reference
Heat exchanger*	Surface area	m^2	900	55	0.71	900	400	Ulrich and Vasudevan (2004, p 383)
Pump†	Work duty	kW	70	38	0.44	280	400	Ulrich and Vasudevan (2004, p 390-391)
Structured packing‡	Packed volume	m^3	1	3,537	1.0	–	400	Ulrich and Vasudevan (2004, p 389)
Direct contact cooler	Gas flow rate	m^3/s	382	17,600	0.60	–	394.3	Rubin et al. (2007b, p 19)
Cooling tower	Water flow rate	m^3/s	0.4	2,652	0.68	10	400	Ulrich and Vasudevan (2004, p 336)

* Carbon steel basis. † Cast iron basis. ‡ Stainless steel basis.

(b) Module factor

Component	Construction material	Module factor	Reference
Heat exchanger	Carbon steel/carbon steel*	3.2	Ulrich and Vasudevan (2004, pp 383-384)
Heat exchanger	Carbon steel/stainless steel*	4.1	Ulrich and Vasudevan (2004, pp 383-384)
Heat exchanger	Stainless steel/stainless steel*	5.8	Ulrich and Vasudevan (2004, pp 383-384)
Pump	Cast iron	3.5	Ulrich and Vasudevan (2004, pp 390-391)
Pump	Stainless steel	4.9	Ulrich and Vasudevan (2004, pp 390-391)
Direct contact cooler	–	1.0†	Rubin et al. (2007b, p 19)
Cooling tower	–	1.0‡	Ulrich and Vasudevan (2004, pp 336)

* Tube side/shell side. † Data provided as 'process facilities cost' in Rubin et al. (2007b) interpreted as equivalent to bare module cost. ‡ Cooling tower row in Table B.4(a) is for bare module cost.

B.4.1 Bare Module method

The Bare Module method described in Ulrich and Vasudevan (2004, 2009) was the method we used to estimate costs for heat integration components in Chapters 2 and 3. This approach is also used here for several components within the CO_2 capture system. In this method, the purchased equipment cost of a component, C_{PE} [\$], is calculated as follows:

$$C_{\mathrm{PE}} = C_{\mathrm{PE,ref}} \left(\frac{S}{S_{\mathrm{ref}}} \right)^{\alpha}, \tag{B.16}$$

where $C_{\mathrm{PE,ref}}$ [\$] is the purchased equipment cost of a reference component, S is the size of the component, S_{ref} is the size of the reference component, and α is a component-specific scaling exponent (available in the literature). Purchased equipment cost and module factor data for the Bare Module method are provided in Table B.4. The term 'CEPCI' refers to the Chemical Engineering Plant Cost Index, which measures escalation for chemical plant equipment and construction costs. All calculations in this work are performed using 2011 dollars, corresponding to a CEPCI of 585.7.

The purchased equpiment cost is then used to calculate the total capital cost C_{TC} [\$] as follows (Ulrich and Vasudevan, 2004):

$$C_{\mathrm{TC}} = C_{\mathrm{PE}} F_{\mathrm{BM}} F_{\mathrm{CF}} F_{\mathrm{AF}}, \tag{B.17}$$

where F_{BM} is a component-specific 'module factor' multiplier, $F_{\mathrm{CF}} = 1.18$ is the 'contingency and fee' multiplier, and $F_{\mathrm{AF}} = 1.30$ is the 'auxiliary facilities' multiplier. The module factor multiplier represents expenses such as piping, structural support, instrumentation, transportation, labor, insurance, and certain other activities, excluding auxiliary and off-site facilities. The contingency and fee multiplier represents other costs that can be expected from experience with construction of process facilities, and the auxiliary facilities multiplier represents costs associated with site preparation, auxiliary buildings, and off-site facilities (Ulrich and Vasudevan, 2004).

For components made from an expensive material such as stainless steel, we use a modified version of Equation B.17, as follows:

$$C_{\mathrm{TC}} = C_{\mathrm{PE}} F_{\mathrm{CF}} \left[F_{\mathrm{BM}}^{\mathrm{b}} \left(F_{\mathrm{AF}} - 1 \right) + F_{\mathrm{BM}}^{\mathrm{a}} \right], \tag{B.18}$$

where $F_{\mathrm{BM}}^{\mathrm{b}}$ is the module factor for a component fabricated from a less expensive material such as carbon steel or cast iron, and $F_{\mathrm{BM}}^{\mathrm{a}}$ is the module factor for a component fabricated from the more expensive material (Ulrich and Vasudevan, 2004). The quantity $F_{\mathrm{BM}}^{\mathrm{a}}$ includes all costs associated with making a component out of the more expensive material, including associated piping (Ulrich and Vasudevan, 2004). Equation B.18 reflects the fact that the cost of auxiliary facilities attributed to a component is not related to the construction material of that component. We use Equation B.18 for the following components: the rich and lean solvent pumps, the rich-lean heat exchanger, and the lean solvent trim cooler. These components are made of stainless steel to be corrosion-resistant because they interact directly with the solvent.

B.4.2 Battery Limits method

The Battery Limits method described in Towler and Sinnott (2013) is used for some components of the CO_2 capture system in Chapter 4, primarily where Ulrich and Vasudevan (2004) provide inadequate or less relevant capital cost data. In the Battery Limits method, the purchased equipment cost of a component is calculated as

$$C_{\mathrm{PE}} = a + bS^n, \tag{B.19}$$

where S is the size of the component (this is the same S as in the Bare Module method), and a, b and n are fitting constants (Towler and Sinnott, 2013). The total capital cost is then calculated as follows:

$$C_{\mathrm{TC}} = C_{\mathrm{PE}} F_{\mathrm{inst}} F_{\mathrm{OEC}}, \tag{B.20}$$

Table B.5: Capital cost data for Battery Limits method, CEPCI = 532.9. From Towler and Sinnott (2013, Chapter 7).

Component	Size metric	Units	a	b	n	$S_{\max}$	F_{inst}
Column vessel (stainless steel)	Shell mass	kg	17,400	79	0.85	250,000	2.4
Reboiler (stainless steel)	Surface area	m^2	29,000	400	0.9	500	3.7
Compressor	Work duty	kW	580,000	20,000	0.6	30,000	2.5

where F_{inst} is a component-specific 'installation factor' multiplier and $F_{\text{OEC}} = 1.82$ is the 'off-site, engineering, and contingency' (OEC, our wording) multiplier for fluid-handling facilities (Towler and Sinnott, 2013). The installation factor, which is analogous to the module factor in the Bare Module method, represents expenses such as construction, piping, instrumentation, transportation, labor, insurance, and certain other costs, excluding auxiliary buildings and off-site facilities, contingency, and engineering (Towler and Sinnott, 2013). The OEC multiplier for fluid-handling facilities represents expenses associated with auxiliary buildings and off-site facilities, engineering and design, and contingencies (Towler and Sinnott, 2013).

In the Battery Limits method, as in the Bare Module method, the use of more expensive construction materials requires special treatment. We account for the use of these materials in determining the installation factors given in Table B.5, in accordance with the procedure prescribed in Towler and Sinnott (2013, pp 330-331). As such, the data presented in Table B.5 are used directly with Equations B.19 and B.20 to calculate total capital cost.

B.4.3 Component-specific capital cost estimation details

The blower is treated as a compressor in the capital cost estimation. We model the compressor intercoolers as heat exchangers with tubes and shells constructed from carbon steel. The trim cooler and regeneration column condenser are treated as heat exchangers with stainless steel tubes and carbon steel shells, while the rich-lean heat exchanger has stainless steel tubes and shells. The lean and rich solvent pumps are constructed from stainless steel, as are the absorption and regeneration columns.

The packing material in both the absorption and regeneration columns is fabricated from stainless steel. We calculate the total capital cost for packing material using Equation B.17, rather than Equation B.18, because cost data for carbon steel structured packing are not available in our column packing material reference (Ulrich and Vasudevan, 2004).

If the number of CO_2 capture trains is greater than one, all trains are assumed to be identical. In this case the total capital cost is the capital cost for one train multiplied by the number of trains, except for the direct contact cooler, flue gas blower, and cooling tower. For these components, we calculate the capital cost of a single unit with sufficient capacity to supply all of the CO_2 capture trains.

B.4.4 Interest during construction

We assume a construction time of three years, uniform construction progress in time, and expenses incurred at midyear. We apply the same escalation factor and nominal discount rate as in the NPV calculation described in Chapter 4, namely escalation rate $r_{\text{esc}} = 0.033/\text{a}$ and nominal discount rate $r_{\text{disc}} = 0.11/\text{a}$. This results in a multiplicative factor of $F_{\text{IDC}} = 1.116$ to account for interest during construction, so that $C_{\text{TCR}} = C_{\text{TC}} F_{\text{IDC}}$.

B.5 Effect of integrated proxy model inaccuracy on TCR and NPV

In this section we describe our method of estimating the impact of prediction inaccuracy in the integrated proxy model on the objective functions of minimum TCR and maximum NPV. The three quantities considered are CO_2 capture rate, regeneration column flood fraction, and specific reboiler heat duty. The first two quantities affect

Table B.6: Integrated proxy model prediction error relative to full-physics model for Pareto-efficient points.

Quantity	Units	Scenario	Mean value*	Prediction error		
				Min	Max	Mean
CO_2 capture rate	kg CO_2/s	West Texas	54.65	+0.63	+2.59	+1.90
		India	48.78	+1.70	+2.60	+2.05
Regen. column flood fraction	–	West Texas	0.777	-0.071	+0.002	-0.024
		India	0.805	-0.047	-0.012	-0.040
Specific reboiler heat duty	MJ_{th}/kg CO_2	West Texas	3.78	-0.21	+0.16	-0.05
		India	3.75	-0.07	+0.02	-0.01

* Mean value for unique CO_2 capture systems of Pareto-efficient points, evaluated using Aspen Plus.

both TCR and NPV, while specific reboiler heat duty affects only NPV. This discussion focuses on the West Texas scenario, but very similar integrated proxy model performance is observed in the India scenario.

Table B.6 summarizes model accuracy for both the West Texas and India scenarios. The results in Table B.6 incorporate all unique CO_2 capture systems of Pareto-efficient full-system designs.

The CO_2 capture rate is consistently overpredicted in the West Texas scenario by a mean of 3.5%, which results in underprediction of capital cost for the CO_2 capture system. We estimate the increase in capital cost of the CO_2 capture system by linearly scaling the total capital cost of the CO_2 capture system for each Pareto-efficient point. For example, if CO_2 capture capacity is underpredicted by 3%, the total capital cost of the CO_2 capture system is increased by 3%. The range of adjustment to CO_2 capture system total capital cost from this effect in the West Texas scenario is +$2.2 million to +$8.9 million, or +1.0% to +4.8% of CO_2 capture system total capital cost.

The regeneration column flood fraction is underpredicted consistently, with mean prediction error in the West Texas scenario of $\varepsilon_{\text{flood}} = -0.024$. For some systems the underprediction of regeneration column flood fraction is not of concern because the full-physics model still evaluates regeneration column flood fraction as less than

0.80. However, for other systems the regeneration column flood fraction in Aspen Plus is greater than 0.80, meaning that the system is infeasible. For these systems, this has the effect of underpredicting capital cost because an increased regeneration column diameter is required to reduce flood fraction below 0.80. We estimate the required increase in regeneration column diameter by performing a one-dimensional search on regeneration column diameter to achieve prediction flood fraction less than $(0.795 - |\varepsilon_{\text{flood}}|)$ using the integrated proxy model. (In doing this, we assume that the integrated proxy model consistently predicts regeneration flood with error $\varepsilon_{\text{flood}}$ in the neighborhood of a given point.) This larger diameter is then used to calculate a revised total capital cost for the CO_2 capture system. The range of adjustment to CO_2 capture system total capital cost from this effect in the West Texas scenario is \$0 to +\$0.7 million (up to +0.4% of CO_2 capture system total capital cost).

Specific reboiler heat duty is underpredicted for some systems and overpredicted for others. This affects NPV because the amount of energy used for CO_2 capture affects the amount of electricity sold. Underpredicted specific reboiler heat duty leads to an overestimate of NPV, while overpredicted specific reboiler heat duty leads to an underestimate of NPV. This effect has no impact on the capital cost of the CO_2 capture system.

We re-evaluate all points along the Pareto frontier using revised total capital cost values for the CO_2 capture system (which incorporate the cost increases for both CO_2 capture rate and regeneration column flood fraction described above), and also apply the specific reboiler heat duty calculated in the full-physics model. For each Pareto-efficient point, this yields revised values of TCR and NPV. The ranges of NPV and TCR obtained after applying this procedure are summarized in Table 4.11.

B.6 Physical properties

Properties within the absorption and regeneration blocks are calculated with the Aspen Plus 7.3 data libraries. Outside these blocks, we do not use Aspen Plus for physical properties.

The specific heat capacity of the flue gas in the direct contact cooler is calculated using data provided in Poling et al. (2007, pp 2-156–2-163). Specific heat capacity of the MEA-water-CO_2 system as a function of temperature and CO_2 loading is interpolated from data given by Hilliard (2008, p 429) and Weiland et al. (1997). Density of the MEA-water-CO_2 system as a function of CO_2 loading and temperature is interpolated based on data given by Amundsen et al. (2009). We treat the compression block as acting on neat CO_2, with physical properties taken from the NIST Chemistry WebBook (Lemmon et al., 2015).

All pressures are absolute pressures except when stated otherwise.

B.7 Workflows

In this section we summarize the workflows used for the integrated proxy model and for the overall full-system optimization procedure of Chapter 4.

B.7.1 Integrated proxy model

A schematic of the workflow for constructing the integrated proxy model is shown in Figure B.7. The main steps in the workflow are as follows: 1) sampling, in which a set of points is constructed and evaluated in Aspen Plus; 2) model fitting, in which statistical proxy models are fit to the set of evaluated points; and 3) optimization-directed retraining, in which more points in the region of interest are identified and evaluated. In addition, we verify the model after model fitting and during the course of optimization-directed retraining. For all function evaluations performed during the course of an optimization, the capital cost of the CO_2 capture system is evaluated using the quantities calculated in the integrated proxy model.

A major purpose of the integrated proxy model is to calculate heat and work duties, which are used in evaluating the performance of the larger facility. We also calculate cooling duty to evaluate the capital cost of the cooling tower. Total duties of heat, cooling and work for the system are calculated as sums of the contributions of

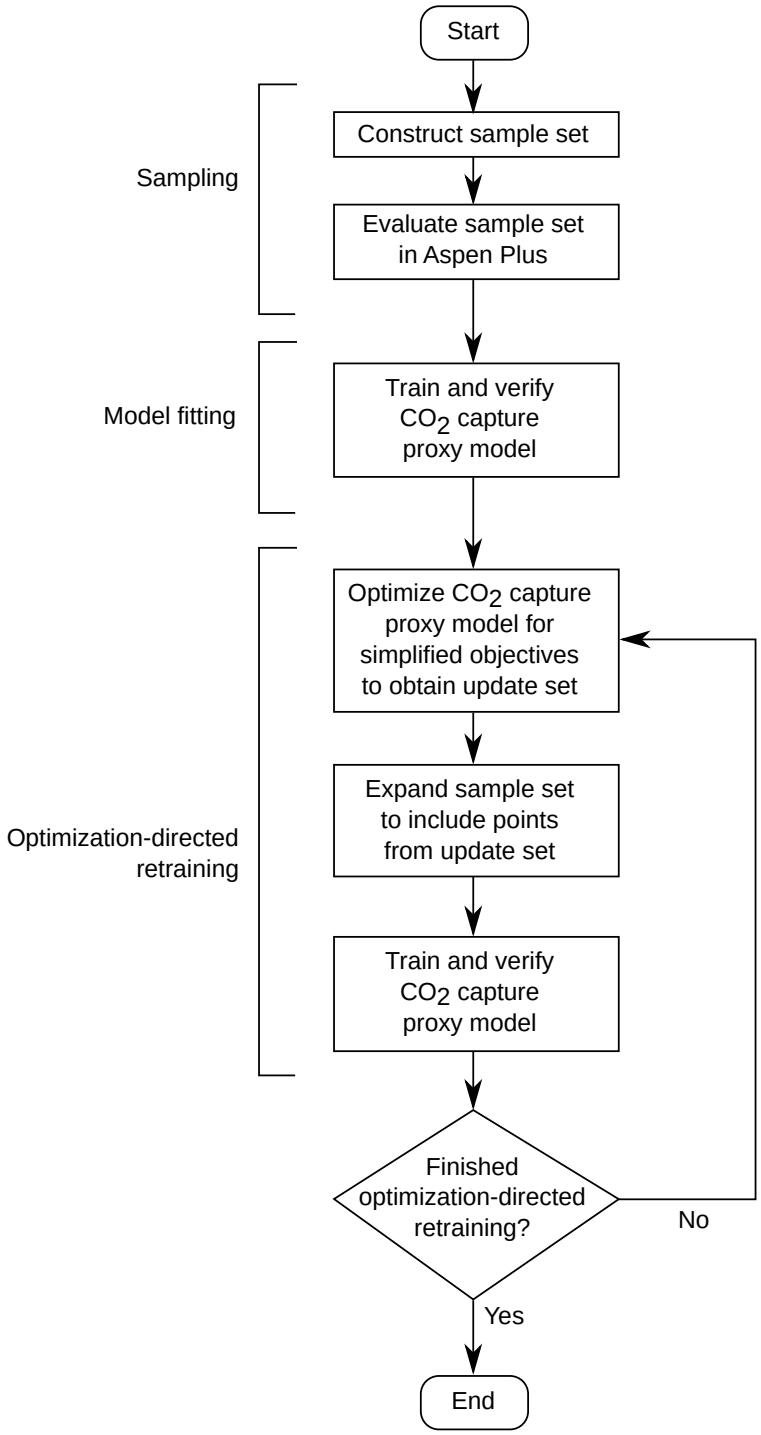

Figure B.7: Workflow for integrated proxy model.

each component, summarized below. All heat is supplied at the regeneration column reboiler, all work duty is supplied as electricity, and all cooling duty is provided by cooling water from the cooling tower. Heat and work duty are both used in the full model of the power station with CO_2 capture, while cooling duty is used in the calculation of capital cost of the cooling tower. The calculations are as follows:

Heat duty: $\dot{Q}_{\text{heat,tot}} = \dot{Q}_{\text{C6,reb}} + \dot{Q}_{\text{C6,regen,makeup}}$

Work duty: $\dot{W}_{\text{tot}} = \dot{W}_{\text{C10,richpump}} + \dot{W}_{\text{C10,leanpump}} + \dot{W}_{\text{C2,blower}} + \dot{W}_{\text{C8,comp}}$

Cooling duty: $\dot{Q}_{\text{cooling,tot}} = \dot{Q}_{\text{C1,dcc}} + \dot{Q}_{\text{C9,trim}} + \dot{Q}_{\text{C8,intercool}} + \dot{Q}_{\text{C7,condenser}}$

B.7.2 Optimization procedure

Figure B.8 depicts a schematic of the workflow used in the optimization procedure. We first construct the integrated proxy model using the workflow described in Section B.7.1. Next, we start the optimization algorithm. At each iteration, the PSO-MADS algorithm specifies a set of points to be evaluated. Each point is run in the integrated proxy model and heat integration model in sequence to evaluate the corresponding objective functions and constraint violations (if any) for each point. These values are then used in the optimization algorithm to inform the selection of the next set of points to evaluate. After we obtain the Pareto frontier from a full-system optimization, we evaluate the set of Pareto-efficient points using the full-physics model. The results of the full-physics model evaluations are used to calculate an adjusted capital cost for each Pareto-efficient point using the procedure described in Section B.5.

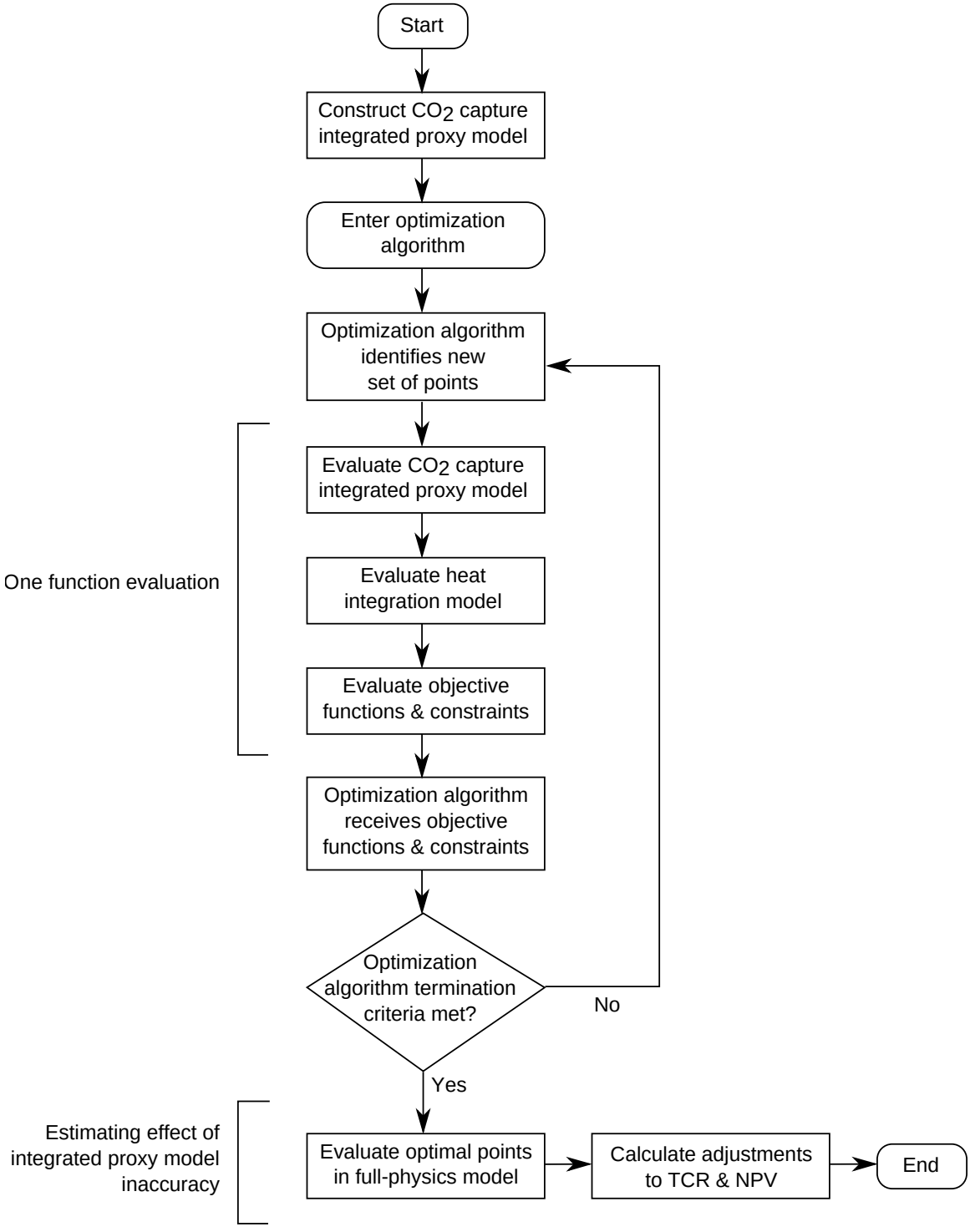

Figure B.8: Optimization procedure workflow.

Nomenclature (and page where symbol is defined)

Abbreviations

BiPSOMADS Bi-objective Particle Swarm Optimization – Mesh Adaptive Direct Search, page 31

CCGT Combined-cycle gas turbine, page 3

CCS Carbon dioxide capture and storage, page 1

CP Coal-fired power plant, page 16

GT Gas turbine, page 21

HRSG Heat recovery steam generator, page 4

IECM Integrated Environmental Control Model, page 17

MADS Mesh Adaptive Direct Search, page 10

MEA monoethanolamine CO_2 capture solvent, page 4

NPV Net present value (also V_{NP}), page 33

O&M Operations and maintenance, page 28

PSO Particle Swarm Optimization, page 10

TCR Total capital requirement (also C_{TCR}), page 25

Greek letters

α Capital cost scaling exponent, page 25

$\Delta h_{\mathrm{ST,actual}}$ [J/kg] Steam turbine stage change in enthalpy, page 134

Δp_{abs} [kPa] Absorption column pressure drop, page 66

Δp_{gas} [kPa] HRSG gas-side pressure drop, page 22

ΔT_{max} [W/K] HRSG element maximum possible temperature difference, page 110

$\Delta T_{\mathrm{rlhx,pinch}}$ [K] Rich-lean heat exchanger pinch temperature, 10 K, page 161

ε HRSG element effectiveness (state variable), page 108

ε_p Effectiveness of a single pass in a multi-pass heat exchanger, page 113

η_{fin} HRSG element fin efficiency, page 126

η_{ST} Steam turbine stage isentropic efficiency, page 134

μ_{g} [m] Flue gas dynamic viscosity, page 125

Ω Optimization bound constraints, page 30

ρ_{gas} [kg/m^3] HRSG element gas density, page 132

σ_{pass} [m^2] HRSG element reference average gas-side surface area per pass, page 122

υ [W/(m^2-K)] HRSG element overall heat transfer relation, page 111

Lower case Latin letters

c Optimization general constraints (can be nonlinear), page 30

$c_{\mathrm{p_g}}$ [J/(kg-K)] Specific heat capacity of gas turbine flue gas, page 110

$d_{\mathrm{t,i}}$ [m] HRSG element tube inner diameter, page 124

$d_{\mathrm{t,o}}$ [m] HRSG element tube outer diameter, page 122

$h_{\mathrm{ST,in}}$ [J/kg] Steam turbine stage inlet enthalpy, page 134

$h_{\mathrm{w,in}}$ [J/kg] Enthalpy of water at inlet of an HRSG element, page 23

$h_{\mathrm{w,out}}$ [J/kg] Enthalpy of water at outlet of an HRSG element, page 23

k_{fin} [W/(m-K)] HRSG element fin construction material thermal conductivity, page 127

k_{g} [W/(m-K)] HRSG flue gas thermal conductivity, page 126

k_{wall} [W/(m-K)] Thermal conductivity of HRSG element wall construction material, page 125

l_{fin} [m] HRSG element fin height, page 123

l_{HRSG} [m] HRSG face height, page 123

$\dot{m}_{\mathrm{g}}$ [kg/s] Mass flow rate of gas turbine flue gas, page 110

$\dot{m}_{\mathrm{w}}$ [kg/s] Mass flow rate of water in an HRSG element, page 23

$\dot{m}_{\mathrm{CP,fgCO_2}}$ [kg CO_2/s] Coal plant flue gas CO_2 emission rate (before CO_2 capture), page 36

$\dot{m}_{\mathrm{S1}}$ [kg flue gas/s] Flue gas flow rate, page 70

$\dot{m}_{\mathrm{S10}}$ [kg CO_2/s] Regeneration column CO_2 desorption rate, page 66

$\dot{m}_{\mathrm{S12}}$ [kg/s] Mass flow rate of lean solvent inlet to rich-lean heat exchanger, page 177

$\dot{m}_{\mathrm{S15}}$ [kg solvent/s] Lean solvent flow rate, page 70

$\dot{m}_{\mathrm{S2}}$ [kg/s] Flue gas flow rate, page 171

$\dot{m}_{\mathrm{S5,S6}}$ [kg/s] Rich solvent flow rate, page 66

$\dot{m}_{S8}$ [kg/s] Mass flow rate of rich solvent inlet to rich-lean heat exchanger, page 177

$\dot{m}_{S9}$ [kg/s] Rich solvent flow rate, page 66

m_{shell} [kg] Process column shell mass, page 168

$n_{fin,t}$ HRSG element number of fins per tube, page 123

n_{rows} HRSG element number of rows of tubes, page 123

p_{ext} [kPa] HRSG pressure of steam extraction, page 34

$p_{HP,rh}$ [kPa] HRSG high pressure reheat steam pressure, page 34

p_{pl} [kPa] HRSG water/steam stream pressure (pl denotes pressure level), page 21

p_{regen} [kPa] Regeneration column operating pressure, page 66

p_{S3} [kPa] Flue gas blower outlet pressure, page 171

$p_{ST,out}$ [kPa] Steam turbine stage outlet pressure, page 134

$\tilde{\dot{q}}_{reb}$ [MJ_{th}/kg CO_2] Approximate specific reboiler heat duty (used in sampling), page 73

r_{disc} Nominal discount rate, 11.0%/a, page 34

r_{esc} Escalation rate, 3.3%/a, page 33

r_{hyd} [m] HRSG element hydraulic radius, page 132

s_{ff} [m] HRSG element open space between fins, page 125

s_{fin} [m] HRSG element fin spacing, fin center to fin center, page 122

s_{GT} [MW_e] Capacity of a single gas turbine, page 34

$s_{ST,in}$ [J/(kg-K)] Steam turbine stage inlet entropy, page 134

s_t [m] HRSG element tube spacing measured from center to center, page 123

t_{fin} [m] HRSG element fin thickness, page 122

$n_{\text{t,row}}$ HRSG element number of tubes per tube row, page 123

t_{shell} [m] Process column shell wall thickness, page 169

t_{tw} [m] HRSG element tube wall thickness, page 122

u_{g} [W/(m^2-K)] HRSG element gas-side heat transfer coefficient, page 119

$u_{\text{g,0}}$ [W/(m^2-K)] HRSG element uncorrected gas-side heat transfer coefficient (excludes fin effects), page 126

$\mathbf{u}_{\text{ops}}$ [$/MWh] Strike prices (operational decision variables), page 34

u_{w} [W/(m^2-K)] HRSG element water-side heat transfer coefficient, page 119

w_{HRSG} [m] HRSG width, page 122

Upper case Latin letters

A_{cond} [m^2] Condenser contact area, page 135

A_{ff} [m^2] HRSG element gas-side free flow area, page 123

A_{g} [m^2] HRSG element gas-side surface area, page 21

$A_{\text{g,fin}}$ [m^2] HRSG element fin-only gas-side surface area, page 126

$A_{\text{m,bare}}$ [m^2] HRSG element mean of inner and outer bare tube surface areas, page 125

A_{reb} [m^2] Reboiler surface area, page 173

A_{rlhx} [m^2] Rich-lean heat exchanger surface area, page 178

$A_{\text{t,i,bare}}$ [m^2] HRSG element bare tube inner surface area, equal to the water-side contact area, page 123

$A_{\text{t,o}}$ [m^2] HRSG element tube outer surface area including fins, page 124

$A_{\mathrm{t,o,bare}}$ [m^2] HRSG element bare tube (excluding fins) outer surface area, page 123

A_{trim} [m^2] Trim cooler surface area, page 178

$A_{\mathrm{tr,o}}$ [m^2] HRSG element tube row outer surface area including fins, page 124

$A_{\mathrm{t,xsec}}$ [m^2] HRSG element tube inner cross-sectional area, page 124

A_{w} [m^2] HRSG element water-side surface area, page 119

C_{cap} [kg CO_2/s] CO_2 capture system capacity, page 34

C_{fuel} [$] Total cost of fuel in one year, page 33

C_{g} [W/K] HRSG element gas stream capacity, page 109

C_{max} [W/K] HRSG element higher capacity stream, page 112

C_{min} [W/K] HRSG element lower capacity stream, page 109

$C_{\mathrm{O\&M}}$ [$] Total cost of operations and maintenance in one year, page 33

C_{PE} [$] Component purchased equipment cost, page 25

$C_{\mathrm{PE,ref}}$ [$] Component reference purchased equipment cost (Bare Module capital cost estimation method), page 25

$C_{\mathrm{tax},y}$ [$] corporate income tax paid in each year, page 33

C_{TCR} [$] Total capital requirement (TCR), page 30

C_{w} [W/K] HRSG element water stream capacity, page 109

D_{abs} [m] Packing diameter of the absorption column, page 86

D_{pack} [m] Process column packing diameter (either D_{abs} or D_{regen}), page 169

D_{regen} [m] Regeneration column packed diameter, page 66

D_{shell} [m] Process column shell diameter, page 169

L_{elem} [m] Bulk length of HRSG element, page 132

L_{lean} [mol CO_2/mol MEA] Lean solvent CO_2 loading, page 86

L_{S9} [mol CO_2/mol MEA] Rich solvent CO_2 loading, page 66

N_{elem} Number of HRSG elements, page 108

N_{pl} Number of HRSG pressure levels, page 109

N_{TU} Heat exchanger number of transfer units (nondimensional size), page 109

P_{op} [$] Capitalized operating profits, page 30

$\dot{Q}_{\text{actual}}$ [W_{th}] Actual heat transfer rate within an HRSG element, page 23

$\dot{Q}_{\text{C6,regen,makeup}}$ [W] Regeneration block 'makeup' heat, page 172

$\dot{Q}_{\text{cond}}$ [MW_{th}] Regeneration column condenser duty, page 66

$\dot{Q}_{\text{cool,tot}}$ [W] Total cooling duty required by the CO_2 capture system, page 179

$\dot{Q}_{\text{dcc}}$ [W] Cooling duty for direct contact cooler, page 175

$\dot{Q}_{\text{heat,tot}}$ [W] Total heat duty in CO_2 capture system, page 173

$\dot{Q}_{\text{max}}$ [W_{th}] Theoretical maximum heat transfer rate within an HRSG element, page 23

$\dot{Q}_{\text{reb}}$ [MW_{th}] Reboiler heat duty, page 66

$\dot{Q}_{\text{rlhx}}$ [W] Thermal energy transfer rate in rich-lean heat exchanger, page 177

R [J/(mol-K)] Universal gas constant, page 157

R_{cond} [m^2-K/W] Thermal conductive resistance of HRSG element construction material, page 119

R_{elec} [$] Revenue from electricity sales in one year, page 33

$R_{\text{L/G}}$ [kg solvent/kg flue gas] Liquid/gas flow rate ratio (L/G ratio), page 70

S_{ref} Reference size of a component (Bare Module capital cost estimation method), page 25

$\bar{T}_{\text{g}}$ [K] HRSG element mean flue gas temperature, page 110

$T_{\text{g,in}}$ [K] Flue gas temperature at HRSG element inlet (state variable), page 109

$T_{\text{g,out}}$ [K] Flue gas temperature at HRSG element outlet (state variable), page 109

T_{S12} [K] Temperature of lean solvent inlet to rich-lean heat exchanger, page 177

T_{S13} [K] Temperature of lean solvent outlet from rich-lean heat exchanger, page 177

T_{S2} [kg/s] Flue gas temperature inlet to flue gas blower, page 171

T_{S9} [K] Temperature of rich solvent outlet from rich-lean heat exchanger, page 161

$T_{\text{w,in}}$ [J/kg] Temperature of water at inlet of an HRSG element, page 23

$T_{\text{w,out}}$ [J/kg] Temperature of water at outlet of an HRSG element, page 23

U [W/(m^2-K)] Overall heat transfer coefficient, page 22

UA_{g} [W/K] HRSG element heat transfer size, page 22

U_{ref} [W/(m^2-K)] HRSG element constant reference overall heat transfer, page 111

V_{NP} [$] Net present value (NPV), page 30

$\dot{V}_{\text{w,cool}}$ [m^3/s] Cooling tower water volumetric flow rate, page 179

$\dot{W}_{\text{blower}}$ [W] Flue gas blower work duty, page 171

$\dot{W}_{\text{pump}}$ [W] Pump work duty, page 176

$\dot{W}_{\text{ST}}$ [W] Steam turbine stage power output, page 134

Z_{abs} [m] Absorption column packed height, page 86

Z_{regen} [m] Regeneration column packed height, page 66

Z_{shell} [m] Process column shell height, page 169

List of references

M. Abramson, C. Audet, G. Couture, J. Dennis, Jr., S. Le Digabel, and C. Tribes. The NOMAD project. Software available at http://www.gerad.ca/nomad. URL `http://www.gerad.ca/nomad`.

M. J. Albrecht, S. R. Sedlak, R. Jain, E. L. Wells, and J. G. DiVitto. Use of a vertical separator design for a natural circulation HRSG boiler. In *Power-Gen International Conference, Dec. 11-13, 2012, Orlando, FL, USA*, number Technical Paper BR-1891, 2012. URL `http://www.babcock.com/library/Documents/BR-1891.pdf`.

T. G. Amundsen, L. E. Oi, and D. A. Eimer. Density and viscosity of monoethanolamine + water + carbon dioxide from (25 to 80) °C. *Journal of Chemical & Engineering Data*, 54(11):3096–3100, 2009. doi: 10.1021/je900188m.

APX Group. UKPX RPD historical data, 2014. URL `http://www.apxgroup.com/market-results/apx-power-uk/ukpx-rpd-historical-data/`. Accessed June 2014.

A. Arce, N. Mac Dowell, N. Shah, and L. Vega. Flexible operation of solvent regeneration systems for CO_2 capture processes using advanced control techniques: Towards operational cost minimisation. *International Journal of Greenhouse Gas Control*, 11:236–250, 2012. doi: 10.1016/j.ijggc.2012.09.004.

C. Audet, G. Svard, and W. Zghal. Multiobjective optimization through a series of single-objective formulations. *SIAM Journal on Optimization*, 19(1):188–210, 2008. doi: 10.1137/060677513.

C. Audet, S. Le Digabel, and C. Tribes. NOMAD user guide. Technical Report G-2009-37, Les cahiers du GERAD, 2009. URL http://www.gerad.ca/NOMAD/Downloads/user_guide.pdf.

A. M. Bassily. Modeling, numerical optimization, and irreversibility reduction of a triple-pressure reheat combined cycle. *Energy*, 32(5):778–794, 2007. doi: 10.1016/j.energy.2006.04.017.

C. F. Beaton. *Heat Exchanger Design Handbook*, volume 5, Physical Properties, Chapter 5.5.12, Thermal and mechanical properties of heat exchanger construction materials, pages 5.5.12-1 – 5.5.12-13. Hemisphere Publishing (Taylor & Francis), New York, 1983.

M. B. Berkenpas, K. Kietzke, H. Mantripragada, S. McCoy, E. S. Rubin, P. L. Versteeg, and H. Zha. IECM technical documentation updates final report. Technical Report DE-AC26-04NT41917, National Energy Technology Laboratory, Carnegie Mellon University, Pittsburgh, PA, USA, Nov. 2009. URL http://www.cmu.edu/epp/iecm/.

Black & Veatch. Cost and performance data for power generation technologies. Technical report, Prepared for the National Renewable Energy Laboratory, February 2012. URL http://bv.com/docs/reports-studies/nrel-cost-report.pdf.

A. Booker, J. Dennis, J.E., P. Frank, D. Serafini, V. Torczon, and M. Trosset. A rigorous framework for optimization of expensive functions by surrogates. *Structural Optimization*, 17(1):1–13, 1999. doi: 10.1007/BF01197708.

M. E. Boot-Handford, J. C. Abanades, E. J. Anthony, M. J. Blunt, S. Brandani, N. Mac Dowell, J. R. Fernandez, M.-C. Ferrari, R. Gross, J. P. Hallett, R. S. Haszeldine, P. Heptonstall, A. Lyngfelt, Z. Makuch, E. Mangano, R. T. J. Porter, M. Pourkashanian, G. T. Rochelle, N. Shah, J. G. Yao, and P. S. Fennell. Carbon capture and storage update. *Energy & Environmental Science*, 7:130–189, 2014. doi: 10.1039/C3EE42350F.

R. Brasington and H. Herzog. Dynamic response of monoethanolamine (MEA) CO_2 capture units. In *Carbon Management Technology Conference, Feb. 7-9, 2012, Orlando, FL, USA*, number 151075-MS, 2012. doi: 10.7122/151075-MS.

J. L. Bravo, J. A. Rocha, and J. R. Fair. Mass transfer in gauze packings. *Hydrocarbon Processing*, 64(1):91–95, 1985.

J. L. Bravo, J. A. Rocha, and J. R. Fair. A comprehensive model for the performance of columns containing structured packings. *Institution of Chemical Engineers Symposium Series*, 128:A489–A507, 1992.

P. G. Brodrick, C. A. Kang, A. R. Brandt, and L. J. Durlofsky. Optimization of carbon-capture-enabled coal-gas-solar power generation. *Energy*, 79(2015):149–162, 2015. doi: 10.1016/j.energy.2014.11.003.

W. M. Budzianowski. Negative carbon intensity of renewable energy technologies involving biomass or carbon dioxide as inputs. *Renewable and Sustainable Energy Reviews*, 16(9):6507–6521, 2012. doi: 10.1016/j.rser.2012.08.016.

M. Bui, I. Gunawan, V. Verheyen, P. Feron, E. Meuleman, and S. Adeloju. Dynamic modelling and optimisation of flexible operation in post-combustion CO_2 capture plants—a review. *Computers & Chemical Engineering*, 61:245–265, 2014. doi: 10.1016/j.compchemeng.2013.11.015.

R. L. Burden and J. D. Faires. *Numerical Analysis*. Thomson Brooks/Cole, Belmont, CA, USA, 8th edition, 2005.

C. Casarosa, F. Donatini, and A. Franco. Thermoeconomic optimization of heat recovery steam generators operating parameters for combined plants. *Energy*, 29 (3):389–414, 2004. doi: 10.1016/S0360-5442(02)00078-6.

H. Chalmers and J. Gibbins. Initial evaluation of the impact of post-combustion capture of carbon dioxide on supercritical pulverised coal power plant part load performance. *Fuel*, 86(14):2109–2123, 2007. doi: 10.1016/j.fuel.2007.01.028.

H. Chalmers, M. Lucquiaud, J. Gibbins, and M. Leach. Flexible operation of coal fired power plants with postcombustion capture of carbon dioxide. *Journal of Environmental Engineering*, 135(6):449–458, 2009. doi: 10.1061/(ASCE)EE.1943-7870.0000007.

H. Chalmers, M. Leach, and J. Gibbins. Built-in flexibility at retrofitted power plants: What is it worth and can we afford to ignore it? *Energy Procedia*, 4:2596–2603, 2011. doi: 10.1016/j.egypro.2011.02.158. 10th International Conference on Greenhouse Gas Control Technologies (GHGT-10), Sept. 19-23, 2010, Amsterdam, The Netherlands.

Q. Chen, C. Kang, and Q. Xia. Modeling flexible operation mechanism of CO_2 capture power plant and its effects on power-system operation. *IEEE Transactions on Energy Conversion*, 25(3):853–861, 2010. doi: 10.1109/TEC.2010.2051948.

Y. Choi. *Simultaneous Analysis and Design in PDE-Constrained Optimization*. PhD thesis, Stanford University, December 2012. URL `http://web.stanford.edu/group/SOL/dissertations/Youngsoo_thesis.pdf`.

S. M. Cohen, G. T. Rochelle, and M. E. Webber. Turning CO_2 capture on and off in response to electric grid demand: A baseline analysis of emissions and economics. *Journal of Energy Resources Technology*, 132(2):021003, 2010. doi: 10.1115/1.4001573.

S. M. Cohen, G. T. Rochelle, and M. E. Webber. Optimizing post-combustion CO_2 capture in response to volatile electricity prices. *International Journal of Greenhouse Gas Control*, 8:180–195, 2012. doi: 10.1016/j.ijggc.2012.02.011.

J. G. Collier and J. R. Thome. *Convective Boiling and Condensation*. Clarendon Press, Oxford, UK, 3rd edition, 1994.

I. Couckuyt, A. Forrester, D. Gorissen, F. D. Turck, and T. Dhaene. Blind kriging: Implementation and performance analysis. *Advances in Engineering Software*, 49 (3):1–13, 2012. doi: 10.1016/j.advengsoft.2012.03.002.

I. Couckuyt, T. Dhaene, and P. Demeester. ooDACE toolbox: A flexible object-oriented kriging implementation. *Journal of Machine Learning Research*, 15:3183–3186, 2014. URL `http://jmlr.org/papers/v15/couckuyt14a.html`.

J. R. Couper, D. W. Hertz, and F. L. Smith. Process Economics. In: D. W. Green and R. H. Perry, editors, *Perry's Chemical Engineers' Handbook*, chapter 9, pages 9-1 – 9-56. McGraw-Hill, New York, 8th edition, 2007.

A. W. Dowling and L. T. Biegler. A framework for efficient large scale equation-oriented flowsheet optimization. *Computers & Chemical Engineering*, 72:3–20, 2015. doi: 10.1016/j.compchemeng.2014.05.013.

A. W. Dowling, J. P. Eason, J. Ma, D. C. Miller, and L. T. Biegler. Coal oxycombustion power plant optimization using first principles and surrogate boiler models. *Energy Procedia*, 63:352–361, 2014. doi: 10.1016/j.egypro.2014.11.038. 12th International Conference on Greenhouse Gas Control Technologies (GHGT-12), Oct. 6-9, 2014, Austin, TX, USA.

Electric Reliability Council of Texas. Historical DAM load zone and hub prices. URL `http://www.ercot.com/mktinfo/prices/`. Accessed July 2013.

B. Elliston, M. Diesendorf, and I. MacGill. Simulations of scenarios with 100% renewable electricity in the Australian national electricity market. *Energy Policy*, 45: 606–613, 2012. doi: 10.1016/j.enpol.2012.03.011.

K. Farhat and S. M. Benson. A technical assessment of CO_2 interim storage in deep saline aquifers. *International Journal of Greenhouse Gas Control*, 15:200–212, 2013. doi: 10.1016/j.ijggc.2013.02.018.

R. Farmer, editor. *Gas Turbine World: 2010 GTW Handbook*, volume 28. Pequot Publishing, Fairfield, CT, USA, 2010.

A. Franco and N. Giannini. Optimum thermal design of modular compact heat exchangers structure for heat recovery steam generators. *Applied Thermal Engineering*, 25(8-9):1293–1313, 2005. doi: 10.1016/j.applthermaleng.2004.08.018.

A. Franco and N. Giannini. A general method for the optimum design of heat recovery steam generators. *Energy*, 31(15):3342–3361, 2006. doi: 10.1016/j.energy.2006.03.005.

A. Franco and A. Russo. Combined cycle plant efficiency increase based on the optimization of the heat recovery steam generator operating parameters. *International Journal of Thermal Sciences*, 41(9):843–859, 2002. doi: 10.1016/S1290-0729(02)01378-9.

J. H. Friedman. Greedy function approximation: A gradient boosting machine. *The Annals of Statistics*, 29(5):1189–1232, 2001. doi: 10.1214/aos/1013203451.

V. Ganapathy. *Waste Heat Boiler Deskbook*. The Fairmont Press, Lilburn, GA, USA, 1991.

V. Ganapathy. *Steam Plant Calculations Manual*. Marcell Dekker, New York, 2nd edition, 1993.

V. Ganapathy. Heat recovery steam generators: understanding the basics. *Chemical Engineering Progress (CEP Magazine)*, pages 32–45, August 1996.

E. Godoy, S. J. Benz, and N. J. Scenna. A strategy for the economic optimization of combined cycle gas turbine power plants by taking advantage of useful thermodynamic relationships. *Applied Thermal Engineering*, 31(5):852–871, 2011. doi: 10.1016/j.applthermaleng.2010.11.004.

T. Grant, D. Morgan, and K. Gerdes. Carbon dioxide transport and storage costs in NETL studies. Technical Report DOE/NETL-2013/1614, National Energy Technology Laboratory, March 2013.

K. M. Guthrie. Data and techniques for preliminary capital cost accounting. *Chemical Engineering*, 76(6):114–142, 1969.

T. Harkin, A. Hoadley, and B. Hooper. Using multi-objective optimisation in the design of CO_2 capture systems for retrofit to coal power stations. *Energy*, 41: 228–235, 2012a. doi: 10.1016/j.energy.2011.06.031.

T. Harkin, A. Hoadley, and B. Hooper. Optimisation of power stations with carbon capture plants—the trade-off between costs and net power. *Journal of Cleaner Production*, 34:98–109, 2012b. doi: 10.1016/j.jclepro.2011.12.032.

E. K. Hart and M. Z. Jacobson. A Monte Carlo approach to generator portfolio planning and carbon emissions assessments of systems with large penetrations of variable renewables. *Renewable Energy*, 36(8):2278–2286, 2011. doi: 10.1016/j.renene.2011.01.015.

E. K. Hart and M. Z. Jacobson. The carbon abatement potential of high penetration intermittent renewables. *Energy & Environmental Science*, 5:6592–6601, 2012. doi: 10.1039/C2EE03490E.

M. M. F. Hasan, R. C. Baliban, J. A. Elia, and C. A. Floudas. Modeling, simulation, and optimization of postcombustion CO_2 capture for variable feed concentration and flow rate. 1. Chemical absorption and membrane processes. *Industrial & Engineering Chemistry Research*, 51(48):15642–15664, 2012. doi: 10.1021/ie301571d.

T. Hastie, R. Tibshirani, and J. Friedman. *The Elements of Statistical Learning*. Springer, New York, 2nd edition, 2009.

M. D. Hilliard. *A Predictive Thermodynamic Model for an Aqueous Blend of Potassium Carbonate, Piperazine, and Monoethanolamine for Carbon Dioxide Capture from Flue Gas*. PhD thesis, University of Texas at Austin, May 2008. URL `http://repositories.lib.utexas.edu/handle/2152/3900`.

Indian Energy Exchange. Area prices, 2014. URL `http://www.iexindia.com/marketdata/areaprice.aspx`. Accessed June 2014.

International Energy Agency, Gas, Coal and Power Division. Medium-term coal market report 2012. Technical report, International Energy Agency, 2012.

International Energy Agency, Renewable Energy Division. Technology roadmap: Solar photovoltaic energy 2014 edition. Technical report, International Energy Agency, 2014.

O. J. Isebor. *Derivative-Free Optimization for Generalized Oil Field Development*. PhD thesis, Stanford University, 2013. URL `https://pangea.stanford.edu/ERE/pdf/pereports/PhD/Isebor2013.pdf`.

O. J. Isebor and L. J. Durlofsky. Biobjective optimization for general oil field development. *Journal of Petroleum Science and Engineering*, 119:123–138, 2014. doi: 10.1016/j.petrol.2014.04.021.

O. J. Isebor, L. J. Durlofsky, and D. Echeverria Ciaurri. A derivative-free methodology with local and global search for the constrained joint optimization of well locations and controls. *Computational Geosciences*, 18(3–4):463–482, 2014. doi: 10.1007/s10596-013-9383-x.

O. Islegen and S. Reichelstein. Carbon capture by fossil fuel power plants: An economic analysis. *Management Science*, 57(1):21–39, 2011. doi: 10.1287/mnsc.1100.1268.

M. S. Jassim and G. T. Rochelle. Innovative absorber/stripper configurations for CO_2 capture by aqueous monoethanolamine. *Industrial & Engineering Chemistry Research*, 45(8):2465–2472, 2006. doi: 10.1021/ie050547s.

I. Jayaweera, P. Jayaweera, R. Elmore, J. Bao, and S. Bhamidi. Update on mixed-salt technology development for CO_2 capture from post-combustion power stations. *Energy Procedia*, 63(0):640–650, 2014. doi: 10.1016/j.egypro.2014.11.070. 12th International Conference on Greenhouse Gas Control Technologies (GHGT-12), Oct. 6-9, 2014, Austin, TX, USA.

C. A. Kang, A. R. Brandt, and L. J. Durlofsky. Optimal operation of an integrated energy system including fossil fuel power generation, CO_2 capture and wind. *Energy*, 36(12):6806–6820, 2011. doi: 10.1016/j.energy.2011.10.015.

C. A. Kang, A. R. Brandt, and L. J. Durlofsky. Impact of CO_2 emissions policy and system configuration on optimal operation of an integrated fossil-renewable energy park. In *Carbon Management Technology Conference, Feb. 7-9, 2012, Orlando, FL, USA*, number CMTC 151446, 2012. doi: 10.7122/151446-MS.

A. G. Kaviri, M. N. M. Jaafar, T. M. Lazim, and H. Barzegaravval. Exergoenvironmental optimization of heat recovery steam generators in combined cycle power plant through energy and exergy analysis. *Energy Conversion and Management*, 67:27–33, 2013. doi: 10.1016/j.enconman.2012.10.017.

W. M. Kays and A. L. London. *Compact Heat Exchangers*. McGraw-Hill, New York, 3rd edition, 1984.

R. Kehlhofer, R. Bachmann, H. Nielsen, and J. Warner. *Combined-cycle gas and steam turbine power plants*. PennWell, Tulsa, OK, USA, 2nd edition, 1999.

R. Khalilpour. Multi-level investment planning and scheduling under electricity and carbon market dynamics: Retrofit of a power plant with PCC (post-combustion carbon capture) processes. *Energy*, 64:172–186, 2014. doi: 10.1016/j.energy.2013.10.086.

R. Khalilpour and A. Abbas. HEN optimization for efficient retrofitting of coal-fired power plants with post-combustion carbon capture. *International Journal of Greenhouse Gas Control*, 5(2):189–199, 2011. doi: 10.1016/j.ijggc.2010.10.006.

T. S. Kim. Comparative analysis on the part load performance of combined cycle plants considering design performance and power control strategy. *Energy*, 29(1): 71–85, 2004. doi: 10.1016/S0360-5442(03)00157-9.

T. S. Kim and S. T. Ro. The effect of gas turbine coolant modulation on the part load performance of combined cycle plants. Part 2: Combined cycle plant. *Proceedings of the Institution of Mechanical Engineers, Part A: Journal of Power and Energy*, 211(6):453–459, Sept. 1997. doi: 10.1243/0957650981537348.

H. Z. Kister, P. M. Mathias, D. E. Steinmeyer, W. R. Penney, B. B. Crocker, and J. R. Fair. Equipment for distillation, gas absorption, phase dispersion, and phase separation. In: D. W. Green and R. H. Perry, editors, *Perry's Chemical Engineers' Handbook*, chapter 14, pages 14-1 – 14-129. McGraw-Hill, New York, 8th edition, 2007.

A. Kothandaraman. *Carbon Dioxide Capture by Chemical Absorption: A Solvent Comparison Study.* PhD thesis, Massachusetts Institute of Technology, June 2010. URL `http://sequestration.mit.edu/pdf/Anusha_Kothandaraman_thesis_June2010.pdf`.

A. Kothandaraman, L. Nord, O. Bolland, H. J. Herzog, and G. J. McRae. Comparison of solvents for post-combustion capture of CO_2 by chemical absorption. *Energy Procedia*, 1:1373–1380, February 2009. doi: 10.1016/j.egypro.2009.01.180. 9th International Conference on Greenhouse Gas Control Technologies (GHGT-9), Nov. 16-20, 2008, Washington DC, USA.

S. Le Digabel. Algorithm 909: NOMAD: Nonlinear optimization with the MADS algorithm. *ACM Transactions on Mathematical Software*, 37(4):1–15, 2011. doi: 10.1145/1916461.1916468.

E. W. Lemmon, M. O. McLinden, and D. G. Friend. Thermophysical properties of fluid systems. In: P. J. Linstrom and W. G. Mallard, editors, *NIST Chemistry WebBook, NIST Standard Reference Database Number 69.* National Institute of Standards and Technology, Gaithersburg, MD, USA. URL `http://webbook.nist.gov`. Accessed Jan. 2015.

N. Mac Dowell and N. Shah. Identification of the cost-optimal degree of CO_2 capture: An optimisation study using dynamic process models. *International Journal of Greenhouse Gas Control*, 13:44–58, 2013. doi: 10.1016/j.ijggc.2012.11.029.

N. Mac Dowell and N. Shah. The multi-period optimisation of an amine-based CO_2 capture process integrated with a super-critical coal-fired power station for flexible operation. *Computers & Chemical Engineering*, 74:169–183, 2015. doi: 10.1016/j.compchemeng.2015.01.006.

J. I. Manassaldi, S. F. Mussati, and N. J. Scenna. Optimal synthesis and design of heat recovery steam generation (HRSG) via mathematical programming. *Energy*, 36(1):475–485, 2011. doi: 10.1016/j.energy.2010.10.017.

M. T. Mansouri, P. Ahmadi, A. G. Kaviri, and M. N. M. Jaafar. Exergetic and economic evaluation of the effect of HRSG configurations on the performance of combined cycle power plants. *Energy Conversion and Management*, 58:47–58, 2012. doi: 10.1016/j.enconman.2011.12.020.

E. Martelli, E. Amaldi, and S. Consonni. Numerical optimization of heat recovery steam cycles: Mathematical model, two-stage algorithm and applications. *Computers & Chemical Engineering*, 35(12):2799–2823, 2011. doi: 10.1016/j.compchemeng.2011.04.015.

E. Martelli, L. O. Nord, and O. Bolland. Design criteria and optimization of heat recovery steam cycles for integrated reforming combined cycles with CO_2 capture. *Applied Energy*, 92:255–268, 2012. doi: 10.1016/j.apenergy.2011.10.043.

B. Metz, O. Davidson, H. de Coninck, M. Loos, and L. Meyer, editors. *IPCC Special Report on Carbon Dioxide Capture and Storage*. Cambridge University Press, Cambridge, UK, 2005.

M. Mohagheghi and J. Shayegan. Thermodynamic optimization of design variables and heat exchangers layout in HRSGs for CCGT, using genetic algorithm. *Applied Thermal Engineering*, 29(2–3):290–299, 2009. doi: 10.1016/j.applthermaleng.2008.02.035.

R. H. Myers, D. C. Montgomery, and C. M. Andersoon-Cook. *Response Surface Methodology: Process and Product Optimization Using Designed Experiments*. John Wiley & Sons, Hoboken, NJ, USA, 3rd edition, 2009.

G. Nellis and S. Klein. *Heat Transfer*. Cambridge University Press, Cambridge, UK, 2009.

T. Neveux, Y. L. Moullec, J.-P. Corriou, and E. Favre. A rigorous optimization method of operating parameters for amine-based CO_2 capture processes. *Energy Procedia*, 37:1821–1829, 2013. doi: 10.1016/j.egypro.2013.06.060. 11th International Conference on Greenhouse Gas Technologies (GHGT-11), Nov. 18-22, 2012, Kyoto, Japan.

L. O. Nord and O. Bolland. HRSG design for integrated reforming combined cycle with CO_2 capture. *Journal of Engineering for Gas Turbines and Power*, 133(1): 011702–1–011702–7, 2011. doi: 10.1115/1.4001822.

E. Norouzi, M. Mehrgoo, and M. Amidpour. Geometric and thermodynamic optimization of a heat recovery steam generator: A constructal design. *Journal of Heat Transfer*, 134:111801–1–111801–12, November 2012. doi: 10.1115/1.4007070.

S. Pelster. *Environomic Modeling and Optimization of Advanced Combined Cycle Cogeneration Power Plants Including CO_2 Separation Options*. PhD thesis, Ecole Polytechnique Federale de Lausanne, 1998. Thesis No 1791.

S. Pelster, D. Favrat, and M. R. von Spakovsky. The thermoeconomic and environomic modeling and optimization of the synthesis, design, and operation of combined cycles with advanced options. *Journal of Engineering for Gas Turbines and Power*, 123(4):717–726, 2001. doi: 10.1115/1.1366323.

B. E. Poling, J. M. Prausnitz, and J. P. O'Connell. *The Properties of Gases and Liquids*. McGraw-Hill, New York, 5th edition, 2000.

B. E. Poling, G. H. Thomson, D. G. Friend, R. L. Rowley, and W. V. Wilding. Physical and Chemical Data. In: D. W. Green and R. H. Perry, editors, *Perry's Chemical Engineers' Handbook*, chapter 2, pages 2-1 – 2-517. McGraw-Hill, New York, 8th edition, 2007.

J. Pye. Freesteam Project. URL `http://freesteam.sourceforge.net/`. Accessed Feb. 2013.

N. V. Queipo, R. T. Haftka, W. Shyy, T. Goel, R. Vaidyanathan, and P. K. Tucker. Surrogate-based analysis and optimization. *Progress in Aerospace Sciences*, 41(1): 1–28, 2005. doi: 10.1016/j.paerosci.2005.02.001.

A. Ragland and W. Stenzel. Combined cycle heat recovery optimization. In *Proceedings of the 2000 International Joint Power Generation Conference, Miami Beach, FL, USA, July 23-26, 2000*, number IJPGC2000-15031. ASME.

G. Rochelle, E. Chen, S. Freeman, D. V. Wagener, Q. Xu, and A. Voice. Aqueous piperazine as the new standard for CO_2 capture technology. *Chemical Engineering Journal*, 171(3):725–733, 2011. doi: 10.1016/j.cej.2011.02.011.

L. M. Romeo, I. Bolea, Y. Lara, and J. M. Escosa. Optimization of intercooling compression in CO_2 capture systems. *Applied Thermal Engineering*, 29(8-9):1744–1751, 2009. doi: 10.1016/j.applthermaleng.2008.08.010.

E. Rubin, M. Berkenpas, and C. Zaremsky. *User Manual: Integrated Environmental Control Model*. Carnegie Mellon University, Pittsburgh, PA, USA, 2007a. URL `https://www.cmu.edu/epp/iecm/IECM_Publications/2007ra%20Rubin%20et%20al,%20IECM%20User.pdf`.

E. S. Rubin, A. B. Rao, and M. B. Berkenpas. Development and application of optimal design capability for coal gasification systems technical documentation: Oxygen-based combustion systems (oxyfuels) with carbon capture and storage (CCS). Technical report, Carnegie Mellon University, Pittsburgh, PA, USA, May 2007b. URL `https://www.cmu.edu/epp/iecm/IECM_Publications/2007rd%20Rao%20et%20al,%20IECM%20Oxy%20Tech.pdf`.

J. Schuetter, S. Mishra, P. R. Ganesh, and D. Mooney. Building statistical proxy models for CO_2 geologic sequestration. *Energy Procedia*, 63:3702–3714, 2014. doi: 10.1016/j.egypro.2014.11.399. 12th International Conference on Greenhouse Gas Control Technologies (GHGT-12), Oct. 6-9, 2014, Austin, TX, USA.

R. K. Shah and D. P. Sekulic. *Fundamentals of Heat Exchanger Design*. John Wiley & Sons, Hoboken, NJ, USA, 2003.

M. G. Shirangi and L. J. Durlofsky. Closed-loop field development optimization under uncertainty. In *SPE Reservoir Simulation Symposium, Feb. 23-25, 2015, Houston, TX, USA*, number SPE 173219. Society of Petroleum Engineers. doi: 10.2118/173219-MS.

D. Steiner and J. Taborek. Flow boiling heat transfer in vertical tubes correlated by an asymptotic model. *Heat Transfer Engineering*, 13(2):43–89, 1992. doi: 10.1080/01457639208939774.

S. J. Tewalt, H. E. Belkin, J. R. SanFilipo, M. D. Merrill, C. A. Palmer, P. D. Warwick, A. W. Karlsen, R. B. Finkelman, and A. J. Park. Chemical analyses in the world coal quality inventory, version 1.1, July 2011. URL `http://pubs.usgs.gov/of/2010/1196/`. Open-File Report 2010-1196.

H. Thee, Y. A. Suryaputradinata, K. A. Mumford, K. H. Smith, G. da Silva, S. E. Kentish, and G. W. Stevens. A kinetic and process modeling study of CO_2 capture with MEA-promoted potassium carbonate solutions. *Chemical Engineering Journal*, 210:271–279, 2012. doi: 10.1016/j.cej.2012.08.092.

G. Towler and R. Sinnott. *Chemical Engineering Design: Principles, Practice and Economics of Plant and Process Design*. Butterworth-Heinemann, Oxford, UK, 2nd edition, 2013.

R. E. Tsai, A. F. Seibert, R. B. Eldridge, and G. T. Rochelle. A dimensionless model for predicting the mass-transfer area of structured packing. *AIChE Journal*, 57(5): 1173–1184, 2011. doi: 10.1002/aic.12345.

G. D. Ulrich and P. T. Vasudevan. *Chemical Engineering Process Design and Economics: A Practical Guide*. Process Publishing, Durham, NH, USA, 2nd edition, 2004.

G. D. Ulrich and P. T. Vasudevan. Capital costs quickly calculated: estimating capital costs early can prevent unnecessary expenditures on dead-end projects. *Chemical Engineering*, pages 46–52, April 2009.

US Energy Information Administration. Short-term energy outlook custom table builder query. URL `http://www.eia.doe.gov/emeu/steo/pub/cf_query/index.cfm`. Accessed Sept. 2013.

US Energy Information Administration. Coal transportation rates to the electric power sector. URL `http://www.eia.gov/coal/transportationrates/`. Accessed June 2014.

US Energy Information Administration. Coal news and markets archive. URL `http://www.eia.gov/coal/news_markets/archive/`. Accessed June 2014.

US Environmental Protection Agency. Standards of performance for greenhouse gas emissions from new stationary sources: Electric utility generating units, September 2013. URL `http://www2.epa.gov/sites/production/files/2013-09/documents/20130920proposal.pdf`.

US Federal Energy Regulatory Commission. FERC: Other Markets–LNG–Archives. URL `http://www.ferc.gov/market-oversight/othr-mkts/lng/archives.asp`. Accessed June 2014.

US Federal Reserve Bank. Data download program. URL `http://www.federalreserve.gov/datadownload/Choose.aspx?rel=H10`. Accessed June 2014.

US Internal Revenue Service. Publication 946: How to depreciate property, Feb. 2013. URL `http://www.irs.gov/pub/irs-pdf/p946.pdf`.

P. Versteeg, D. L. Oates, E. Hittinger, and E. S. Rubin. Cycling coal and natural gas-fired power plants with CCS. *Energy Procedia*, 37:2676–2683, 2013. doi: 10.1016/j.egypro.2013.06.152. 11th International Conference on Greenhouse Gas Technologies (GHGT-11), Nov. 18-22, 2012, Kyoto, Japan.

W. Wagner, J. R. Cooper, A. Dittmann, J. Kijima, H.-J. Kretzschmar, A. Kruse, R. Mares, K. Oguchi, H. Sato, I. Stöcker, et al. The IAPWS industrial formulation 1997 for the thermodynamic properties of water and steam. *Journal of Engineering for Gas Turbines and Power*, 122(1):150–182, 2000. doi: 10.1115/1.483186.

R. L. Webb and N.-H. Kim. *Principles of Enhanced Heat Transfer*. Taylor & Francis, Boca Raton, FL, USA, 2nd edition, 2005.

R. H. Weiland, J. C. Dingman, and D. B. Cronin. Heat capacity of aqueous monoethanolamine, diethanolamine, n-methyldiethanolamine, and n-methyldiethanolamine-based blends with carbon dioxide. *Journal of Chemical & Engineering Data*, 42(5):1004–1006, 1997. doi: 10.1021/je960314v.

N. Woudstra, T. Woudstra, A. Pirone, and T. van der Stelt. Thermodynamic evaluation of combined cycle plants. *Energy Conversion and Management*, 51(5):1099–1110, 2010. doi: 10.1016/j.enconman.2009.12.016.

A. Yang and Y. Cui. Global coal risk assessment: Data analysis and market research. Nov. 2012. URL `http://www.wri.org/sites/default/files/pdf/global_coal_risk_assessment.pdf`. WRI Working Paper.

M. Zaman and J. H. Lee. Optimization of the various modes of flexible operation for post-combustion CO_2 capture plant. *Computers & Chemical Engineering*, 75:14–27, 2015. doi: 10.1016/j.compchemeng.2014.12.017.

Y. Zhang, H. Chen, C.-C. Chen, J. M. Plaza, R. Dugas, and G. T. Rochelle. Rate-based process modeling study of CO_2 capture with aqueous monoethanolamine solution. *Industrial & Engineering Chemistry Research*, 48:9233–9246, 2009. doi: 10.1021/ie900068k.

Y. Zhao, H. Chen, M. Waters, and D. N. Mavris. Modeling and cost optimization of combined cycle heat recovery generator systems. In *Proceedings of ASME Turbo Expo 2003 Power of Land, Sea, and Air, June 16-19, Atlanta, GA, USA*, number ASME-GT-2003-38568, 2003. URL `http://hdl.handle.net/1853/6362`.

S. Ziaii, S. Cohen, G. T. Rochelle, T. F. Edgar, and M. E. Webber. Dynamic operation of amine scrubbing in response to electricity demand and pricing. *Energy Procedia*, 1:4047–4053, 2009a. doi: 10.1016/j.egypro.2009.02.211. 9th International Conference on Greenhouse Gas Control Technologies (GHGT-9), Nov. 16-20, 2008, Washington DC, USA.

S. Ziaii, G. T. Rochelle, and T. F. Edgar. Dynamic modeling to minimize energy use for CO_2 capture in power plants by aqueous monoethanolamine. *Industrial & Engineering Chemistry Research*, 48(13):6105–6111, 2009b. doi: 10.1021/ie801385q.

D. J. Zigrang and N. D. Sylvester. Explicit approximations to the solution of Colebrook's friction factor equation. *AIChE Journal*, 28(3):514–515, 1982. doi: 10.1002/aic.690280323.